Skoltech

Skolkovo Institute of Science and Technology

Design, Modeling, and Control of Cable-suspended Aerial Manipulator

Doctoral Thesis

by

Yuri Sarkisov

Doctoral Program in Engineering Systems

Supervisor

Associate Professor Dzmitry Tsetserukou

Skolkovo Institute of Science and Technology

Co-Supervisor

Dr.-Ing. habil. Konstantin Kondak

German Aerospace Center (DLR)

Co-Supervisor

Dr.-Ing. Christian Ott

German Aerospace Center (DLR)

Moscow - 2022

I hereby declare that the work presented in this thesis was carried out by myself at DLR Institute of Robotics and Mechatronics (Wessling) and Skolkovo Institute of Science and Technology (Moscow), except where due acknowledgment is made, and has not been submitted for any other degree.

Candidate (Yuri Sarkisov):

Supervisor (Assoc. Prof. Dzmitry Tsetserukou):

Co-Supervisor (Dr.-Ing. habil. Konstantin Kondak):

Co-Supervisor (Dr.-Ing. Christian Ott):

Design, Modeling, and Control of Cable-suspended Aerial Manipulator

by

Yuri Sarkisov

Submitted to the Skoltech Space Center
on February 2022, in partial fulfillment of the requirements for the
Doctoral Program in Engineering Systems

Abstract

Aerial manipulation is a modern and prospective field in interaction robotics with many industrial applications in remotely located and dangerous environments. The typical aerial manipulator is a flying system; the manipulation is conducted by utilizing a robotic arm, while the translation of the arm's base in the space is done by an aerial vehicle. Such systems have found utilization in the inspection of different structures, e.g., bridges, electric lines, and pipelines, assembly/repair of remote constructions, and various operations in conditions hazardous or dangerous for human safety, e.g., decommissioning damaged nuclear power plants.

Despite the functional benefits, the manipulator serves as an additional payload, requiring more powerful actuation and, consequently, a bigger flying vehicle. Thus, the high risk of a collision between the aerial vehicle and the obstacles in a complex environment imposes restrictions on aerial manipulation in industry. To overcome this issue and achieve higher safety, a novel approach, a cable-suspended aerial manipulator, is recently proposed. Instead of attaching a robotic manipulator directly to an aerial carrier, it can be mounted on a compact actuated platform, which is suspended by a cable on the external mobile crane and responsible for the system stabilization and non-vertical motion. However, due to the physics of the suspended aerial manipulator, static and dynamics disturbances occur during manipulation that affect the system: pendulum-like cable oscillations due to external perturbation or the platform tilt because of the robotic arm weight.

To this end, this thesis brings three major contributions that jointly aim at the development of the control framework and the extensive investigation of the described cable-suspended aerial manipulation concept.

We first present an approach for oscillation damping of the critical pendulum-like motion caused by suspension cable. It turns out that the considered concept of the aerial manipulation might be modeled by a double pendulum with a first bob corresponding to the mobile crane's hook and the second - to the platform itself. The main challenge is the presence of only one onboard Inertial Measurement Unit sensor, which does not provide complete information on the system state, i.e., crane's chain motion remains unknown. Moreover, common onboard actuation for aerial vehicles, propeller-based actuation, is integrated at the platform, so we cannot affect pendulum joints directly. To cope with these difficulties, we design a controller motivated by a simplified model. The proposed controller is very simple

yet robust to uncertainties. Moreover, we propose a gain tuning rule by formulating the proposed controller in the form of output feedback Linear Quadratic Regulator problem. Consequently, it is possible to dampen oscillations with minimal energy consumption quickly. The proposed approach is validated through simulations and experiments aimed at the robustness investigation with respect to the influence of the unmodeled aspects such as wind, robotic arm motion, suspension point motion, and others.

Additionally, to achieve smooth manipulation of the aerial system, we introduce a winch-based actuation for the cable-suspended aerial manipulator. Three controllable rigging cables link the suspension point (the crane's hook) with the platform and allow to change its translational pose. Such an actuation approach reduces the effect of disturbing gravitational torque caused by the robotic arm weigh distribution on the aerial base. In order to coordinate robotic arm and winch dynamics, a Hierarchical impedance-based Whole-Body Controller is elaborated. It resolves two tasks: keeping the robotic arm end effector at the desired pose and shifting the platform Center Of Mass to the location with zero torque due to Gravity. Additionally, in order to pass torque commands to the position-controlled winch motors, the admittance interface is accommodated. The performance of the introduced actuation system under the considered control strategy is validated through experimental studies.

Finally, it is worth highlighting that research work in the scope of this thesis was conducted within the H2020 AEROARMS project, which addresses the development of the aerial manipulation technologies for industrial inspection and maintenance. Therefore, the last contribution of this thesis is devoted to the extensive field investigation of the system demonstrator under the developed controllers in industrial-like conditions. It should allow validating the performance, safety, and robustness of the overall framework. The prepared industrial-like environment is complex due to various obstacles in close proximity and challenging due to wind and absence of a direct line of sight. Three industrial scenarios are implemented for investigation of the concept and controllers efficiency: deployment of a mobile inspection robot at the remotely-located pipe, peg-in-hole assembly, and turning a valve.

The research results significantly update the state of the art in the aerial manipulation field and facilitate the topic toward the enhanced technology readiness level.

Publications

Lead author

1. Yuri S Sarkisov, Min Jun Kim, Andre Coelho, Dzmitry Tsetserukou, Christian Ott, and Konstantin Kondak. Optimal oscillation damping control of cable-suspended aerial manipulator with a single imu sensor. In *2020 IEEE International Conference on Robotics and Automation (ICRA)*, pages 5349–5355. IEEE, 2020. doi:10.1109/ICRA40945.2020.9197055

2. Yuri S Sarkisov, Min Jun Kim, Davide Bicego, Dzmitry Tsetserukou, Christian Ott, Antonio Franchi, and Konstantin Kondak. Development of SAM: cable-suspended aerial manipulator. In *2019 International Conference on Robotics and Automation (ICRA)*, pages 5323–5329. IEEE, 2019. doi:10.1109/ICRA.2019.8793592

Co-author

1. Andre Coelho, Yuri S Sarkisov, Jongseok Lee, Ribin Balachandran, Antonio Franchi, Konstantin Kondak, and Christian Ott. Hierarchical control of redundant aerial manipulators with enhanced field of view. In *2021 International Conference on Unmanned Aircraft Systems (ICUAS)*, pages 994–1002. IEEE, 2021b

2. Andre Coelho, Yuri Sarkisov, Xuwei Wu, Hrishik Mishra, Harsimran Singh, Alexander Dietrich, Antonio Franchi, Konstantin Kondak, and Christian Ott. Whole-body teleoperation and shared control of redundant robots with applications to aerial manipulation. *Journal of Intelligent & Robotic Systems*, 102 (1):1–22, 2021a

3. Jongseok Lee, Ribin Balachandran, Yuri S Sarkisov, Marco De Stefano, Andre Coelho, Kashmira Shinde, Min Jun Kim, Rudolph Triebel, and Konstantin Kondak. Visual-inertial telepresence for aerial manipulation. In *2020 IEEE International Conference on Robotics and Automation (ICRA)*, pages 1222–1229. IEEE, 2020. doi:10.1109/ICRA40945.2020.9197394

4. Chiara Gabellieri, Yuri S Sarkisov, Andre Coelho, Lucia Pallottino, Konstantin Kondak, and Min Jun Kim. Compliance control of cable-suspended aerial ma-

nipulator using hierarchical control framework. In *2020 IEEE/RSJ International Conference on Intelligent Robots and Systems (IROS)*, pages 7196–7202. IEEE/RSJ, 2020. doi:10.1109/IROS45743.2020.9340703

Side topic

1. Yuri S Sarkisov, Grigoriy A Yashin, Evgeny V Tsykunov, and Dzmitry Tsetserukou. Dronegear: A novel robotic landing gear with embedded optical torque sensors for safe multicopter landing on an uneven surface. *IEEE Robotics and Automation Letters*, 3(3):1912–1917, 2018a. doi:10.1109/LRA.2018.2806080

2. Yuri S Sarkisov, Grigoriy A Yashin, Evgeny V Tsykunov, and Dzmitry Tsetserukou. Dronegear: a compliant robotic landing gear for multicopters. In *3-rd Skoltech-MIT conference: Collaborative Solutions for Next Generation Education, Science and Technology*. Skoltech, 2018b

To my beloved family and friends

Acknowledgments

Every adventure has its end, they said. So, mine led me to the doctorate accomplishment at the most innovative and technological Russian university, Skolkovo Institute of Science and Technology (Skoltech). It was full of excitement, exploration, joy, and, especially luck which gave me a golden opportunity to perform the research in the dreamland of every roboticist, Institute of Robotics and Mechatronics of the German Aerospace Center (DLR). Being a part of such unique and vibrant environments allowed me not only to work with cutting-edge robotic systems and technologies but, most notably, to meet the incredible and talented people to whom I owe for the final result of my journey.

I am extremely grateful to Dr.-Ing. habil. Konstantin Kondak and Dr.-Ing. Christian Ott, first of all, for giving me a unique chance to join DLR and taking me on board as a member of the Flying Robots group and Analysis and Control of Advanced Robotic Systems (ARR) department and secondly, for guiding me through all the undertaken research path. Christian has been as a lighthouse in times when I felt lost in fundamental research, while discussions with Konstantin have always been enlightening in applied science. In the end, your experience, knowledge, and ideas served as strong pillars for my thesis.

I am deeply indebted to Dr. Min Jun Kim for helping me to adapt at DLR and for my first steps in the world of advanced robotics. In particular, I am profoundly thankful for his illuminating supervision, for pushing me toward my research goals approaching my limits, for fueling me with the courage to try despite any mind borders, for always being in a good mood, and, finally, for his patience that cannot be overestimated.

I would like to acknowledge the invaluable contribution and to show my greatest appreciation to Andre Coelho for persistent help, priceless insights into whole-body control, for all you have taught me, and, especially for finding our wonderful student Maihara Gabrieli Santos whose positive mood, diligence, and self-discipline helped us to complete what seemed impossible at that time.

Alone we go faster, together we go further. So, without the contribution of the rest of the Flying Robots group, this thesis would not have been possible. I am deeply grateful to Ribin Balachandran, visiting researcher Dr. Davide Bicego, Jongseok Lee, Khizer Shaikh, Dr. Marco De Stefano, and Michael Vilzmann, with whom I not just worked shoulder to shoulder during late and sleepless nights but also

traveled a lot and had a lot of fun. Thank you for your belief in my work, countless hours of discussions, constant feedback, and unparalleled support you have provided during all these years. At the same time, I am very grateful to the ARR department colleagues who provided a friendly and motivating environment. I learned a lot from working with you, chatting with you, your presentations at the department meetings. I am super grateful for your advices and wisdom. I could name so many, but I would like to particularly thank Dr. Gianluca Garofalo for answering all those sudden phone calls with my questions and organizing internal classes for sharing his knowledge. My special thanks go to Prof. Alin Albu-Schäffer for interesting and inspiring occasional discussions during late nights within institute walls. I also thank all DLR Institute of Robotics and Mechatronics colleagues, especially those in electrical and mechanical workshops for their great support and maintenance.

I would like to express my deepest appreciation to my doctoral father, Associate Professor Dzmitry Tsetserukou, for opening the doors of the robotics world, teaching me fundamentals, profound belief in my abilities, constructive criticism, dedication, and resourcefulness, for showing me the value of hard work.

I cannot begin to express my thanks to doctoral committee members, Dr. Clement Fortin and Dr. Alessandro Golkar. I profited a lot from their wisdom and experience. I am grateful for all your comments, teaching me the art of critical thinking, advising me on academic matters, and always being ready to meet, despite your many demanding duties. I am particularly grateful to Dr. Rupert Gerzer for bridging the Skoltech and DLR and for kindly hosting me at (pre)Christmas in his house.

I want to show my appreciation for the sponsorship and extensive support to the German Academic Exchange Service, DLR, and Skoltech at different years.

Despite being far from home, I managed to keep my friends close and even made new ones. I am thankful to all of them, especially to my school friends, Vova, Yan, Vlad, my BMSTU friends, Kolya, Sanych, Kostya, my (non-)German mates, Kamila, Sushil, Maged, Jazzy, Katya, Hiroshi, my Skoltech comrades, Sasha, Vadim, Grisha, Dasha, Dina, Eldar, who constantly supported me despite "always busy" lifestyle and some laziness in communication. I would not be where I am without you.

Finally, thanks and love to my family, especially to my parents, Violetta and Sergey, and to my elder brother Nikolay, for letting me use much of the time that was meant for them to finish this thesis. Without their unconditional love, faith, and emotional support, none of these would have been possible. Thank you for showing me the value of knowledge and for everything I have.

Yura

"Mark my words! This drill will open a hole in the universe! ...
Drilling a path towards tomorrow!"
Simon
(Tengen Toppa Gurren Lagann, 2007)

Contents

List of Symbols

In this thesis, all scalar quantities are denoted by a plain font (e.g., l_1, n). Vectors are described by bold lower case letters (e.g., $\boldsymbol{l}$, $\boldsymbol{\lambda}$), and matricies are printed in bold upper case (e.g., $\boldsymbol{M}$, $\boldsymbol{A}$). Total derivatives with respect to time are abbreviated by dots (e.g., $\dot{\boldsymbol{x}} = \frac{d}{dt}\boldsymbol{x}$). We denote a n-order unit matrix as $\boldsymbol{I}_n$ and a vector of all ones in $\mathbb{R}^n$ as $\mathbb{1}_{n\times 1}$.

The various subsctipts are used with quantities through the thesis. The most imortant among them are b (body), w (world), a (actuator), m (manipulator), p (platform), and e (end effector). Moreover, for the rotation matrices the subscript and superscript are used simultaneously as $\boldsymbol{v}_{to} = \boldsymbol{R}^{to}_{from}\ \boldsymbol{v}_{from}$ to denote the initial ($from$) and transformed (to) frames of the vector $\boldsymbol{v}$.

Here, only key quantities are listed without or with certain subscripts that are of the prominent importance. Specific meaning of the same parameters with different subsctips as well as non-defined mathematical operations in the thesis become clear when they are inroduced in the text.

Kinematics notation

$\boldsymbol{R}^w_b$	Rotation matrix representing the orientation of the body frame with respect to the world frame
$\boldsymbol{\phi} = [\varphi,\ \theta,\ \psi]^T$	Roll, pitch, and yaw angles
$\boldsymbol{v}$	Vector of the linear velocities
$\boldsymbol{\omega}_b = [p,\ q,\ r]^T$	Vector of the angular velocities expressed in the body frame
$\boldsymbol{V} = [\boldsymbol{v},\ \boldsymbol{\omega}]^T$	Twist coordinates representing the rigid body velocity

Aerial platform modeling

t_i	Thrust force generated by $i-$th rotor group
$\boldsymbol{t} = [t_1,\ ...,\ t_n]^T$	Vector of thrust forces generated by n rotor groups
$\boldsymbol{t}_i$	Unit thrust vector defined in $\mathcal{F}_b$
α	Roll angle with respect to the actuator frame $\mathcal{F}_a$
β	Pitch angle with respect to the actuator frame $\mathcal{F}_a$

$\boldsymbol{A}$	Allocation matrix
$\boldsymbol{f} = [f_x,\ f_y,\ f_z]^T$	Three dimensional force vector
$\boldsymbol{\tau} = [\tau_x,\ \tau_y,\ \tau_z]^T$	Three dimensional torque vector
$\boldsymbol{w} = [\boldsymbol{f},\ \boldsymbol{\tau}]^T$	Wrench

Dynamics notation

$\boldsymbol{q}$	Vector of generalized coordinates (joint displacements for the robotic system)
$\boldsymbol{x}(\boldsymbol{q})$	Vector of task space coordinates (Position and orientation of the end effector for the robotic system)
$\boldsymbol{M}(\boldsymbol{q})$	Symmetric and positive definite inertia matrix
$\boldsymbol{C}(\boldsymbol{q},\ \dot{\boldsymbol{q}})$	Matrix containing centrifugal and Coriolis terms
$\boldsymbol{g}(\boldsymbol{q})$	Gravity vector
$\boldsymbol{\tau}$	Vector of generalized torques
$\boldsymbol{J}(\dot{\boldsymbol{q}})$	Jacobian matrix defining relation between joint space and task space velocities

Others

$\mathcal{F}_i:\ \{O_i,\ x_i,\ y_i,\ z_i\}$	Orthogonal reference frame centered at O_i with axis x_i, y_i, and z_i for $i \in \{w,\ b,\ h,\ a,\ p,\ com,\ t\}$, where w stands for world, b - for body, h - for hook, a - for actuator, p - for platform, com - for COM, t - for tool
$\mathcal{PD}(.)$	Proportional-derivative operator applied to the value (.)

List of Acronyms

Notation	Description
BLDC	BrushLess Direct Current motor. xvii, 37, 45, 50, 51, 53, 54, 78, 156, 182
CAD	Computer Aided Design. xvii, 61, 64, 71
CCW	CounterClockWise. 29, 30, 46, 47, 155
COM	Center Of Mass. iv, xviii, xxiii, 7, 14, 15, 20, 27, 30, 33, 37, 39, 58, 60, 62, 63, 68, 70, 79, 81, 86, 99–102, 107–110, 114, 116–118, 142, 143, 145, 149, 150, 155, 172, 173, 175–178
CW	ClockWise. 29, 46, 155
DLR	German Aerospace Center. xxiii, 7, 11, 38, 71, 73, 74, 158, 161
DOF	Degree Of Freedom. xvi, xxiv, 6, 7, 10–12, 14, 19, 25–28, 32, 36, 41, 44, 51, 58, 63, 69, 75, 95, 104–106, 108, 112, 117, 122, 150, 168, 179, 181, 190
ESC	Electronic Speed Controller. 47, 50–52, 54, 182
FCC	Flight Control Computer. 70, 71, 74, 75, 176
FFT	fast Fourier transform. 59, 90, 119, 123, 125
FTS	Force Torque Sensor. 35, 51, 71, 74, 141, 167, 168, 179, 180
GC	Geometric Center. 42, 58, 71, 77, 79, 116, 149, 150
GPS	Global Positioning System. 5, 70, 74, 77, 181
H2020 AEROARMS	AErial RObotic system integrating multiple ARMS and advanced manipulation capabilities for inspection and maintenance. iv, 8, 11, 15, 38, 158

Notation	**Description**
HWBC	Hierarchical impedance-based Whole-Body Controller. iv, xx–xxii, 14, 17, 109, 119, 140, 143–147, 149, 151, 152, 154, 158, 168, 170, 172, 173, 177–180
IK	Inverse Kinematics. xviii, 25, 35, 105, 106, 108, 110, 114–116, 188
IMU	Inertial Measurement Unit. iii, xviii, 5, 14, 58, 59, 70, 73, 74, 77, 79, 81, 83–85, 91, 92, 96, 99, 119, 120, 150, 158, 176, 177, 181
LiDAR	Light Detection and Ranging. 5, 181
MATLAB Simulink	MathWorks MATLAB Simulink. 48, 92, 117
ofLQR	output feedback Linear Quadratic Regulator. iv, 88, 89
OODC	Optimal Oscillation Damping Controller. 14, 17, 119, 124, 127, 129, 130, 133, 135, 136, 139, 149, 150, 152, 158, 168, 170, 171, 176–180
PWM	Pulse Width Modulation. 51, 53–55, 73, 75
RCC	Robot Control Computer. 70, 71, 74
RMC	Robotics and Mechatronics Center. 11, 33, 120, 140
RQ	Research Question. 12, 13, 15, 174
SAM	cable-Suspended Aerial Manipulator. xi, xvi–xx, xxii–xxiv, 11, 16, 36–40, 42–45, 48, 49, 58–60, 62, 63, 66, 69–77, 79, 83, 84, 94, 99, 100, 102, 119, 120, 123, 127–130, 132, 136, 140, 142, 144, 149, 153, 156, 158, 161–170, 175–178, 180
UAV	Unmanned Aerial Vehicle. 2, 4–11, 38, 56
VPC	Vision Processing Computer. 70, 74

List of Figures

List of Tables

"We keep moving forward, opening new doors, and doing new things, because we're curious and curiosity keeps leading us down new paths."

Walt Disney

Chapter 1

Introduction

1.1 Motivation

Aerial robotics has significantly impacted human lives in the past decades. The rapid growth in this field is driven by the technology development, maturing of the open-source, scientific, and industrial communities, and an availability of the wide range of important applications where such highly mobile robots can contribute [Siciliano and Khatib, 2007, Valavanis and Vachtsevanos, 2014]. Among the most common applications, it is essential to highlight the following:

- mapping, surveillance, and monitoring of the remotely-located areas and objects such as agricultural fields, international borders, urban traffics, or epidemic spots [Irizarry et al., 2012, Kaleem and Rehmani, 2018, Mogili and Deepak, 2018, Ventura et al., 2016],
- search and rescue for missing people or other objects of interest [Mishra et al., 2020, Tomic et al., 2012],
- transportation of the various payloads, e.g., shipment of medical supplies, spraying fertilizer for crops, package delivery in an urban environment [Balasingam, 2017, Villa et al., 2019],
- deployment of communication services,e.g., internet or radio broadcasting in disaster areas [Mayor et al., 2019, Naqvi et al., 2018],
- filming/photography for cinematography and entertainment [Bonatti et al., 2018, Kim et al., 2020],
- various military applications [Asaro, 2013, Hartmann and Giles, 2016].

(a) Inspection of the George Washington Bridge [Stantec, 2017]

(b) Maintenance of the wind turbine blade by a technician [Altitec, 2019]

(c) Window cleaning in the Burj Khalifa tower by climbers [Marmet, 2019]

(d) Replacement of the light bulb at the 457 meter TV tower [Prairie Aerial, 2014]

(e) Inspection of high-power lines by linemen in Faraday suits [World Channel, 2016]

(f) Taking of the soil samples in the toxic environment by the researcher [Gandy, 2020]

Figure 1-1: Application scenarios for aerial manipulation.

All applications above are linked by the same work principle, in which the free-flying Unmanned Aerial Vehicle (UAV) operates within an open environment without direct interaction. However, a significant number of potential applications is required physical interaction with surroundings. The unaccomplished need has led researchers to an investigation toward such a capability within last years. The field of direct interaction with the environment performed by UAV is commonly known as the *aerial manipulation*.

The aerial manipulator can generally be defined as the aerial base with an endowed manipulation device, e.g., a robotic manipulator or gripper. Developing a system combining robotic manipulator capabilities and UAV dexterity is complex and requires in-depth research, analysis, and significant experience. Among many potential applications for the aerial manipulators, it is vital to list the operations which involve significant human risks and time costs, i.e., the inspection and maintenance of various remotely located structures (e.g., bridges, electric lines, or pipelines, wind turbine blades, communication towers, skyscraper windows) and any operations in hazardous/dangerous conditions for human safety (e.g., decommissioning of damaged nuclear power plants, installation sensors, taking samples), see Figure 1-1.

The most relevant and promising industrial domains for the aerial manipulators in the Russian Federation are the following:

- *Wind turbines.* The most promising and profitable renewable energy market supported by Russian Government programs is wind power generation. According to experts, the economic potential of wind generation in Russia is approximately 17,100 billion $\frac{\text{kWh}}{year}$ [Ermolenko et al., 2017], while the total output of the existing wind power plants barely exceeds 1.5 billion $\frac{\text{kWh}}{year}$[1].

- *Pipelines.* Trunk and industrial pipelines are used to transport a variety of substances, including flammable liquids and gases. According to the EMERCOM of Russia[2], the total length of trunk pipelines in Russia is 217,000 km, some of which are installed above the ground level on separate supports and overpasses through water and relief obstacles.

- *Bridges and overpasses.* According to Rosstat[3], there are about 42,000 bridges and overpasses in Russia with a total length of 2.1 million meters. Inspection and repair of such structures is a challenging task. Thus, in 2020, 60 climbers cleaned and repaired the cables of the cable-stayed bridge, the Russky Bridge, in Vladivostok in extreme conditions: at an altitude of more than 300 meters with wind gusts reaching 20 $\frac{\text{m}}{\text{s}}$[4].

- *Power lines.* According to the Great Russian Encyclopedia[5], the total length of the active power lines is about 3 mln km.

- *Cell and TV towers.* According to Roskomnadzor data for 2019[6], the total number of TV and cell towers in Russia is about 800,000.

- *Offshore drilling rigs.* The share of offshore drilling is growing every year. By 2030, Russia should double the number of drilling rigs according to CDU TEK[7].

More examples of the aerial manipulation applications with detailed description can be found in [Khamseh et al., 2018, Korpela et al., 2012, Ladig et al., 2021, Mohiuddin et al., 2020, Ollero et al., 2018, Ollero et al., 2021, Orsag et al., 2018, Ruggiero

[1] https://www.so-ups.ru
[2] https://www.mchs.gov.ru
[3] https://rosstat.gov.ru
[4] https://www.interfax.ru
[5] https://bigenc.ru
[6] https://rkn.gov.ru
[7] https://www.cdu.ru

et al., 2018]. Nevertheless, despite the growing interest in aerial contact interaction, the tremendous amount of research in the field, dozens of experimental setups globally, only a few research projects have resulted in industry-level technology ready for the market.

1.2 Literature overview

1.2.1 Aerial robotics

According to the [Ben-Ari and Mondada, 2018], all robots can be classified by environment and interaction mechanism in the following manner. There are two big groups: fixed-base and mobile robots. The first one includes robotic manipulators, cable-driven robots, and other representatives with a constantly fixed point in the space. In contrast, the mobile robots can move without any connection to a particular environment. Further, they can be divided into three subgroups depending on the environment properties, i.e., aerial, aquatic, and terrestrial robots. Let us consider the aerial type in more detail.

The aerial robot is a mobile robot that can fly, i.e., it can change its pose in three-dimensional aerial space. Such a robot type can also be referred in the literature as UAV, UAS (Unmanned Aerial System), or simply drone. In general, all aerial robots can be modeled as a floating platforms. Depending on the aerodynamic configuration [Belmonte et al., 2019, Lozano, 2010], four classes with particular characteristics can be distinguished, see Figure 1-2. The first one is a fixed-wing UAV. This class is

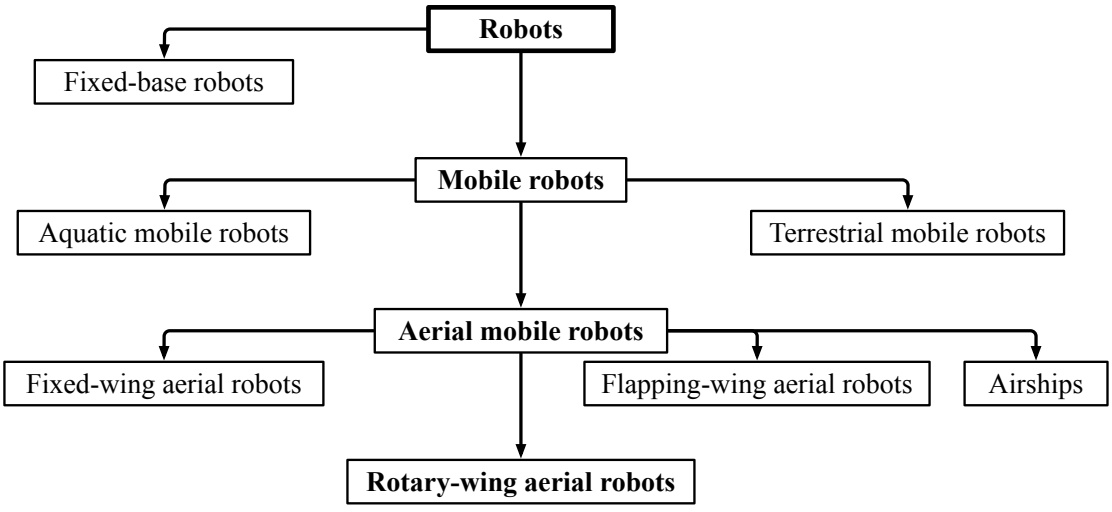

Figure 1-2: Robotics taxonomy in terms of environment and interaction mechanism.

featured by the capability to fly long distances with high efficiency. The second class includes rotary-wing UAVs (or rotorcrafts), which are highly maneuverable in hovering and short-distance movements during relatively short flight time. The next class is a flapping-wing UAV which is inspired by nature: it reproduces the flight of insects or birds. This class can be characterized by low power consumption, the best potential toward miniaturization, and an extremely low-weight payload. The last class is devoted to aerostatic aircraft, i.e., airships. They have low power consumption, a low-weight payload, and big size. By investigating the advantages and disadvantages of the classes mentioned above, humanity has started to mix them into separate systems. For example, convertiplane and gyrodyne are aerial systems that combine flight endurance of the fixed-wing class and capability for the hovering and VTOL (Vertical Take-Off and Landing) of the rotorcrafts [Robb, 2006].

One of the main aspects of the rotorcrafts is the number of rotors that generate the thrust. There are single-rotor and multirotor types. The typical representative of the former kind is the helicopter. The latter type includes various configurations, e.g., well-known quadcopter, hexacopter, or octocopter [Basset et al., 2014].

In the scope of this thesis, multirotor type is of most significant interest. Let us consider the related technical challenges, which reflect recent research activity. One of the most critical among them is the development of robust perception, navigation, and control methods which provide UAV with efficient and intelligent capability to operate in various environments. The primary sensors which help with three-dimensional state estimation and mapping for the aerial robots include Global Navigation Satellite Systems (Global Positioning System (GPS), Global Navigation Satellite System (GLONASS), Galileo, BeiDou), Inertial Measurement Unit (IMU), stereo and mono cameras, and Light Detection and Ranging (LiDAR) scanner [Sanfourche et al., 2012]. In terms of control algorithms, various nonlinear methods such as sliding mode control, model predictive control, and adaptive techniques reinforced by data-driven approaches are exploited [Luukkonen, 2011, Mo and Farid, 2019].

Another challenge in this field is the human-machine interface. Researchers have designed and investigated different tools for intuitive and reliable drone control by human operators. As a control source, not only the joystick or touchscreen commands but also the gestures, speech, or even brain signals are utilized [Cauchard et al., 2015, Peschel and Murphy, 2012, Tezza and Andujar, 2019]. The last ones become especially practical in swarm coordination when one human operator should control multiple UAVs simultaneously. To facilitate novel human-machine interface,

different approaches, e.g., leader-following or single-controlled methods [Bashyal and Venayagamoorthy, 2008, Nagi et al., 2014], and embedded technologies such as augmented reality or tactile wearable interfaces [Hoenig et al., 2015, Tsykunov et al., 2019, Yashin et al., 2019] have been recently developed.

The last challenge that we list here is the interaction with the surrounding environment, such as landing or manipulation. During contact tasks, the dynamics of the drone evolves because of the appeared physical constraints. It significantly complicates the control of the drone. To overcome this issue during landing, extended dynamics in control algorithms or auxiliary mechanical systems are developed, e.g., robotic landing gear [Sarkisov et al., 2018, Shi et al., 2019]. In general, the physical interaction of the drone with the environment is quite broad research direction, which will be covered in more detail in the following subsection.

1.2.2 Aerial interaction and manipulation

Aerial interaction is a modern and prospective field in robotics with a significant number of industrial applications. Two main branches can be distinguished in this area. The first one is the use of the specific mechanisms (e.g., gripper) for a particular type of aerial interaction with an environment. For example, in [Thomas et al., 2013], an avian-inspired aerial vehicle capable of grasping and transporting different objects was demonstrated. The UAV equipped with a brush for cleaning of the vertical surfaces was proposed in [Albers et al., 2010]. In [Bernard and Kondak, 2009], slung-load transportation and deployment by single and multiple UAVs utilizing slung-load state observer for disturbance reduction were demonstrated. In [Raz et al., 1989], two damping wings were installed directly on the slung-load in order to further facilitate damping of the suspended load. Mechanisms that enable compliant interaction with the environment by utilizing passive springs were shown in [Bartelds et al., 2016, Keemink et al., 2012].

Another important branch is integrating a robotic arm (or even multiple arms) into the UAV. Thus, in [Kim et al., 2013, Korpela et al., 2012, Suárez et al., 2016], light-weight 2-4 Degree Of Freedom (DOF)s manipulators were used to perform grasping and surface detection tasks. Furthermore, in [Caraballo et al., 2017, Jimenez-Cano et al., 2013], aerial manipulators were exploited to perform assembly tasks. In order to explore further capabilities of aerial manipulation, a 7-DOF torque-controlled KUKA LWR robot was integrated into a UAV [Huber et al., 2013, Kim et al., 2018, Kondak et al., 2014]. Although 7-DOF robotic arm provides ability

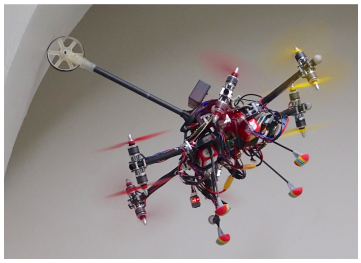

(a) ETH Zurich aerial inspection platform [Bodie et al., 2019, Kamel et al., 2018]

(b) DLR Flettner with 7-DOF robotic arm [Huber et al., 2013]

(c) University of Seville dual lightweight aerial manipulator [Suárez et al., 2018]

Figure 1-3: Systems for the aerial interaction and manipulation.

to operate with heavy payload and advanced manipulation capabilities (kinematic redundancy [Kondak et al., 2014, Lippiello and Ruggiero, 2012] and full task space formulation [Kim et al., 2018]), due to the heavy weight (roughly 16 kg), the manipulator had ot be mounted on the autonomous high-payload helicopter system with 3.7-meter diameter rotor blades. With such dimensions, approaching to a target object might be challenging and unsafe in a complex environment. Moreover, dynamic turbulence caused by ground effect near wide surfaces might serve as an additional source of danger for the helicopter and makes it even harder to operate. Another approach for the aerial manipulation is utilizing aerial articulated manipulator [Endo et al., 2018, Zhao et al., 2018] which represents a multi-DOF manipulator, each link of which is a small-scale UAV.

Following the definition presented in section 1.1, aerial manipulator represents the coupled robotic system containing the aerial base and manipulation device, see Figure 1-3. Both elements are subject to various disturbances that have to be compensated for precise manipulation. Most of the disturbances during an operation can be grouped into dynamic and static by the nature of the source. The dynamic disturbances include wind, signal noise, inertia couplings [Mebarki et al., 2014, Zhang et al., 2019], while examples of static disturbances are internal displacement of the system Center Of Mass (COM) and external wrench induced to the system during interaction with environment [Bodie et al., 2019, Gardecki et al., 2017, Heredia et al., 2014]. The most efficient way to deal with the first group of disturbances is to use the standard actuation system for the aerial base, propeller-based propulsion [Cunio et al., 2009, Tran, 2016, Zhang et al., 2016]. However, the static perturbations bring the most troubles for precise and robust aerial manipulation. To cope with them, the researchers have proposed and investigated the direct weight sliding at the aerial base during the operation, e.g., the motion of additional masses or bat-

tery [Haus et al., 2016, 2017, Kim et al., 2018, Lanteigne et al., 2016]. In the case of cooperative aerial manipulation, where a swarm of drones carries the common manipulation device or tool [Gioioso et al., 2014, Kim et al., 2018, Michael et al., 2011], the static perturbations can be compensated by centralized control strategy for the whole UAV formation [Aghdam et al., 2016, Chung et al., 2018].

The use of aerial manipulators in the industry has been the subject of interest for many research groups and companies over the past decade [Ollero and Siciliano, 2019]. As a result, many international consortia have been established to facilitate the topic progress toward increasing the technology readiness level. The European consortium has achieved the most significant results during several projects such as Aerial Robotics Cooperative Assembly System (ARCAS)[8], AErial RObotic system integrating multiple ARMS and advanced manipulation capabilities for inspection and maintenance (H2020 AEROARMS)[9], and H2020 collaborative AErial RObotic WORKerS (AEROWORKS)[10]. In the scope of these projects, applied industrial tasks have been performed, including pipeline inspection, deployment of mobile robots at a remote location, and the use of two robotic arms for carrying objects. In addition, different research groups worldwide have demonstrated the possibility of performing other complex tasks, such as a valve turn [Korpela et al., 2014], the weaving of a rope bridge by a swarm of drones [Augugliaro et al., 2013], inspecting complex surfaces [Jimenez-Cano et al., 2015, Nayak et al., 2018], and joint cooperation of the industrial robot and aerial manipulator [Staub et al., 2018].

1.2.3 Long reach aerial manipulation

Recently, a new branch in the field of aerial manipulation has begun to emerge, it is entitled as long reach aerial manipulation. Long reach implies that the robotic manipulator is decoupled with the aerial base by a long link or cable instead of being mounted directly [Caballero et al., 2017, Sarkisov et al., 2019, Shimonomura, 2019, Suárez et al., 2020]. The idea of the long reach aerial manipulation is motivated by applications from the different fields: remediation of the waste storage tanks [Burks et al., 1991], inspection of the underground closed-space places [Mavroidis et al., 1995], and manipulation in space [Yoshida et al., 1996]. This approach brings to the aerial manipulation certain advantages including:

[8] https://www.arcas-project.eu
[9] https://www.aeroarms-project.eu
[10] https://www.aeroworks2020.eu

- ability to operate in a narrow and complex environment at which UAV cannot be placed, e.g., because of the size,
- improving manipulation performance:
  - by increased manipulation workspace without any UAV-related constraints such as landing gear,
  - by reduced influence of the aerial carrier on the environment and the manipulation device, e.g., UAVs downwash or ground effect,
- ensuring safety distance between the operator, object of manipulation, environment, and aerial base,
- increasing the safety of the aerial base by removing rigid coupling with manipulation device and thereby preventing propagation of the wrenches generated from the interaction of robotic arm with the environment.

Despite the benefits mentioned above, there are a number of disadvantages that long reach configuration possesses. The most critical among them is increased weight due to an additional element adding and resulted underactuation of the system, which complicates the control problem.

1.2.3.1 Link-decoupled aerial manipulators

The first group of the long reach aerial manipulation systems exploits the passive link to decouple the robotic arm from the aerial base, see Figure 1-4. It is worth

(a) Rigid link-decoupled aerial manipulator [Suárez et al., 2018]

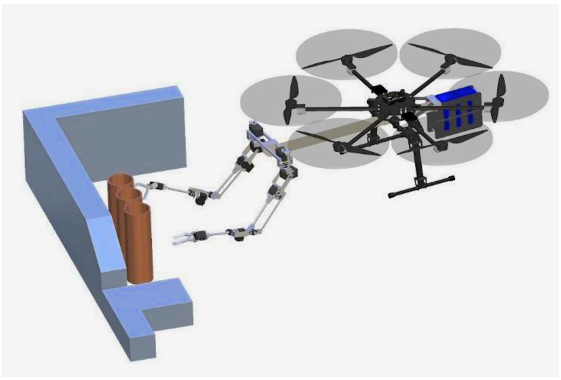

(b) Flexible link-decoupled aerial manipulator [Suárez et al., 2018]

Figure 1-4: Link-decoupled aerial manipulation systems.

mentioning that dual-arm manipulation is also realized using this approach [Caballero et al., 2018]. The most significant contribution to this direction is provided by GRVC Robotics Labs[11] of the University of Seville. In [Suárez et al., 2018], rigid one-meter link separates hexacopter with a 2-DOF robotic arm for pipe inspection. This link contains the passive rotational joint in the base, so it behaves as a passive pendulum state of which is measured and utilized in the control law formulation. On the other hand, in [Suárez et al., 2018], flexible link rigidly attached to the both, aerial base and manipulator, is exploited. For such a system, undesired oscillations of the flexible link are suppressed by a coordinated motion of the dual-arm manipulator. It is worth mentioning that the use of the non-controllable (passive) links, which serve as an extension, requires constant and direct contact with the environment in order to operate, while during the flight, it becomes a source of oscillations which implies limitations on the aerial base trajectory.

1.2.3.2 Cable-decoupled aerial manipulators

In pursuit of increased performance and safety in aerial manipulation, cable-suspended aerial manipulators have been recently proposed [Miyazaki et al., 2020, Sarkisov et al., 2019, Yiğit et al., 2021]. Decoupling of the UAV and manipulation device is performed using a length-controllable cable. Although such a modification presents an additional benefit via increased workspace via changing the cable length during the mission, utilizing such a solution in real world scenarios is also challenging because of the pendulum motion caused by the cable suspension.

It is critical to dampen the oscillation of the cable as quickly as possible when it occurs due to any disturbances such as the motion of the aerial base, robotic arm's activity, or wind gust. To this end, one may control the aerial carrier itself [Lee et al., 2015, Yoshikawa et al., 2017] to cancel out the payload oscillations. However, these methods can provide only indirect damping.

To damp out the oscillations directly, we can consider having an auxiliary small-scale actuated platform attached to the manipulation device. In [Kim et al., 2018], Min Jun Kim proposed a concept of the UAV carrying a slung-load equipped with moving masses to damp out the oscillations caused by the pendulum configuration. Although the generated by moving masses torques can dampen oscillations of the suspended load, this type of actuation is not practical in interaction problem. Additionally, the moving masses unnecessarily increase the total system weight.

[11] https://grvc.us.es

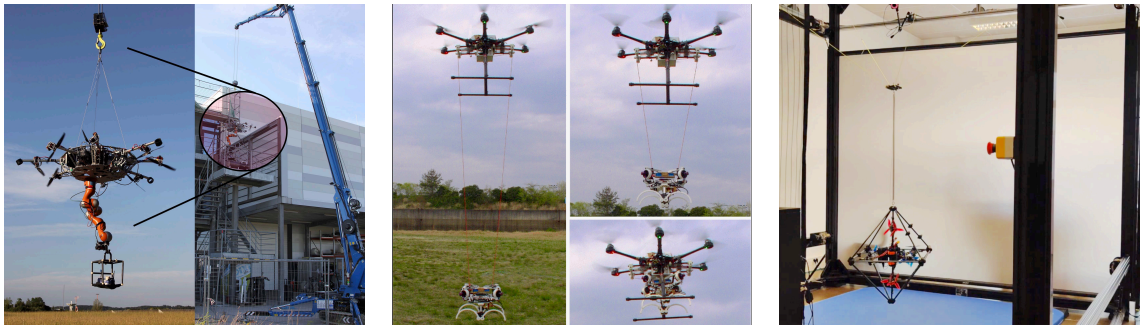

(a) Cable-suspended aerial manipulator SAM [Sarkisov et al., 2019]

(b) Long reach aerial manipulator with wire-suspension [Miyazaki et al., 2019]

(c) Spring suspended aerial manipulator dextAIR [Yiğit et al., 2020]

Figure 1-5: Cable-suspended aerial manipulation systems.

To this end, researchers from German Aerospace Center (DLR) Robotics and Mechatronics Center (RMC)[12] within the H2020 AEROARMS project have developed the so-called cable-Suspended Aerial Manipulator (SAM) platform which is suspended to the mobile crane and equipped with dual actuation: winches and omnidirectional propeller-based actuation. The former allows compensating for the static disturbances while the latter is capable of generating three-dimensional wrench, which is beneficial during interaction with the environment as well as for the oscillation damping, see Figure 1-5a. One may refer to chapter 3, [Coelho et al., 2020, Gabellieri et al., 2020, Lee et al., 2020, Sarkisov et al., 2019] for more details about design and application of the SAM. *The main results of this thesis, including design investigation, modeling, and development of control strategies, are validated on the demonstrator SAM and will be considered in more detail in the following chapters.*

Long reach aerial manipulator with wire-suspension and swing-suppression system is proposed by Ryo Miyazaki et al. from the Integrated Sensors and Intelligence Lab of Ritsumeikan University[13] [Miyazaki et al., 2019]. The main UAV carries the wire-suspended device equipped with a 1-DOF gripper and the four ducted fans to dampen pendulum-like oscillations in the roll and pitch directions, see Figure 1-5b. The unique feature of this system is the suspension by two wires, which allows to avoid twisting around the yaw axis [Miyazaki et al., 2018].

Recently, a novel suspended aerial manipulator dextAIR has been presented by Arda Yiğit et al. from the ICube Laboratory of the University of Strasbourg[14] [Yiğit et al., 2020]. In contrast to the previously described systems, dextAir is suspended

[12]https://www.dlr.de/rmc
[13]http://www.ritsumei.ac.jp/∼skazu/
[14]http://www.avr.icube.unistra.fr

to a carrier by a low-stiffness spring with a long elastic range, see Figure 1-5c. It compensates for gravity and reduces a power consumption by avoiding the use of a winch-controllable cable. Also, due to the spring the vertical dynamics of the aerial robot is fully decoupled from the carrier dynamics. The system is actuated by six pairs of contra-rotating propellers generating a 6-DOF wrench and can be equipped with any gripper.

To the best of the author knowledge, there are no more systems related to the cable-suspended aerial manipulation so far.

1.3 Main contribution

It could be seen from the previous sections that the research in the aerial manipulation field is growing rapidly. Nevertheless, the existing technology level is not mature enough to be exploited in the industrial environment mainly because of the low safety and unsatisfactory performance.

To address these challenges, at the beginning of the research path behind this thesis, we have formulated the main Research Question (RQ) reflected through the SMART (Specific, Measurable, Attainable, Relevant, and Time-Bound) framework [Simmons, 2015] as follows:

> **RQ:** How to enhance **manipulation performance** and **operational safety** for the aerial manipulation in industrial applications, e.g., valve turn, peg-in-hole assembly?

The RQ contains two key factors: manipulation performance and operational safety. Let us provide some clarifications on these terms. Manipulation performance is defined by accuracy and level of manipulation capabilities. High-level implies advanced manipulation skills [Khatib, 2005], including full task formulation, kinematic redundancy, dexterous manipulation, robustness to the external constraints, and operation with a heavy payload. Operational safety implies preserving all participants during the process, i.e., operator, environment, an object of manipulation, and aerial manipulator. Deeper investigation of state of the art led us to the novel concept for the aerial manipulation, namely, cable-suspended aerial manipulator, which laid the foundation of our primary *hypothesis*:

Hypothesis: Adequately controlled cable-suspended stabilizing platform equipped with a robotic arm can provide high performance and safety in aerial robotic manipulation.

Hypothesis illustration is shown in Figure 1-6. As seen in the schematic diagram, the robotic manipulator is decoupled from a carrier by utilizing a cable. The cable-suspended stabilizing platform is equipped with actuation means to counter various disturbances and the robotic arm to perform manipulation. At the same time, the carrier at which the platform is suspended has high payload capability and compensates for the whole system gravity, so actuation efforts at the platform for stabilization should not be high. It allows to make the platform compact and safe. Such a concept completely meets two key factors established in the RQ. Indeed, due to heavy payload capable carrier, one or several redundant robotic arms with full task formulation and high operating weight can be installed at the stabilizing platform. Moreover, the absence of gravitational effect allows to use small-scale and safe platform. Additionally, the cable decoupling ensures the safe distance between the environment and carrier.

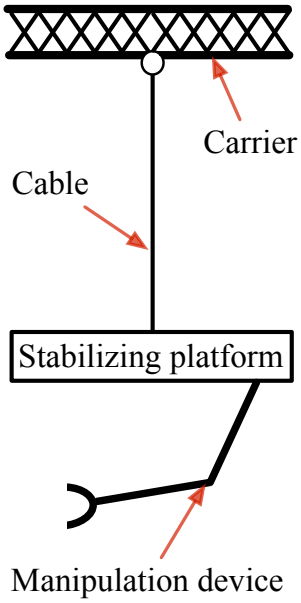

Figure 1-6: Hypothesis illustration.

Based on the preceding discussion, let us define the three *research objectives* and corresponding results which will form the main scientific contribution of this thesis:

- *To develop a robust control approach that can compensate for dynamic disturbances during transportation and manipulation of the cable-suspended platform without access to the system entire state and characterize its performance.*

  A research gap for defined objective can be formulated as follows: the long reach configuration is affected by dynamic disturbances, which lead to the pendulum-like oscillations and restrict the exploitation of the system. Dynamic disturbances are expected to alter with high frequency. To this end, fully-actuated propeller-based propulsion, which can generate omnidirectional wrench, is utilized. Since the carrier for the cable-suspended platform is not unique, the system controller should not rely on the specific model. There-

fore, it is natural to consider model-free approaches which are robust to the uncertainties and disturbances [Damak et al., 2020, Iskandar et al., 2019, Ma and Cai, 2011]. As a result, onboard IMU-based Optimal Oscillation Damping Controller (OODC) for confronting dynamic disturbances by virtue of the propeller-based actuation is developed. The controller provides high performance in disturbance countering and low power consumption during the operation. It resolves three main challenges. The first one is the cable partial state estimation exploiting single onboard IMU data. This task is complicated by the fact that the overall system behaves as double pendulum [Singhose et al., 2008, Vaughan et al., 2010]. The second issue is related to the transformation of the onboard generated omnidirectional wrench to the double pendulum passive joints. Lastly, the strategy for the optimal selection of the control gains is proposed based on the minimization of a quadratic cost function balancing energy consumption and system performance. To validate the controller performance, simulational and experimental studies are conducted. Moreover, stability analysis is performed.

- *To develop a control approach to facilitate a manipulation performance of cable-suspended platform endowed with kinematically redundant robotic manipulator by compensation for static disturbances and evaluate its performance.*

  The research gap here is the following: weight of the heavy robotic arm causes the static disturbances in the system. Namely, a shift of the system COM results in undesirable platform tilt. To compensate for this type of disturbances, exploitation of a slow winch-based actuation is proposed. It allows regulating the translational DOFs of the platform relative to the suspension point. Considering that the static disturbances are caused by known (measured) robotic arm motion, the total system (robotic arm and winches) is self-contained in terms of the internal dynamics for the case when the carrier is motionless and propellers do not exert any wrench. To this end, model-based control approach might be utilized [Brosilow and Joseph, 2002, Kool et al., 2016, Todorov et al., 2012]. Based on the state-of-the-art methods [Henze et al., 2015, Sentis and Khatib, 2005], a Hierarchical impedance-based Whole-Body Controller (HWBC) framework is designed using the winch suspension and robotic arm real-time simulated model. A number of challenges within this objective are resolved. First, the complex closed-chain winch cabling is modeled by Lagrangian constrained dynamics and mapped to the intuitive

quasi-state [Blajer, 1997] defined by equal open-chain coordinates for further control formulation. Secondly, task space definition is introduced. Namely, two tasks with different priorities are defined: regulation of the robotic arm in the task space toward desired pose and keeping system COM at zero location to compensate for the static disturbances. Both tasks are regulated under the impedance-based control. Lastly, the admittance interface is introduced and tuned to transform controller torque commands to the position-controlled winch servos. Resulted actuation and control approach is validated in various experimental studies.

- *To assess manipulation performance and operational safety of the cable-suspended stabilizing platform through extensive experimental studies in a similar to the industrial environment.*

  To demonstrate and investigate the applicability of the proposed hypothesis and the performance of designed control approaches in terms of the key factors defined in RQ, manipulation performance and operational safety, extensive experimental studies are conducted under the effect of various disturbances such as external perturbations, the motion of the suspension point, and motion of the robotic arm, in indoor and outdoor conditions. Moreover, the proposed solution is tested in a similar to industrial environment to demonstrate efficiency of the approach in the real-case challenging tasks. In particular, deployment of the mobile inspection robot on the remotely located pipeline surrounded by fence, peg-in-hole assembly, and valve turn are performed in a complex environment with various obstacles.

We would like to highlight that most of the work in the scope of this thesis has been performed within the H2020 AEROARMS project. We are extremely grateful to all consortium partners for their valuable comments and feedback regarding the work. We believe that the proposed concept and thesis results will facilitate the aerial manipulation field in both research and development directions and bridge the gap between laboratory research and real world applications.

1.4 Thesis structure

This section provides a description of the thesis organization to help in navigation within the manuscript and facilitate a reading experience. The thesis contains in

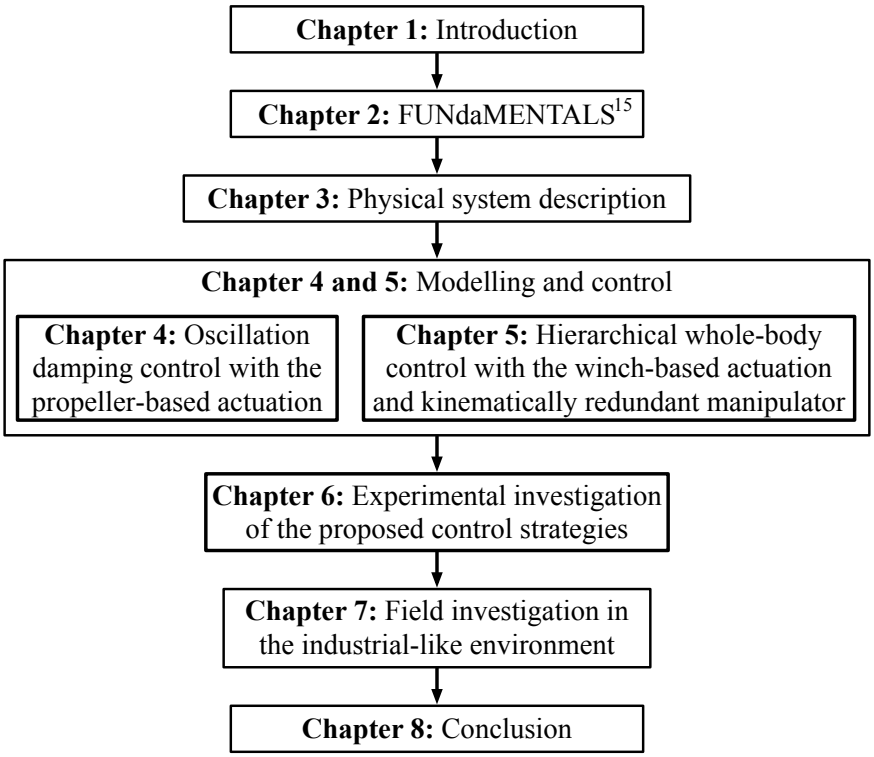

Figure 1-7: Thesis structure.

total eight chapters and has coherent information flow illustrated at the diagram depicted in Figure 1-7.

Chapter 2 - Fundamentals - recalls the basic mathematical and robotic principles which are utilized in the scope of this thesis. In particular, general approaches for the physical modeling and control are considered, main concepts of the aerial, cable-driven, and manipulation robotics are provided.

Chapter 3 - Physical system description.

In this chapter, we form the foundation and investigate the cable-suspended aerial manipulation concept. Specifically, we consider potential operational scenarios at which the system can operate, formulate the qualitative requirements to this type of system, and finally, we consider the detailed design of a specific representative, system demonstrator, the SAM, including main features, quantitative requirements, sensors, mechanical and electronic design.

Chapter 4 - Oscillation damping control with the propeller-based actuation.

This chapter is devoted to the development of the OODC, which relies on the

[15]Spelling is inspired by http://pergatory.mit.edu/resources/fundamentals.html

propeller-based actuation. Modeling of the general and reduced cases is considered. Further, control goal, detailed controller derivation, gain tuning rule, stability analysis, and controller performance evaluation are established. Additionally, model behavior with regard to the variation of system parameters is investigated. In the end, the developed approach is validated on the toy problem.

Chapter 5 - Hierarchical whole-body control with the winch-based actuation and kinematically redundant manipulator.

The chapter presents the HWBC framework for the winch actuated platform with the attached redundant robotic arm. Original constrained dynamics of the winch cabling is derived and further presented in the reduced form by introducing assumptions to formulate control law. A whole-body control framework with included system inverse kinematics, task definition, and admittance interface is described. In the end, performance evaluation on the toy problem is presented.

Chapter 6 - Experimental investigation of the proposed control strategies.

Within this chapter, validation and experimental investigation of designed controllers developed in the scope of the chapter 4 and chapter 5 on the system demonstrator are conducted. At the beginning of the chapter, we describe the experimental environments in which validation is performed. Further, OODC performance is analysed through experiments for various situations including the robotic arm's motion, external disturbances, and changes in the operational environment. Next, we investigate the functionality of the elaborated controller with common operational tasks, namely, robotic arm motion and pick and place. In the end, both controllers are integrated and tested.

Chapter 7 - Field investigation in the industrial-like environment - considers and evaluates an operation of the hypothesis-based system demonstrator under the developed controllers in outdoor similar to the industrial environment for three proposed missions: deployment of the mobile inspection robot, peg-in-hole assembly, and the valve turn at the remotely located pipeline.

Chapter 8 - Conclusion - focuses on the discussion of the obtained results, learned lessons, limitations, and future potential of the cable-suspended aerial manipulation technology.

"The good thing about science is that it's true whether or not you believe in it."

Neil deGrasse Tyson

Chapter 2

Fundamentals

In chapter 2, we briefly review the basic foundations exploited in the scope of this thesis. At first, we define the general terms from the robot kinematics and dynamics. Secondly, the modeling approaches applied to the aerial and cable-driven robots are discussed. Lastly, we explain control methodologies on which we relied in our developments. More complete and elaborated discussions on the topics can be found in the commonly used literature [Asada and Slotine, 1986, Corke, 2017, Craig, 2009, Murray, 1994, Siciliano and Khatib, 2007, Siciliano et al., 2010].

2.1 Modeling of physical systems

The physical systems with which we deal in the scope of this thesis consist of single or multiple rigid bodies (links) connected to the unified *chain* through *joints*. Each joint provides one DOF motion for pair of surfaces. Two main joint types for our applications can be distinguished. Namely, *prismatic* joint provides translational motion of two surfaces relative to each other, and a *revolute* type allows to rotate one surface around another. Further, we will introduce the *kinematic* and *dynamic* modeling basics for the single rigid body, and then briefly provide some insights on modeling of multirotor, cable-driven, and serial manipulation robotic systems.

2.1.1 Notes on kinematics and dynamics

2.1.1.1 Rigid body transformation

The location of any rigid body is fully described by its position and orientation (in brief, a *pose*) with respect to a certain reference frame.

Reference frames

The pose of the rigid body can be defined relative to the reference frame. Let us denote by $\mathcal{F}_w: \{O_w,\ x_w,\ y_w,\ z_w\}$ the *world (inertial* or *fixed) frame* placed in inertial space and by $\mathcal{F}_b: \{O_b,\ x_b,\ y_b,\ z_b\}$ the *body frame* attached to the COM of the rigid body and aligned with its principal axes, see Figure 2-1. Both frames are right-handed and with orthogonal axes. Then, the position of the O_b with respect to the world reference frame can be defined by a vector $\boldsymbol{p}_b^w = [x_{O_b},\ y_{O_b},\ z_{O_b}]^T \in \mathbb{R}^3$. At the same time, the rotation of the rigid body can be expressed in multiple ways.

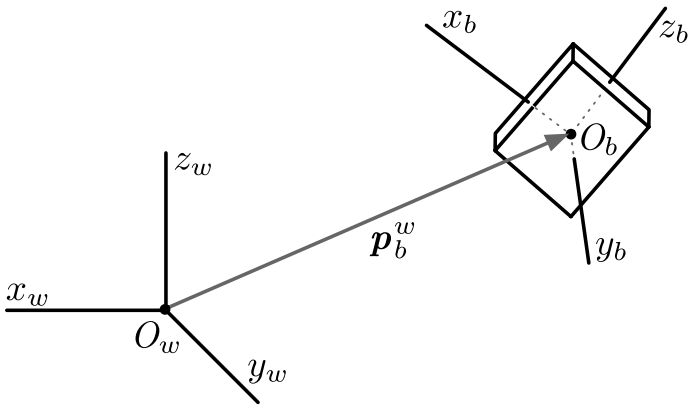

Figure 2-1: Reference frames for the rigid body.

Rotational motion

Let us consider the case when only the rotational motion of the rigid body is performed. There are different strategies to represent the rotation of one coordinate frame with respect to another. All of them are interchangeable and have their own advantages and disadvantages. Let us introduce the most common:

- A *rotation matrix* expresses the orthonormal basis vectors of the body frame, i.e., unit vectors $\boldsymbol{i}_b,\ \boldsymbol{j}_b,\ \boldsymbol{k}_b$, with respect to the world frame:

$$\boldsymbol{R}_b^w = \begin{bmatrix} \boldsymbol{i}_b, & \boldsymbol{j}_b, & \boldsymbol{k}_b \end{bmatrix}.$$

  The rotation matrix belongs to the special orthogonal group SO(3) of the real 3×3 matrices with orthonormal columns and determinant equal to 1:

$$\mathrm{SO}(3) = \{\boldsymbol{R} \in \mathbb{R}^{3\times 3}:\ \boldsymbol{R}\boldsymbol{R}^T = \boldsymbol{I}_3,\ det(\boldsymbol{R}) = 1\}. \tag{2.1}$$

Due to properties of the SO(3) group, the *composition rule* for rotation matrices can be formulated: rotation matrices can be combined using matrix multiplication, i.e., $\boldsymbol{R}_a^c = \boldsymbol{R}_b^c \boldsymbol{R}_a^b$, where a, b, c represent some reference frames. It is worth mentioning that from (2.1) the interesting result for rotation matrix follows: $\boldsymbol{R}^{-1} = \boldsymbol{R}^T$.

- *Roll, Pitch, Yaw (RPY) angles* is the set of Euler angles $\boldsymbol{\phi} = [\varphi,\ \theta,\ \psi]^T$ to describe the rigid body orientation around the world frame axes. It consists of 3 independent parameters and corresponds to the minimal representation of spatial rotation (in contrast to the rotation matrix with nine redundant elements).

  One of the critical disadvantages of the representation through Euler angles is discontinuity for a singular configuration when two rotational axes are parallel. This effect is known as gimbal lock.

- A *unit quaternion* is a four-parameter rotation representation defined as:

$$\boldsymbol{\varrho} = \{\eta,\ \boldsymbol{\epsilon}\},$$

  where $\eta = \cos\frac{\varepsilon}{2}$ and $\boldsymbol{\epsilon} = [\epsilon_x,\ \epsilon_y,\ \epsilon_z]^T = \boldsymbol{r}\sin\frac{\varepsilon}{2}$ are the scalar and vector parts of the quaternion representation which decodes rotation of an angle ε around of rotation axis represented by unit vector $\boldsymbol{r}$. Quaternion is constrained by the following condition that explains the title *unit*:

$$\eta^2 + \epsilon_x^2 + \epsilon_y^2 + \epsilon_z^2 = 1.$$

Rigid motion

As we mentioned above, the rigid body transformation is composed from the rotational and translational motions. Thus, configuration of the rigid body with respect to certain reference frame is completely described by pair $\boldsymbol{g} = (\boldsymbol{p}, \boldsymbol{R})$. The product of $\mathbb{R}^3$ and SO(3) is called special Euclidean group SE(3)[1]:

$$\mathrm{SE}(3) = \{\boldsymbol{g} = (\boldsymbol{p}, \boldsymbol{R}) : \boldsymbol{p}_b^w \in \mathbb{R}^3, \boldsymbol{R}_b^w \in \mathrm{SO}(3)\} = \mathrm{SO}(3) \times \mathbb{R}^3.$$

[1]In general, groups can be defined for any dimension n, i.e., SE(n) or SO(n). In three-dimensional space $n = 3$.

Let us denote by $\boldsymbol{e}_w$ and $\boldsymbol{e}_b$ the coordinates of some point E in the world and body frames, respectively. Then, we can formulate relation between these two sets of coordinates through $\boldsymbol{g}_b^w$ configuration as follows:

$$\boldsymbol{e}_w = \boldsymbol{p}_b^w + \boldsymbol{R}_b^w \boldsymbol{e}_b,$$

or exploiting so-called *homogeneous transformation matrix*, $\bar{\boldsymbol{g}}_b^w$:

$$\begin{bmatrix} \boldsymbol{e}_w \\ 1 \end{bmatrix} = \underbrace{\begin{bmatrix} \boldsymbol{R}_b^w & \boldsymbol{p}_b^w \\ \boldsymbol{0}_{3\times 1}^T & 1 \end{bmatrix}}_{\bar{\boldsymbol{g}}_b^w} \begin{bmatrix} \boldsymbol{e}_b \\ 1 \end{bmatrix}.$$

It is worth mentioning that similar to rotation matrices, the composition rule might be applied to homogeneous transformation, i.e., $\bar{\boldsymbol{g}}_a^c = \bar{\boldsymbol{g}}_b^c \bar{\boldsymbol{g}}_a^b$, where a, b, c denote some reference frames.

Twist and wrench

The two groups, special Orthogonal and special Euclidean, are of particular interest to us. Both of them are representatives of the Lie group, which is a group and a differentiable manifold[2]. First, we need to introduce a Lie algebra of the group as the tangent space at the identity element.

Let $\boldsymbol{\omega} = [\omega_x,\ \omega_y,\ \omega_z]^T \in \mathbb{R}^3$ be an angular velocity vector specifying the direction of rotation in the world frame. Then, we can define Lie algebra of SO(3) group as:

$$\mathrm{so}(3) = \{\hat{\boldsymbol{\omega}} \in \mathbb{R}^{3\times 3} : \hat{\boldsymbol{\omega}}^T = -\hat{\boldsymbol{\omega}}\},$$

where $\wedge$ (wedge) sign maps the vector to the skew-symmetric matrix as follows:

$$\hat{\boldsymbol{\omega}} = \begin{bmatrix} 0 & -\omega_z & \omega_y \\ \omega_z & 0 & -\omega_x \\ -\omega_y & \omega_x & 0 \end{bmatrix}.$$

A general element of Lie algebra for the SE(3) group is a partitioned matrix:

$$\boldsymbol{S} = \begin{bmatrix} \hat{\boldsymbol{\omega}} & \boldsymbol{v} \\ \boldsymbol{0} & \boldsymbol{0} \end{bmatrix} \in \mathrm{se}(3).$$

[2]The manifold is a topological space that is locally Euclidean.

Here, $\boldsymbol{v} = [v_x,\ v_y,\ v_z]^T \in \mathbb{R}^3$ is the linear velocity vector. Then, Lie algebra of special Euclidean group is defined as follows:

$$\mathrm{se}(3) = \{(\boldsymbol{v}, \boldsymbol{\omega}) : \boldsymbol{v} \in \mathbb{R}^3, \hat{\boldsymbol{\omega}} \in \mathrm{so}(3)\}.$$

We call the element of Lie algebra se(3) as a *twist*. Such an element $\boldsymbol{S}$ might be conveniently represented in the vector form of *twist coordinates* $\boldsymbol{s}$ by utilizing $\vee$ (vee) map as:

$$\boldsymbol{s} = \underbrace{\begin{bmatrix} \hat{\boldsymbol{\omega}} & \boldsymbol{v} \\ \boldsymbol{0} & \boldsymbol{0} \end{bmatrix}^{\vee}}_{\boldsymbol{S}} = \begin{bmatrix} \boldsymbol{v} \\ \boldsymbol{\omega} \end{bmatrix} \in \mathbb{R}^6.$$

Similar to the SO(3) group, the inverse operator wedge, $\wedge$, transforms twist coordinates $\boldsymbol{s}$ to the twist $\boldsymbol{S}$:

$$\underbrace{\begin{bmatrix} \boldsymbol{v} \\ \boldsymbol{\omega} \end{bmatrix}^{\wedge}}_{\boldsymbol{s}} = \underbrace{\begin{bmatrix} \hat{\boldsymbol{\omega}} & \boldsymbol{v} \\ \boldsymbol{0} & \boldsymbol{0} \end{bmatrix}}_{\boldsymbol{S}}.$$

Let us define *wrench* as the six dimensional force-torque vector:

$$\boldsymbol{w} = \begin{bmatrix} \boldsymbol{f} \\ \boldsymbol{\tau} \end{bmatrix} \in \mathbb{R}^6,$$

where the first vector $\boldsymbol{f}$ is the linear force, and the second one $\boldsymbol{\tau}$ is the rotational torque vector. As a vector, the wrench can be expressed with respect to the different reference frames. Thus, the *spatial wrench* is represented in the world frame, and the *body wrench* is the wrench in the instantaneous body frame.

Rigid body velocity

Let us denote the configuration of the body frame with respect to the world frame by homogeneous transformation matrix $\bar{\boldsymbol{g}}_b^w$:

$$\bar{\boldsymbol{g}}_b^w = \begin{bmatrix} \boldsymbol{R}_b^w & \boldsymbol{p}_b^w \\ \boldsymbol{0}_{3\times1}^T & 1 \end{bmatrix}.$$

Let us define the *spatial velocity* expressed in the world frame as the following twist:

$$\hat{\boldsymbol{V}}_w = \dot{\bar{\boldsymbol{g}}}_b^w (\bar{\boldsymbol{g}}_b^w)^{-1},$$

and the *body velocity* expressed in instantaneous body coordinate frame as:

$$\hat{\boldsymbol{V}}_b = (\bar{\boldsymbol{g}}_b^w)^{-1} \dot{\bar{\boldsymbol{g}}}_b^w. \tag{2.2}$$

The spatial and body velocities are related as follows:

$$\hat{\boldsymbol{V}}_b = (\bar{\boldsymbol{g}}_b^w)^{-1} \hat{\boldsymbol{V}}_w (\bar{\boldsymbol{g}}_b^w).$$

Corresponding twist coordinates of these two frames are connected by 6×6 matrix, *adjoint transformation* associated with $\boldsymbol{g}_b^w$:

$$\underbrace{\begin{bmatrix} \boldsymbol{v}_w \\ \boldsymbol{\omega}_w \end{bmatrix}}_{\boldsymbol{V}_w} = \underbrace{\begin{bmatrix} \boldsymbol{R}_b^w & \hat{\boldsymbol{p}}_b^w \boldsymbol{R}_b^w \\ \boldsymbol{0}_3^T & \boldsymbol{R}_b^w \end{bmatrix}}_{\mathbf{Ad}_{\boldsymbol{g}_b^w}} \underbrace{\begin{bmatrix} \boldsymbol{v}_b \\ \boldsymbol{\omega}_b \end{bmatrix}}_{\boldsymbol{V}_b}.$$

Error elements

Based on the composition rule, we can define error elements between two frames, i.e., desired and current pose of the rigid body in terms of:

- homogeneous transformation

  $$\boldsymbol{g}_{error} = \bar{\boldsymbol{g}}_{des}^{-1}\, \bar{\boldsymbol{g}}_{real} = (\boldsymbol{R}_{error},\ \boldsymbol{p}_{error}),$$

  here $\boldsymbol{g}_{des}$ is the homogeneous transformation that describes desired pose, $\boldsymbol{g}_{real}$ is the homogeneous transformation that describes current pose of the object.

- unit quaternion

  $$\boldsymbol{\varrho}_{error} = \boldsymbol{\varrho}_{des} \circ \boldsymbol{\varrho}_{real}^{-1} = (\eta_{error},\ \boldsymbol{\epsilon}_{error}),$$

  here $\boldsymbol{\varrho}_{des}$ is the unit quaternion that indicates desired pose, $\boldsymbol{\varrho}_{real}$ is the unit quaternion that describes current pose of the object, $\circ$ is the operator of quaternion multiplication.

Additionally, it is worth introducing a velocity error element as follows:

$$\boldsymbol{V}_{error} = \boldsymbol{V}_{real} - \mathbf{Ad}_{\boldsymbol{g}_{error}^{-1}} \boldsymbol{V}_{des}.$$

2.1.1.2 Robot kinematics

A regular robotic system contains several rigid bodies (links) and can be described by joint coordinates $\boldsymbol{q} \in \mathbb{R}^n$, where n is the number of robot DOF. Here, $\boldsymbol{q}$ is the vector of displacements in translational and rotational robot joints at which the system evolves naturally. It defines the *joint* (or *configuration*) *space*.

However, as a rule, we want to control certain DOF $\boldsymbol{x}(\boldsymbol{q}) \in \mathbb{R}^m$ along desired direction instead of direct robot joints. For example, in robotic manipulation, we can control either joint displacements or end effector location. The values of vector $\boldsymbol{x}(\boldsymbol{q})$ establish the *task* (or *Cartesian, operational*) *space*. In the case of $m < n$, the robot is *kinematically redundant*, i.e., while maintaining the main task in $\boldsymbol{x}(\boldsymbol{q})$ coordinates, the internal motion of the robot is possible by utilizing $(n - m)$ DOFs *null space*.

Two main kinematics problems can be distinguished. The *forward kinematics* solves the task of finding position and orientation of the end effector based on the joint displacements:

$$\boldsymbol{x}(\boldsymbol{q}) = \boldsymbol{f}(\boldsymbol{q}).$$

In contrast, an *Inverse Kinematics (IK)* solves the task of calculating the joint displacements for a certain end effector configuration:

$$\boldsymbol{q} = \boldsymbol{f}^{-1}\boldsymbol{x}(\boldsymbol{q}).$$

Then, let us define a linear map of the *joint velocities* space to the *task velocities* space as follows:

$$\dot{\boldsymbol{x}}(\boldsymbol{q}) = \frac{\boldsymbol{\partial f}(\boldsymbol{q})}{\boldsymbol{\partial q}} \dot{\boldsymbol{q}} = \boldsymbol{J}(\boldsymbol{q})\dot{\boldsymbol{q}}. \tag{2.3}$$

The matrix $\boldsymbol{J}(\boldsymbol{q}) \in \mathbb{R}^{m \times n}$ which defines relation between velocities is referred to as the analytic *Jacobian* matrix. Differential kinematic map $\boldsymbol{J}(\boldsymbol{q})$ is illustrated in Figure 2-2. Two subspaces *range* $\mathcal{R}(\boldsymbol{J})$ and *null* $\mathcal{N}(\boldsymbol{J})$ can be distinguished. The range subspace of $\boldsymbol{J}(\boldsymbol{q})$ represents the set of all task velocities that can be achieved

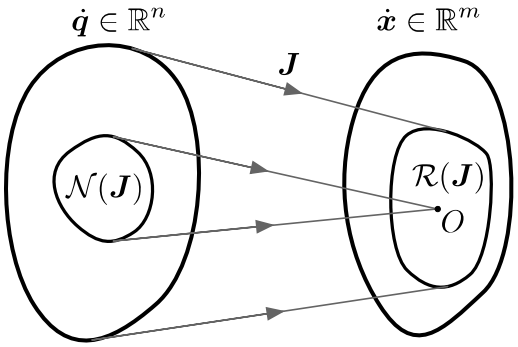

Figure 2-2: The Jacobian map between the joint velocity space $\dot{\boldsymbol{q}}$ and the task velocity space $\dot{\boldsymbol{x}}$.

by the joint velocities for current robot configuration. The null subspace of $\boldsymbol{J}(\boldsymbol{q})$ is the set of joint velocities that does not generate any motion in the task velocities space for given robot posture.

Due to the law of energy conservation, the power generated by joint motion should be equal to the power produced by task motion. It allows us to exploit the Jacobian matrix for establishing the map between an end effector wrench $\boldsymbol{F} \in \mathbb{R}^6$ and vector of joint torques $\boldsymbol{\tau} \in \mathbb{R}^n$ as well:

$$\boldsymbol{\tau} = \boldsymbol{J}(\boldsymbol{q})^T \boldsymbol{F}. \tag{2.4}$$

Additionally, the Jacobian matrix analysis can provide some valuable insights on the instantaneous robot configuration. Primarily, we are interested in the *singularity* and *manipulability* of the robot.

At the singular configuration, the Jacobian matrix is rank-deficient, i.e., the determinant of the Jacobian is 0. At such configurations, the singularity causes the loss of one or more DOF. Therefore the joint velocities required to maintain desired task velocities in specific directions become close to infinite [Williams II, 1999].

One of the possible metrics to evaluate robot proximity to the singular configuration is to estimate its manipulability by calculating *manipulability ellipsoid* volume [Vahrenkamp et al., 2012]:

$$\texttt{EV}(\boldsymbol{q}) = \frac{4\pi}{3}\sqrt{\det(\boldsymbol{J}(\boldsymbol{q})\boldsymbol{J}(\boldsymbol{q})^T)}. \tag{2.5}$$

Here, $\texttt{EV}(\boldsymbol{q})$ is the volume of the manipulability ellipsoid, $\boldsymbol{J}(\boldsymbol{q}) \in \mathbb{R}^{m \times n}$ is the robot Jacobian defined by its instantaneous joints configuration.

2.1.1.3 Dynamics

Two main approaches for the derivation of the rigid body dynamic equations exist. In general, the equations of motion describe the robotic system dynamic response to input joint torques.

Newton-Euler formulation

The *Newton-Euler formulation* of equations of motion is based on the direct interpreting of the momentum conservation and angular momentum conservation laws. These two laws result in dynamic translational and rotational equations of motion, respectively. The first one is well-known as the Newton's Second Law. Let us write it down in the world frame:

$$\frac{\boldsymbol{dp}}{dt} = \frac{m\boldsymbol{dv}}{dt} = m\boldsymbol{a} = \boldsymbol{f},$$

where $\boldsymbol{p} = m\boldsymbol{v}$ is the momentum of the system. Similarly, we can write down the *Euler's equation* in the body frame as follows:

$$\frac{\boldsymbol{dL}}{dt} = \frac{\boldsymbol{Y}\boldsymbol{d\omega}_b}{dt} + \boldsymbol{\omega}_b \times \boldsymbol{L} = \boldsymbol{\tau},$$

where $\boldsymbol{L} = \boldsymbol{Y}\boldsymbol{\omega}_b$ is the angular momentum, and $\boldsymbol{Y}$ is the diagonal inertia tensor with respect to the principal axes. We use the aerospace notation to denote the angular velocity expressed in the body frame $\boldsymbol{\omega}_b = [p,\ q,\ r]^T$.

Formulated equations form the Newton-Euler formulation and describe the translational and rotational motion of the rigid body COM under the applied forces and torques. Robot modeling utilizing this formulation is performed by generating and combining the equations of motions for every robot link.

Lagrangian formulation

The *Lagrangian formulation* describes the system behavior in terms of the stored energy. Let $\boldsymbol{q} \in \mathbb{R}^n$ be *generalized coordinates* that effectively describe the n-DOFs robot, e.g., for robotic manipulator this set of coordinates might be the vector of the joint angles. Then, the Lagrangian of the mechanical system can be defined as

the difference between system *kinetic energy* $\mathcal{T}(\boldsymbol{q}, \dot{\boldsymbol{q}})$ and *potential energy* $\mathcal{U}(\boldsymbol{q})$:

$$\mathcal{L}(\boldsymbol{q}, \dot{\boldsymbol{q}}) = \mathcal{T}(\boldsymbol{q}, \dot{\boldsymbol{q}}) - \mathcal{U}(\boldsymbol{q}).$$

By utilising the Lagrangian, the Lagrange's equations of motion in terms of generalized coordinates are expressed as follows:

$$\frac{d}{dt}(\frac{\partial \mathcal{L}}{\partial \dot{\boldsymbol{q}}})^T - (\frac{\partial \mathcal{L}}{\partial \boldsymbol{q}})^T = \boldsymbol{Q}, \tag{2.6}$$

where $\boldsymbol{Q}$ contains generalized and external torques.

Serial and closed chains

Regardless of the selected formulation, the resulted equation of motions for the robotic systems can be described in general by the following dynamic equations:

$$\begin{aligned} \boldsymbol{M}(\boldsymbol{q})\ddot{\boldsymbol{q}} + \boldsymbol{C}(\boldsymbol{q}, \dot{\boldsymbol{q}})\dot{\boldsymbol{q}} + \boldsymbol{g}(\boldsymbol{q}) &= \boldsymbol{\tau} + \boldsymbol{A}^T\boldsymbol{\lambda} + \boldsymbol{\tau}_{ext}, \\ \boldsymbol{A}(\boldsymbol{q})\dot{\boldsymbol{q}} &= 0, \end{aligned}$$

where $\boldsymbol{M}$ is the symmetric and positive definite inertia matrix, $\boldsymbol{C}$ contains the centrifugal/Coriolis terms, $\boldsymbol{g}$ is the gravity vector, $\boldsymbol{\tau}$ is the vector of the generalized torques, and $\boldsymbol{\tau}_{ext}$ are external forces and torques.

Given the generalized torques and the initial system conditions, the forward dynamics equations evaluate the robot motion, expressed in terms of the generalized coordinates and their derivatives, i.e., $\ddot{\boldsymbol{q}}$, $\dot{\boldsymbol{q}}$, and $\boldsymbol{q}$. So, the generalized torques serve as inputs, and kinematic parameters - as outputs. For the serial chain, the matrix $\boldsymbol{A}$ is a zero matrix, while for the closed chains, it represents system constraints. There are two types of constraints, namely, *holonomic* and *nonholonomic constraints*. The former constrains the configuration and consequently reduces the configuration space, i.e., the DOF. The latter type puts constraints on the velocity and does not reduce the configuration space. Constrains in the form $\boldsymbol{A}(\boldsymbol{q})\dot{\boldsymbol{q}} = 0$ are called Pfaffian constraints, they might be both holonomic or nonholonomic.

2.1.2 Multirotor systems

Let us introduce the multirotor aerial robot. Such a system represents a single rigid body with several propeller-based actuators, each of which can produce a force.

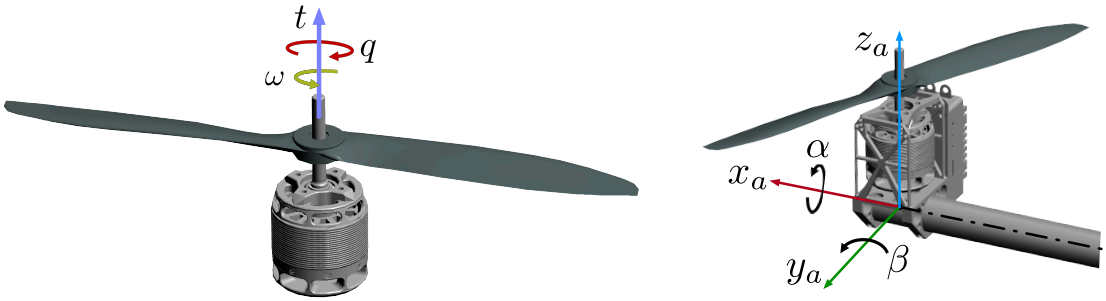

(a) CCW propeller thrust force t, drag torque q, and angular velocity ω directions

(b) Orientation angles of the propeller relative to the frame arm

Figure 2-3: Propeller actuation.

2.1.2.1 Performance of the propeller

First of all, let us provide some details about the actuation. Namely, let us consider the motor with the attached propeller at the shaft, see Figure 2-3a.

While spinning, the propeller creates a reduced pressure zone on the top of the blade. Due to Bernoulli's principle [Lindsay, 1952], the air molecules result in an upward-lifting force. Let us call it as the *thrust force* [Spakovszky et al., 2008] and define it for the environment with constant parameters and particular propeller geometry design as follows:

$$t = f(D, \omega, \rho, u_0, K) = k_t \omega^2.$$

Here, D is the propeller diameter, ρ is the air density, K is the fluid bulk elasticity modulus, u_0 is the flight velocity, ω is the propeller angular velocity in $[\frac{rad}{s}]$. While operating in the same conditions, most of those parameters remain constant and can be combined in one gain, thrust coefficient, k_t, such that the thrust force is proportional to the square of the propeller angular velocity.

Since the propeller spins in the air environment the *drag torque*, q, directed opposite to the angular velocity, is generated as well:

$$q = f(D, \omega, \rho, u_0, K) = k_q \omega^2 = k_{ad} t. \tag{2.7}$$

Here, k_q is the constant drag coefficient that depends on the propeller design and environment conditions, and k_{ad} is the aerodynamic gain presenting ratio between drag torque and thrust force of the propeller.

It is worth noting here that there are two types of propellers: ClockWise (CW)

and CounterClockWise (CCW) propellers. The first one generates the vertical thrust and co-directional drag torque when the propeller performs clockwise motion, as seen from the tip of the thrust vector. The latter generates vertical thrust and contradirectional drag torque when the propeller spins in the counterclockwise direction. Both vectors, thrust and drag, are aligned with the motor spinning axis.

2.1.2.2 Unidirectional and multidirectional thrusts

First of all, let us define an actuator frame $\mathcal{F}_a : \{O_a,\ x_a,\ y_a,\ z_a\}$ which is centered in the COM of the actuator and placed such that x_a is aligned with the installation frame arm and pointed outward, z_a is aligned with motor spinning axis, and y_a complements the frame to the right-handed, see Figure 2-3b. Then, the propeller rotor group can be placed with various orientations with respect to the installation arm. Namely, two installation angles might be introduced, α and β which represent the rotation around x_a and y_a, respectively.

Now, we consider two representatives of the multirotors. The first one is a quadcopter with collinear propellers, that can generate unidirectional thrust. The second system is a hexacopter with tilted propellers, i.e., installed with certain α and β angles, see Figure 2-4. The latter is able to produce the thrust in multiple directions.

Let us denote by $\boldsymbol{w}_b$ a wrench that is produced in the body frame by thrust forces generated by propellers.

$$\boldsymbol{w}_b = \begin{bmatrix} \boldsymbol{f}_b \\ \boldsymbol{\tau}_b \end{bmatrix} = \boldsymbol{A}\boldsymbol{t}. \tag{2.8}$$

Here, $\boldsymbol{A}$ is the *allocation matrix* that maps the thrust vector $\boldsymbol{t}$ to the generated body wrench. Thus, the allocation matrix reflects the general design and depends on the geometric parameters (number of propellers, dimension of the arm frame, propeller installation angles) of the particular system.

Let us assume we want to generate the upward lifting force $\boldsymbol{f}$ by introduced multirotor systems, see Figure 2-4a and Figure 2-4b. In this case, both systems can produce such an amount of thrust that can satisfy the task, i.e., provide zero torque and non-zero force:

$$\boldsymbol{w}_b = \begin{bmatrix} \boldsymbol{f}_b \\ \boldsymbol{\tau}_b \end{bmatrix} = \begin{bmatrix} \boldsymbol{f} \\ \boldsymbol{0} \end{bmatrix}.$$

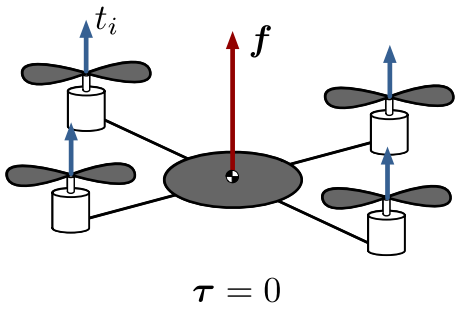

(a) Quadcopter case. The desired wrench contains a vertical force and zero torque

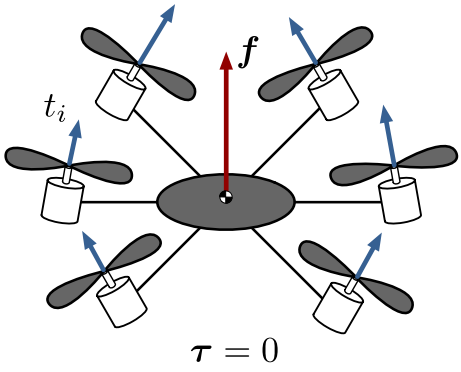

(b) Hexacopter case. The desired wrench contains a vertical force and zero torque

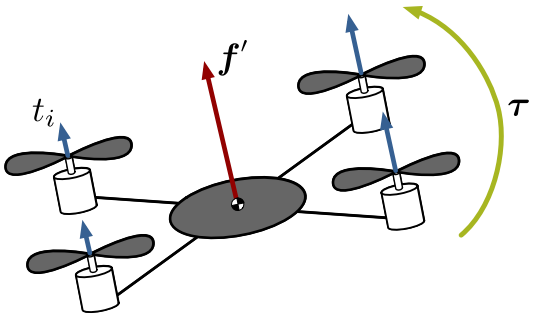

(c) Quadcopter case. The desired wrench contains a tilted force and zero torque

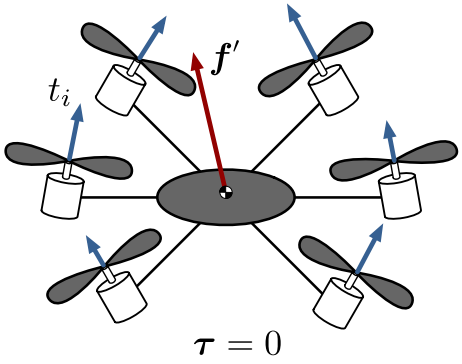

(d) Hexacopter case. The desired wrench contains a tilted force and zero torque

Figure 2-4: Wrench generation by the common quadcopter with collinear thrusts (left) and hexacopter with tilted thrusts (right).

Now, let us consider the case when we would like to generate slightly tilted force $\boldsymbol{f}'$, see Figure 2-4c and Figure 2-4d. In the case of the quadcopter with collinear propellers, we need to tilt the whole system in order to align each thrust force with desired force $\boldsymbol{f}'$. Thus, we have to generate additional torque $\boldsymbol{\tau}$. On the other hand, hexacopter with tilted propellers can generate desired force with zero torque.

The first system is a representative of unidirectional thrust multirotor [Hamandi et al., 2020]. Such a system is underactuated and has coupled dynamics. The second system with multidirectional thrusts has partially decoupled dynamics. So, it could generate the desired force without exerting any torques. It is worth mentioning that to fully decouple translational and rotational dynamics, at least 7 unidirectional thrusts are required, as was shown by Marco Tognon in [Tognon and Franchi, 2018].

The linear map diagram shown in Figure 2-5 can help interpret the equation (2.8)

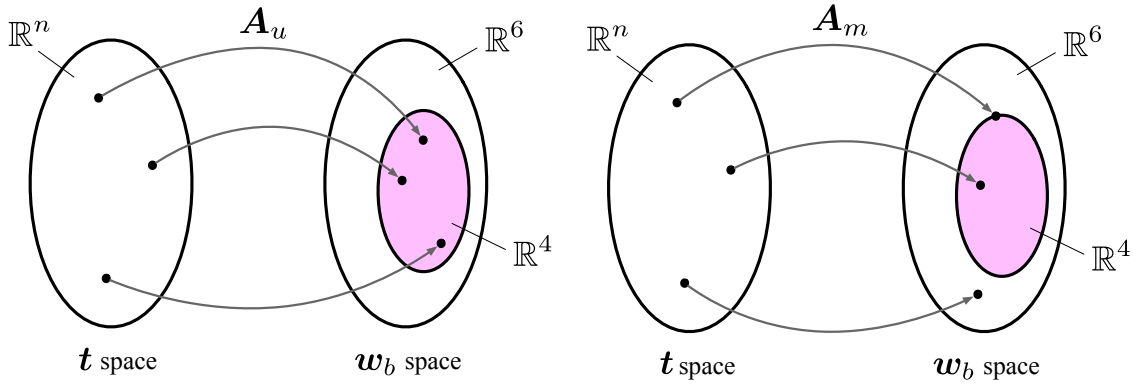

(a) Allocation matrix map for the quadcopter with collinear thrusts. All configurations of the $\boldsymbol{t}$ space generate the coupled wrench

(b) Allocation matrix map for the hexacopter with tilted thrusts. Certain configurations in the $\boldsymbol{w}_b$ space result in the decoupled wrench

Figure 2-5: The allocation matrix map between the thrust space $\boldsymbol{t}$ and the body wrench space $\boldsymbol{w}_b$.

more rigorously. Let us define two spaces, namely the space of thrust vector and the generated body wrench space. Then, the allocation matrix maps the former one to the latter. Analysis of the allocation matrix can help us to extract the properties of the propeller allocation design. Particularly, the rank of the allocation matrix reflects the number of DOF that we can generate independently. Thus, for the considered above underactuated quadcopter with $\boldsymbol{t} \in \mathbb{R}^4$ (4 propellers), we can state that the corresponding $rank(\boldsymbol{A}_u) = 4$. On another hand, for the multirotor system with $\boldsymbol{t} \in \mathbb{R}^{7+}$, we can write down that the $rank(\boldsymbol{A}_m) = 6$.

2.1.3 Cable-driven robots

The typical cable-driven robot contains two main functional nodes, the base at which the world frame might be placed and the end effector platform the pose of which is defined by the body frame. The end effector is attached to the base through multiple length-controlled cables. The actuators which regulate the cable length are usually located in the base. Thus, controlling the cable length of multiple actuators, we can change the end effector pose. The forward kinematics for cable-driven robots is known to be challenging to resolve [Merlet and Alexandre-dit Sandretto, 2015], while the inverse kinematics problem might be addressed in straightforward manner [Bosscher et al., 2006, Pott and Kraus, 2016]. Indeed, let us have a look in Figure 2-6. By point A_i we denote the location of the i-th actuator that controls the length of the cable, while point B_i would represent

the connection of the cable to the end effector platform. Vector $\boldsymbol{a}_i$ defines the position of the point A_i in the world frame, vector $\boldsymbol{b}_i$ represents the location of point B_i in the body frame. The vector $\boldsymbol{u}_i$ is a unit vector directed toward the cable length vector $\boldsymbol{l}_i$. Thus, vector $\boldsymbol{u}_i$ is aligned with the cable tension force.

Based on the Figure 2-6, the vector closure loop can be written as follows:

$$\boldsymbol{l}_i = \boldsymbol{a}_i - \boldsymbol{p}_b^w - \boldsymbol{R}_b^w \boldsymbol{b}_i.$$

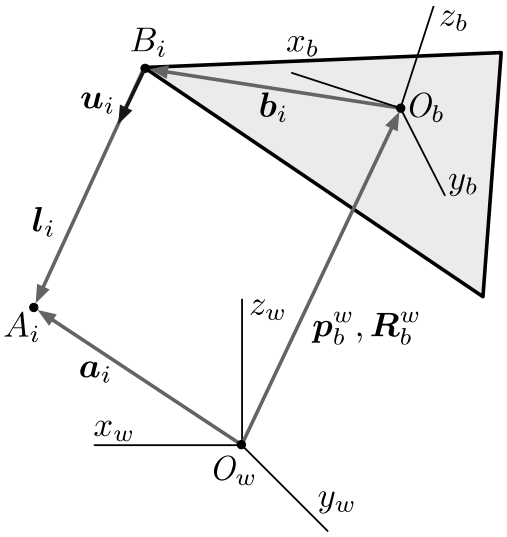

Figure 2-6: Kinematics of the cable-driven robot.

2.1.4 Luca Dynamics library

The Luca Dynamics is a powerful kinematics and dynamics library that has been created at RMC [Garofalo et al., 2013]. It allows calculating the quantities used in rigid body robotics based on the Universal Robotic Description Format (URDF). Namely, based on the model and updated full state of a rigid body system, it provides the following outputs: inertia tensor, gravity vector, Coriolis/centrifugal terms, the position of COM, homogeneous transformation, centroidal momentum matrix, and Jacobian transformation for the point of interest.

2.2 Control of physical systems

A control of the dynamic system entails finding actuator efforts in order to provide a desired motion. In case when we command the desired joint motion, we deal with joint space control. The system dynamics for the serial chain and control input are related as follows:

$$\boldsymbol{M}(\boldsymbol{q})\ddot{\boldsymbol{q}} + \boldsymbol{C}(\boldsymbol{q}, \dot{\boldsymbol{q}})\dot{\boldsymbol{q}} + \boldsymbol{g}(\boldsymbol{q}) = \boldsymbol{\tau} + \boldsymbol{\tau}_{ext}.$$

In contrast, if we formulate the control law in the task space, then we deal with a task space control. By utlizing (2.3), we can write down the following:

$$\dot{\boldsymbol{q}} = \boldsymbol{J}(\boldsymbol{q})^{-1}\dot{\boldsymbol{x}}(\boldsymbol{q}),$$
$$\ddot{\boldsymbol{q}} = \boldsymbol{J}(\boldsymbol{q})^{-1}\ddot{\boldsymbol{x}}(\boldsymbol{q}) + \dot{\boldsymbol{J}}(\boldsymbol{q})^{-1}\dot{\boldsymbol{x}}(\boldsymbol{q}).$$

Then, system dynamics and control law in the task space can be rewritten as:

$$\underbrace{\bar{\boldsymbol{M}}(\boldsymbol{q})}_{\boldsymbol{J}^{-T}\boldsymbol{M}\boldsymbol{J}^{-1}}\ddot{\boldsymbol{x}} + \underbrace{\bar{\boldsymbol{C}}(\boldsymbol{q},\dot{\boldsymbol{q}})}_{\boldsymbol{J}^{-T}(\boldsymbol{M}\dot{\boldsymbol{J}}^{-1}+\boldsymbol{C}\boldsymbol{J}^{-1})}\dot{\boldsymbol{x}} + \underbrace{\bar{\boldsymbol{g}}(\boldsymbol{q})}_{\boldsymbol{J}^{-T}\boldsymbol{g}} = \underbrace{\boldsymbol{F}}_{\boldsymbol{J}^{-T}\boldsymbol{\tau}} + \underbrace{\bar{\boldsymbol{\tau}}_{ext}}_{\boldsymbol{J}^{-T}\boldsymbol{\tau}_{ext}}.$$

Here, $\bar{\boldsymbol{M}}(\boldsymbol{q}), \bar{\boldsymbol{C}}(\boldsymbol{q},\dot{\boldsymbol{q}})$, and $\bar{\boldsymbol{g}}(\boldsymbol{q})$ are the effective parameters of the system dynamics as viewed from the task space.

Besides, it is worth mentioning that when we control each robotic subsystem (e.g., joint) independently, we utilize the so-called *decentralized control* approach. On the other hand, if we take into account the interaction between robotic subsystems, we work with *centralized control* strategy.

2.2.1 Compliant motion control

In the scope of this thesis, the *compliant motion control* is widely utilized. It involves methods for the interaction of the robot with the environment. This type of control includes two basic strategies: *impedance control* and *admittance control* [Hogan, 1985, Ott et al., 2010].

The impedance control treats the robotic system as admittance while the controller itself is considered as mechanical impedance, see Figure 2-7a. It can be defined as follows:

$$\boldsymbol{F}_{des} = \boldsymbol{C}_{des}(\dot{\boldsymbol{x}}_{des} - \dot{\boldsymbol{x}}) + \boldsymbol{K}_{des}(\boldsymbol{x}_{des} - \boldsymbol{x}).$$

Here, $\boldsymbol{C}_{des}$ and $\boldsymbol{K}_{des}$ describe desired contact damping and stiffness matrices, respectively, $\boldsymbol{x}_{des}$ and $\dot{\boldsymbol{x}}_{des}$ are the desired location and velocity of the system. As we can see, the presented controller for *regulation task* has a proportional-derivative structure. This is a special case of the impedance control called compliance control. In case of *tracking problem*, such a controller might be extended with feedforward term proportional to the desired acceleration $\ddot{\boldsymbol{x}}_{des}$ through reflected inertia. The controller outputs the desired wrench, which is kinematically mapped through Ja-

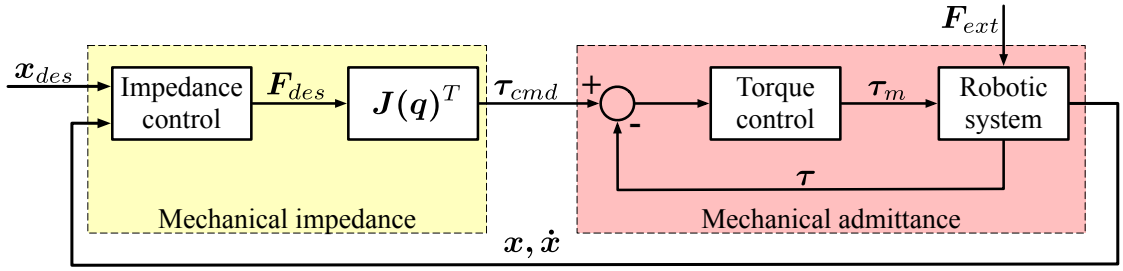

(a) Cartesian impedance control

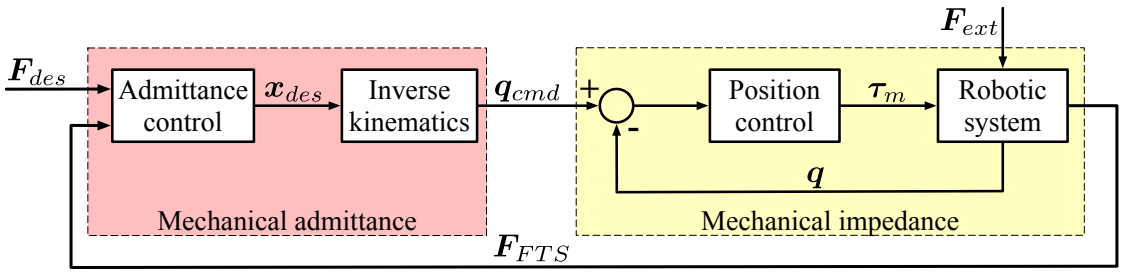

(b) Cartesian admittance control

Figure 2-7: Cartesian impedance and admittance control loops for the task space.

cobian $\boldsymbol{J(q)}^T$ to the joint torques, which are directly applied to the robotic system torque controller.

In case, if we deal with position-controlled system, the admittance control technique can be utilized. In opposite to the impedance control, the robotic system is considered as mechanical impedance while admittance controller represents the mechanical admittance. It can be described as:

$$\boldsymbol{M}_{adm}\ddot{\boldsymbol{x}}_{\boldsymbol{s,p}}^{\boldsymbol{des}} + \boldsymbol{D}_{adm}\dot{\boldsymbol{x}}_{\boldsymbol{s,p}}^{\boldsymbol{des}} = \boldsymbol{F}_{des} - \boldsymbol{F}_{FTS}.$$

As shown in Figure 2-7b, the admittance controller takes as input the difference between desired force we want to generate and external force, e.g., measured by Force Torque Sensor (FTS), and outputs the desired pose in the task space. Further, the pose is transformed to the joint angles by IK to receive joint corrections $\boldsymbol{q}_{cmd}$. These are fed to the position controller of the robotic system, which generates the torques $\boldsymbol{\tau}_m$ applied to the robot joints. It is worth highlighting that the admittance controller allows tuning dynamics with desired inertia $\boldsymbol{M}_{adm}$ and damping $\boldsymbol{D}_{adm}$ matrices.

"Above all, don't fear difficult moments. The best comes from them."

Rita Levi-Montalcini

Chapter 3

Physical system description

This chapter elaborates the cable-suspended aerial manipulator concept into more details and presents the particular demonstrator, cable-Suspended Aerial Manipulator (SAM), which is utilized for the experimental investigation in the scope of this thesis.

The chapter is organized as follows. First, an overview of the SAM is given. Secondly, the operational scenario for the cable-suspended aerial manipulator is discussed. Lastly, the main design features and frameworks are described for the SAM platform.

3.1 The cable-Suspended Aerial Manipulator (SAM)

In the chapters devoted to the experimental validation and investigation (chapter 6 and chapter 7), the cable-Suspended Aerial Manipulator (SAM) system is utilized. The SAM belongs to the cable-decoupled long-reach aerial manipulation type and serves for the conduction of safe aerial manipulation in a complex industrial environment, see detailed concept description and advantages in subsection 1.2.3.

The SAM is equipped with rate-controlled propeller-based actuation and position-controlled winch-based actuation in order to cope with any type of disturbances imposed on the aerial manipulator. During operation, the system is suspended by a long cable to the *external carrier* which brings the SAM close to the target point. Attached to the bottom of the platform, the redundant 7-DOF robotic arm KUKA-LWR4 performs the manipulation tasks while both actuation systems keep the system close to the motionless state by compensating for the undesired platform motion in a coordinated way. The overall integration concept of the manipulation

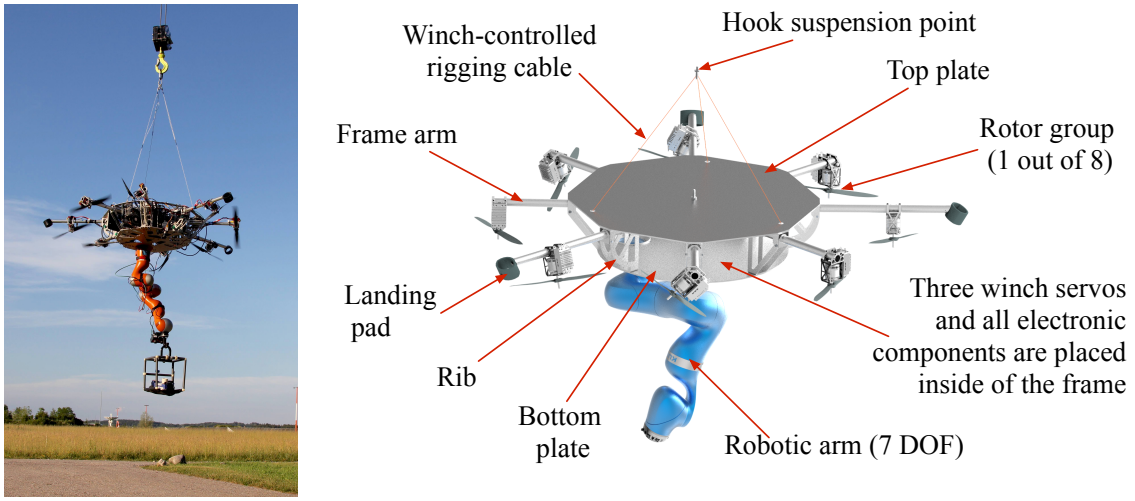

(a) The SAM hanged at the crane's hook

(b) The SAM composition

Figure 3-1: The SAM platform.

platform with external carrier and detailed design of the SAM system is shown in Figure 3-1. The presented system design is envisioned for the outdoor experimental scenarios in rough conditions in order to conduct industrial applications, e.g., the industrial inspection and maintenance of the cell towers, transmission towers, refinery pipelines, bridge supports, offshore drilling rigs.

The propeller-based actuation contains eight propellers, each of which is driven by BrushLess Direct Current motor (BLDC)[1], and serves for the compensation of the dynamic disturbances by exerting agile omnidirectional wrench at the platform's geometric center [Franchi et al., 2018]. Such a wrench can be realized by installing eight propellers in the special optimized configuration in order to generate a set of independent forces and torques. Obtained well-balanced force and torques allow to decouple the control of the position and the orientation.

The winch-based actuation consists of three servos, each of which can change the rigging cable length that connects the platform to the suspension cable point. Intuitively, when the length of the cables is equal, the SAM can be seen as equilateral triangular pyramid edges of which represent the cables. This actuation allows maintaining the SAM COM under the hanging point via control of horizontal displacements and the height of the platform. Due to integrated breaks, such an actuation helps to withstand quasi-static disturbances, e.g., the slow COM shift due to the motion of the robotic arm.

[1]Through the thesis we also call this pair as a rotor group or propulsion unit.

The exploitation of two actuation systems in parallel, i.e., propellers and winches, to stabilize the manipulator base allows reducing the amount of consumed energy on propeller motors since long-term continuous loads might be compensated by winches.

The SAM is suspended by means of the cable to the external carrier. The leading feature of such a configuration is that the weight of the SAM is supported by the external carrier. Since there is no need to compensate for the gravity, the required amount of thrust generated by the propeller propulsion in the manipulation platform is relatively low. As a result, the diameter of the propellers can be significantly scaled down. Having a compact size, the SAM can independently counter any disturbances and freely perform manipulation tasks in close proximity to obstacles in complex environments. Therefore, the safety of this system is higher.

It is worth mentioning that as external carrier the different types of aerial vehicles as well as a crane can serve. The latter is important for places and applications where the operation of UAVs is restricted or the permission to fly is difficult to obtain. The former can have any size rotor blades since it distanced by cable from the operational environment.

The SAM is developed in the scope of the H2020 AEROARMS project by joint efforts of the several partners: DLR, Elektra Solar GmbH[2], LAAS-CNRS[3], GRVC Robotics Labs[4] of the University of Seville with contribution provided by Robo-Technology GmbH[5] in design and manufacturing. The development process took less than 2 years, it is a very short time period for turning such a complex system from idea to working experimental setup.

3.2 Operational scenario

As shown in the schematic diagram in Figure 3-2, the aerial manipulator is hanged to the external carrier utilizing a long cable. At the beginning of the operation, the external carrier should deliver the cable-based platform to the target location. After that, the carrier central role is to maintain its own location while the system performs the manipulation task independently. Thus, the typical mission for the cable-suspended aerial manipulator is composed of two steps: *transportation* and *manipulation*.

[2]https://www.elektra-solar.com
[3]https://www.laas.fr
[4]https://grvc.us.es
[5]https://www.robo-technology.de

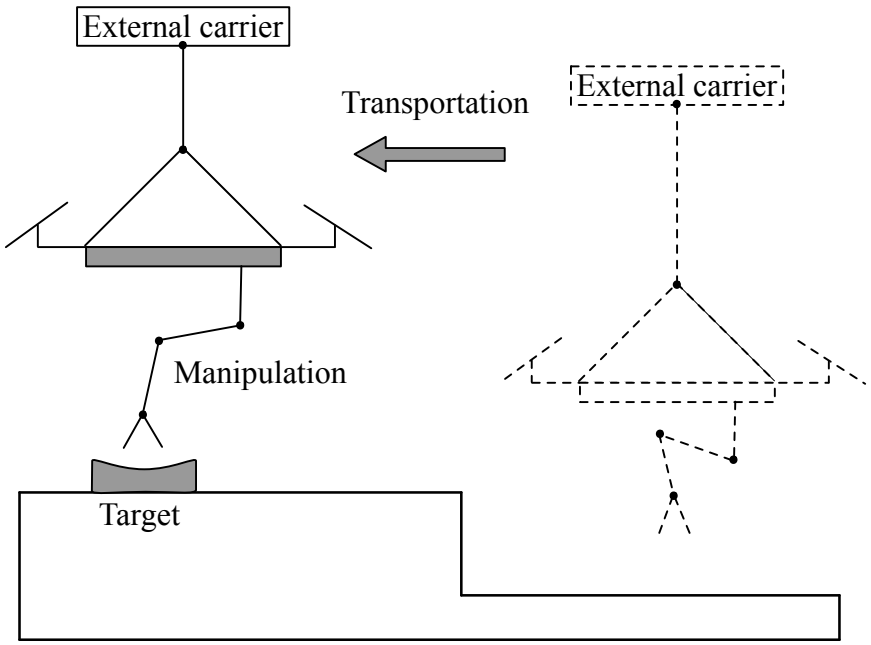

Figure 3-2: Two main steps of the typical operational scenario for the cable-suspended aerial manipulator.

During the first step, the SAM should follow the external carrier with minimum pendulum behavior. It achieves by exploiting the agile oscillation damping controller with the propeller-based actuation. Within the transportation, the robotic arm configuration is fixed, so winches are not utilized. The suspension cable length can be regulated depending on the operation height and type of the external carrier.

During the manipulation, the external carrier is motionless while the SAM conducts the task and should compensate for all disturbances depending on the certain task. At this step, both actuations should be activated, the propeller-based propulsion for reducing oscillation effect and winch-based actuation for compensating for the COM displacement due to robotic arm weight and external wrench due to contact with the environment.

It is worth noting that several critical operational aspects should be taken into account at the mission planning stage:

- environmental conditions might impose restrictions on the particular mission, i.e., weather (wind, rain), the proximity of obstacles, type of contact, type of disturbances the SAM should counter for safe operation,

- local aviation regulations dictate operational requirements, e.g., a type of carrier, the required length of the suspension cable, time of operation,

- emergency policy of the specific company might require additional measures such as the presence of firefighting apparatus on the site,
- level of autonomy is characterized by a certain task and defines the proportion of efforts between the manual control by the operator and autonomous control by the system.

We can distinguish two main external carrier types, see Figure 3-3. The first one is a heavy payload capable aerial vehicle, e.g., a helicopter with long rotor blades. In this case, it can operate far away from the environment obstacles while compact stabilizing platform SAM directly manipulates in close proximity to the object of manipulation. The second type is a *crane*. In this case, the SAM is suspended directly to the hook of the crane. The latter option is especially beneficial in terms of reliability, safety, and cost. Reliability and safety are due to the well-developed crane technological level, ease of its exploitation, and advanced operational control tools, e.g., remote joystick. Reduced cost is defined by low maintenance, deployment, exploitation expenses of the crane compared to the helicopter, no need in flight permission and piloting license since the system is considered just as a payload of the crane.

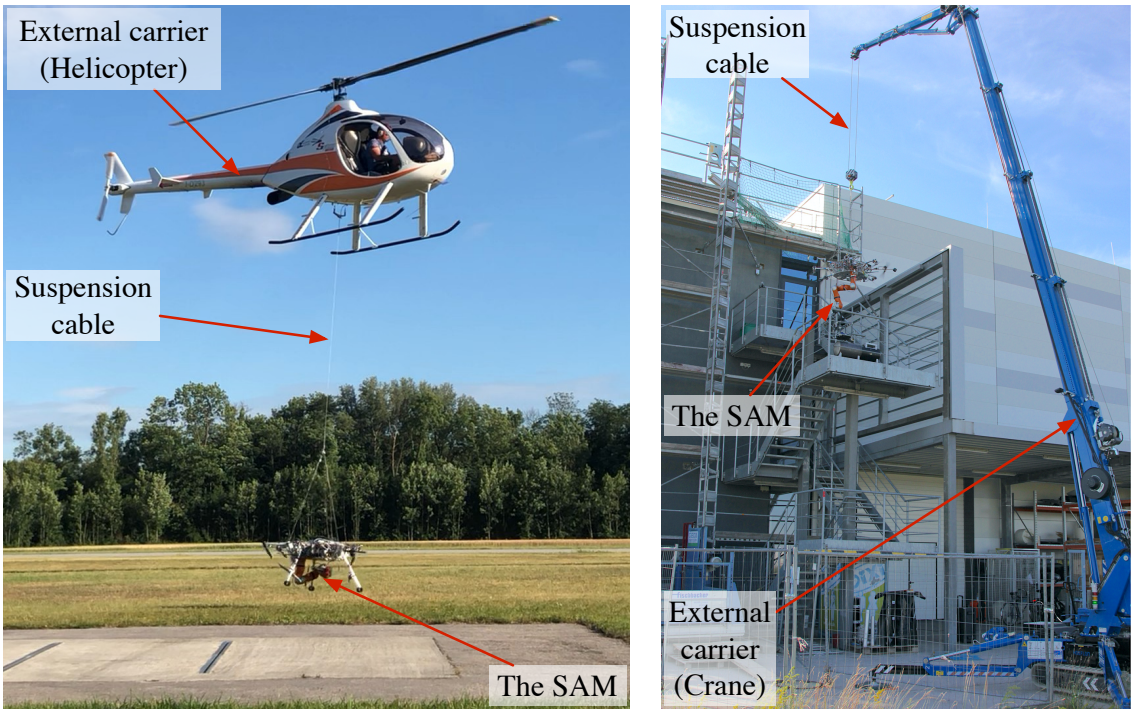

(a) The helicopter-based setup (b) The crane-based setup

Figure 3-3: Carrier variety for the cable-suspended aerial manipulators.

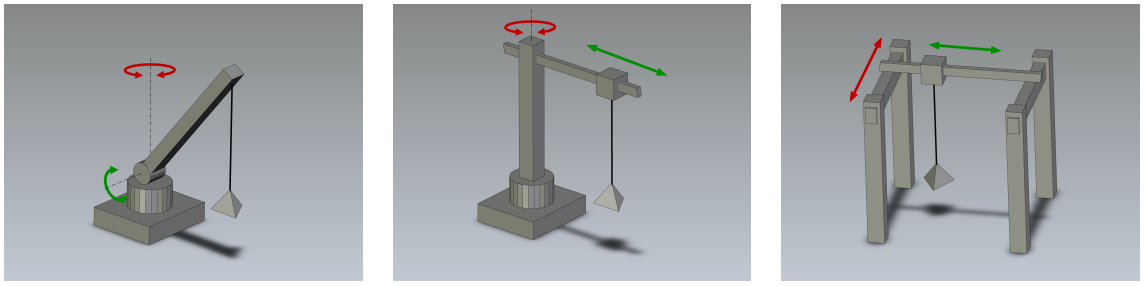

(a) The boom crane (b) The tower crane (c) The overhead crane

Figure 3-4: Types of the crane kinematics. Green and red arrows correspond to the available DOFs at the presented crane concepts.

Moreover, since in the scope of this thesis we aim at the industrial applications, we consider the crane as a major external carrier leading by the following ideas:

- most of the objects for industrial inspection are built by the crane, so cranes can reach them to establish contact,
- cranes are widely accessible at the industrial spots,
- cranes have a high payload capability,
- the exploitation of the aerial manipulator should be affordable for the industry.

Let us briefly consider a crane taxonomy. All cranes might be categorized by two key principles [Ali et al., 2021, Ramli et al., 2017]. The first one is mobility, there are *fixed* and *mobile* cranes. The former is rigidly fixed to the ground and has a high payload capability, while the latter represents the crane attached to the crawler or truck vehicles. The second principle is kinematic structure. Three groups might be distinguished according to their type of motion, see Figure 3-4. Namely, a *boom crane* provides rotational motion of the base as well as the rotational motion of the boom, at the tip of which the payload might be hoisted up and down. It is typically utilized at the ships. A *tower crane* has a rotational DOF of the jib around the vertical axis at the base and translational DOF of the trolley along the jib. The payload can be moved up and down as well. Typically, the tower cranes might be found at the constructions sites. Lastly, an *overhead crane* (also known as a bridge crane or similar gantry crane) contains an elevated runway rails along which the bridge is traveling. The trolley with a hoist can move along the bridge. The overhead cranes are common for warehouses and factories.

It is worth noting that depending on the crane type, different requirements and a set of onboard sensors might be used for the task implementation. For example, the

overhead crane has a constant height of the trolley, so an onboard barometer at the SAM might be used in order to estimate the length of the crane's chain for control purpose. At the same time, at the boom crane, the height of the boom's tip varies, so the barometer would not help in estimating the crane's chain length. Another example is conditioned by the dynamic coupling between the suspended platform and the trolley through the chain. The overhead crane has a rigid structure, so whenever the SAM oscillates, the trolley is fixed. On the other hand, at the boom crane, any oscillations of the system would result in the oscillations of the crane's jib as well.

3.3 System design

In this subsection, we will describe the central functional nodes and present the key features of the SAM in detail.

3.3.1 Propeller-based actuation

The cable-suspended platform is equipped with 8 propeller-based rotor groups to resist disturbances induced by the pendulum nature and to stabilize its own dynamics. Below we consider the complete cycle of the propeller-based actuation development, including modeling, optimized allocation, hardware selection for specific requirements, design, and identification of the main parameters.

3.3.1.1 Propeller allocation

Let us introduce the following coordinate frames:

- world frame $\mathcal{F}_w$: $\{O_w,\ x_w,\ y_w,\ z_w\}$ fixed in the inertial space,
- body (platform) frame[6] $\mathcal{F}_b$: $\{O_b,\ x_b,\ y_b,\ z_b\}$ attached to the Geometric Center (GC) of the SAM base with origin O_b,
- $i-$th actuator frame $\mathcal{F}_a^i$: $\{O_a^i,\ x_a^i,\ y_a^i,\ z_a^i\}$ defined in subsubsection 2.1.2.2.

The $\mathcal{F}_a^i$ can be described by three angles through three sequenced successive rotations as $\boldsymbol{R}_{a_i}^b = \boldsymbol{R}(\gamma_i)_z \boldsymbol{R}(\alpha_i)_x \boldsymbol{R}(\beta_i)_y$ with respect to $\mathcal{F}_b$. Here, γ_i defines a rotational

[6]Throughout the text we would use notation *body frame* whenever we deal with model containing single platform, and *platform frame* in cases when we deal with multi-body dynamics, i.e., platform with integrated robotic arm.

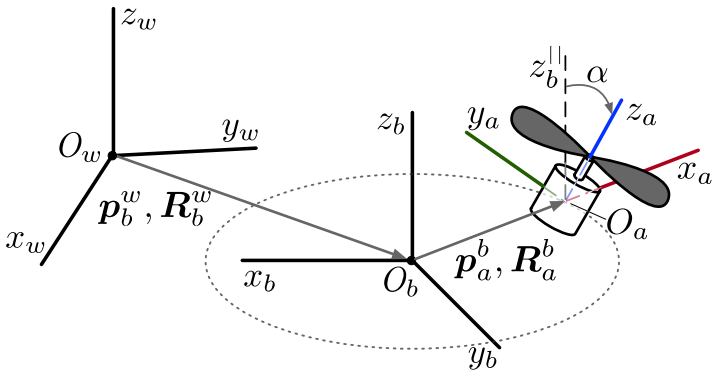

(a) The SAM kinematics

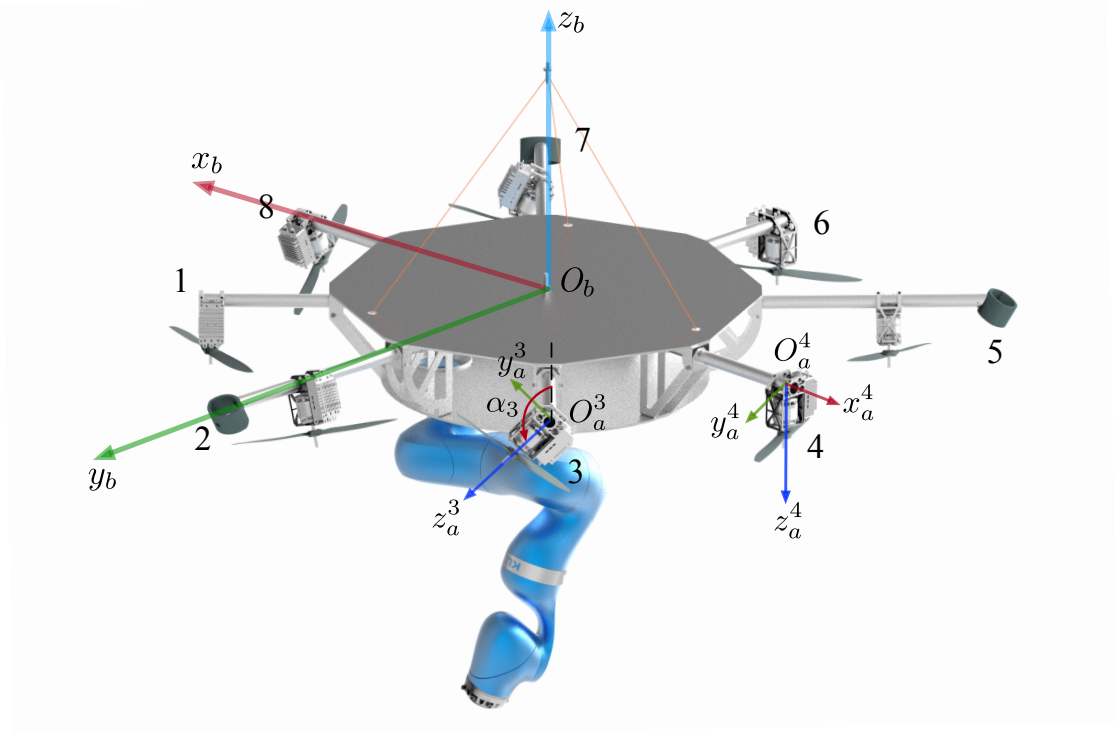

(b) Orientation of the $\mathcal{F}_b$ and $\mathcal{F}_a$ with respect to the SAM structure

Figure 3-5: Reference frames for the SAM platform.

shift of the $i-$th frame arm in the $x_b y_b$ plane of $\mathcal{F}_b$. The α_i describes the tilting angle of the $i-$th actuator spinning axis around x_a, and β_i - around y_a. Relation between the aforementioned frames is illustrated in Figure 3-5, and convention of rotor-group installation angles α and β is illustrated in Figure 2-3b. It is worth mention that all actuators lay on the same plane and equally spaced, i.e., they lay at the same circle centered in O_b. Such a design allows to minimize a collision risk with rigging cables and robotic arm.

Recent research results [Allenspach et al., 2020, Park et al., 2018, Ryll et al., 2016] have been shown that by installing propellers in the particular arrangement

(non-collinear), an omnidirectional 6 DOF wrench can be realized.

Remark. *It would be worthwhile to mention that the minimum required number of rotor groups to realize 6 DOF wrench equals 7 [Tognon, 2018]. In the SAM, it was decided to use 8 units to lower the effort of each actuator, provide a rotor failure robustness, and address the exploitation of redundancy in the future studies.*

As was discussed in subsubsection 2.1.2.2, the body wrench $\boldsymbol{w}_b$ and the thrust input vector $\boldsymbol{t}$ can be related by the allocation matrix $\boldsymbol{A}$:

$$\boldsymbol{w}_b = \boldsymbol{A}\boldsymbol{t}. \tag{3.1}$$

Following the line of [Tognon and Franchi, 2018], to design the desirable arrangement for the 8 propellers at the SAM, an optimization was carried out by LAAS-CNRS researchers. In particular, given the number of propellers, their aerodynamic parameters, and positions, the cost function to minimize was chosen as the condition number of the allocation matrix in order to guarantee the equal distribution between the rotor group efforts required to generate an omnidirectional wrench. Additionally, the following constraints were imposed:

C.1 the imposition of a particular (the unitary) eigenvector $\mathbb{1}_{8\times1}$ for the allocation matrix such that $\boldsymbol{A}\mathbb{1}_{8\times1} = \boldsymbol{0}$, in order to obtain a symmetrical design which maintains balanced effort distribution between all the actuators

C.2 the normalization constraint for the unit vector defining the directions of the unidirectional thrusters

C.3 an imposition of minimal installation angle of the rotor group $\forall j \in \{2,\ 5,\ 7\}$ around the frame arm, α_j, which guarantees the lifting of the landing legs with attainable motor thrust[7]

C.4 the perpendicularity between the thrust directions and the frame arm axes for an ease of mechanical implementation, i.e., angle around the axis perpendicular to the frame arm, β_i is equal to 0 for $\forall i \in \{1, \ldots, 8\}$.

The mathematical treatment of **C.1** and **C.2** can be found in [Tognon and Franchi, 2018]. The constraint **C.3** is added to provide a minimum projection of

[7]Three out of eight frame arms serve as the landing gear for the SAM. More elaborated explanation of this constraint will be given in subsection 3.3.3.

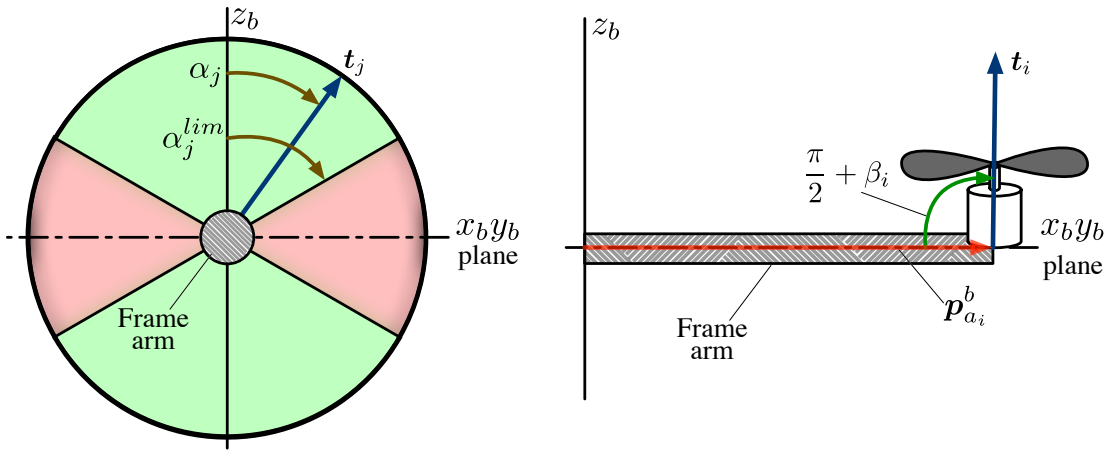

(a) The **C.3** constraint: axial view on the $j-$th frame arm

(b) The **C.4** constraint: lateral view on the $i-$th frame arm

Figure 3-6: Constrains in the propeller allocation.

the motor thrust vector along the z-axis of the body frame. It guarantees the lifting of the landing leg by utilized rotor group for selected installation configuration. This constraint can be mathematically expressed as $|\mathbf{z}_B^T \boldsymbol{t}_j| \geq cos(\alpha_j^{lim})$, where $\boldsymbol{t}_j$ is the unit vector indicating the direction of the rotor group thrust expressed in the body frame and related to the landing $j-$th leg. $\mathbf{z}_B$ is the z-axis of the body frame, and $\alpha_j^{lim} = \frac{\pi}{3}$ is the limitation angle selected to allow the lifting of a leg given the maximum thrust attainable by the selected actuator in the worst configuration, the more details on that can be found in subsection 3.3.3. Such a constraint prevents allocation of the thrust vectors in the red area for the legs, see Figure 3-6a, and is needed to ensure the lifting of the landing gear legs after the take-off.

The constraint **C.4**, see Figure 3-6b, ensures $\beta_i = 0$ and can be written as $|\boldsymbol{p}_{a_i}^b \boldsymbol{t}_i| = 0$, where $\boldsymbol{p}_{a_i}^b$ is the vector of the $i-$th frame arm expressed in the body

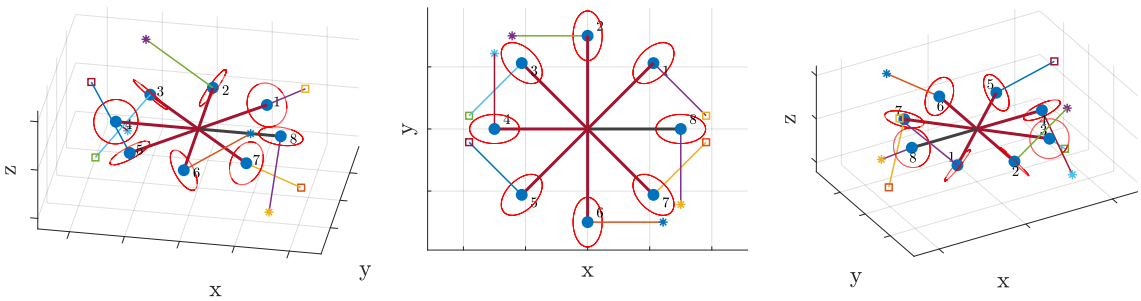

Figure 3-7: Optimized omnidirectional design for the propeller-based actuation of the SAM. The blue spheres represent the placement of the BLDC motors. The colored lines point to the thrust direction of each motor. The star symbol denotes the counterclockwise propeller, and the square indicates the clockwise propeller.

i	γ_i, [deg]	α_i, [deg]	β_i, [deg]	Propeller type	Thrust direction	Drag direction	Addition
1	45	53.1	0	CW	upward	upward	-
2	90	-54.2	0	CCW	upward	downward	leg, y_b
3	135	-126.9	0	CW	downward	downward	-
4	180	125.9	0	CCW	downward	upward	-
5	225	53.1	0	CW	upward	upward	leg
6	270	-54.1	0	CCW	upward	downward	-
7	315	-126.9	0	CW	downward	downward	leg
8	360	125.9	0	CCW	downward	upward	x_b

Table 3.1: Configuration parameters of the propeller-based actuation

frame. Such a constraint limits the mechanical complexity of the structure and also helps to avoid possible collision of the propellers with the frame arms.

The obtained design for the rotor group placement is depicted in Figure 3-7. The result of optimization, with respect to the angle definition is presented in Table 3.1.

With the obtained propulsion configuration, the octorotor platform is capable of generating a set of independent forces and torques, thus allowing to decouple the control of the position and the orientation. The allocation matrix[8] can be defined as follows:

$$\boldsymbol{A} = \begin{bmatrix} \boldsymbol{J}_1 & \boldsymbol{J}_2 & \dots & \boldsymbol{J}_8 \end{bmatrix} = \begin{bmatrix} \boldsymbol{A}_1^{3\times 8} \\ \boldsymbol{A}_2^{3\times 8} \end{bmatrix} = \\ \begin{bmatrix} \boldsymbol{t}_1 & \boldsymbol{t}_2 & \dots & \boldsymbol{t}_8 \\ \boldsymbol{p}_{a_1}^b \times \boldsymbol{t}_1 + k_{ad}\boldsymbol{t}_1 & \boldsymbol{p}_{a_2}^b \times \boldsymbol{t}_2 + k_{ad}\boldsymbol{t}_2 & \dots & \boldsymbol{p}_{a_8}^b \times \boldsymbol{t}_8 + k_{ad}\boldsymbol{t}_8 \end{bmatrix},$$

where $\boldsymbol{J}_i = \begin{bmatrix} \boldsymbol{t}_i \\ \boldsymbol{p}_{a_i}^b \times \boldsymbol{t}_i + k\boldsymbol{t}_i \end{bmatrix}$ and the aerodynamic gain $k_{ad} = (-1)^{i+1}\frac{q}{t}$ is the constant ratio introduced in (2.7). The sign of the k_{ad} is positive (negative) when $i-$th propeller angular velocity has the same direction of $-\boldsymbol{t}_i$ ($\boldsymbol{t}_i$), i.e., propeller spins CW

[8]It can be seen from the structure that the allocation matrix represents a geometric Jacobian.

(CCW) seen from its tip. It results in the various drag torque directions as well.

The vector distance to the propeller hub from the O_b^i is defined as follows:

$$\boldsymbol{p}_{a_i}^b = \boldsymbol{R}(\gamma_i)_z \begin{bmatrix} L \\ 0 \\ 0 \end{bmatrix},$$

where L is the length of each frame arm and $\gamma_i = i\frac{2\pi}{8}$ with respect to the x_b in CCW direction.

The unit thrust for $i-$th propeller in $\mathcal{F}_b$ can be defined as:

$$\boldsymbol{t}_i = \boldsymbol{R}_{a_i}^b \begin{bmatrix} 0 \\ 0 \\ 1 \end{bmatrix}.$$

Thus, each unit thrust generates three entities in $\mathcal{F}_b$. The first one is the force applied to the O_b , the second one is the torque applied around O_b at the leverage $\boldsymbol{p}_{a_i}^b$, the last one is the aerodynamic drag produced by the propeller and proportional to the thrust force.

With resulted optimization angles and for $k_{ad} = (-1)^{i+1}\ \frac{0.2\,\mathrm{Nm}}{10\,\mathrm{N}} = (-1)^{i+1}0.02$[9], the final allocation matrix is defined as:

$$\boldsymbol{A} = \begin{bmatrix} 0.57 & -0.81 & -0.57 & 0.00 & -0.57 & 0.81 & 0.57 & 0.00 \\ -0.57 & 0.00 & -0.57 & 0.81 & 0.57 & 0.00 & 0.57 & -0.81 \\ 0.60 & 0.50 & -0.60 & -0.59 & 0.60 & 0.59 & -0.60 & -0.59 \\ 0.33 & 0.46 & -0.33 & 0.00 & -0.33 & -0.46 & 0.33 & 0.00 \\ -0.33 & 0.00 & -0.33 & -0.46 & 0.33 & 0.00 & 0.33 & 0.46 \\ -0.59 & 0.60 & 0.59 & -0.50 & -0.59 & 0.60 & 0.59 & -0.60 \end{bmatrix},$$

it corresponds to the optimized condition number of 1.8230.

3.3.1.2 Quantitative requirements

The remaining design parameter, which is not considered in the optimization problem, is the required thrust value per motor. Dual actuation provides a possibility to share stabilization efforts between winch-based and propeller-based actuations. We

[9]The values are taken from the rotor group identification results for the input width of the ESC pulse of 1563 μs as shown in Figure 3-13a.

(a) Robotic arm configurations

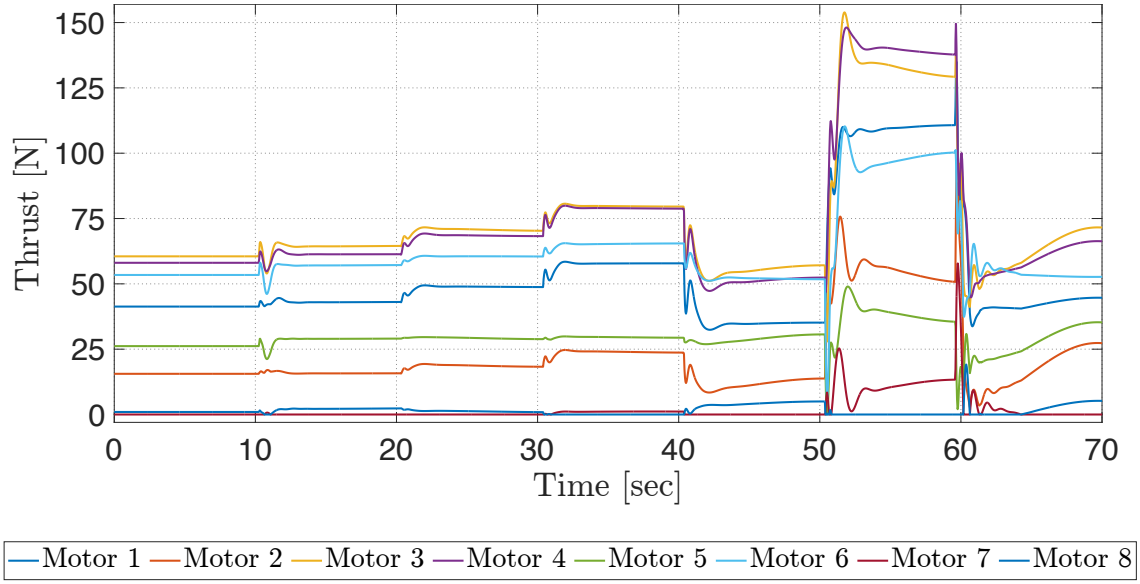

(b) Exerted stabilizing thrust by propeller-based actuation

Figure 3-8: Results of the simulation study on the required thrust to compensate for the dynamic disturbances (robotic arm motion).

assume that slow disturbances should be suppressed by the winches while disturbing dynamic transients should be counterbalanced by agile propellers. Thus, we need to obtain a rough estimation of typical disturbances during manipulation in order to understand the required magnitude for the actuator thrusts. To this end, we conducted a simulational study at which the SAM was modeled as a double pendulum[10] without winches with zero-length of the second pendulum link. Initial conditions of the pendulum joints had zero values, while the robotic arm started the motion from the parking pose. The simulation was performed in the MathWorks MATLAB Simulink (MATLAB Simulink) utilizing Luca Dynamics library (subsection 2.1.4).

During the simulation, the robotic arm moved through several configurations typical for the manipulation tasks, see Figure 3-8a. Namely, the following sequence of the robotic arm configurations $\boldsymbol{q}_m$ was performed with 10 second step:

- parking: $\boldsymbol{q}_m = [-\frac{\pi}{6.2},\ -\frac{\pi}{2},\ -\frac{\pi}{2},\ -\frac{\pi}{2} + 0.343,\ 0,\ \frac{\pi}{2},\ 0]^T$,

[10]Validation of the double pendulum model fairness will be provided in chapter 6.

- operational: $\boldsymbol{q}_m = [0,\ -\frac{\pi}{2.8},\ 0,\ -\frac{\pi}{2.8},\ 0,\ 0,\ 0]^T$,
- pick and place: $\boldsymbol{q}_m = [0,\ -\frac{\pi}{4},\ 0,\ -\frac{\pi}{4},\ 0,\ 0,\ 0]^T$,
- pick and place V2: $\boldsymbol{q}_m = [0,\ -\frac{\pi}{4},\ 0,\ -\frac{\pi}{2},\ 0,\ -\frac{\pi}{4},\ 0]^T$,
- stretched: $\boldsymbol{q}_m = [0,\ -\frac{\pi}{4.5},\ 0,\ \frac{\pi}{4},\ 0,\ 0,\ 0]^T$,
- stretched V2: $\boldsymbol{q}_m = [\pi,\ -\frac{\pi}{4.5},\ 0,\ \frac{\pi}{4},\ 0,\ 0,\ 0]^T$,
- parking: $\boldsymbol{q}_m = [-\frac{\pi}{6.2},\ -\frac{\pi}{2},\ -\frac{\pi}{2},\ -\frac{\pi}{2} + 0.343,\ 0,\ \frac{\pi}{2},\ 0]^T$.

The wrench $\boldsymbol{w}_b$, required for the stabilization of the platform during arm motion, see Figure 3-9, was mapped to the thrust $\boldsymbol{t}$ space, see Figure 3-8b. As it can be seen, the trust values reach pretty high values, e.g., 150 N. It is evident that the winch compensation at the static levels is a significant simplification for the real system, and the required thrust per actuator can be defined by transient magnitude between configurations, i.e., typically is less than 30 N per motor. For the stretched v2 pose, when manipulation is performed on the side of the SAM, the most significant jump for motor 4 reaches 96 N.

It is worth noting that the direct solution of (3.1) using Moore-Penrose pseudo inverse $\boldsymbol{t}^* = \boldsymbol{A}^\dagger \boldsymbol{w}_b$ would always contain at least one negative term, which cannot be exerted by unidirectional thruster [Hamandi et al., 2020]. To this end, the final thrust values contain additional term needed to meet the unidirectionality requirement and is defined as follows:

Mapper 1:

$$\boldsymbol{t} = \boldsymbol{A}^\dagger \boldsymbol{w}_b + \lambda^o \boldsymbol{b} \tag{3.2}$$

Here, $\|\boldsymbol{b}\| = 1$ is the unit eigenvector of matrix $\boldsymbol{A}$ in its null-space, i.e., $\boldsymbol{b} \in \mathcal{N}(\boldsymbol{A})$, $\lambda^o = min(\boldsymbol{t}^*) \in \mathbb{R}^+$ is the smallest scalar to meet the constraint inequality $\boldsymbol{t} \geq t_{min}\mathbb{1}_{8\times1}$, t_{min} is the minimum possible thrust, and $\mathbb{1}_{8\times1}$ is the vector of once with dimension 8.

As a result, the continuous thrust value per motor required for most operations is around 30 N, while the maximum value might reach 100 N. Selecting a maximum thrust value of 150 N for each motor guarantees some margin toward additional payload, disturbances, and insufficient winch performance.

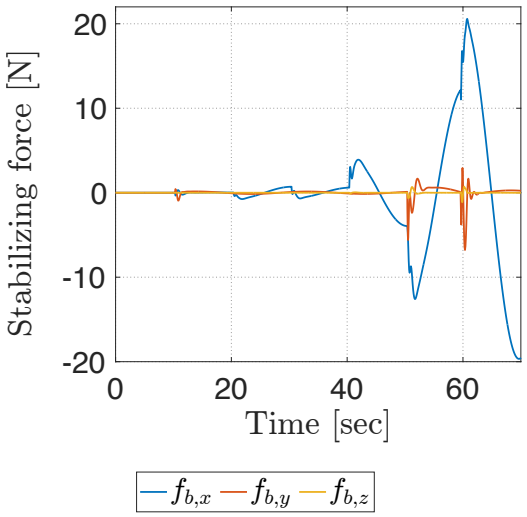

(a) Stabilizing forces applied to the aerial platform

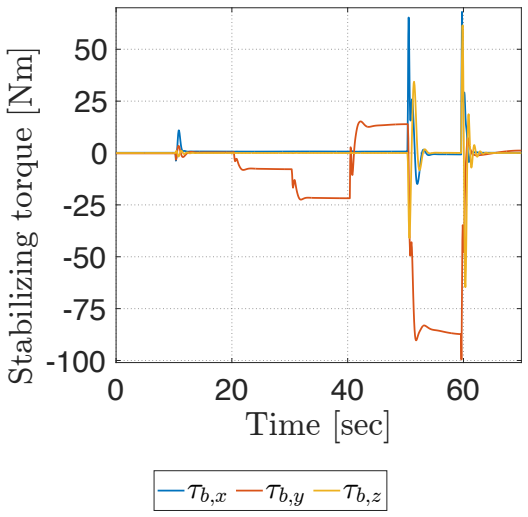

(b) Stabilizing torques applied to the aerial platform

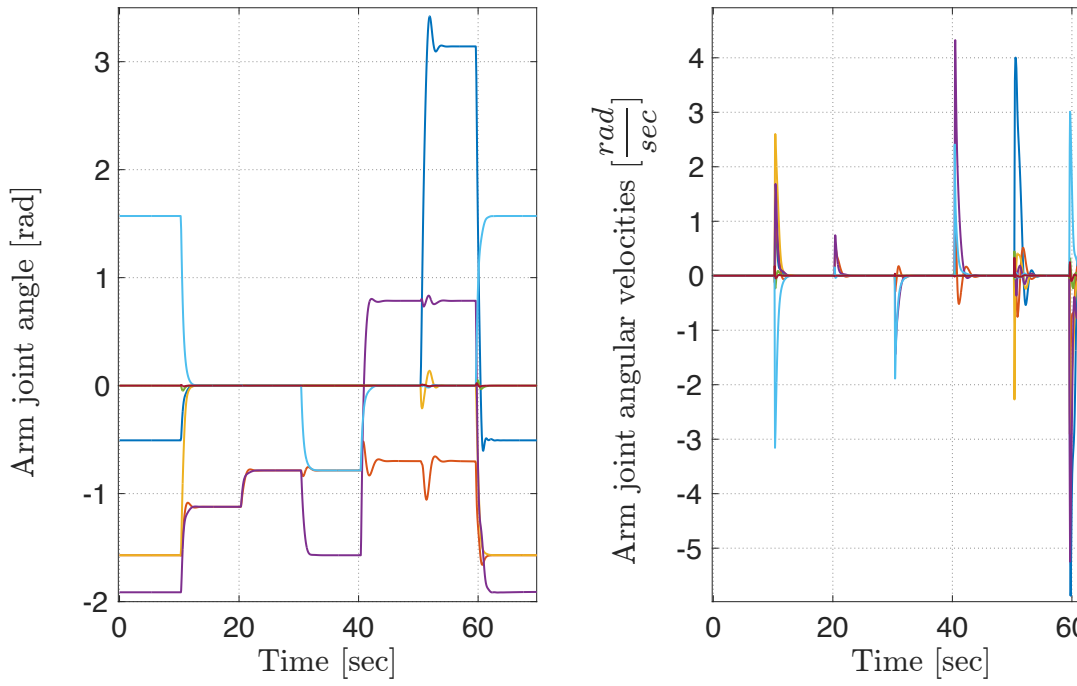

(c) Joint angles (left) and angular velocities (right) of the robotic arm

Figure 3-9: Simulation study conditions.

3.3.1.3 Hardware

To provide the estimated thrust value, the BLDC Kontronik Pyro 650-65 [SOB, 2017] in pair with Aeronaut CAM carbon light-prop 16x6" (40.5 x15) propeller and Electronic Speed Controller (ESC) JIVE PRO 120+ HV [SOB, 2017] is chosen for the

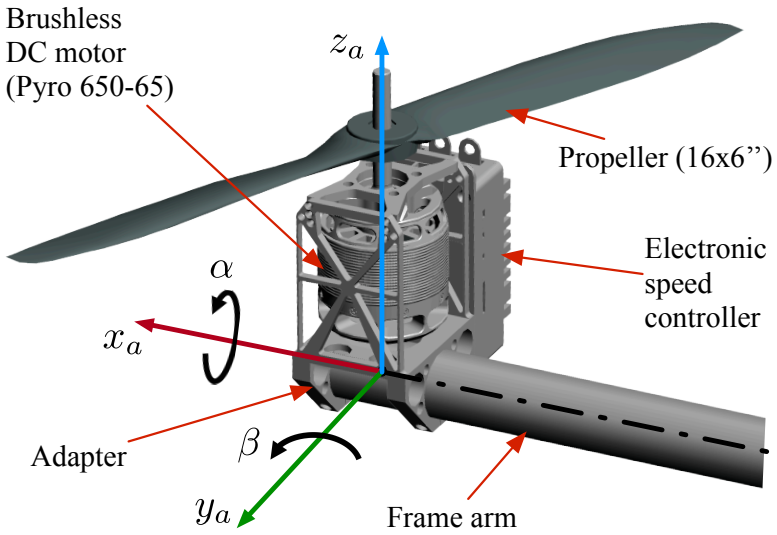

Figure 3-10: Composition of the rotor group.

rotor group. In such a setup, a Pulse Width Modulation (PWM) signal proportional to the square of the propeller spinning velocity is generated to control the motor speeds and ranged in [1500, 2000] μs[11].

Mechanically the rotor group is fixed on the frame arm by utilizing the special holder, see Figure 3-10. It allows to rotate rotor group around the frame arm freely (α angle) and change its configuration on $\pm 12^o$ around the axis perpendicular to the arm frame (β angle). The ESC is placed below the propeller for additional cooling during the operation.

Technical characteristics of the rotor group might be found in Table 3.2.

3.3.1.4 Identification

The rotor group parameter identification is performed at the specially designed testbench. The testbench contains the *measurement unit* installed at the long *isolation pillar* placed at the *stand*, see Figure 3-11a. The length of the isolation pillar is about 1.5 m, which is higher than 3 propeller diameters. Such a condition is required to avoid a ground effect [Zerihan and Zhang, 2000]. As shown in Figure 3-11b, the measurement unit includes the non-contact digital tachometer to measure angular velocity by registering white tape mark at the BLDC, 6-DOF FTS at which

[11]It is worth noting that common range of the pulse width pulse is of [1000, 2000] μs. However, due to additional use of the propeller-based actuation for the landing gear, the ESC are programmed to operate in the bidirectional mode, so the range of [1500, 2000] corresponds to the direct rotation and the range of [1000, 1500] to the reverse rotation.

Parameter	**Value**	**Unit**
Estimated maximum thrust	150	N
Input voltage	16-50	V
Motor velocity constant	650	$\frac{\text{RPM}}{\text{V}}$
Number of poles	10	-
Maximum motor power	3000	W
ESC continuous current	120	A
Motor weight	295	g
ESC weight	140	g
k_t	0.3736	-
b_t	- 573.5526	-
k_q	0.0081	-
b_q	-12.4640	-

Table 3.2: Technical characteristics of the propeller-based actuation.

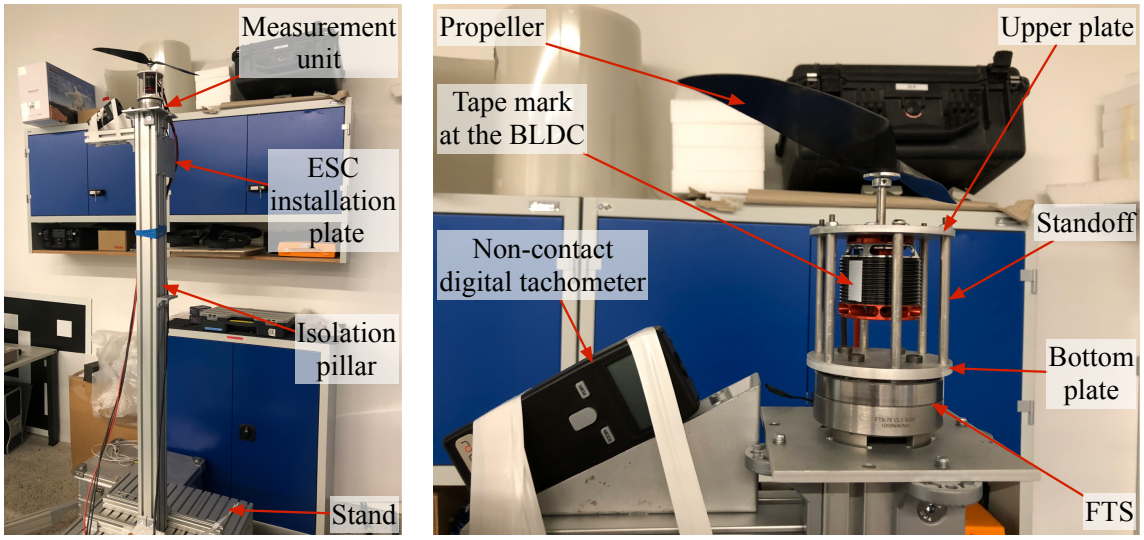

(a) The composition of the test-bench

(b) The scaled view of the measurement unit of the test-bench

Figure 3-11: Testbench for the rotor group parameter identification.

the BLDC is installed to measure thrust force and drag torque, and additionally a current is roughly estimated by virtue of current clamp (not shown in the figure).

As a result, the thrust force, drag torque, angular velocity, and current data was collected for the operational range $[1518 - 1635]$ μs of PWM signal, see Figure 3-12. In this experiment, selected hardware could exert continuous 41 N thrust at 27 % throttle level. At the same time, the drag torque did not exceed even 1 Nm. Angular

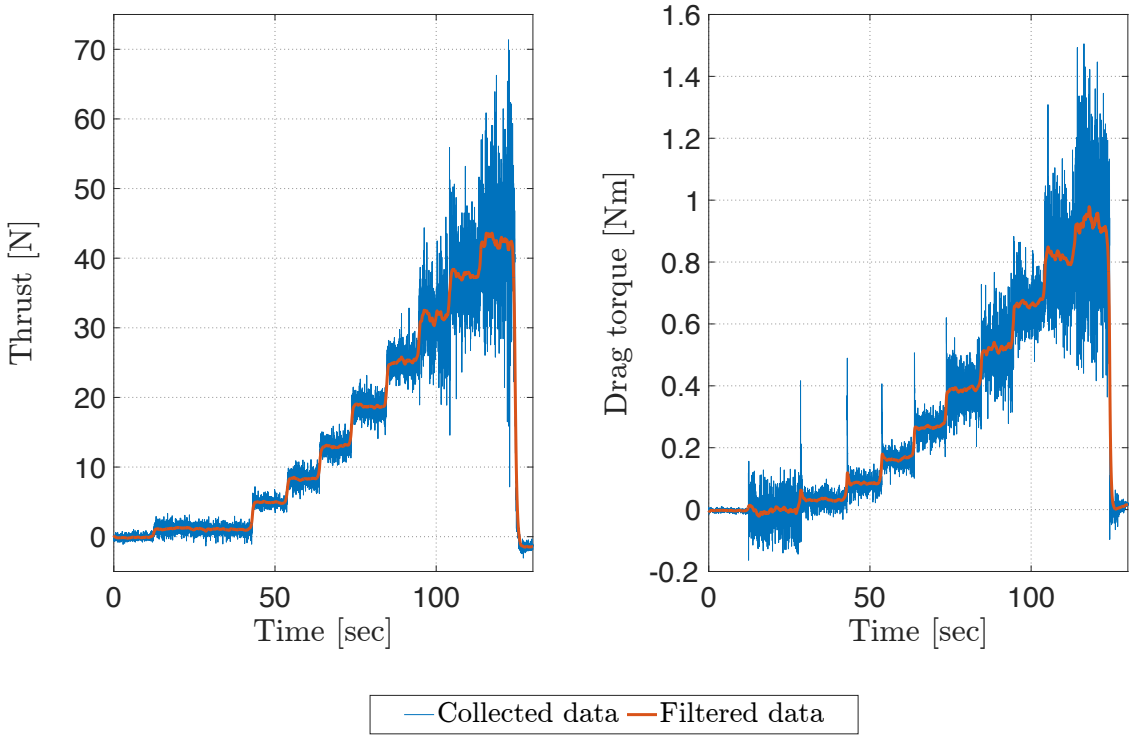

(a) Thrust force (left) and drag torque (right)

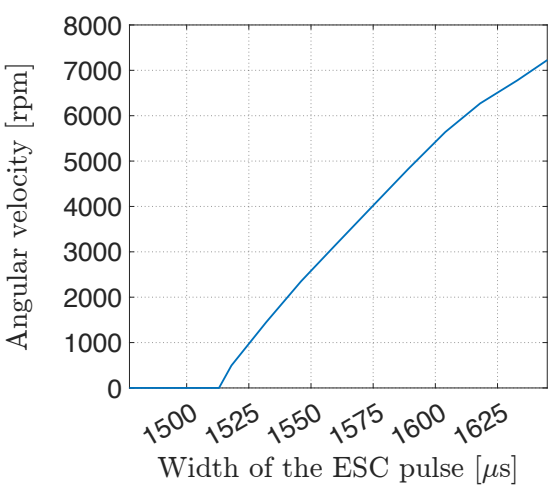

(b) Angular velocity

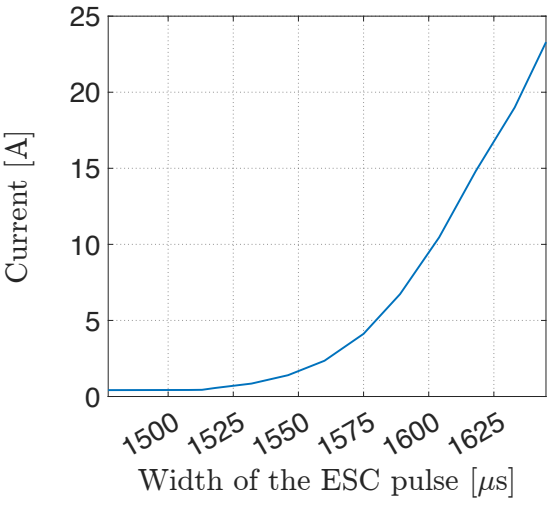

(c) Current

Figure 3-12: Collected data at the testbench for the rotor group identification.

velocity and current demonstrated quadratic behavior with respect to a width pulse.

After processing the raw data, see Figure 3-13, we could define the mapping between the thrust value as well as drag torque of the $i-$th rotor group and PWM control signal as follows:

$$t_i = k_t \cdot \text{PWM} + b_t, \tag{3.3}$$
$$q_i = k_q \cdot \text{PWM} + b_q,$$

with the linear gains k_t, b_t, k_q, b_q, which can be found in Table 3.2. Thus, PWM command is proportional to exerted thrust and drag torque as well as to the square of the angular velocity of the BLDC.

As it can be seen, at the low PWM commands, the behavior is different from linear (outliers in Figure 3-13a), so we defined two complementary regions in addition to the operational one. The first one is the *dead zone* (blue piece) at which the motor does not spin at all (blue line) due to zero back electromotive force (BEMF), and the second one is the *nonlinear piece* (yellow line) at which the motor starts to spin with low BEMF, i.e., a transition between dead zone and *operational range* (green piece), see Figure 3-13b. During this transition, the minimum angular speed is generated in order to measure BEMF required for the rotor position estimation [Damodharan and Vasudevan, 2010]. As soon as the measurement of BEMF is reliable (when angular velocity exceeds a certain low threshold), the characteristic behaves linearly. Due to strong linear dependency, we plotted estimated thrust-PWM mapping for the whole PWM range as well.

Using the received characteristics, we can formulate the **Mapper 2**, which relates thrust vector and PWM control signal of the rotor group as follows:

Mapper 2:

$$\mathbf{PWM} = \frac{\boldsymbol{t} - b_t}{k_t} \tag{3.4}$$

It is worth mentioning that there is no built-in voltage regulator in ESC, so changing battery voltage level over time produces varying thrust output for the similar PWM command. Moreover, motor characteristics including BEMF coefficient might change. We will neglect this issues since all motors are powered by the same battery, so we assume that reducing in the thrust will be the same for all motors simultaneously. In general, such problems may be overcome by a feedback voltage regulator at the ESC [Franchi and Mallet, 2017].

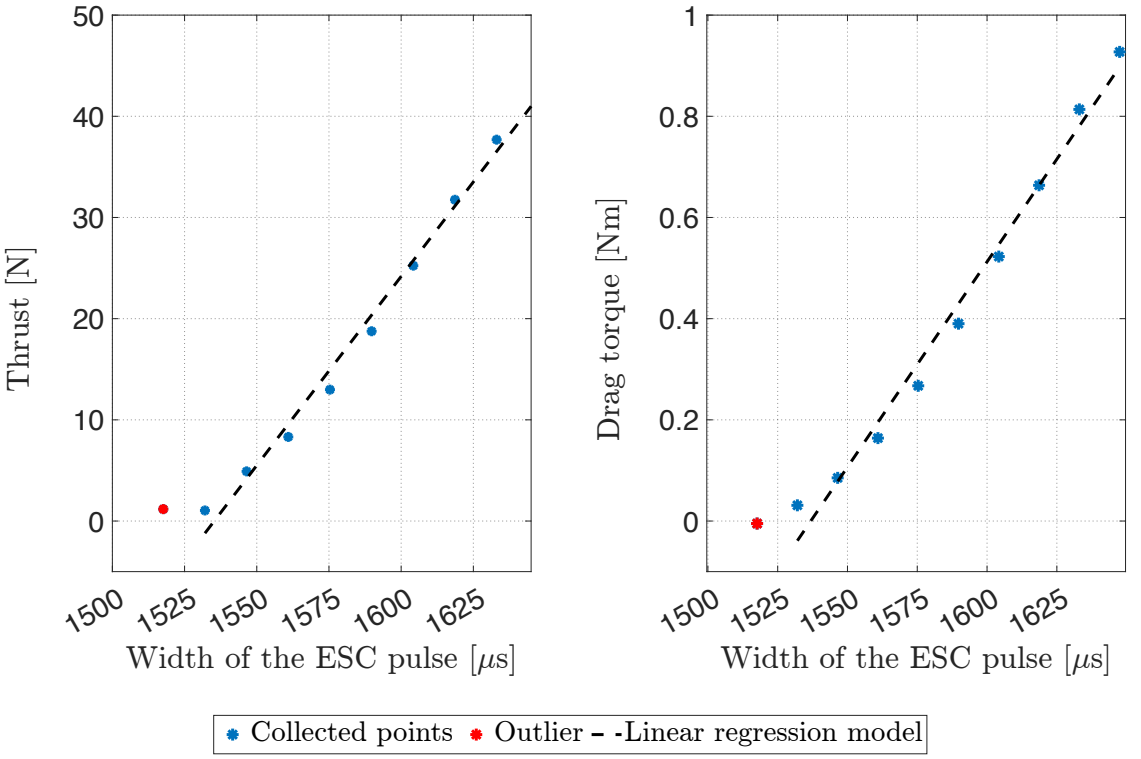

(a) Linear regression model of the thrust (left) and drag (right) with respect to the PWM signal for the operational range

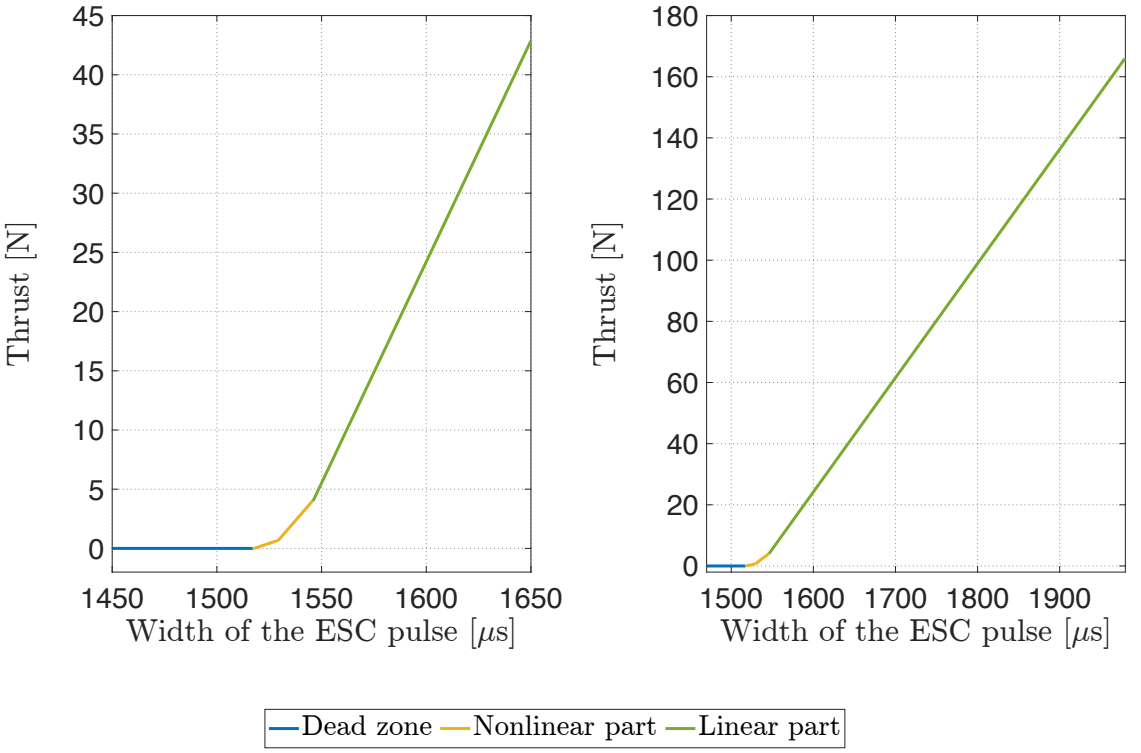

(b) Regression model of the thrust with respect to the PWM signal based on the data collected for the operational (left) and the whole (right) ranges

Figure 3-13: Processed data for the rotor group identification.

3.3.1.5 Force and torque envelopes

To evaluate the reachable dynamic capabilities of the designed actuation system, it is worth analyzing the allocation matrix and corresponding wrench in $\mathcal{F}_b$. Since the wrench is a six-dimensional vector, we utilize two projections of the wrench on three-dimensional spaces [Hamandi et al., 2020]. Namely, we analyze the set of body-frame *admissible forces* with zero torque and the set of *admissible torques* with zero force. In this analysis, we impose the saturation limit of 150 N on the identified propeller thrust.

Let us introduce the following space of positive thrust vectors $\boldsymbol{\lambda}$:

$$\Lambda = \left\{ \boldsymbol{\lambda} \in \mathbb{R}^8 \mid \forall \lambda_i \in \{0,\ 150\},\ i = 1, \ldots, 8 \right\}.$$

By utilizing the definition of allocation matrix (3.1), we can calculate the envelopes of *total force* and *total torque* volumes corresponding to the whole space of $\boldsymbol{\lambda}$ as follows:

$$\boldsymbol{w}_b^{total} = \begin{bmatrix} \boldsymbol{f}_b^{total} \\ \boldsymbol{\tau}_b^{total} \end{bmatrix} = \boldsymbol{A}\boldsymbol{\lambda} = a_1 \boldsymbol{J}_1 \lambda_1^{max} + \cdots + a_8 \boldsymbol{J}_8 \lambda_8^{max}, \tag{3.5}$$

where $\lambda_i^{max} = 150$, gain a_i is defined as $\forall a_i \in \{0,\ 1\}$ to realize all extreme combinations of the thrust vector, $\boldsymbol{w}_b^{total}$ is the six-dimensional shell of possible body-frame forces and torques. It is worth noting here that in contrast to cable-suspended systems, for common UAV the (3.5) should also contain the gravity force.

The total force and total torque represents the coupled dynamic capabilities. Due to omnidirectionallity, the platform is able to operate in decoupled manner. To this end, we aim to evaluate the set of admissible forces with zero torque and admissible torques with zero forces. First, let us introduce the following two spaces:

$$\mathcal{X} = \left\{ \boldsymbol{x} \in \mathbb{R}^8 \mid \boldsymbol{x} \in \mathcal{N}(\boldsymbol{A}_2^{3\times 8}) \ \wedge\ 0 \leq x_i \leq 150,\ i = 1, \ldots, 8 \right\},$$
$$\mathcal{Y} = \left\{ \boldsymbol{y} \in \mathbb{R}^8 \mid \boldsymbol{y} \in \mathcal{N}(\boldsymbol{A}_1^{3\times 8}) \ \wedge\ 0 \leq y_i \leq 150,\ i = 1, \ldots, 8 \right\},$$
$$\mathcal{X} \subseteq \Lambda,\ \mathcal{Y} \subseteq \Lambda.$$

The space $\mathcal{X}$ (or $\mathcal{Y}$) contains all thrust vectors $\boldsymbol{x}$ (or $\boldsymbol{y}$), which result in the zero torque (or force) of the generated wrench, i.e., it is placed in the null-space of the $\boldsymbol{A}_2$ (or $\boldsymbol{A}_1$). In order to select only $\mathcal{X}$ space among the whole Λ space, the following

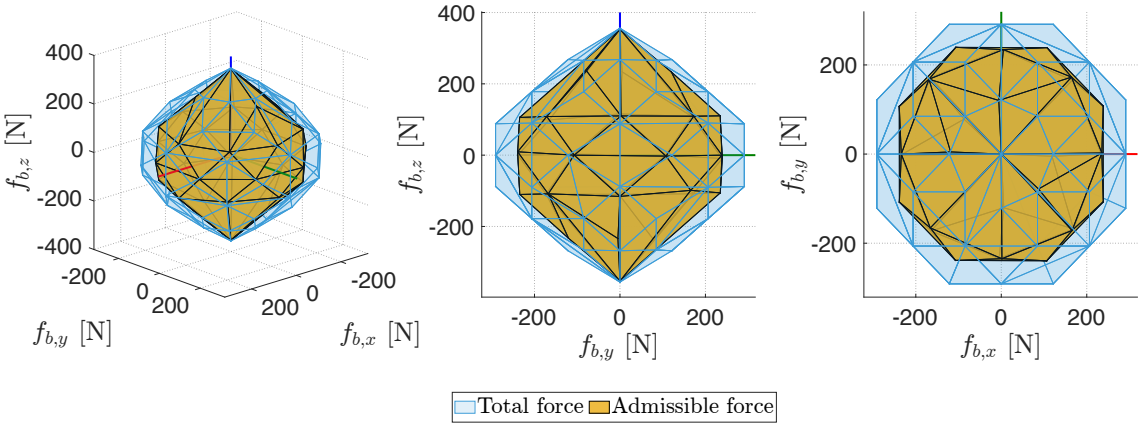

(a) Set of admissible forces with zero torque

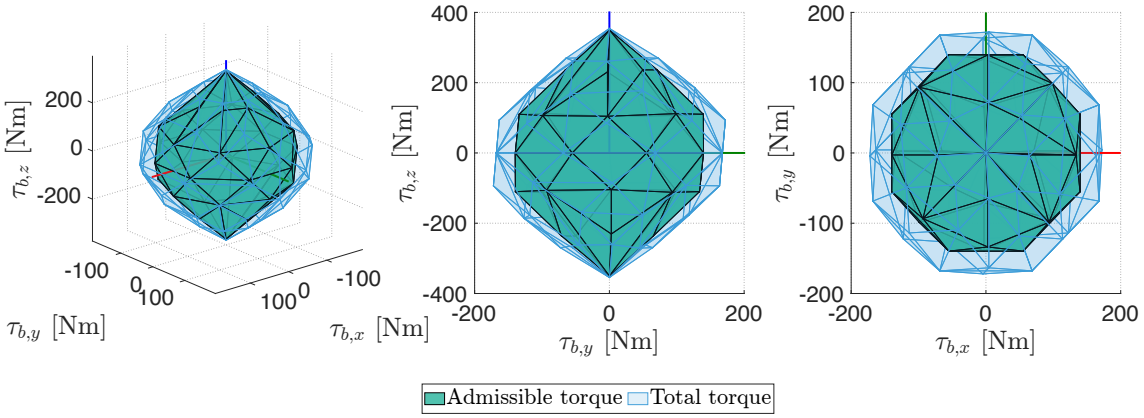

(b) Set of admissible torques with zero force

Figure 3-14: Admissible forces and torques.

minimization problem should be resolved:

$$\begin{aligned} \underset{\boldsymbol{x}}{\text{minimize}} \quad & \|\boldsymbol{x} - \boldsymbol{\lambda}\|^2 \\ \text{subject to} \quad & \boldsymbol{A_2 x} = 0, \\ & 0 \leq x_i \leq 150, \ i = 1, \ldots, 8. \end{aligned}$$

Thus, $\boldsymbol{x} \in \mathbb{R}^8$ is the vector of propeller thrusts which generate zero torque in the $\mathcal{F}_b$. Thus, the vector of resulted thrusts is located in the null space of the matrix $\boldsymbol{A_2}$, i.e. $\boldsymbol{x} \in \mathcal{N}(\boldsymbol{A_2})$, which corresponds to the first constraint. The second constraint imposes the lower and upper bounds on the thrust vector elements related to the physical limits of the rotor group. The main optimization condition implies minimization of a difference between total and admissible shell. The same approach might be applied to calculate the set of $\boldsymbol{y}$ thrust vectors. Figure 3-14 displays the resulted total envelopes and admissible sets.

Then, the resulted sets of admissible forces and admissible torques can be calculated using any solver that can find a minimum of constrained multivariable function[12] as:

$$\boldsymbol{w}_b^{adm,f} = \begin{bmatrix} \boldsymbol{f}_b^{adm} \\ \mathbf{0} \end{bmatrix} = \boldsymbol{A}\boldsymbol{x},$$

$$\boldsymbol{w}_b^{adm,\tau} = \begin{bmatrix} \mathbf{0} \\ \boldsymbol{\tau}_b^{adm} \end{bmatrix} = \boldsymbol{A}\boldsymbol{y}.$$

It is interesting to highlight the high control authority around the yaw axis, which is useful since this DOF cannot be controlled by winch actuation and critical to maintain during the manipulation. Moreover, the force along the z_b axis is not required at first look since an external carrier performs the gravity compensation. However, any motion of the arm will result in the displacement of the system COM with respect to the platform GC. In this case, in order to generate the torque around horizontal axes through the new COM location, the force along z_b is required.

3.3.1.6 Frequency analysis

When the propellers start to spin, the IMU measurements become noisy. The frequency of the IMU noise is related to the propeller rotational speed. Thus, the noise is induced by propeller vibrations. They might have different sources, e.g., rotor and propeller imbalance or slight speed difference of several rotor groups. For a deeper investigation, 8 rotor groups were activated with 10 % of the maximum achievable thrust, while the SAM was placed on the table and pressed with additional weights to prevent movements. The IMU-provided angular velocity in the body frame, i.e., $\boldsymbol{\omega}_b = [p,\ q,\ r]^T$, was collected and processed through fast Fourier transform (FFT), see Figure 3-15. It can be seen that when the motors are activated, the high-frequency noise with a frequency of 39.2 Hz appears. Since a periodic sources (8 rotor groups) produce the noise containing dominant harmonic component, the higher rotor group's rpm the higher noise frequency. Thus, vibrations induced by rotor groups in a range higher than in the considered experiment would have even higher frequency (it is worth mentioning that intensity might vary). In general, adaptive notch filtering could be applied to reject noise spikes in the IMU measurement for the commanded rpm.

[12] In particular, the function *fmincon* in MATLAB environment was utilized.

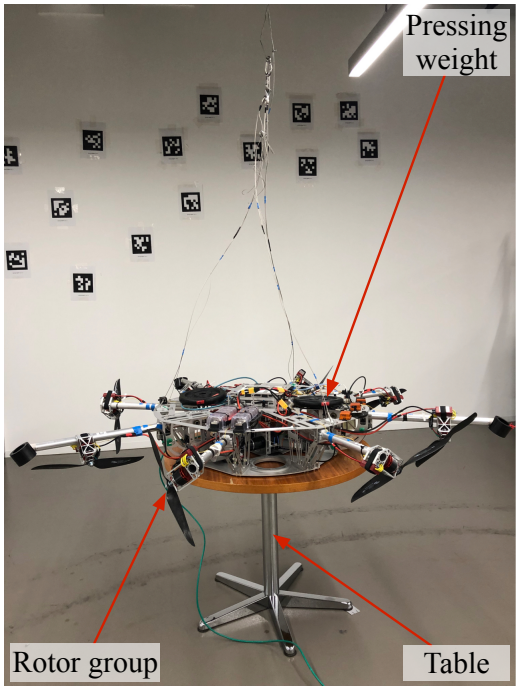

(a) The SAM pressed at the table

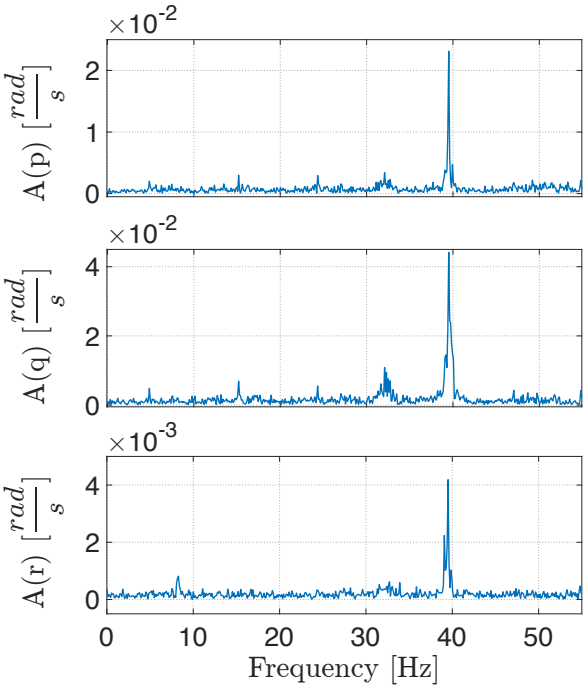

(b) Single-sided amplitude spectrum of the IMU angular velocities. The A(.) stands for Amplitude

Figure 3-15: Frequency analysis of the rotor group.

3.3.2 Redundant robotic arm

In order to perform various manipulation tasks, a 7-DoF KUKA LWR IV[13] [Albu-Schäffer et al., 2007] is mounted on the bottom side of the platform, see Figure 3-16.

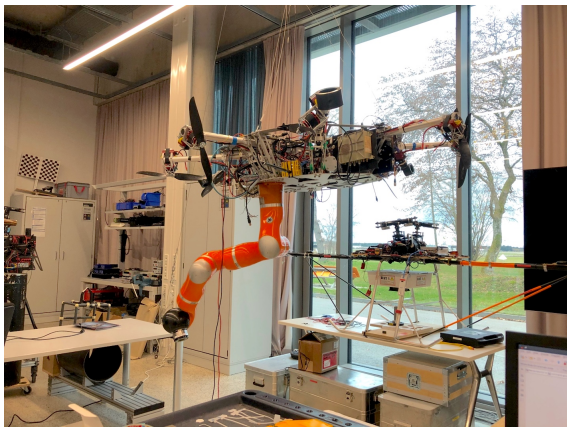

(a) The KUKA LWR IV at the SAM operates on the side of the platform

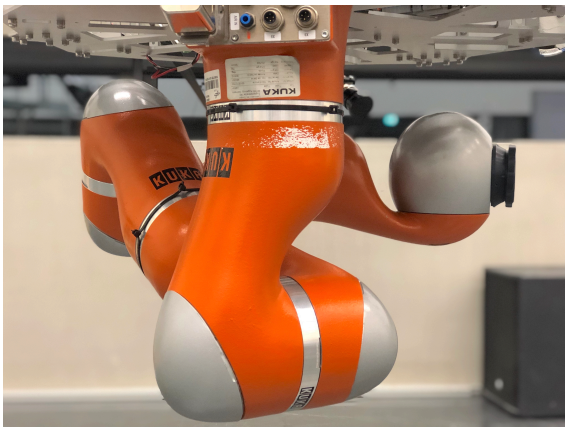

(b) The KUKA LWR IV is folded into the parking configuration

Figure 3-16: The KUKA LWR IV.

[13]https://www.kuka.com

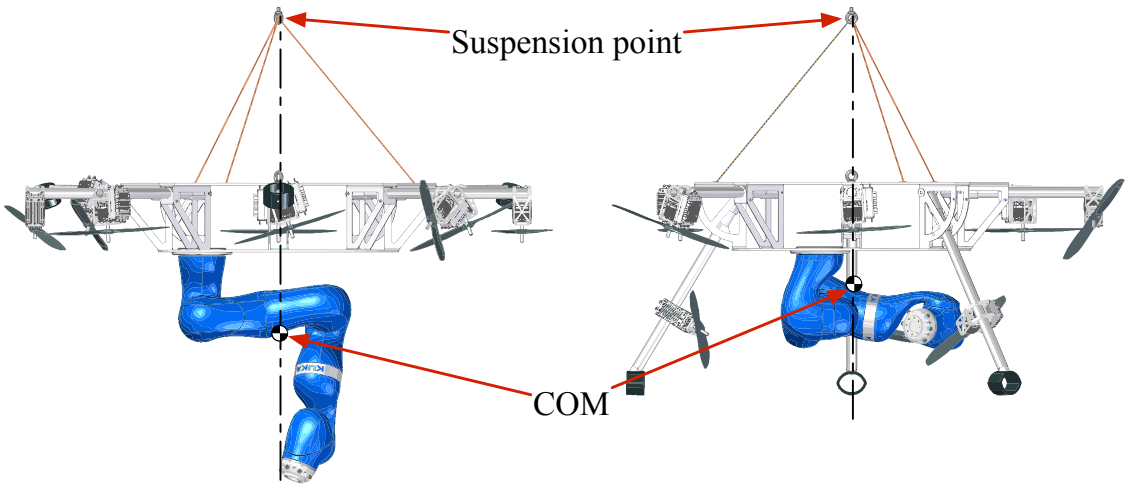

Figure 3-17: Operational (left) and parking (right) configurations of the SAM.

The arm contains $7\mathcal{R}$ joints and has the total length of 1 meter. Two main postures of the robotic arm should be defined (Figure 3-17):

- operational with the following joint angle values:

$$\boldsymbol{q}_m = [0,\ -\frac{\pi}{2.8},\ 0,\ -\frac{\pi}{2.8},\ 0,\ 0,\ 0]^T,$$

- parking with the following joint angle values:

$$\boldsymbol{q}_m = [-\frac{\pi}{6.2},\ -\frac{\pi}{2},\ -\frac{\pi}{2},\ -\frac{\pi}{2} + 0.343,\ 0,\ \frac{\pi}{2},\ 0]^T.$$

During the transportation and landing, the manipulator should be in the parking position in order to avoid collision between the robotic manipulator and the ground. The main advantage of this position is its compactness. Before initiating any manipulation task such as pick and place or peg-in-hole, the manipulator should be placed in the operational configuration as fewer movements are required to perform tasks from this position.

Additionally, it is worth mentioning that the manipulator mounting point is shifted from the center of the platform on 0.24 m. It allows to define the parking and operational configurations so that the resulting COM of the whole system is the same for both cases (in the horizontal plane) and is located under the suspension point, see the COM position in Figure 3-17. Therefore, the COM of the whole system for both configurations evolves close to the same point, minimizing required actuation during the transition.

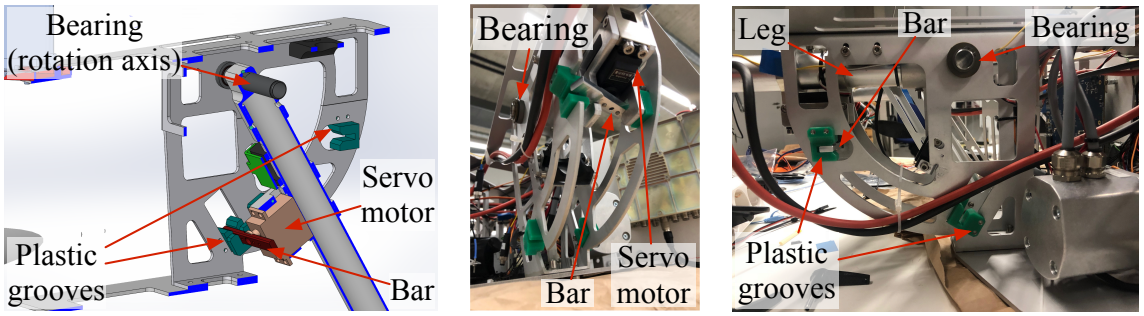

(a) The CAD model

(b) The real system (front view)

(c) The real system (side view)

Figure 3-18: The operating principle of the locker mechanism.

3.3.3 Foldable landing gear

In order to reduce the total weight and accommodate the large manipulation workspace, the traditional landing gear is not installed in the cable-suspended platform. To land, three out of eight frame propeller arms can be folded and converted to the frame legs of the landing gear, see Figure 3-17. Thus, the legs have a dual-use: landing legs and propeller arms. In order to switch from the landing leg to the propeller arm, each leg has to be risen from the lower to the upper position. In this transition, the leg rotates in the bearing through about 60 degrees. To lift up the leg, the thrust force of the rotor group is used. In order to compensate for a non-zero wrench caused by mentioned thrust during this procedure, the remaining five propellers are utilized. The movement downwards (transition from the frame arm to the landing leg) is done by the gravity force, damped by the thrust force.

3.3.3.1 Hardware

To fix the position of the leg/arm in the bottom and top points, the locker mechanism is used, see Figure 3-18. As it can be seen, the locker mechanism contains two fixed plastic grooves and a servo motor (Futaba S3152). The grooves are manufactured from "S" green plastic material with low friction, long lifetime, and high wear resistance. In order to lock the position, the servo motor should turn a bar installed at the shaft. A ground reaction force during landing is pointed toward the rotational bearing to avoid load on servo motor shafts. At the tip of each leg, the landing pad is installed to dampen the structure during the hard landing.

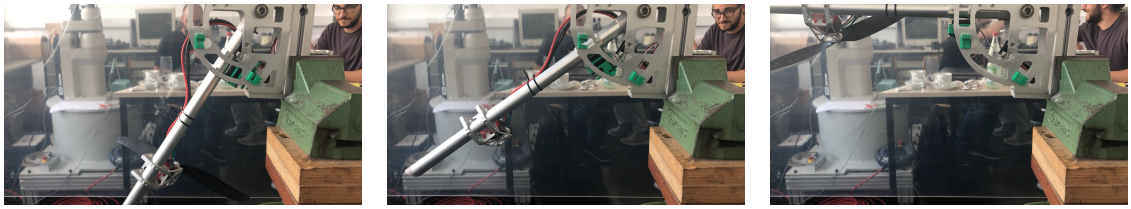

(a) The leg in the lower position (b) The leg in the transition (c) The leg in the upper position

Figure 3-19: Lifting of the frame leg by the thrust.

3.3.3.2 Quantitative requirements

The main requirement for the landing gear is defined by the lift force generated by propeller vertical thrust projection. The length of the arm till the motor hub, i.e., the leverage at which thrust is applied is 0.75 m, while the estimated weight of the leg (aluminum tube, rotor group, holder, landing pad, and servomotor) which has to be lifted is 1.55 kg.

3.3.3.3 Validation

Based on the allocation matrix optimization results, the rotor group at one out of three frame legs is supposed to spin during the lifting in the opposite direction with respect to the designed one in regular operation. In such a scenario, the thrust coefficient is much lower than the identified one for the proper spinning direction in (3.3). To this end, the constraint angle of $\alpha^{lim} = 60^o$ w. r. t. the z_b axis was found for the particular hardware selection and added as a constraint **C.3** to the optimization problem for allocation matrix calculation.

Validation of the leg lifting was performed experimentally for the frame arm with the worst configuration resulted from the optimization in terms of the thrust generation. Figure 3-19 demonstrates the validation of the final configured propulsion unit that is tilted around alpha for 120 degrees, i.e., 30 degrees with respect to to the horizontal plane, and spins in the opposite direction. As a result, the selected hardware completely satisfies the task requirements.

3.3.4 Winch-based actuation

The winch-based actuation, see Figure 3-20, allows controlling the length of three rigging cables that suspend the SAM platform to the crane's hook in order to maintain the SAM COM location below the suspension point. With such an actuation,

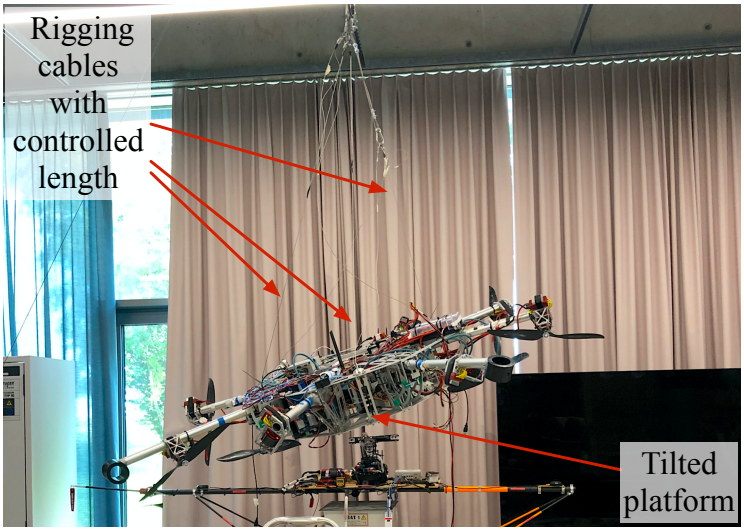

Figure 3-20: Winch-based actuation integrated into the SAM platform.

we can affect 3 out of 5 DOFs: platform roll, pitch, and COM displacement. Control of the height using winches allows us to completely exclude external carrier from the aerial manipulation.

3.3.4.1 Kinematics

Three rigging cables cross the platform plane $x_b - y_b$ at points denoted by W_i for $i-$th winch. All three points are located at the circle with radius $\|\boldsymbol{a}_i\| = 415.7$mm and center at the O_b. Here, $\boldsymbol{a}_i$ is the vector pointing to the W_i in the body frame. All vectors are displaced with 120^o shift around z_b axis, see Figure 3-21. The $\boldsymbol{a}_3$ is turned with respect to the axis x_b at angle $\gamma' = 52.49^o$.

3.3.4.2 Hardware

Each winch, see Figure 3-22a, is based on a motor assembly that contains the Maxon RE50 DC motor [Max, 2021] , a planetary gearhead GP 52 C with reduction ratio 343/8 [Max, 2021], a 3 channel high precision encoder HEDL 9140 with 500 counts per turn [Max, 2021], and a static brake AB 44 [Max, 2020]. The regulation of each assembly is performed by controller EPOS4 compact 50/5 CAN with integrated motion controller based on the encoder feedback [Max, 2021].

The motor assemblies are installed inside of the platform, see Figure 3-22b. The controlled steel cable is wounded on the guided spool, which is attached to the motor gearhead output shaft, see Figure 3-23. The guided spool has special holes for weight reduction and is covered with a protection cover. The length of the cable

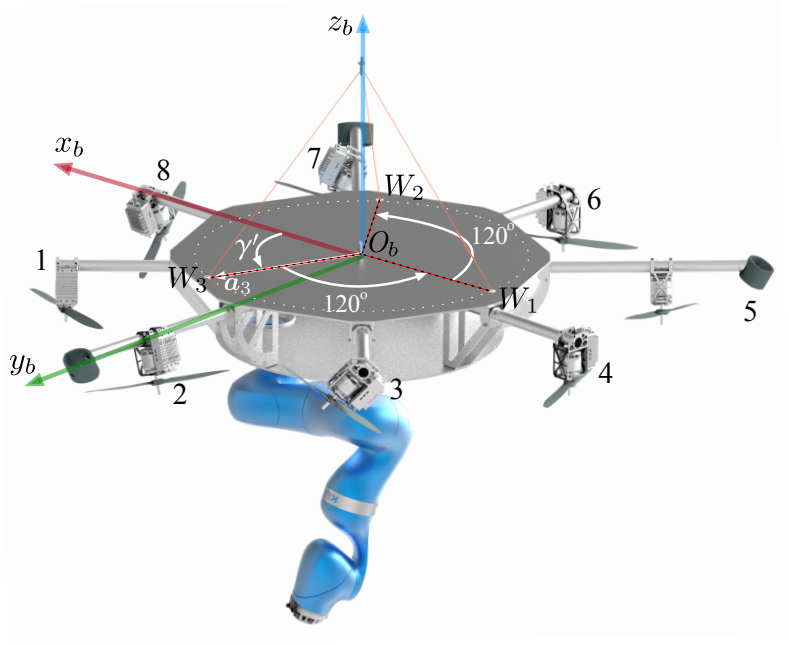

Figure 3-21: Allocation of all actuators with respect to the body frame. The point W_i denotes $i-$th winch suspension point, and Arabic numbers indicate the corresponding rotor group.

corresponding to the one rotation of the guided spool is calculated as: $\pi \cdot d_{gs} = 3.14 \cdot 60.2 = 189$ mm. It can vary from 0.5 m to 2 m starting at W_i point, marked by yellow circle in Figure 3-24a. For safety reasons, we limited an operational length range in bounds of 0.5-1.3 meters. In order to keep cable length within the operational range, an optical fiber sensing system from Keyence is used. If the cable length exceeds the precalibrated limit range, the light beam of the fiber unit will be interrupted as shown in Figure 3-24b, and the motor motion will be paused.

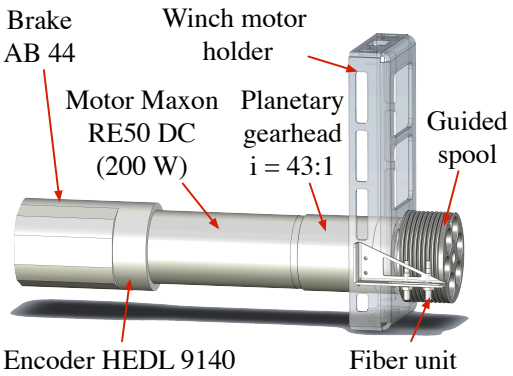

(a) Assembly of the winch servo

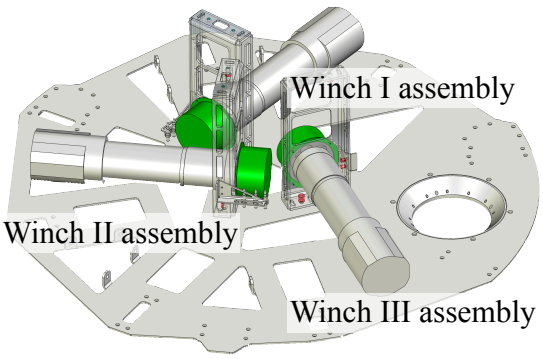

(b) Placement of three winch servos inside the platform

Figure 3-22: Winch-based actuation composition (CAD model).

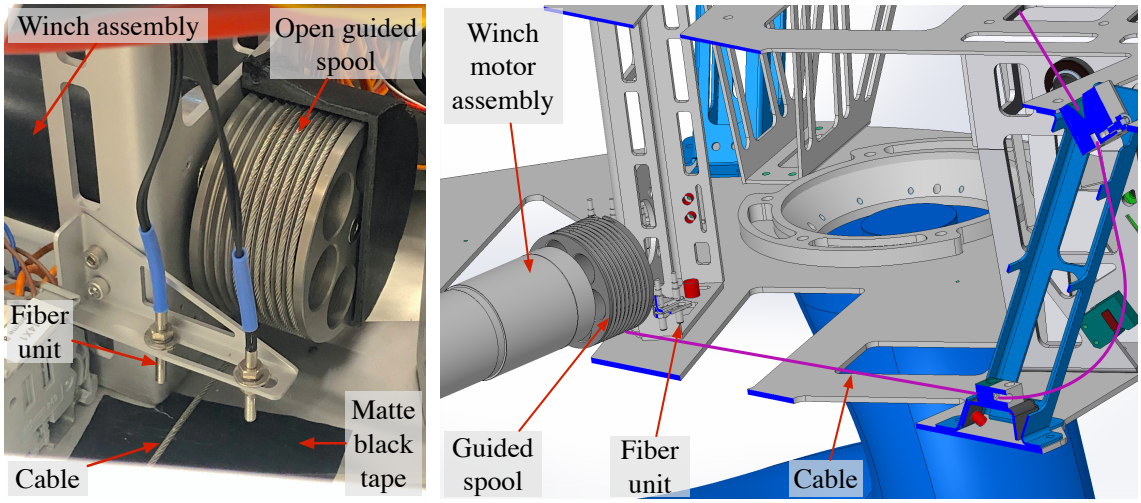

(a) The cable is wound at the guided spool

(b) Cabling of the winch suspension inside the platform

Figure 3-23: Winch suspension cabling inside the platform.

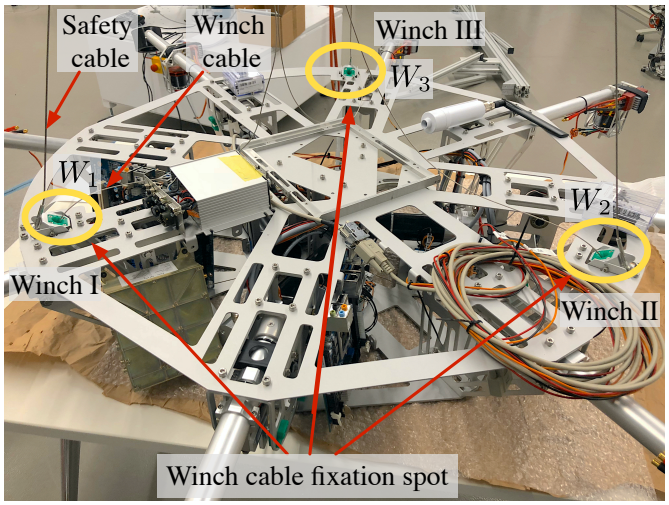

(a) Winch suspension points W_i at the SAM

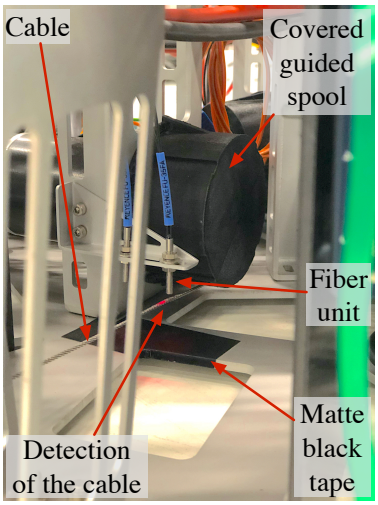

(b) Interruption of the fiber unit light beam by cable

Figure 3-24: Winch-based actuation (Real system).

The list of all elements of the winch-based actuation is presented in Table 3.3.

3.3.4.3 Communication

The overall architecture diagram of the winch-based actuation is presented in Figure 3-25. Three motor assemblies are integrated into a single communication Controller Area Network bus (CANbus) composed of the can-high and can-low signals and terminated by a 120 Ω resistance on both sides. The communication is established via the higher layer CANopen protocol [CAN, 2011] with a transmission

Parameter	**Value**	**Unit**
Motor power	200	W
Nominal voltage	48	V
Nominal speed	4620	rpm
Nominal torque	0.420	Nm
Nominal current	4.58	A
Torque constant	93.4	$\frac{\text{mNm}}{\text{A}}$
Speed constant	102	$\frac{\text{rpm}}{\text{V}}$
Motor profile velocity	1500	rpm
Gearbox reduction ratio	343/8	-
Gearbox efficiency ν	75	%
Encoder counts per turn	500	-
Encoder max speed	12000	rpm
Break torque	2.5	Nm
Spool nominal diameter	60.2	mm
Baudrate	1	$\frac{\text{Mbits}}{\text{s}}$
Cable length range	[0.5-2]	m

Table 3.3: Technical characteristics of the winch-based actuation.

rate of 1 Mbits/s. Based on the CANopen addressing and communication scheme, each controller in the assembly, i.e., EPOS4, has an object dictionary (OD), which contains parameters that describe the behavior of the device, e.g., motor constants, controller gains. This standard also defines two communication objects. The first one is the Service Data Object (SDO) used to configure the device. The second is the Process Data Object (PDO), which is exploited to control the motor and to read measurement data in real-time.

Onboard flight control computer (FCC) with deployed QNX Neutrino Real-time Operating System (RtOS) is utilized as a leader device. In order to establish the Leader/Followers communication between FCC and EPOS4 controllers, a unique library to manage the CANopen stack for QNX Neutrino RtOS is developed. It allows the operation of the motors in the so-called Profile Position Mode [Max, 2019] at which the desired rotational angle in increments (encoder measurement

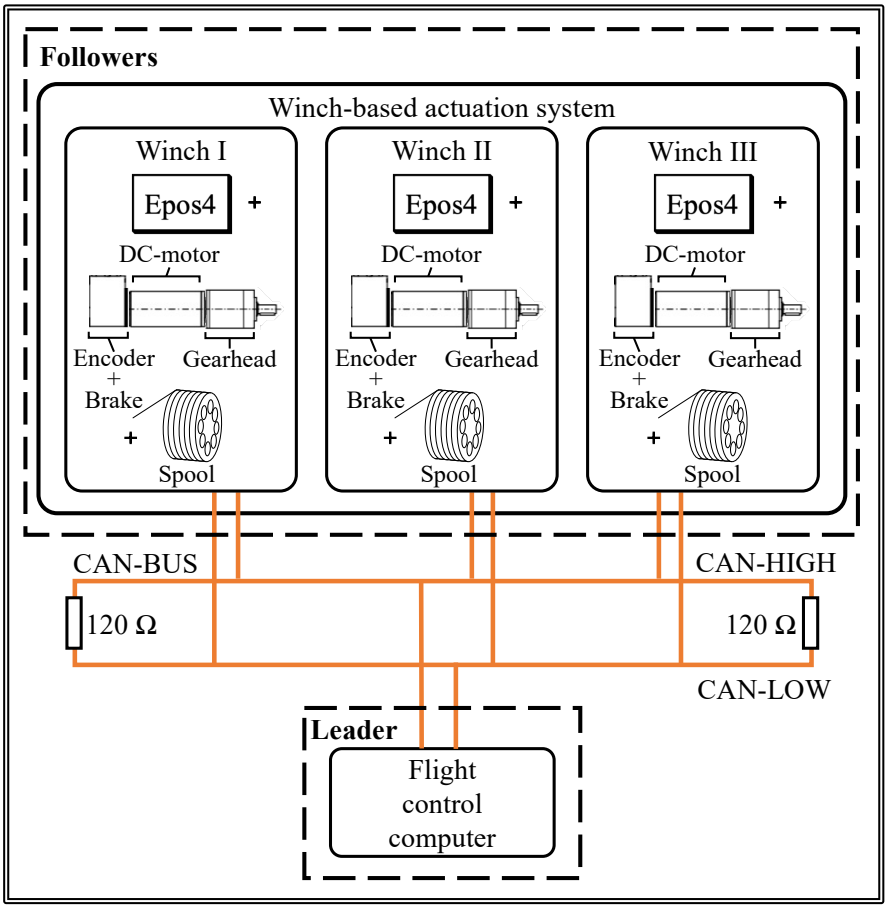

Figure 3-25: The architecture of the winch-based actuation.

unit) is used as an input. At the same time, in this mode, real-time information about angular position and velocity is provided by EPOS4 back to the user.

3.3.4.4 Quantitative requirements

In order to provide a reliable performance, the winch-based actuation should satisfy two main requirements. The first one ensures that the minimum value of the motor output torque and speed mapped via the gearhead ratio is higher than a load torque and velocity during the operation. Since we imply slow motion for the winch actuation, we consider the quasi-static process at which the system moves slowly enough to consider it static. The second demand is to provide brake torque high enough to hold the system arbitrary configuration. It is worth mentioning that the static breaks are integrated into the winch assemblies. It means that they should be turned on only after the full stop of the winch servos.

In the static or quasi-static regime, the tension forces N along the winch cables

balance the gravitational force applied to the system COM. Depending on the angle κ between the $i-$th rigging cable and the vector $\boldsymbol{a}_i$ located in the platform plane $(O_b x_b y_b)$, the gravity compensation term of the tension force is varied. We consider the critical case defined by the system structure with $\kappa = 25^o$. In other words, κ cannot be less than 25^o due to the risk of touching the equipment located at the top of the platform by rigging cable. The weight of the platform is around 55 kg, then the force balance along the vertical axis might be formulated as follows:

$$mg = 3Nsin(\kappa).$$

Then the tension force for the critical angle is defined as $N(\kappa = 25^o) = 425.56$ N.

The tension force is applied to the gearhead via guided spool and generate the torque M_{load}:

$$M_{load} = N\frac{d_{gs}}{2} = 12.80 \text{ Nm},$$

where $d_{gs} = 0.0602$m is the diameter of the guided spool.

Since the torque ratio between guided spool and gearhead is one and between the gearhead and the motor is $i_{gh} = 43$, the torque at the motor shaft can be calculated as:

$$M_{motor} = \frac{M_{load}}{i_{gh}\nu} = \frac{M_{load}}{43 \cdot 0.75} = 0.3983 \text{ Nm}.$$

Let us compare this value with torque parameters of the selected hardware:

$$M_{re50} = 0.42 > M_{motor} = 0.3983,$$
$$M_{ab44} = 2.5 > M_{motor} = 0.3983.$$

In order to analyze the motor speed parameter, we assume that the cable slowly moves with linear velocity of $v_{cable} = 10 \ \frac{\text{cm}}{\text{sec}}$, then:

$$n_m = i_{gh} n_{gh} = \frac{60 i_{gh} v_{cable}}{\pi d_{gh}} = 1364.8 \text{ rpm}.$$

Here, g_{gh} is ta nominal diameter of the gearhead. Estimated torque-speed motor parameters fully comply with the continuous operating range for the selected Maxon RE50 motor. Moreover, due to system symmetry, defined parameters are the same for all three winch motors.

Additionally, it is worth noting that each winch actuator is also unidirectional (in terms of tension): cables can be pulled but not pushed. Since we have an under constrained system, i.e., the SAM platform has 6 DOF and only 3 cables, there is no null-space at which we can set additional control effort as we did in (3.2). So, the corresponding allocation matrix relating the positive tension forces and corresponding generated wrench will not provide arbitrary solution [Borgstrom et al., 2009]. This restriction leads to the limitation in the workspace that has to be kept in mind during the control strategy selection.

3.3.5 Mechanical structure

As seen in Figure 3-26, the SAM consists of the two plates. The winch motors are placed inside of the platform, while other electronic blocks are either attached to the top plate or installed on the special fiberglass plates connected to the installation

(a) Prepared details for assembly

(b) Fitting of the details at the wooden plate

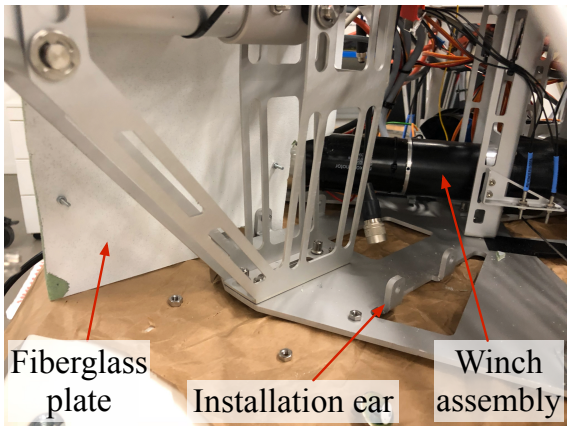

(c) Ears for electronics plates installation

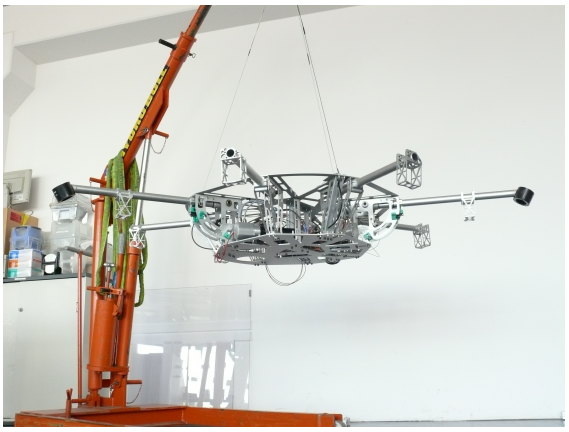

(d) Preassembly of the SAM

Figure 3-26: The SAM assembly process.

ears between two plates, see Figure 3-26c, the redundant robotic arm is mounted on the bottom plate. The possibility to remove the top plate provides easy and fast access to all electronic components. The rotor groups are installed on the frame arms. The orientation of each propulsion unit can be adjusted in the range of 0 to 360 degrees around α and ± 12 degrees around β, using a clamping mechanism.

A weight reduction is one of the main challenges in the design and production of common aerial manipulators. Thus, the general mechanical frame, including arms, plates, ribs (stiffeners), and motor holders, is manufactured from insulated

Parameter	**Value**	**Unit**
Number of propellers	8	-
Number of winches	3	-
Diameter of placement circle for propeller hubs	1.5	m
Diameter of circle where winch cable crosses the platform plane	0.831	m
Frame arm length	0.765	m
Frame leg length	0.905	m
Robotic arm length	1	m
Weight of the frame with integrated electronic components	35.7	kg
Battery pack weight	3.7	kg
Weight of the robotic arm with FTS and tool	16.7	kg
Principal components of the inertia tensor (obtained from the CAD detailed model)	$diag(4.275,\ 4.275,\ 8.438)$	kgm^2
Displacement of the arm installation point with respect to GC	0.24	m
Cable length range	[0.5-2]	m

Table 3.4: Key parameters of the SAM system.

lightweight aluminum. Applying a set of methods for the weight optimization in the mechanical structure after several iterations, we managed to achieve the total weight of the SAM with the installed manipulator, electronics, and batteries roughly 55 kg. The stiffness of the platform with conducted design optimization is high enough and is validated by finite element analysis. Namely, the stress-strain analysis was performed by engineers from the Robo-Technology GmbH for the flight mode when all actuators exert non-zero forces and for the hard landing when the system is dropped at the ground from 10 cm height.

It is worth noting that with given weight-geometric characteristics even for fully horizontally stretched robotic arm with maximum payload at the end effector, in the quasi-static condition, the COM of the SAM will be located below the mechanical frame border. Moreover, it will be mostly inside of triangle $W_1W_2W_3$, see Figure 3-21. Thus, the slacking of the rigging cables in normal and close to the extreme (but possible) conditions is unattainable for the considered system.

The list of all geometric-weigh parameters of the SAM is presented in Table 3.4

3.3.6 Architecture

The architecture of the SAM is presented in Figure 3-27. As it can be seen, three different computers are installed onboard: Robot Control Computer (RCC), Vision Processing Computer (VPC), and Flight Control Computer (FCC). The FCC is based on a field-programmable gate array and responsible for the control of the winch-based and propeller-based actuation systems. Also, it is directly connected to the set of sensors for estimation of the platform state during the operation: Inertial Measurement Unit (IMU) and Global Positioning System (GPS) with real-time kinematics (RTK). The VPC is connected to the two cameras and processes vision data for robot localization. It is worth noting that cameras have a dual-use. Their second purpose is to provide visual feedback to the human operator during teleoperation tasks. The main task of the RCC is to control the robotic arm. The connection between computers is established via a network switch, which is connected to the access point. Through the access point, the point-to-point communication channel between the SAM and the ground station is established. Additionally, there is a communication channel between the FCC and manual command transmitter via a radio link.

A data management between computers is organized through the Links and Nodes (LN) package. The LN is the software framework developed at DLR that

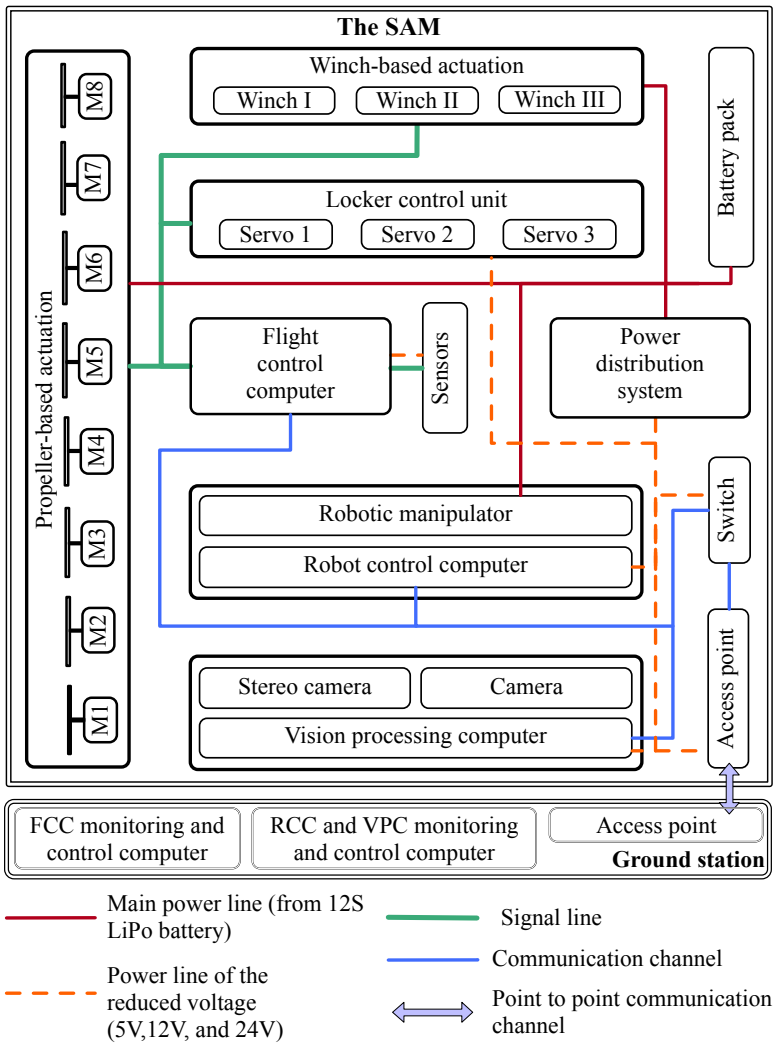

Figure 3-27: The SAM architecture.

provides middleware, process management, and monitoring functionalities.

The power distribution system is mounted at the top-plate of the platform and contains three main blocks, see Figure 3-28:

- Two power bars to distribute power from battery pack to all actuators and robotic arm.
- Specially designed at DLR power distribution system to power all components with reduced input voltage.
- 12S Battery pack installed in the case that can be easily mounted and dismounted.

The battery pack can provide more than 250 A output current with nominal voltage of 48 V. Different electronic components onboard require 5 V, 12 V, and 24

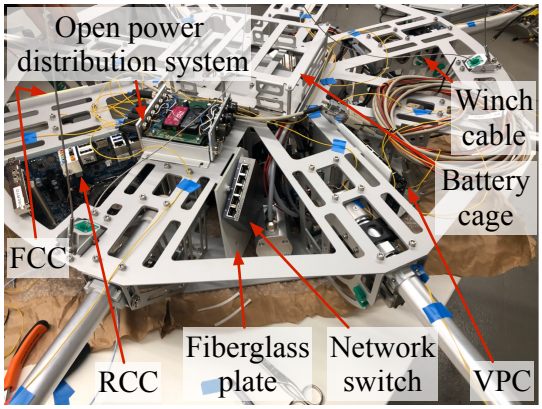

(a) View 1

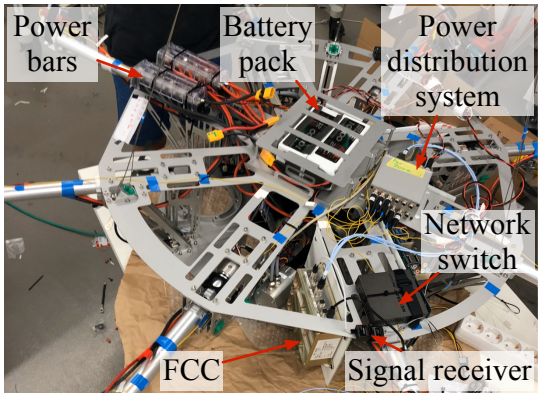

(b) View 2

Figure 3-28: Placement of the electronic components in the SAM platform.

V as an input, and the total current consumption of the cable-suspended platform is around 120 A during the common manipulation task. Thus, to power the whole system, 48 V with 120 A input is enough in terms of power consumption. As a battery pack, SLS 12S 21000 mAh is used. Then, selected battery pack can maintain the SAM during the time period of:

$$\frac{V \cdot Capacity}{P_{consumption}} = \frac{12 \cdot 3.7 \cdot 21 \cdot 60}{48 \cdot 120} = 9.71\,\text{min}.$$

The complete list of the SAM components is presented in Table 3.5.

3.3.7 Control framework

Taking into account aforedescribed design process, a special control framework is deployed onboard, see Figure 3-29. It includes two main blocks. The first one is a *control block* which represents the black box for now. It contains the control algorithms that should generate control signals for system actuation to fulfill specific tasks. This block will be developed and investigated in the following chapters. The second block is the *actuation-perception block*. It includes actuators and sensors that will be utilized in the scope of this thesis for proposed control algorithms: propeller-based actuation, winch-based actuation, robotic arm, and IMU.

Since actuators exploit different control interfaces, the control signals should be appropriately transformed before being applied. Thus, two above developed mappers, (3.2) and (3.4), are utilized for propeller-based actuation in order to calculate control PWM signal from the desired body wrench. The robotic arm and winch servos are fred with inputs corresponding to their control interfaces, i.e, required

Functional role	**Item**	**Qty**	**Current [A]**
48 V consumers			
Robotic arm	KUKA LWR IV	1	10
Rotor group	Kontronik-based	8	up to 100 per group
Winch assemblies	Maxon-based	3	up to 5 per group
24 V consumers			
Winch break	Maxon-based	1	1.5
Stereo camera	Roboception RC Visard 65	1	1
Access point	Ubiquiti Bullet M5	1	0.3
Red button	custom-built	1	0.1
12 V consumers			
Robot Control Computer (RCC)	Kontron KTH81 Flex	1	1.5-3.3
Flight Control Computer (FCC)	Elekra Solar-based	1	0.6
Vision Processing Computer (VPC)	NVIDIA Jetson series	1	4-8.5
Network switch	Netgear GS105	1	0.25
Lidar	Velodyne series	1	up to 1
5 V consumers			
Force Torque Sensor (FTS)	DLR custom-built	1	-
Leg locker servo	Futaba S3152	3	1
Others			
8-channel S.BUS receiver 2.4 Ghz	Futaba R6308SBT	1	FCC-powered
IMU	Xsens MTi 100-Series	1	FCC-powered
GPS module	-	1	FCC-powered
Monocular camera	Allied Prosilica GC1600H	1	VPC-powered
Power distribution system	DLR custom-built	1	passive
Remote transmitter	Futaba FX-30 2.4GHz	1	External power
12S battery pack	SLS Magnum APL V2 6S1P 22.2v 21000 mAh	2	Power source

Table 3.5: List of the SAM components and their functional roles.

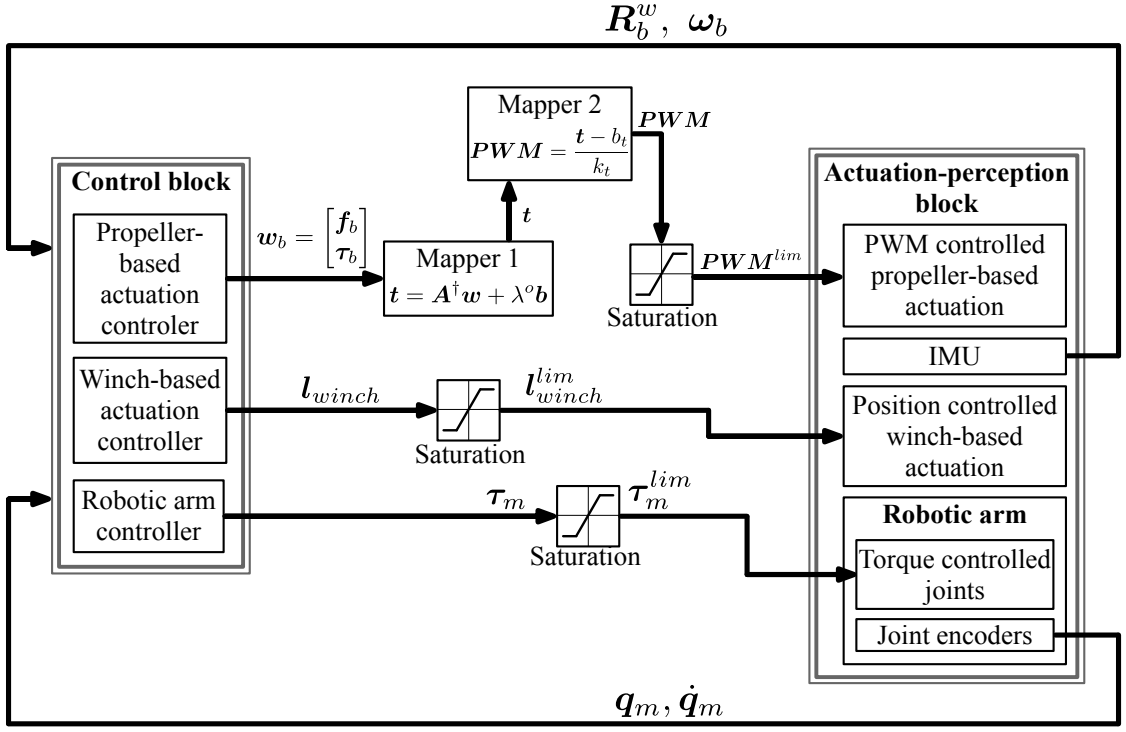

Figure 3-29: The control framework.

Subsystem	**DOF**	**Control interface**
Propeller-based actuation	$3\mathcal{R}3\mathcal{T}$	PWM
Winch-based actuation	$3\mathcal{T}$	Position
Robotic manipulator	$7\mathcal{R}$	Torque

Table 3.6: Actuated DOF and corresponding control interfaces.

mapping should be performed withing the controllers. Moreover, all control signals are transmitted through saturation blocks for safety reasons. All actuated DOFs of the SAM and corresponding control interfaces are listed in the Table 3.6.

The main control loop at the FCC, which is responsible for the control of winches and rotor groups, runs with a frequency of 200 Hz, while the manipulator joint torque controller operates at a sampling rate of 3 kHz.

"Research is to see what everybody else has seen, and to think what nobody else has thought."

Albert Szent-Györgyi

Chapter 4

Oscillation damping control with the propeller-based actuation

4.1 Problem statement

The cable-suspended aerial manipulation system is designed to perform various manipulation tasks in complex industrial sites. The manipulation platform is suspended on the crane's hook by means of cable and equipped with a robotic arm. Thus, the system can approach most of the task locations. Once it is close to the target, the robotic arm performs a manipulation task. As an example, Figure 4-1 shows how the SAM performs a mobile crawler deployment on the pipe. In this task, the SAM should press the cage (with a crawler) to the pipe with a certain force to maintain

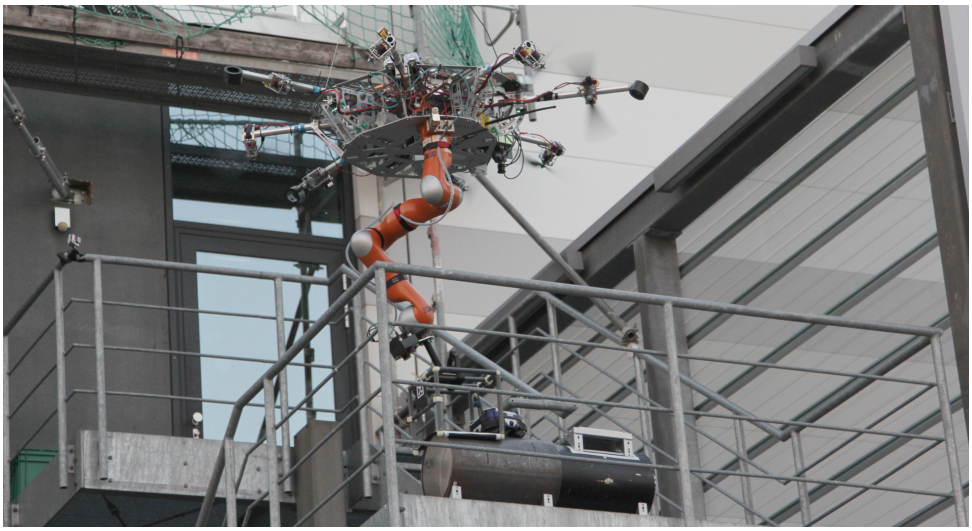

Figure 4-1: The SAM platform deploys the mobile inspection robot.

enough contact force required for secure extraction.

The main challenge to utilize the cable-suspended aerial manipulator in such a scenario is the pendulum motion caused by the suspension chain, so a self-stabilization of the system is essential. In particular, this chapter is interested in an oscillation damping of the suspended aerial manipulator, because it is crucial to dissipate the pendulum motion as quickly as possible in order to perform manipulation precisely. To this end, the SAM is equipped with an agile propeller-based actuation system that can produce the omnidirectional wrench at the GC of the platform. Here, we rely only on the IMU sensor for designing the controller because it is the most robust one among all onboard options. Indeed, GPS may not provide an accurate position in a complex industrial or indoor environment, and the lighting conditions limit the reliability of the vision sensor. In contrast, modern IMU with AHRS functionalities exploits real-time gyroscope drift correction and yaw adaptation to the disturbed magnetic environment [xse].

However, as will be discussed in detail later, the cable-suspended aerial manipulator behaves like a double pendulum, not a single pendulum. Indeed, suspended aerial manipulator is hanged to the crane's hook, which has a significant own mass. Thus, resulted oscillation (vibration) of the platform consists of sum of two vibration modes. Since the resulted motion of a double pendulum is more complex, the onboard IMU sensor does provide neither all vibration modes nor all the states needed for the damping control. In this chapter, to overcome this issue, we design a controller motivated by a simplified model of the SAM. Moreover, we consider two criteria in the control design. First, as addressed earlier, oscillation damping should be accomplished as quickly as possible to perform manipulation tasks. Second, since the aerial system is operated by a battery, we should take the power consumption into account. To this end, we seek an optimal controller that minimizes linear-quadratic function that balances two criteria. Additionally, it is worth noting that various crane might be used as the carrier for the cable-suspended aerial manipulator. Therefore, we design the model-free controller that should be robust to uncertainties and disturbances.

Thus, the *main objective* of the chapter is to design an oscillation damping controller for the cable-suspended aerial manipulator to achieve fast damping behavior while minimizing power consumption using data from a single onboard IMU sensor. The rest of the chapter is organized as follows. Section 4.2 presents the mathematical modeling and behavior analysis of the system. Section 4.3 describes an entire

cycle of the controller design, including control goal formulation, control derivation, stability analysis, and performance assessment in simulation studies.

4.2 Cable-suspended aerial manipulator modeling

4.2.1 Modeling assumptions

To model the cable-suspended aerial manipulator and to derive equations of motion that highlight the main system features, several assumptions were taken into account:

- The aerodynamic effects, e.g., blade flapping, platform drag and lift, airflow disruption, are negligible.
- The influence of the crane motion on the platform dynamics is negligible. Thus, we consider the crane as a fixed base. This assumption is reasonable since the crane is stopped as soon as the platform reaches the target location.
- The crane's chain is a massless link with negligible inertia. Although this assumption reduces the model accuracy for a particular setup, the future controller should be robust enough to adapt to different crane chains. As an additional consequence, the wave effect along the chain might be neglected.
- The crane's chain might be modeled as the rigid link with passive spherical joints at the tips. Such an assumption is valid since the platform suspension is always under tension because of the hook and the platform weight.
- The chain's hook and the platform might be considered as rigid bodies.
- The motion of the platform suspended at the chain's hook can be described by the double pendulum model restricted to small angles.
- The chain length, i.e., the length of the pendulum's first link, changes with a slow constant speed which is reasonable for most cranes.
- The rotor group dynamics is negligible, i.e., we assume an immediate propeller response. Namely, actuator dynamics is ignored because the bandwidth of the BLDC is much larger (subsubsection 3.3.1.6) than the suppositional frequencies of the pendulum oscillation modes (section 6.2)).

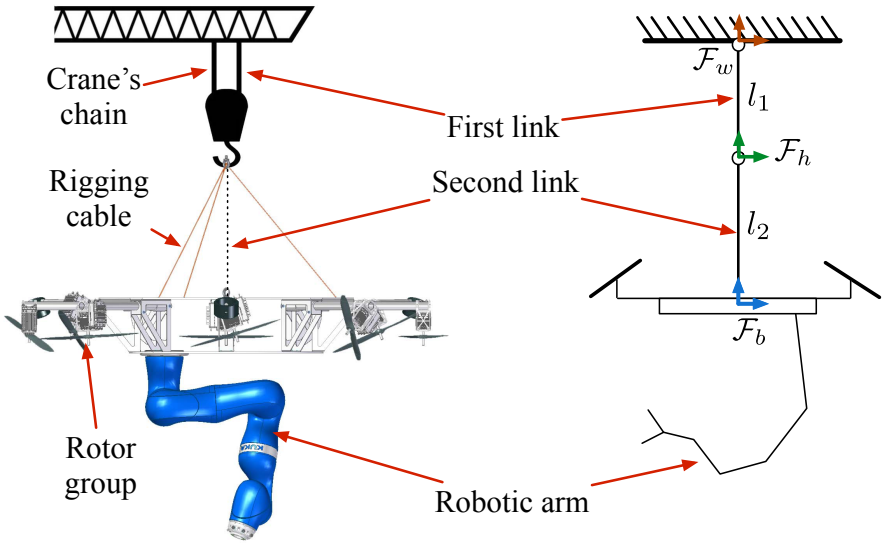

Figure 4-2: The model of the SAM platform (side view).

- The full system state is not available. It is possible to install the second IMU at the middle of the crane's chain [Neupert et al., 2009] to track the hook motion, but the system applicability will be significantly reduced in such a case.

4.2.2 Dynamic formulation

In general, the cable-suspended aerial manipulator can be modeled as a spherical double pendulum, where the first link of length l_1 is the chain between the crane's jib tip and crane's hook, and the second link is the distance between the hook and the platform itself with length l_2, see the link depiction for the SAM system described in chapter 3 in Figure 4-2. Thus, the state of such a system can be characterized by 6 generalized coordinates: the Euler angles of the first ($\boldsymbol{q}_1 \in \mathbb{R}^3$) and the second ($\boldsymbol{q}_2 \in \mathbb{R}^3$) spherical passive joints of the double pendulum.

Let us consider three coordinate frames. The body frame $\mathcal{F}_b$ is located at the GC of the platform[1], while its y_b axis is aligned with the pendulum second link and directed upward. A *hook frame* $\mathcal{F}_h$: $\{O_h,\ x_h,\ y_h,\ z_h\}$ is placed at the second spherical passive joint, and its y_h axis is aligned with the first link and also directed upward. Finally, the world frame $\mathcal{F}_w$ is placed at the suspension point. Its orientation coincides with the body frame at the moment when onboard IMU is initialized, i.e., in the beginning of the operation. Thus, onboard IMU provides

[1]It is worth noting that in the scope of this chapter, we consider platform without robotic arm in our model. To this end, platform GC and COM coincide.

orientation $\boldsymbol{R}_b^w$ and angular velocity $\boldsymbol{\omega}_b$ of the platform. The weight of the links is neglected, and the two masses, m_1 and m_2, which correspond to the weight of the hook and cable-suspended aerial manipulator, are located at the origins of the $\mathcal{F}_h$ and $\mathcal{F}_b$ frames, respectively.

It is worth mentioning that joints of the double pendulum are not actuated, i.e., they are passive. To control the system, as described previously, we can generate a body wrench $\boldsymbol{w}_b = [\boldsymbol{f}_b,\ \boldsymbol{\tau}_b]^T$ at the origin of $\mathcal{F}_b$ frame. Based on the preceding description, the equation of motion for the suspended aerial manipulator can be written as follows:

$$\boldsymbol{M}(\boldsymbol{q})\ddot{\boldsymbol{q}} + \boldsymbol{C}(\boldsymbol{q}, \dot{\boldsymbol{q}})\dot{\boldsymbol{q}} + \boldsymbol{g}(\boldsymbol{q}) = \begin{bmatrix} \boldsymbol{J}^{\boldsymbol{T}}\boldsymbol{w}_{\boldsymbol{b}} \\ \boldsymbol{\tau}_{\boldsymbol{m}} \end{bmatrix}, \tag{4.1}$$

where $\boldsymbol{M}(\boldsymbol{q})$ is the inertia matrix, $\boldsymbol{C}(\boldsymbol{q}, \dot{\boldsymbol{q}})$ is the centrifugal/Coriolis terms, and $\boldsymbol{g}(\boldsymbol{q})$ is the gravity vector. The double pendulum configuration is defined as:

$$\boldsymbol{q} = [\boldsymbol{q}_1,\ \boldsymbol{q}_2,\ \boldsymbol{q}_m]^T \in \mathbb{R}^{13}. \tag{4.2}$$

Here, $\boldsymbol{q}_m,\ \boldsymbol{\tau}_m$ represent the robotic arm generalized coordinates and torque input. $\boldsymbol{J}$ is the Jacobian matrix that maps pendulum joint velocities to a body twist coordinates $\boldsymbol{V}_b$:

$$\underbrace{\begin{bmatrix} \boldsymbol{v}_b \\ \boldsymbol{\omega}_b \end{bmatrix}}_{\boldsymbol{V}_b} = \boldsymbol{J} \begin{bmatrix} \dot{\boldsymbol{q}}_1 \\ \dot{\boldsymbol{q}}_2 \end{bmatrix}.$$

In order to reinforce an intuition behind the complex system, the following analysis is performed for the simplified planar case, while the controller evaluation will be conducted for a generalized 3D case.

4.2.3 Double pendulum physics

Based on introduced assumptions, the cable-suspended aerial manipulator can be modeled as a double pendulum. Let us investigate the planar double pendulum dynamics in order to grasp some useful insights for later convenience. Hereafter, we will denote by a bar over a parameter $\bar{(.)}$ the 2D version (planar case) of the corresponding parameter (.).

Figure 4-3a illustrates the planar double pendulum configuration which is de-

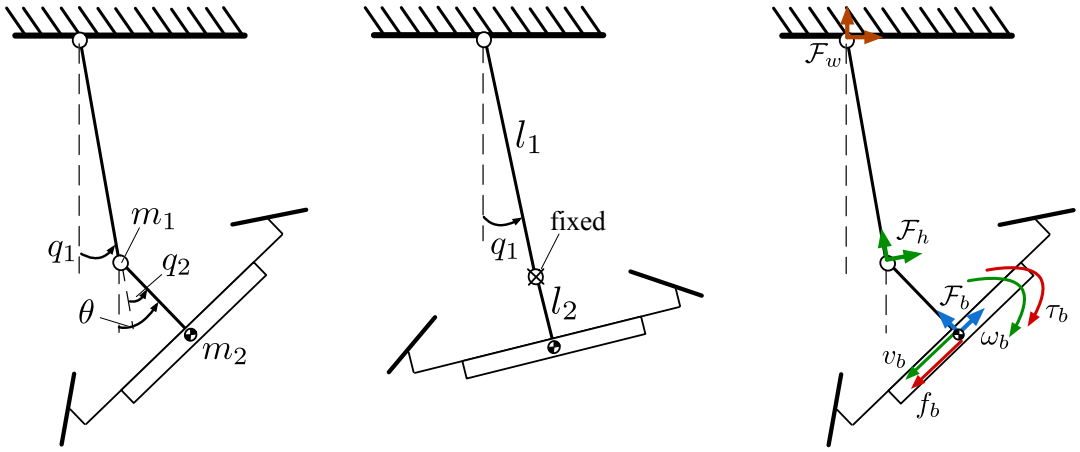

(a) Planar double pendulum (b) Planar single pendulum (c) Wrench and twist

Figure 4-3: Planar pendulum modeling.

scribed by vector of generalized coordinates $\bar{\boldsymbol{q}} = [q_1,\ q_2]^T$ and angle $\theta = q_1 + q_2$ corresponding to the onboard IMU measurement.

Let us define the hook and platform COM locations with respect to $\mathcal{F}_w$ as:

$$\begin{cases} x_1 = l_1 \sin(q_1) \\ y_1 = -l_1 \cos(q_1) \end{cases} \quad \begin{cases} x_2 = x_1 + l_2 \sin(\theta) \\ y_2 = y_1 - l_2 \cos(\theta) \end{cases} . \tag{4.3}$$

Taking the first and second derivatives over time in (4.3) and applying Lagrangian formulation (2.6), the equations of motion for such a system can be formulated as follows:

$$\begin{aligned} &(m1 + m_2) l_1 \ddot{q}_1 + m_2 l_2 \ddot{\theta} \cos(q_1 - \theta) + m_2 l_2 \dot{\theta}^2 \sin(q_1 - \theta) + (m_1 + m_2) g \sin(q_1) = 0, \\ &m_2 l_2 \ddot{\theta} + m_2 l_1 \ddot{q}_1 \cos(q_1 - \theta) - m_2 l_1 \dot{q}_1^2 \sin(q_1 - \theta) + m_2 g \sin(\theta) = 0. \end{aligned} \tag{4.4}$$

The solution of (4.4) linearized around equilibrium point $\bar{\boldsymbol{q}}_{des} = [0,\ 0]^T$ can be found in the following form [Morin, 2002]:

$$\bar{\boldsymbol{q}} = \begin{bmatrix} q_1 \\ q_2 \end{bmatrix} = \begin{bmatrix} C_{11} \\ C_{21} \end{bmatrix} q^{slow} + \begin{bmatrix} C_{12} \\ C_{22} \end{bmatrix} q^{fast}, \tag{4.5}$$

where $q^i = A_i \cos(\nu_i t + \phi_i)$ is the oscillation term with amplitude A_i, frequency ν_i, and phase shift ϕ_i for $i \in \{slow,\ fast\}$, C_{ij} with $i, j \in \{1,\ 2\}$ are constant parameters determined by the weight-geometric parameters and initial conditions

of the system.

Thus, the double pendulum (coupled) system contains two oscillation motions [Magnus, 1965]: the first component with low frequency, ν_{slow}, is modulating the second one with a high frequency, ν_{fast}. Although the solution for joint angles q_1 and q_2 contains both high and low frequency motions, in the system with parameter relation such as $l_1 > l_2$ and $m_1 < m_2$, roughly speaking, the slow motion dominates in q_1, and fast motion - in q_2.

Fast and slow frequencies of the planar double pendulum system can be calculated using the following:

$$\nu^2_{fast,slow} = \frac{g(m_1+m_2)}{8\pi^2 m_1 l_1 l_2}\left((l_1+l_2) \pm \sqrt{(l_1+l_2)^2 - \frac{4m_1 l_1 l_2}{m_1+m_2}}\right).$$

Moreover, in [Singhose and Kim, 2007], it was shown that in case of $l_1 = l_2$ and $m_1 < m_2$, the ν_{slow} is maximized and amplitude C_{i1} is much higher than C_{i2}, so both links oscillate with the same frequency, and system behavior can be described by a single pendulum, see Figure 4-3b.

In the case of a single pendulum, the system can be described by the equation:

$$(m_1 l_1^2 + m_2 l_2^2)\ddot{q}_1 = -g(m_1 l_1 + m_2 l_2)\sin(q_1). \tag{4.6}$$

Let us denote the squared oscillation frequency by $\nu^2_{pend} = g\frac{m_1 l_1 + m_2 l_2}{m_1 l_1^2 + m_2 l_2^2}$, the amplitude by A_1, and the phase shift as ϕ_1, then for small oscillations ($\sin(q_1) \approx q_1$) the solution of (4.6) can be formulated as $q_1 = A_1 cos(\nu_{slow} t + \phi_1)$.

4.3 Optimal oscillation damping controller

4.3.1 Control goal

Let us consider unforced double pendulum dynamics (4.4) at a steady state. It can be seen that there are 4 equilibrium points:

$$\bar{\boldsymbol{q}}^* = \begin{bmatrix}0\\0\end{bmatrix} = \begin{bmatrix}\pm\pi\\0\end{bmatrix} = \begin{bmatrix}0\\\pm\pi\end{bmatrix} = \begin{bmatrix}\pm\pi\\\pm\pi\end{bmatrix}.$$

Among all of them, there is only one stable equilibrium which we consider as the *operational point* of interest. It corresponds to the bottom position with the stretched

configuration, $\bar{\boldsymbol{q}}^* = [0,\ 0]^T$, i.e., where the potential energy is minimum. Nevertheless, any external perturbation in this position can cause an oscillation of the platform. In fact, due to the internal joint damping, the system itself is asymptotically stable with respect to the equilibrium point without any control. However, the damping value is very low, so natural stabilization takes a long time which is not acceptable for real industrial applications. Therefore, our goal is to design an oscillation damping controller to achieve faster damping behavior with minimal power consumption. One challenge is that, as will be shown shortly, the IMU sensor does not provide enough information for the control.

4.3.2 Reduced model for control design

In this chapter, we utilize a decentralized control strategy. Namely, the suspended platform control and manipulator control are decoupled. Regardless of chosen control strategy [Albu-Schäffer et al., 2007, Iskandar et al., 2020, Tsetserukou et al., 2008] and compensators [Iskandar and Wolf, 2019, Kim et al., 2019, Wolf and Iskandar, 2018] for the robotic arm, from the platform's point of view, the dynamic behavior of the manipulator is treated as an external disturbance that causes oscillations.

In subsubsection 3.3.1.5, we found out experimentally that yaw control of the SAM can be independently performed because:

(i) we have a good control authority in yaw direction as shown in Figure 3-14

(ii) dynamics of yaw is rather decoupled from the others around the operational point. Indeed, we have achieved very strong yaw control by applying a common geometric control approach [Lee et al., 2010], see Appendix A.

Therefore, we can eliminate yaw- and manipulator-related variables in (4.1), which then reduces to:

$$\tilde{\boldsymbol{M}}(\tilde{\boldsymbol{q}})\ddot{\tilde{\boldsymbol{q}}} + \tilde{\boldsymbol{C}}(\tilde{\boldsymbol{q}}, \dot{\tilde{\boldsymbol{q}}})\dot{\tilde{\boldsymbol{q}}} + \tilde{\boldsymbol{g}}(\tilde{\boldsymbol{q}}) = \tilde{\boldsymbol{J}}^{\boldsymbol{T}}\tilde{\boldsymbol{w}}_{\boldsymbol{b}} + \boldsymbol{d}, \tag{4.7}$$

where $\tilde{\boldsymbol{q}} = [\tilde{\boldsymbol{q}}_{\boldsymbol{1}}^T,\ \tilde{\boldsymbol{q}}_{\boldsymbol{2}}^T]^T$ is the configuration (4.2) without variables related to yaw and manipulator; $\tilde{\boldsymbol{M}}(\tilde{\boldsymbol{q}})$, $\tilde{\boldsymbol{C}}(\tilde{\boldsymbol{q}}, \dot{\tilde{\boldsymbol{q}}})$, $\tilde{\boldsymbol{g}}(\tilde{\boldsymbol{q}})$, $\tilde{\boldsymbol{w}}_b$, and $\tilde{\boldsymbol{J}}$ represent components of remaining dynamics of (4.1). Motion of manipulator causes an uncertain disturbance $\boldsymbol{d}$ that we further omit and treat as a source of oscillations that have to be dampened by controller.

If we restrict the pendulum motion in the plane (see Figure 4-3), we can further simplify the model as follows:

$$\bar{\boldsymbol{M}}(\bar{\boldsymbol{q}})\ddot{\bar{\boldsymbol{q}}} + \bar{\boldsymbol{C}}(\bar{\boldsymbol{q}}, \dot{\bar{\boldsymbol{q}}})\dot{\bar{\boldsymbol{q}}} + \bar{\boldsymbol{g}}(\bar{\boldsymbol{q}}) = \bar{\boldsymbol{J}}^T \bar{\boldsymbol{w}}_b, \tag{4.8}$$

where, $\bar{\boldsymbol{q}} = [q_1,\ q_2]^T$ corresponds to angles of first and second links, and $\bar{\boldsymbol{w}}_b = [f_b,\ \tau_b]^T$ is the control wrench, see Figure 4-3c. The IMU measurement is then $\theta = q_1 + q_2$ for the planar case. The body twist coordinates $\bar{\boldsymbol{V}}_b = [v_b,\ \omega_b]^T$ and configuration $\dot{\bar{\boldsymbol{q}}}$ are related by the Jacobian matrix $\bar{\boldsymbol{J}}$:

$$\underbrace{\begin{bmatrix} v_b \\ \omega_b \end{bmatrix}}_{\bar{\boldsymbol{V}}_b} = \underbrace{\begin{bmatrix} l_1 \cos q_2 + l_2 & l_2 \\ 1 & 1 \end{bmatrix}}_{\bar{\boldsymbol{J}}} \underbrace{\begin{bmatrix} \dot{q}_1 \\ \dot{q}_2 \end{bmatrix}}_{\dot{\bar{\boldsymbol{q}}}} = \underbrace{\begin{bmatrix} l_1 \cos q_2 & l_2 \\ 0 & 1 \end{bmatrix}}_{\bar{\boldsymbol{J}}_\theta} \begin{bmatrix} \dot{q}_1 \\ \omega_b \end{bmatrix}. \tag{4.9}$$

The Jacobian matrix $\bar{\boldsymbol{J}}$ can be calculated by utilizing (2.2). For later convenience, we also express a mapping $\bar{\boldsymbol{J}}_\theta$ of the body twist coordinates to the $[\dot{q}_1,\ \omega_b]^T$. Let us notice that in a certain range of q_2 ($q_2 < 90°$), the both mappings are invertible.

In the later section, we design a controller using the simplified planar model, while stability analysis and validation will be performed for the original system model (4.7).

4.3.3 Controller derivation

In the planar model (4.8), we first apply coordinate transformation from $\bar{\boldsymbol{q}}$ to $\bar{\boldsymbol{V}}_b$ using (4.9). Then, we obtain:

$$\boldsymbol{\Lambda}(\bar{\boldsymbol{q}})\dot{\bar{\boldsymbol{V}}}_b + \boldsymbol{\Gamma}(\bar{\boldsymbol{q}}, \dot{\bar{\boldsymbol{q}}})\bar{\boldsymbol{V}}_b + \boldsymbol{\zeta}(\bar{\boldsymbol{q}}) = \bar{\boldsymbol{w}}_b, \tag{4.10}$$

where $\boldsymbol{\Lambda}(\bar{\boldsymbol{q}}), \boldsymbol{\Gamma}(\bar{\boldsymbol{q}}, \dot{\bar{\boldsymbol{q}}}), \boldsymbol{\zeta}(\bar{\boldsymbol{q}})$ represent inertia, Coriolis/centrifugal, and gravity terms in the new coordinate system. This coordinate transformation is valid since the Jacobian matrix $\bar{\boldsymbol{J}}$ is invertible for angle q_2 which can be experienced in the real setup, e.g., the SAM. From (4.10), damping can be artificially injected by letting:

$$\bar{\boldsymbol{w}}_b = \begin{bmatrix} f_b^{des} \\ \tau_b^{des} \end{bmatrix} = \begin{bmatrix} -K_v v_b \\ -K_\omega \omega_b \end{bmatrix}, \tag{4.11}$$

where K_v, K_ω are positive control gains. Using (4.11), the control goal addressed earlier can be achieved.

However, this control law cannot be directly applied because we have no measurements for v_b, whereas w_b is directly obtained by IMU sensor. Assuming small angle for q_2 (hence, $\cos(q_2) \approx 1$) in (4.9), f_b^{des} can be approximated as:

$$f_b^{des} = -K_v(l_1\dot{q}_1 + l_2\omega_b).$$

As addressed in subsection 4.2.3, $\dot{q}_1$ is dominated by slow oscillation motion with a low-frequency mode while $\omega_b = \dot{q}_1 + \dot{q}_2$ contains both modes. Therefore, using the frequency separation technique [Kuo and Puvvala, 2006, Sakata et al., 2013], we can extract $\dot{q}_1$ from $\omega_b = \dot{\theta}$ by applying a low-pass filter (LPF) to the signal, i.e., $\hat{\dot{q}}_1 \approx \omega_b^{lpf}$, where $\hat{(.)}$ is the estimation of parameter $(.)$. Then, (4.11) can be rewritten as follows:

$$\bar{\boldsymbol{w}}_b^{des} = \begin{bmatrix} f_b^{des} \\ \tau_b^{des} \end{bmatrix} = \begin{bmatrix} -K_v(l_1\omega_b^{lpf} + l_2\omega_b) \\ -K_\omega\omega_b \end{bmatrix}, ewi \tag{4.12}$$

where

$$\omega_b^{lpf} = \frac{1}{\tau s + 1}\omega_b$$

is the ω_b processed through the first-order LPF with the time constant τ. The time constant for the low-pass filter can be calculated as $\tau = \frac{1}{2\pi\nu_{cutoff}}$ based on the cut-off frequency ν_{cutoff}[Hz]. In our control design, the cut-off frequency of the LPF is selected in the middle between slow and high frequency modes, i.e.,

$$\nu_{cutoff} = \frac{\nu_{slow} + \nu_{fast}}{2}. \tag{4.13}$$

Let us extend the presented control law to the original system (4.7) as follows:

$$\tilde{\boldsymbol{w}}_b = \begin{bmatrix} \tilde{\boldsymbol{f}}_b \\ \tilde{\boldsymbol{\tau}}_b \end{bmatrix} = -\underbrace{\begin{bmatrix} \boldsymbol{K}_v & \boldsymbol{0} \\ \boldsymbol{0} & \boldsymbol{K}_\omega \end{bmatrix}}_{\boldsymbol{F}} \tilde{\boldsymbol{V}}_b = \begin{bmatrix} -\boldsymbol{K}_v(l_1\tilde{\boldsymbol{\omega}}_b^{lpf} + l_2\tilde{\boldsymbol{\omega}}_b) \\ -\boldsymbol{K}_\omega\tilde{\boldsymbol{\omega}}_b \end{bmatrix}. \tag{4.14}$$

Here, $\boldsymbol{K}_v$ and $\boldsymbol{K}_\omega$ are diagonal positive definite gain matrices.

The presented control approach is shown in Figure 4-4. It is interesting to notice that the controller does not contain a gravity compensation because the gravity works toward the control goal, i.e., stabilization around the operational point.

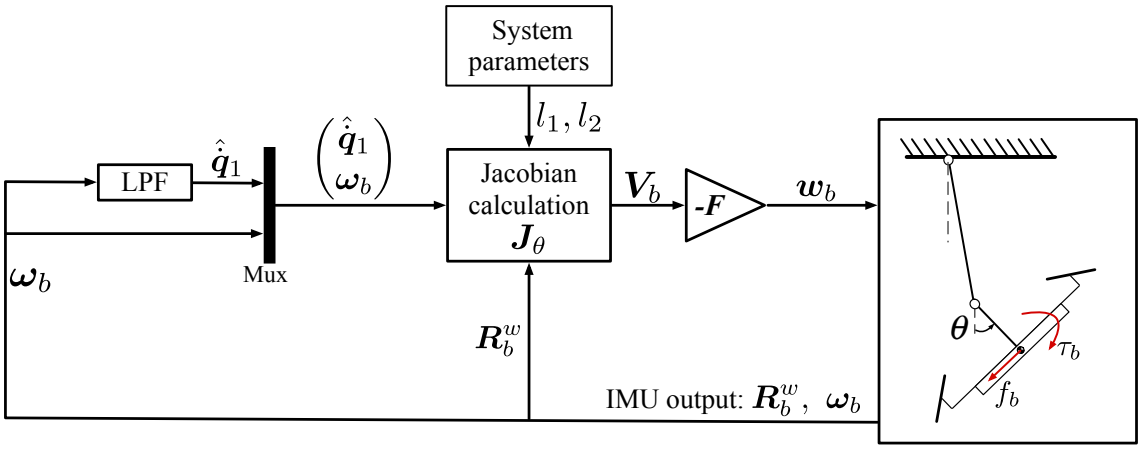

Figure 4-4: Oscillation damping control diagram.

4.3.4 Stability analysis

Let us select the total energy of the system (4.7) as the Lyapunov function candidate:

$$V = \mathcal{T}(\tilde{\boldsymbol{q}}, \dot{\tilde{\boldsymbol{q}}}) + \mathcal{U}(\tilde{\boldsymbol{q}}) = \frac{1}{2}\dot{\tilde{\boldsymbol{q}}}^T \tilde{\boldsymbol{M}}(\tilde{\boldsymbol{q}})\dot{\tilde{\boldsymbol{q}}} + \sum_{i=1}^{2} \boldsymbol{g}^T \boldsymbol{r}_i(\tilde{\boldsymbol{q}}) m_i,$$

where $\boldsymbol{g} = [0,\ 0,\ g]^T$ is the vector giving the direction of the gravitational acceleration $g = 9.81\frac{m}{s^2}$ in the world frame and the vector $\boldsymbol{r}_i$ gives the coordinates of the COM of $i-$th pendulum weight. Derivation of the inertia tensor $\tilde{\boldsymbol{M}}(\tilde{\boldsymbol{q}})$ and $\boldsymbol{r}_i(\tilde{\boldsymbol{q}})$ is shown in Appendix B.

It can be seen that V is a positive definite function, derivative of which with respect to time is defined as:

$$\dot{V} = \frac{1}{2}(\ddot{\tilde{\boldsymbol{q}}}^T \tilde{\boldsymbol{M}}(\tilde{\boldsymbol{q}})\dot{\tilde{\boldsymbol{q}}} + \dot{\tilde{\boldsymbol{q}}}^T \dot{\tilde{\boldsymbol{M}}}(\tilde{\boldsymbol{q}})\dot{\tilde{\boldsymbol{q}}} + \dot{\tilde{\boldsymbol{q}}}^T \tilde{\boldsymbol{M}}(\tilde{\boldsymbol{q}})\ddot{\tilde{\boldsymbol{q}}}) + \tilde{\boldsymbol{g}}^T(\tilde{\boldsymbol{q}})\dot{\tilde{\boldsymbol{q}}}. \tag{4.15}$$

Extracting $\ddot{\tilde{\boldsymbol{q}}}$ from (4.7) and inserting it into (4.15), we receive the following:

$$\begin{aligned}\dot{V} &= \dot{\tilde{\boldsymbol{q}}}^T \tilde{\boldsymbol{M}}(\tilde{\boldsymbol{q}})\tilde{\boldsymbol{M}}(\tilde{\boldsymbol{q}})^{-1}(\tilde{\boldsymbol{J}}^{\boldsymbol{T}}\tilde{\boldsymbol{w}}_{\boldsymbol{b}} - \tilde{\boldsymbol{C}}(\tilde{\boldsymbol{q}}, \dot{\tilde{\boldsymbol{q}}})\dot{\tilde{\boldsymbol{q}}} - \tilde{\boldsymbol{g}}(\tilde{\boldsymbol{q}})) + \frac{1}{2}\dot{\tilde{\boldsymbol{q}}}^T \dot{\tilde{\boldsymbol{M}}}(\tilde{\boldsymbol{q}})\dot{\tilde{\boldsymbol{q}}} + \tilde{\boldsymbol{g}}^T(\tilde{\boldsymbol{q}})\dot{\tilde{\boldsymbol{q}}} \\ &= \dot{\tilde{\boldsymbol{q}}}^T(\tilde{\boldsymbol{J}}^{\boldsymbol{T}}\tilde{\boldsymbol{w}}_{\boldsymbol{b}} - \tilde{\boldsymbol{g}}(\tilde{\boldsymbol{q}})) + \frac{1}{2}\dot{\tilde{\boldsymbol{q}}}^T(\dot{\tilde{\boldsymbol{M}}}(\tilde{\boldsymbol{q}}) - 2\tilde{\boldsymbol{C}}(\tilde{\boldsymbol{q}}, \dot{\tilde{\boldsymbol{q}}}))\dot{\tilde{\boldsymbol{q}}} + \tilde{\boldsymbol{g}}^T(\tilde{\boldsymbol{q}})\dot{\tilde{\boldsymbol{q}}}.\end{aligned} \tag{4.16}$$

Due to passivity property that implies a skew-symmetry nature of $\dot{\tilde{\boldsymbol{M}}}(\tilde{\boldsymbol{q}}) - 2\tilde{\boldsymbol{C}}(\tilde{\boldsymbol{q}}, \dot{\tilde{\boldsymbol{q}}})$ [Murray, 1994], (4.16) can be rewritten as follows:

$$\dot{V} = \dot{\tilde{\boldsymbol{q}}}^T \tilde{\boldsymbol{J}}^{\boldsymbol{T}} \tilde{\boldsymbol{w}}_{\boldsymbol{b}} = -\dot{\tilde{\boldsymbol{q}}}^T \tilde{\boldsymbol{J}}^T \boldsymbol{F} \tilde{\boldsymbol{J}} \dot{\tilde{\boldsymbol{q}}} = -\dot{\tilde{\boldsymbol{q}}}^T \boldsymbol{F}_q \dot{\tilde{\boldsymbol{q}}}.$$

Since the control gain matrix $\boldsymbol{F}_q$ scaled to the joint space is diagonal positive definite, the $\dot{V}$ is negative semi-definite. Therefore, the system is locally stable at the equilibrium point. Let us notice that $\dot{V} = 0$ only at the origin $\dot{\tilde{\boldsymbol{q}}} = 0, \tilde{\boldsymbol{q}} = 0$. Thus, by invoking the LaSalle's invariance principle [Khalil, 2014], global asymptotic stability of the equilibrium point is followed.

As shown, the spherical double pendulum system with artificially injected damping in joints is asymptotically stable. This statement is true for the general case. However, the phase-lag introduced by LPF might compromise the passivity and induce the instability to the system with a feedback. In order to validate that introduced time delay does not penalize strongly the damping performance, additionally, we have numerically investigated the stability of our controller in a simulator. We report that for the $l_1 = 4..10$[m] while changing the initial angles of the passive joints from 2 till 45 degrees in arbitrary configuration with a step of 7 degrees, the closed-loop system is always stable. Moreover, initial angular velocities at these joints were varied from 0 to 1 $\frac{\text{rad}}{\text{s}}$ with a step of 0.5. The performed analysis also confirms that the proposed controller is robust against model uncertainties.

4.3.5 Gain tuning rule

Since the system is stable for (almost) any choice of parameters and gains, it is important to seek the best gain in some sense. In particular, we seek for the control gains which minimize the following linear quadratic cost function:

$$J = \int_0^t \left(\boldsymbol{X}(t)^T \boldsymbol{Q} \boldsymbol{X}(t) + \boldsymbol{U}(t)^T \boldsymbol{R} \boldsymbol{U}(t) \right) \, dt, \tag{4.17}$$

where weighting matrix $\boldsymbol{Q} \geq \boldsymbol{0}$ penalizes the state $\boldsymbol{X}$, and weighting matrix $\boldsymbol{R} > \boldsymbol{0}$ penalizes the amount of control input $\boldsymbol{U}$.

In this subsection, we again use the planar double pendulum for simplicity. Let us first linearize (4.8) around operational point as follows:

$$\dot{\boldsymbol{X}} = \boldsymbol{A}\boldsymbol{X} + \boldsymbol{B}\boldsymbol{U}, \tag{4.18}$$

where the state is $\boldsymbol{X} = [q_1,\ \dot{q}_1,\ \theta,\ \omega_b,\ \omega_b^{lpf}]^T$ and state and input matrices[2] are:

[2]It is worth mentioning that in 3D case the linearized system can be modeled as two decoupled planar pendulums each of which can be described by similar matrices $\boldsymbol{A}$ and $\boldsymbol{B}$.

$$\boldsymbol{A} = \begin{bmatrix} 0 & 1 & 0 & 0 & 0 \\ -\dfrac{g(m_1+m_2)}{m_1 l_1} & 0 & \dfrac{m_2 g}{m_1 l_1} & 0 & 0 \\ 0 & 0 & 0 & 1 & 0 \\ \dfrac{g(m_1+m_2)}{m_1 l_2} & 0 & -\dfrac{g(m_1+m_2)}{m_1 l_2} & 0 & 0 \\ 0 & 0 & 0 & \dfrac{1}{\tau} & -\dfrac{1}{\tau} \end{bmatrix}, \quad \boldsymbol{B} = \begin{bmatrix} 0 & 0 \\ 0 & -\dfrac{1}{m_1 l_1 l_2} \\ 0 & 0 \\ \dfrac{1}{m_2 l_2} & \dfrac{(m_1+m_2)}{m_1 m_2 l_2^2} \\ 0 & 0 \end{bmatrix}.$$

The last row of matrix $\boldsymbol{A}$ corresponds to the dynamics of the low-pass filter:

$$\tau \dot{\omega}_b^{lpf} + \omega_b^{lpf} = \omega_b.$$

To express the control input (4.12) in an output feedback form, we define output as follows:

$$\boldsymbol{Y} = \boldsymbol{C}\boldsymbol{X}, \tag{4.19}$$

where

$$\boldsymbol{C} = \begin{bmatrix} 0 & 0 & 0 & l_2 & l_1 \\ 0 & 0 & 0 & 1 & 0 \end{bmatrix}.$$

Consequently, the control input $\boldsymbol{U}$ is presented as the output feedback form:

$$\boldsymbol{U} = -\boldsymbol{F}\boldsymbol{Y} = -\begin{bmatrix} K_v & 0 \\ 0 & K_\omega \end{bmatrix} \boldsymbol{Y}. \tag{4.20}$$

For our system described by (4.18)-(4.19), we apply the output feedback Linear Quadratic Regulator (ofLQR) technique, which can be formulated using linear matrix inequalities (LMIs). Quadratic stability criteria of ofLQR [Kučera and De Souza, 1995, Veselỳ, 2001, 2002] are defined directly in terms of LMIs.

Theorem 1. *Let us consider the system (4.18) with the output (4.19). There exists an optimal controller in the form of (4.20) which minimizes the cost function (4.17), if the following problem has a solution for the given matrix* $\boldsymbol{\Xi} > \boldsymbol{0}$ *and weighting matrices* $\boldsymbol{Q} \geq \boldsymbol{0}$, $\boldsymbol{R} > \boldsymbol{0}$*:*

$$\min_{\boldsymbol{F},\boldsymbol{P}} trace(\boldsymbol{P})$$

subject to LMIs:

$$\boldsymbol{M} \leq 0, \quad \boldsymbol{P} > 0,$$

where

$$\boldsymbol{M} = \begin{bmatrix} \boldsymbol{A}^T\boldsymbol{P} + \boldsymbol{P}\boldsymbol{A} + \boldsymbol{Q} + \boldsymbol{H} & \boldsymbol{G}^T \\ \boldsymbol{G} & -\boldsymbol{R}^{-1} \end{bmatrix},$$

with

$$\begin{aligned} \boldsymbol{G} =& \boldsymbol{F}\boldsymbol{C} - \boldsymbol{R}^{-1}\boldsymbol{B}^T\boldsymbol{P}, \\ \boldsymbol{H} =& -(\boldsymbol{\Xi}\boldsymbol{B})\boldsymbol{R}^{-1}(\boldsymbol{B}^T\boldsymbol{P}) - (\boldsymbol{P}\boldsymbol{B})\boldsymbol{R}^{-1}(\boldsymbol{B}^T\boldsymbol{\Xi}) \\ & + (\boldsymbol{\Xi}\boldsymbol{B})\boldsymbol{R}^{-1}(\boldsymbol{B}^T\boldsymbol{\Xi}). \end{aligned}$$

To solve the given LMI problem, we used ofLQR library [Ilka, 2018] with the LMI solver in YALMIP [Löfberg, 2004]. Such a controller guarantees the robust closed-loop stability (quadratic stability) and minimizes the quadratic cost function [Amato, 2006, Lewis et al., 2012, Veselỳ, 2006]. Moreover, the stability is provided by checking the eigenvalues of the closed-loop system. In our control design, we selected $\boldsymbol{Q}$ and $\boldsymbol{R}$ matrices as follows:

$$\boldsymbol{Q} = diag\{0, 10, 0, 1, 0\} \text{ and } \boldsymbol{R} = \sigma \cdot diag\{1, 10\}. \tag{4.21}$$

Since our control goal is to dampen the oscillations, we penalized only $\dot{q}_1$ and ω_b. Moreover, we applied stronger control action on slow oscillation mode, which might be more critical when performing manipulation tasks in a real industrial scenario. For this reason, we penalized $\dot{q}_1$ more than ω_b in $\boldsymbol{Q}$, and allowed more control input for f_b in $\boldsymbol{R}$ design.

In (4.21), σ is a new parameter that allows us to investigate the optimal control gains over admissible control inputs; note that smaller $\boldsymbol{R}$ implies more considerable control input. Therefore, we solved the optimization problem with varying σ: from $1e^{-6}$ to $8e{-}5$, as shown in Figure 4-5. Depending on the designer's choice (balance between oscillation damping and power consumption), we can select one proper combination of gains. It might be useful to consider the rotor group saturation at the specific system as one of the criteria for the σ selection so we do not command too high wrench. Another beneficial criterion might be the proximity of the obstacles in

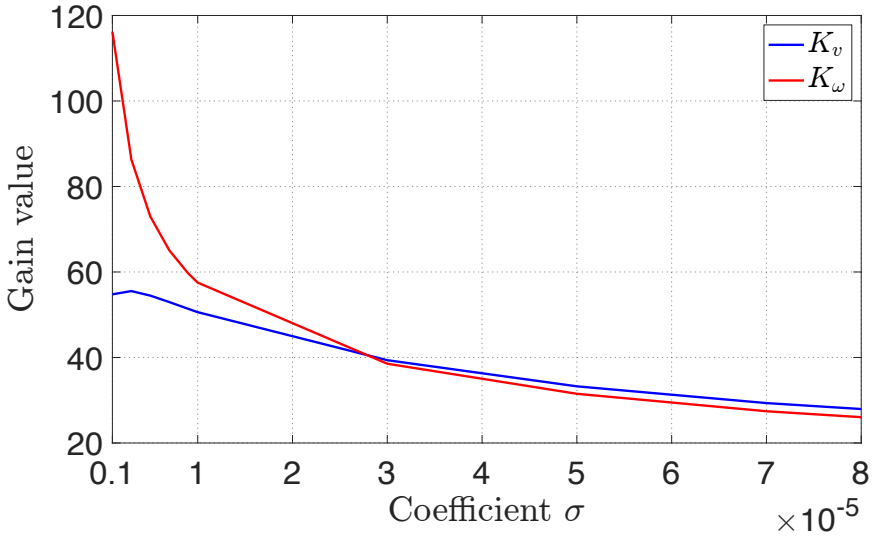

Figure 4-5: Relation between optimal control gains K_v, K_ω and parameter σ.

the environment. The deep investigation on strategies for the σ selection is beyond the scope of this thesis.

Optimization was conducted using parameters measured for the real system:

$$m_1 = 18.5\ [kg],\quad m_2 = 55\ [kg],\quad l_1 = 6\ [m],\quad l_2 = 2.2\ [m]. \tag{4.22}$$

The cut-off frequency $\nu_{cutoff} = 0.4499$ Hz was estimated by utilizing (4.13) for obtained $\nu_{slow} = 0.1665$ Hz and $\nu_{fast} = 0.7334$ Hz using FFT applied to the platform angular velocity ω_b for simulation data, see Figure 4-6.

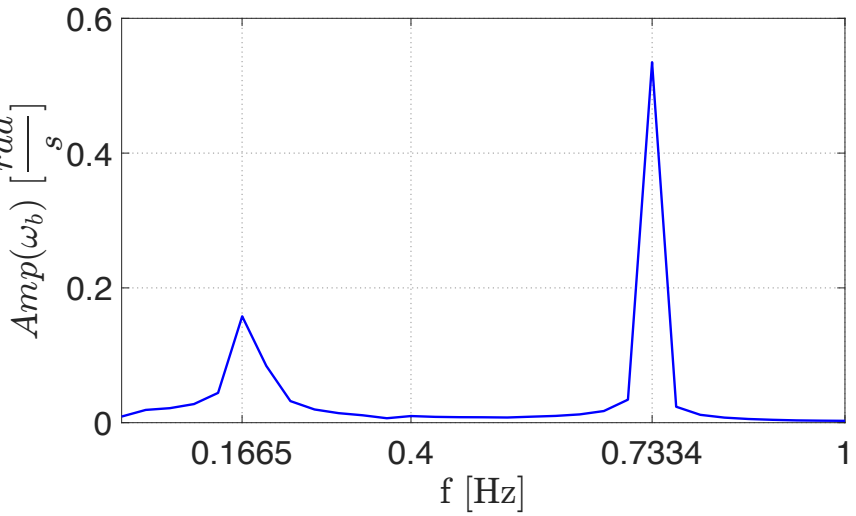

Figure 4-6: Single-sided amplitude spectrum of the platform angular velocity. Amp stands for Amplitude.

4.3.5.1 Pendulum link length variation

In real applications, it is essential to change the length of the crane's chain during the operation, e.g., to overcome the obstacles. That is why it is important to analyze the gain evolution over the different lengths of the first link. To this end, the optimization was conducted for the arbitrarily selected $\sigma = 1e^{-5}$, weight matrices as in (4.21), and $l_1 = \{1,\ 2,\ 4,\ 6,\ 8,\ 10\}$, see Figure 4-7. As we can see, the optimal gain K_v changes within a reasonable range regardless of the length l_1, while the gain K_ω increases dramatically for the short length of the first link. It might be explained by decreased contribution of the q^{fast} term in (4.5) when $l_1 \approx l_2$.

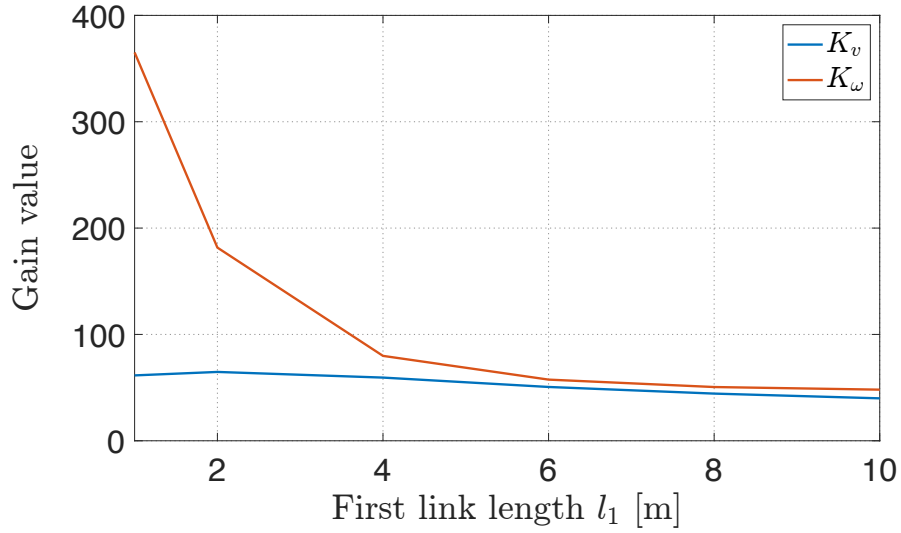

Figure 4-7: Relation between optimal control gains K_v, K_ω and first link length l_1 for the $\sigma = 1e^{-5}$.

As we discussed in subsection 4.2.3, when the length of the crane's chain is equal to the distance from the hook to the platform, the system demonstrates a single pendulum behavior. Such behavior provides us with a significant advantage of being able to estimate the full system state by utilizing onboard IMU. Thus, it is essential to introduce a separated controller for such a case, see Appendix C.

4.3.6 Simulation studies

Extensive simulation studies were conducted to validate the proposed control approach performance. The suspended aerial manipulator was modeled as a double pendulum with parameters chosen to be as close as possible to the real setup given in (4.22). In addition, gyro noise density 0.009 $[\frac{^\circ}{s}/\sqrt{Hz}]$ from the calibration certificate of IMU was introduced in simulation. The optimal control gains were selected

from Figure 4-5 for the $\sigma = 5e^{-6}$ as $K_v = 54.47$ and $K_\omega = 72.98$. The influence of unmodeled dynamics (e.g., the weight of the link), airflow, and actuator dynamics was not considered in the simulation. In the scope of the simulation, the σ was selected to provide high control gains, and, consequently, to decrease convergence time.

Several different numerical simulations were studied and performed in the MathWorks MATLAB Simulink (MATLAB Simulink) utilizing Luca Dynamics environment (subsection 2.1.4).

4.3.6.1 Planar double pendulum

First, we tested controller at the planar double pendulum model with rigid links. Initial conditions for the system state were selected as $\bar{\boldsymbol{q}} = [\frac{\pi}{25},\ \frac{\pi}{20}]^T$ and $\dot{\bar{\boldsymbol{q}}} = [0,\ 0]^T$, and actuators were not saturated by any limits.

The behavior of the undamped (free)[3] double pendulum is shown in Figure 4-8a. The corresponding joint parameters are presented in Figure 4-9a and Figure 4-9b. It can be seen that joint angles contain two modes, but as we mentioned before, the low frequency motion dominates in q_1, while the high frequency motion has a strong effect on q_2. The θ angle contains both motions with approximately equal influence.

The behavior of the planar double pendulum with non-zero initial conditions under the proposed controller with optimal gains is shown in Figure 4-8b. Simulational results are presented in Figure 4-9c and Figure 4-9d. The gravitational field applied to the platform (second pendulum weight) forces the q_1 angle of the hook deflection to slightly increase in the beginning for the given initial conditions. After that, the platform quickly converges to its equilibrium point, so the system behaves as a damped double pendulum. The corresponding control torques applied to the pendulum joints are presented in Figure 4-10. The generated control torque is based on the angular velocities with added high-frequency IMU noise. It can be seen that it does not affect the stability of the system.

Let us calculate the required planar wrench corresponding to the resulted maximum torques. As can be seen in Figure 4-9 and Figure 4-10, at $t = 0.285\ s$ the $\tau_1 = 1172.62\ Nm$, $\tau_2 = 332.42\ Nm$, and $q_2 = 4.62$ degrees. The planar wrench can be expressed from (2.4) after calculating the Jacobian matrix (4.9) as $\bar{\boldsymbol{w}}_b = \begin{bmatrix} 140.48 & N \\ 23.35 & Nm \end{bmatrix}$. As we can see in Figure 3-14, the calculated wrench is reachable

[3]The model contained very small internal damping.

(a) Main postures of the free double pendulum

(b) Main postures of the damped double pendulum under the proposed controller

Figure 4-8: The behavior of the planar double pendulum modeled in the Luca Dynamics environment.

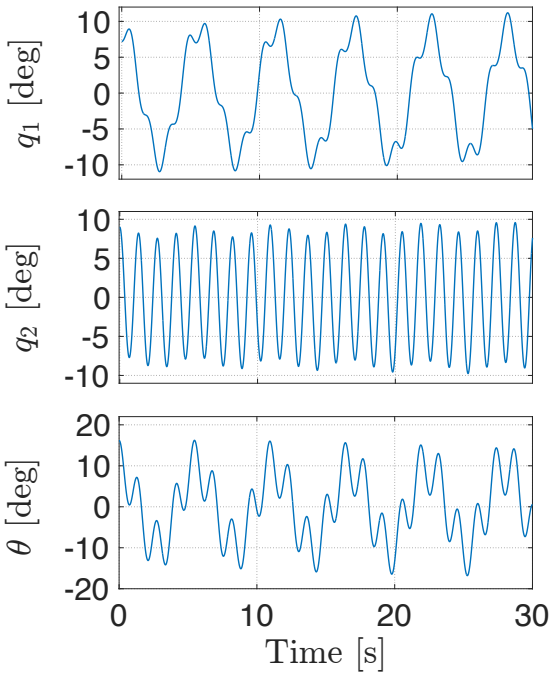

(a) Joint angles (Undamped case)

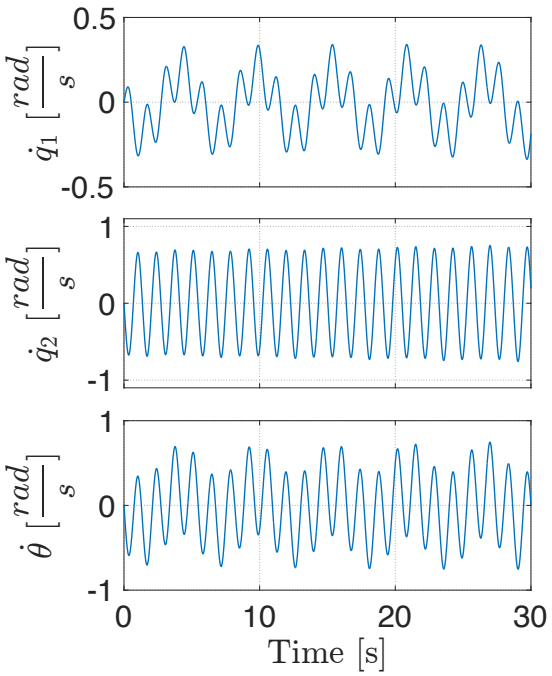

(b) Joint velocities (Undamped case)

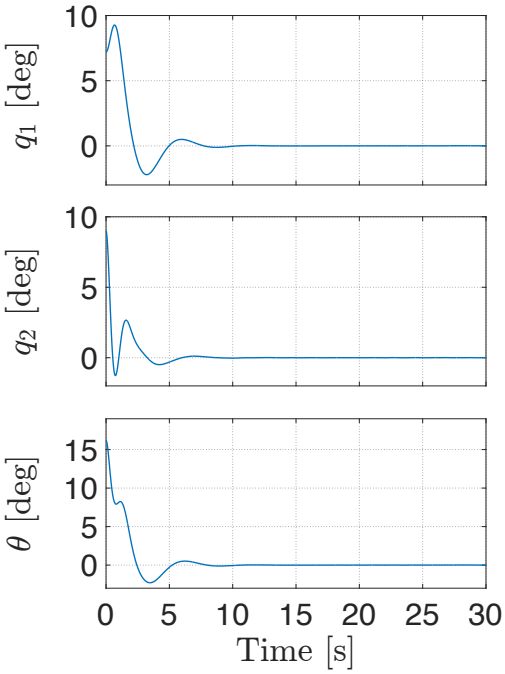

(c) Joint angles (Damped case)

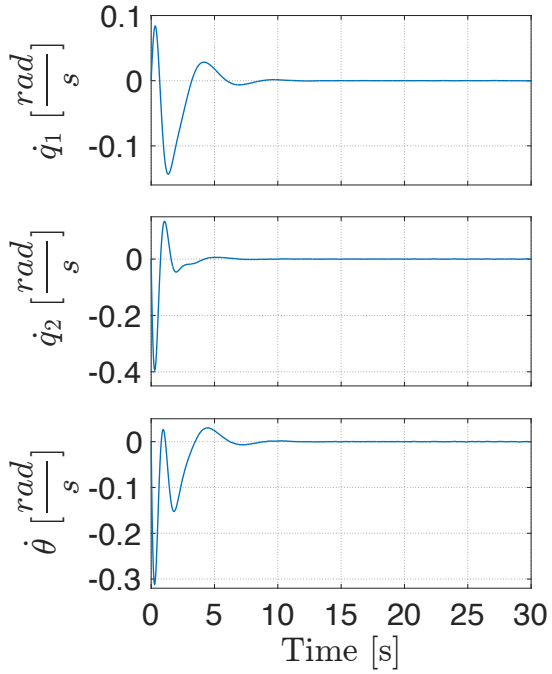

(d) Joint velocities (Damped case)

Figure 4-9: Joint angles and velocities of the planar double pendulum.

by the SAM platform presented in chapter 3.

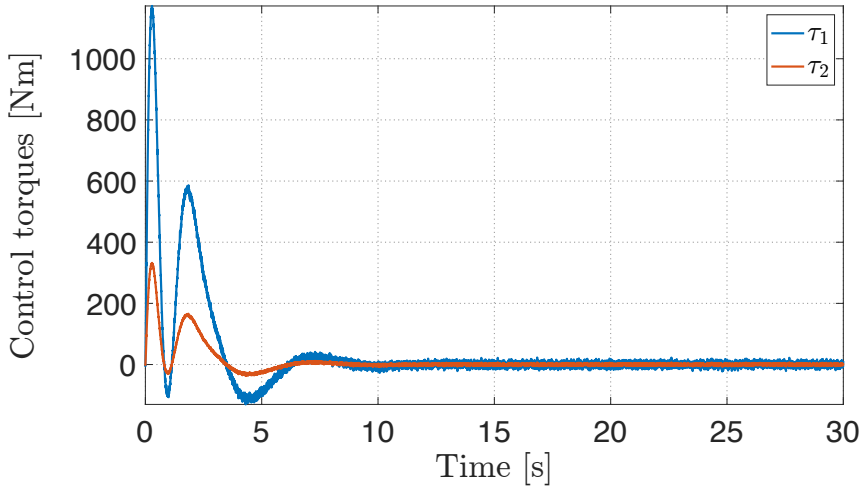

Figure 4-10: Dampening torques in the planar double pendulum joints.

4.3.6.2 Cable-suspended aerial manipulator equipped with the robotic arm

Additionally, the behavior of the real system equipped with 7-DOF robotic arm in 3D space under the proposed controller with optimal gains has been studied through the validation simulation. The suspension was modeled as a spherical double pendulum. The first spherical joint is modeled by three rotational DOFs in $\mathcal{RPY}$ sequence, and the second one - by $\mathcal{YPR}$. Since we designed the oscillation damping controller with the decentralized control approach (subsection 4.3.2), we investigate its performance under various external disturbances such as oscillations caused by non-zero initial angles and robotic arm motion. To this end, the system starts with non-zero pendulum conditions, while the robotic arm is placed in the parking configuration. After 10 seconds (when stabilization is fully finished), the system experiences the jerky maneuver performed by the robotic arm. Namely, it moves from the parking configuration to the stretched one as defined in subsubsection 3.3.1.2. At the 12-th second after starting, the arm goes back to the parking position, see Figure 4-11. In addition, during the whole operation, the desired yaw angle is set to be 25 degrees. The initial configuration of the system is described by zero velocities and $[\boldsymbol{q}_1,\ \boldsymbol{q}_2]^T = [0,\ pi/12,\ 0,\ 0,\ -pi/21,\ 0]^T$ for the pendulum joints and parking configuration for the robotic arm.

Simulation results are presented in Figure 4-12 and Figure 4-13. It can be seen that the proposed controller successfully dissipated the oscillations caused by releasing from non-zero initial conditions within 6.7 seconds and by the jerky motion of the robotic arm within 1.5 seconds. The desired yaw was reached gradually within

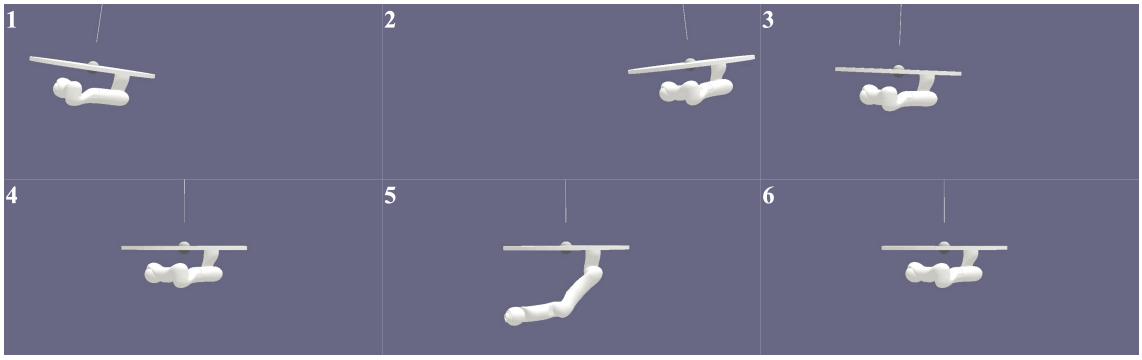

Figure 4-11: Illustration of the validation simulation. Here, at **1** double pendulum starts to move from non-zero initial conditions, at **2** it reaches the maximum negative oscillation displacement, at $\mathbf{3}-\mathbf{4}$ it comes to the equilibrium point, at **5** is the 10-th second of simulation when arm performs the jerky motion by placing in the stretched configuration, at **6** is the 13.5-th second of simulation when the arm comes back to the parking configuration.

12 seconds with poorly tuned control gains. It is worth mentioning here that initial configuration angles of the pendulum were selected twice higher than expected in normal operational condition, and maximum robotic arm joint velocity in the

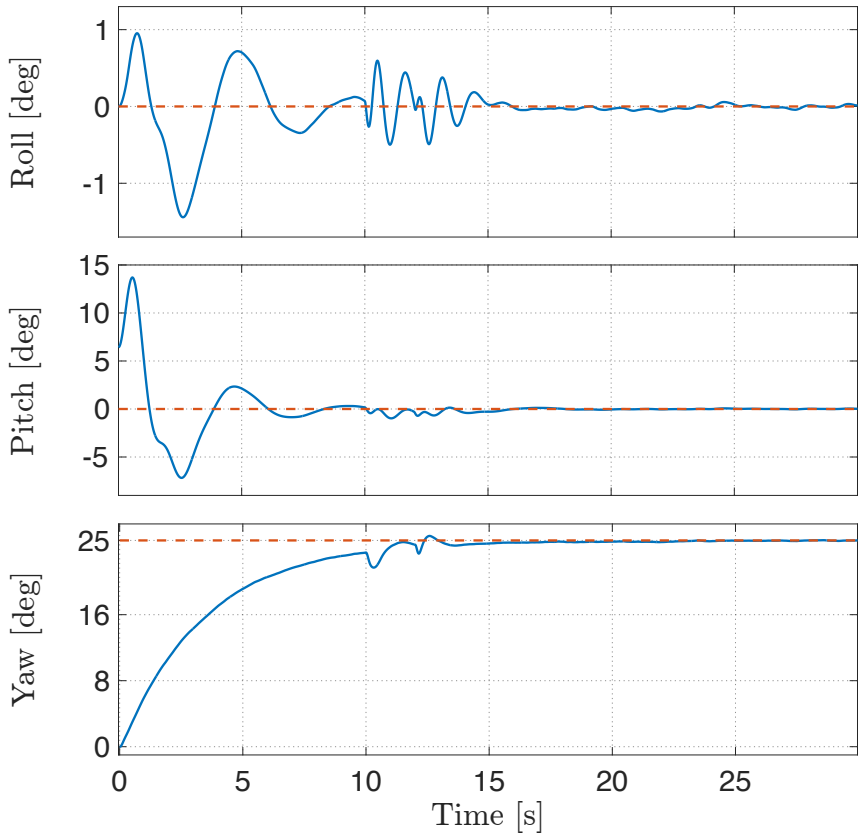

Figure 4-12: Results of the validation simulation. Platform orientation angles (virtual onboard IMU data).

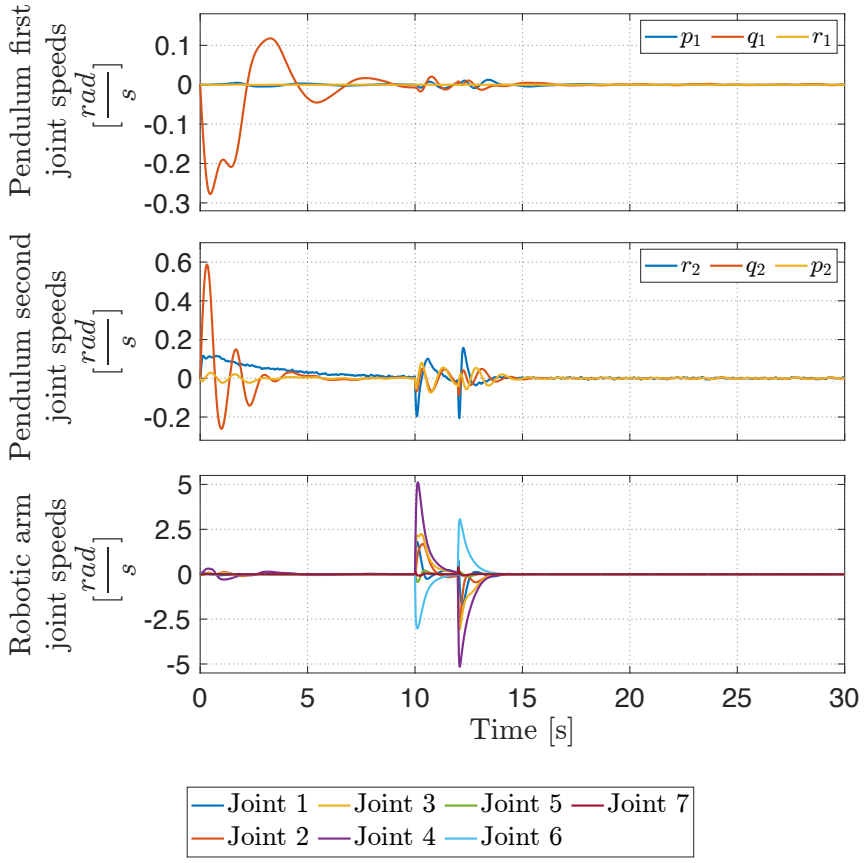

Figure 4-13: System joint velocities during the validation simulation.

simulation equals to the 5 $\frac{\text{rad}}{\text{s}}$, while for the real robot it reaches a value of 3 $\frac{\text{rad}}{\text{s}}$ only in extreme conditions. So, simulation conditions can be considered as tough in comparison with a real mission.

At the second step, we compared the proposed control law (4.14), and the "*ideal*" controller defined as:

$$\boldsymbol{w}_b^{des} = \begin{bmatrix} \boldsymbol{f}_b^{des} \\ \boldsymbol{\tau}_b^{des} \end{bmatrix} = \begin{bmatrix} -K_v \boldsymbol{v}_b \\ -K_\omega \boldsymbol{w}_b \end{bmatrix},$$

which is the 3D version of (4.11). By "ideal", we call the controller, which has access to the full state of the system. Recall that we proposed (4.14) because $\boldsymbol{v}_b$ is not measurable for the real system. As shown in Figure 4-14, overall shapes of resulting behavior were quite similar for both controllers. In fact, the proposed controller resulted in fewer oscillations than the ideal one due to the effect of filters. At $t = 10$, the robotic arm was commanded to cause jerky motions to generate some disturbances on the platform. The simulation results validate that the proposed control dissipates the oscillations caused by the dynamic disturbances.

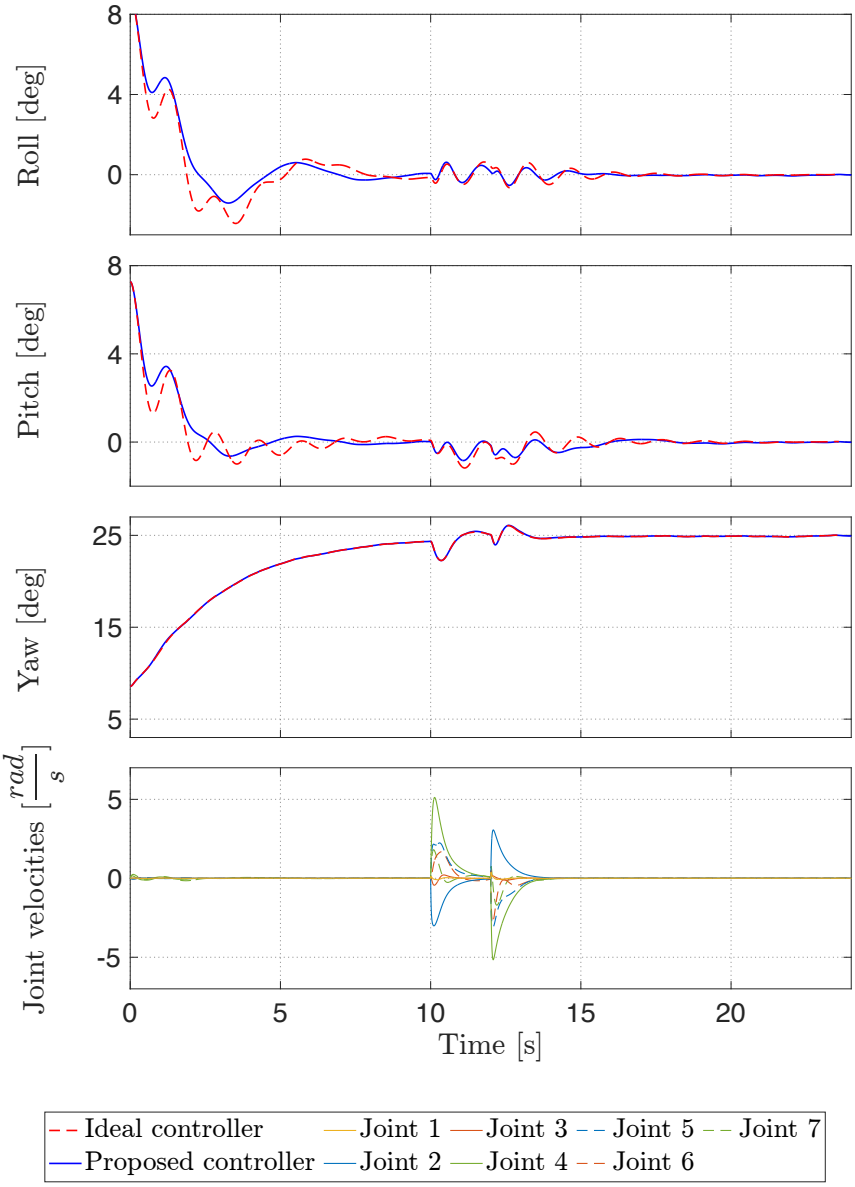

Figure 4-14: Comparison of the proposed (blue) and "ideal" (red) controllers.

"Nothing in life is to be feared, it is only to be understood. Now is the time to understand more, so that we may fear less."

Marie Curie

Chapter 5

Hierarchical whole-body control with the winch-based actuation and kinematically redundant manipulator

5.1 Problem statement

During the operation, the cable-suspended aerial manipulator encounters two types of disturbances: dynamic and static. As was shown in the previous chapter, the former might be effectively compensated by the short-term actions produced by the propeller-based actuation, while the latter requires a constant long-term impact that cannot be generated by the rotor groups because of the possible overheating. Most common examples of static disturbances in aerial manipulation include the displacement of the system COM because of the robotic arm motion and external wrench applied to the system during the interaction with the environment. In fact, the static disturbances negatively affect manipulation performance by perturbating the base dynamics and, consequently, the IMU measurements and onboard vision camera's field of view.

To this end, to further enhance the manipulation and stabilization performance of the SAM, the second actuation system, winch-based actuation, is integrated into the considered system. Three rigging cables are connecting the SAM platform to the hook of the crane. Winch-based actuation inherited from the cable-driven robotics [Begey et al., 2018, Bosscher et al., 2006, Kraus et al., 2014] allows to slowly change the length of these cables affecting the tension force distribution and, consequently, the SAM pose relative to the hook. The exploitation of two actuation systems should

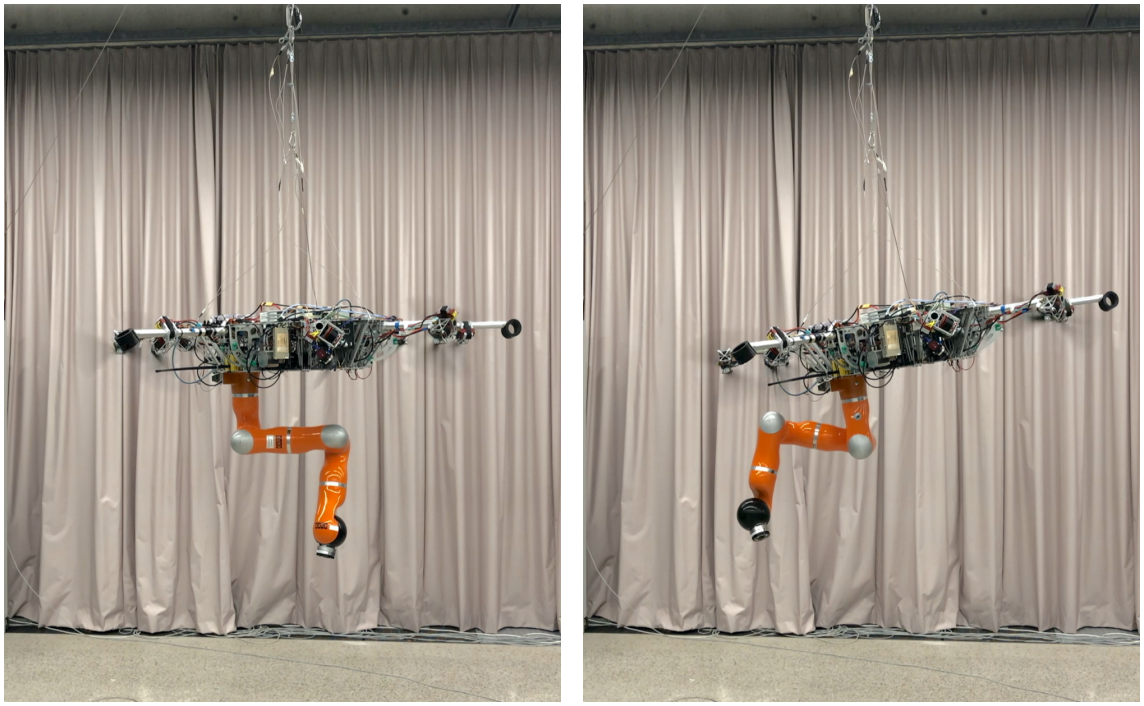

(a) The platform keeps close to the horizontal orientation

(b) The platform tilts because of the shifted robotic arm weight

Figure 5-1: The behavior of the SAM while manipulating below the platform (left) and on the side (right).

reduce the amount of the consuming energy.

In the scope of this chapter, we investigate a winch-based actuation utilized to compensate for the static gravitational torque caused by the weight of the robotic manipulator, see Figure 5-1. During the operation below the platform, the system COM is located close to the vertical axis, passing through the suspension point. However, whenever the robotic arm manipulates on the side of the platform, the shifted system COM generates the strong gravitational torque resulting in the platform tilt.

The main challenges for the winch-based actuation utilization include complex modeling of closed-chain dynamics [Freitas et al., 2011, McGrath et al., 2017, Murray and Lovell, 1989] and mixed actuation in terms of control input: winch servos are position controlled, while the robotic arm is torque controlled. To this end, modeling is performed in terms of the equal quasi-joint dynamics directly representing the translational motion of the platform and robotic arm joints. Also, an admittance interface is used for the winch servos to transform control torques to position commands. Moreover, as will be shown below, the system under investigation is redundant. Therefore, it is decided to adapt a hierarchical whole-body controller

aimed at two main control tasks: to cope with static disturbances and to perform manipulation.

Therefore, the *main objective* of the chapter is to design a whole-body controller that compensates for the system COM displacement without degradation of manipulation performance by utilizing kinematically redundant robotic arm and winch-based actuation. The rest of the chapter is organized as follows. The section 5.2 shows a modeling process of the winch suspension integrated into the double pendulum and formulates the dynamics. The section 5.3 provides the adaptation of a hierarchical whole-body controller with an integrated admittance interface.

5.2 Winch suspension modeling

5.2.1 Modeling assumptions

In this section, we aim to derive the winch suspension model. Due to high system complexity, in addition to the list of previously defined assumptions in subsection 4.2.1, we adopt several more points:

- The winch-based actuation switches on only after the platform reaches the target point and the propeller-based actuation dissipates all oscillations. This assumption fully meets our operational strategy at which the static disturbances appear mainly during the robotic arm motion, i.e., during the manipulation process.
- The rigging cables controlled by winches are under tension, so they can be represented as massless rigid links without sagging (mass of each rigging cable is around 40-50 grams). Each tip of the cable is modeled as a rotational joint.
- The actuator dynamics is negligible, i.e., we assume an immediate winch servo response due to a high gain controller.

To gain better intuition behind the complex system, first, we investigate a planar case that can be further generalized to the 3D model.

5.2.2 Dynamic formulation

5.2.2.1 Coordinate frames

Let us introduce the following coordinate frames[1], see Figure 5-2:

- The world frame $\mathcal{F}_w$ centered in the suspension point O such that its vertical axis is opposite to downward gravity direction, and the horizontal axis is perpendicular to it.
- The hook frame $\mathcal{F}_h$ attached at point A represents a crane's chain swinging, i.e., rotational angle of the pendulum first link relative to the world frame, q_1. The vertical axis of this frame is aligned with the chain, and the horizontal axis complements it to the right-hand frame.
- The *platform frame* $\mathcal{F}_p$ is placed at the point C[2], which is located in the platform center. It is aligned with the principal platform axes.
- The *COM frame* $\mathcal{F}_{com}$ is located at the total system (platform and robotic arm) COM, at point G, i.e., the location of the frame origin changes over-time and depends on the configuration of the arm. Thus, for the double pendulum system without the integrated manipulator, the point G coincides with point C. The vertical axis of the frame is pointing towards rigging cable suspension point A, and the horizontal one is perpendicular to it. The *COM* frame represents the rotation of the pendulum's second link relative to the first one, q_2.

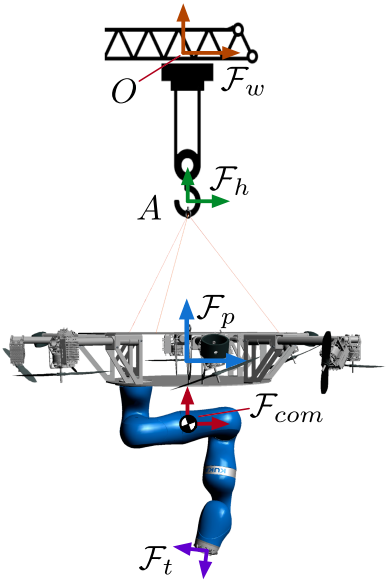

Figure 5-2: Reference frames depicted at the SAM.

- The *tool frame* $\mathcal{F}_t$: $\{F,\ x_t,\ y_t,\ z_t\}$ (or *end effector frame*) is attached to the manipulator end effector at point F. The point F is also named as tool center point (TCP). The orientation of the $\mathcal{F}_t$ is task dependent.

[1]The color of the font corresponds to the color of the frame in figures.

[2]It is worth noting that in chapter 4 we addressed this frame as the body frame since we dealt with a single body (platform) model. In this chapter, to avoid confusion and distinguish the "platform" and the "platform with the integrated robotic arm", we introduce the platform frame.

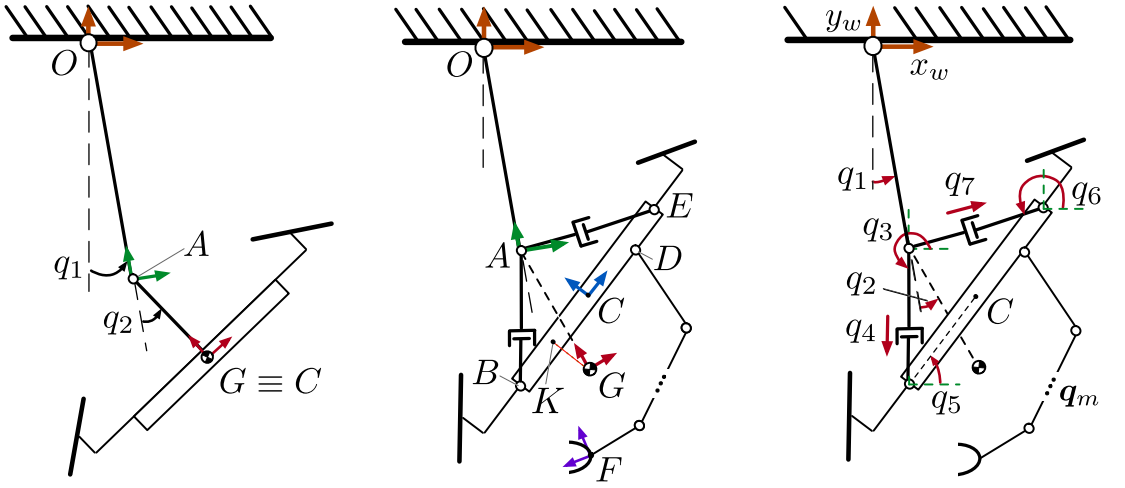

(a) Double pendulum model (b) Coordinate frames (c) Closed-chain coordinates

Figure 5-3: The winch suspension modeling.

5.2.2.2 Planar model

As we mentioned in the previous chapter, with fixed-length rigging cables the system can be represented as a double pendulum suspended to the crane jib's tip, O, see Figure 5-3a. The length of the first link, OA, is equal to the length of the chain, l_1. We assume that the weight of the hook, m_1, is concentrated at point A. The second link consists of two objects: the platform and the manipulator with masses m_p and m_m, respectively. Rigging cables of the winches correspond to AB and AE, see Figure 5-3b. The rigging cable lengths can be controlled and initially are equal to each other, l_0. The robotic arm is rigidly attached to the platform at point D.

Resulted system model contains a closed chain, see Figure 5-3c. The state of such a model can be described by the vector of *redundant generalized coordinates*:

$$\boldsymbol{q} = [q_1, \underbrace{q_3,\ q_4,\ q_5,\ q_6,\ q_7}_{\boldsymbol{q}^r_{winch}},\ \boldsymbol{q}_m]^T \in \mathbb{R}^{6+m}. \tag{5.1}$$

Here, $\boldsymbol{q}^r_{winch}$ is the vector of redundant winch joints containing passive revolute joints, q_3, q_5, q_6, representing the connectors of the rigging cables relative to the platform[3] and active prismatic joints, q_4 and q_7, corresponding to the rigging cable length. For the sake of readability, we imply that q_4 and q_7 include l_0 and represent the total current lengths of the rigging cable. Finally, $\boldsymbol{q}_m \in \mathbb{R}^m$ is the vector of the robotic arm joint angles. It is worth noting that q_2 is not a part of the state since it is a

[3]There is one more revolute joint q_8 that coincides with q_3, it can be easily eliminated from the state $\boldsymbol{q}$ by considering angle constraint of the closed-chain [Tang, 2010].

virtual quantity that might be computed based on the system state $\boldsymbol{q}$.

Since our model contains a closed chain ABE, the system dynamics is partially constrained. Applying Lagrangian formulation, equation of motion can be written as follows:

$$\hat{\boldsymbol{M}}(\boldsymbol{q})\ddot{\boldsymbol{q}} + \hat{\boldsymbol{C}}(\boldsymbol{q}, \dot{\boldsymbol{q}})\dot{\boldsymbol{q}} + \hat{\boldsymbol{g}}(\boldsymbol{q}) = \hat{\boldsymbol{\tau}} + \boldsymbol{A}^T\boldsymbol{\lambda} + \hat{\boldsymbol{\tau}}_{ext},$$
$$\boldsymbol{A}(\boldsymbol{q})\dot{\boldsymbol{q}} = 0,$$

where $\hat{\boldsymbol{M}}(\boldsymbol{q})$ is the symmetric and positive definite inertia matrix, $\hat{\boldsymbol{C}}(\boldsymbol{q}, \dot{\boldsymbol{q}})$ contains the centrifugal/Coriolis terms, $\hat{\boldsymbol{g}}(\boldsymbol{q})$ is the gravity vector, $\hat{\boldsymbol{\tau}} \in \mathbb{R}^{6+m}$ is the vector of the joint torques, $\hat{\boldsymbol{\tau}}_{ext} \in \mathbb{R}^{6+m}$ are external forces and torques. Let us denote by $n_w = 5$ a number of passive and active DOFs of the winch-related joints which cannot be controlled independently because of the $n_c = 2$ loop-closure constraints. Thus, there are only $n_p = n_w - n_c = 3$ DOFs along which platform can be moved by utilizing winch-based actuation. Then, $\boldsymbol{A} \in \mathbb{R}^{n_c \times 6+m}$ is the Pfaffian matrix which will be defined later, and $\boldsymbol{\lambda} \in \mathbb{R}^{n_c}$ are Lagrange multipliers that parametrize the interaction forces acting along the constraints.

In order to formulate holonomic constraints in the system dynamics, let us formulate a vector loop-closure equation which represents the forward kinematics of the point $C = [x_c,\ y_c]^T$ at which weight of the platform is concentrated as follows:

$$\begin{bmatrix} x_c \\ y_c \end{bmatrix} = \underbrace{OA + AB + BC}_{=f(q_1,\ q_3,\ q_4,\ q_5)} = \underbrace{OA + AE + EC}_{=f(q_1,\ q_5,\ q_6,\ q_7)}. \tag{5.2}$$

Projecting (5.2) on x_w and y_w axes of the world frame and taking its time-derivative, we can derive two constraints in the Pfaffian form:

$$\boldsymbol{A}(\boldsymbol{q})\dot{\boldsymbol{q}} = \boldsymbol{0}.$$

To resolve constraints and reduce the dimension of the state (5.1), we might apply a coordinate transformation. To this end, let us define a vector of constraint-consistent *independent generalized coordinates* as follows:

$$\boldsymbol{\delta} = [q_1,\ \underbrace{q_4,\ q_5,\ q_7}_{\boldsymbol{q}_{winch}},\ \boldsymbol{q}_m]^T \in \mathbb{R}^{4+m},$$

and a vector of dependent generalized coordinates as:

$$\boldsymbol{z} = [q_3,\ q_6]^T \in \mathbb{R}^2.$$

Then, the relation between $\dot{\boldsymbol{\delta}}$ and $\dot{\boldsymbol{q}}$ can be formulated as:

$$\dot{\boldsymbol{q}} = \boldsymbol{S}(\boldsymbol{q})\dot{\boldsymbol{\delta}}, \tag{5.3}$$

where $\boldsymbol{S}(\boldsymbol{q}) \in \mathbb{R}^{(6+m)\times(4+m)}$ is chosen such that:

$$\boldsymbol{S}^T(\boldsymbol{q})\boldsymbol{A}^T(\boldsymbol{q}) = 0. \tag{5.4}$$

With (5.3), one can conduct a coordinate transformation. Then the unconstrained dynamics in terms of the independent generalized coordinates can be formulated as follows:

$$\underbrace{\bar{\boldsymbol{M}}(\boldsymbol{q})}_{\boldsymbol{S}^T\hat{\boldsymbol{M}}\boldsymbol{S}}\ddot{\boldsymbol{\delta}} + \underbrace{\bar{\boldsymbol{C}}(\boldsymbol{q},\dot{\boldsymbol{\delta}})}_{\boldsymbol{S}^T(\hat{\boldsymbol{M}}\dot{\boldsymbol{S}}+\hat{\boldsymbol{C}}\boldsymbol{S})}\dot{\boldsymbol{\delta}} + \underbrace{\bar{\boldsymbol{g}}(\boldsymbol{q})}_{\boldsymbol{S}^T\hat{\boldsymbol{g}}} = \underbrace{\bar{\boldsymbol{\tau}}}_{\boldsymbol{S}^T\hat{\boldsymbol{\tau}}} + \underbrace{\bar{\boldsymbol{\tau}}_{ext}}_{\boldsymbol{S}^T\hat{\boldsymbol{\tau}}_{ext}}. \tag{5.5}$$

As we mentioned above, there are $n_p = 3$ DOFs along which platform can perform motion using winches, i.e., q_4, q_5, q_7. In terms of practical application, we are interested in more intuitive motion directions, e.g., platform horizontal x_c, vertical y_c, and one rotational q_5 motions with respect to the world frame. To this end, solving an IK for (5.2) it is possible to express winch parameters $\boldsymbol{q}_{winch} = [q_4,\ q_5,\ q_7]^T$ as vector of the platform state $\boldsymbol{q}_p = [x_c,\ q_5,\ y_c]^T$and q_1.

Thus, we can define an equal *quasi-state vector of feasible motions*, see Figure 5-4, as follows:

$$\boldsymbol{\eta} = [q_1,\ \underbrace{x_c,\ q_5,\ y_c}_{\boldsymbol{q}_p},\ \boldsymbol{q}_m]^T \in \mathbb{R}^{4+m},$$

such that:

$$\dot{\boldsymbol{\delta}} = \boldsymbol{B}\dot{\boldsymbol{\eta}}.$$

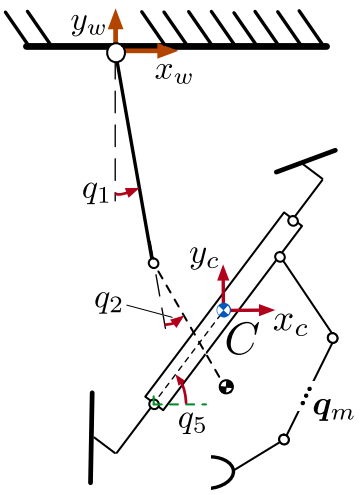

Figure 5-4: Serial chain (quasi-state) coordinates of the feasible motions.

The vector $\boldsymbol{\eta}$ corresponds to the equal serial-chain representation of the independent generalised coordinates describing closed-chain dynamics.

Then, the dynamics (5.5) with respect to $\boldsymbol{\eta}$ can be rewritten as follows:

$$\underbrace{\tilde{\boldsymbol{M}}(\boldsymbol{q})}_{\boldsymbol{B}^T\bar{\boldsymbol{M}}\boldsymbol{B}}\ddot{\boldsymbol{\eta}} + \underbrace{\tilde{\boldsymbol{C}}(\boldsymbol{q},\dot{\boldsymbol{\eta}})}_{\boldsymbol{B}^T(\bar{\boldsymbol{M}}\dot{\boldsymbol{B}}+\bar{\boldsymbol{C}}\boldsymbol{B})}\dot{\boldsymbol{\eta}} + \underbrace{\tilde{\boldsymbol{g}}(\boldsymbol{q})}_{\boldsymbol{B}^T\bar{\boldsymbol{g}}} = \underbrace{\tilde{\boldsymbol{\tau}}}_{\boldsymbol{B}^T\bar{\boldsymbol{\tau}}} + \underbrace{\tilde{\boldsymbol{\tau}}_{ext}}_{\boldsymbol{B}^T\bar{\boldsymbol{\tau}}_{ext}}. \tag{5.6}$$

A vector of generalized torques applied to the serial dynamics (5.6) can be defined as $\tilde{\boldsymbol{\tau}} = [\tau_{q_1},\ \tilde{\boldsymbol{\tau}}_p,\ \boldsymbol{\tau}_m]^T \in \mathbb{R}^{4+m}$, where τ_{q_1} is the torque applied to the pendulum first joint, $\tilde{\boldsymbol{\tau}}_p = [\tau_{x_c},\ \tau_{q_5},\ \tau_{y_c}]^T$ is the vector of control inputs applied to the quasi joints corresponding to the platform motion, and $\boldsymbol{\tau}_m$ are torques applied to the joints of the robotic arm. Since in the winch-based actuation we have only two actuated joints, q_4 and q_7, we should select two out of three quasi joints that we aim to control. In our case, x_c and y_c are of main interest. Thus, the vector of actuated torques, $\tilde{\boldsymbol{\tau}}_a = [\tau_{q_1},\ \tau_{x_c},\ \tau_{y_c},\ \boldsymbol{\tau}_m]^T \in \mathbb{R}^{3+m}$ can be defined such that $\tilde{\boldsymbol{\tau}} = \boldsymbol{O}^T\tilde{\boldsymbol{\tau}}_a$. Here, $\boldsymbol{O} \in \mathbb{R}^{(3+m)\times(4+m)}$ maps actuated torques $\tilde{\boldsymbol{\tau}}_a$ to the generalized torques $\tilde{\boldsymbol{\tau}}$. As it will be shown later, in our control strategy we utilize IK to map the desired motion in quasi state joints to the actuated joints, so we do not need to calculate the $\boldsymbol{O}$. For detailed derivation of the matrices $\boldsymbol{A}$, $\boldsymbol{S}$, $\boldsymbol{B}$, and $\boldsymbol{O}$, the reader is referred to Appendix D.

5.2.2.3 3D case

Since winches cannot affect the motion of the platform around the yaw, a spatial case might be represented as two decoupled planar dynamics similar to the considered above. Therefore, the first joint of the double pendulum can be modeled by spherical joint with corresponding coordinates $\boldsymbol{q}_{s,pend_1} = [q_1,\ q_2,\ q_3]^T$, each tip of the rigging cables can be modeled as a universal joint with 2 DOF at each fixation point, and three closed-chain loops in the space provide 9 constraint equations. The platform can be moved by winch-based actuation in the space along 3 translational DOFs, i.e., $\boldsymbol{x}_{s,p} = [x_c,\ y_c,\ z_c]^T$ and 2 rotational DOFs corresponding to the roll and pitch, i.e., $\boldsymbol{q}_{s,p} = [\boldsymbol{x}_{s,p},\ \varphi,\ \theta]^T$. Then, a quasi-state vector of feasible motions can be rewritten as: $\boldsymbol{\xi} = [\boldsymbol{q}_{s,pend_1},\ \boldsymbol{q}_{s,p},\ \boldsymbol{q_m}]^T \in \mathbb{R}^{15}$, where m = 7 for the redundant robotic arm, and resulted dynamics in terms of the quasi-state vector in 3D space can be formulated

as follows:

$$\boldsymbol{M}_s(\boldsymbol{\xi})\ddot{\boldsymbol{\xi}} + \boldsymbol{C}_s(\boldsymbol{\xi},\dot{\boldsymbol{\xi}})\dot{\boldsymbol{\xi}} + \boldsymbol{g}_s(\boldsymbol{\xi}) = \boldsymbol{O}_s^T \underbrace{\begin{bmatrix} \boldsymbol{\tau}_{s,pend_1} \\ \tau_{x_c} \\ \tau_{y_c} \\ \tau_{z_c} \\ \boldsymbol{\tau}_m \end{bmatrix}}_{\boldsymbol{\tau}_{s,a}} + \boldsymbol{\tau}_{s,ext}. \tag{5.7}$$

All values with subscript "s" in the dynamics (5.7) correspond to the same values of dynamics (5.6) generalized for the 3D case. For further convenience, let us also define a vector of the spherical joint $\boldsymbol{q}_{s,pend_2} \in \mathbb{R}^3$ corresponding to the motion of the second link of the double pendulum. Similar to the q_2 for the planar case, $\boldsymbol{q}_{s,pend_2}$ is an abstract quantity that can be calculated based on the $\boldsymbol{\xi}$ vector.

5.3 Hierarchical impedance-based whole-body controller

5.3.1 Reduced model for control design

The received equations of motion (5.7) for the cable-suspended aerial manipulator with integrated winch suspension are highly complex. Therefore, we want to simplify them by finding a reasonable trade-off between the system behavior description and equations that can be efficiently utilized in the controller.

In the previous chapter, we have introduced the oscillation damping controller that can eliminate oscillations in the pendulum joints while keeping the constant yaw of the platform using propeller-based actuation. Thus, in the case when the oscillation damping controller is applied to the system (5.7), the dynamics of the pendulum joints can be neglected, i.e., $\dot{\boldsymbol{q}}_{s,pend_1} = 0$ and $\dot{\boldsymbol{q}}_{s,pend_2} = 0$, and corresponding pendulum joint angles will be defined over time only by effect of the external and gravitational torques. The latter one appears because of the robotic arm weight, which shifts the total system COM. As a result, gravity force generates disturbing torque around the suspension point, which leads to the undesired non-zero configuration in pendulum joints of the system[4], see Figure 5-5, and, consequently, to the platform tilt, shift in end effector pose, and the onboard sensor perturbations.

[4]Here we neglected by the hook weight for clarity of explanation.

The winch-based actuation affects three controllable rigging cables that allow translational shifts of the platform with respect to the suspension point in order to counterbalance the COM displacement. Such action should result in zero pendulum joints. To this end, we define a *reduced configuration* $\boldsymbol{\gamma}$ which contains only joints responsible for the system COM location and robotic arm end effector pose as follows:

$$\boldsymbol{\gamma} = [\underbrace{x_c,\ y_c,\ z_c}_{\boldsymbol{x}_{s,p}},\ \boldsymbol{q_m}]^T \in \mathbb{R}^{10}.$$

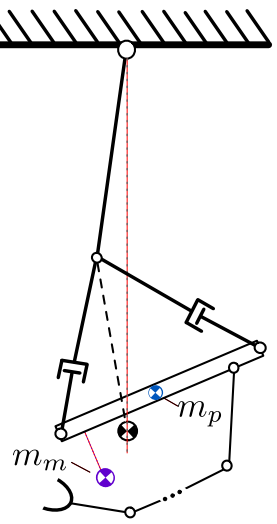

Figure 5-5: Gravitational torque brings the system COM under the suspension point by changing the pendulum configuration.

The $\boldsymbol{\gamma}$ defines DOFs that will be accessed by the controller. In our case, based on the desired quasi-state of the platform, we have to calculate control inputs to the real system, i.e., cable lengths, by utilizing IK. This task is fully determined as it will be shown in subsubsection 5.3.3.5. Thus, we can always generate such cable lengths that nullify the tilting angles (φ, θ) while keeping desired displacements (x_c, y_c, z_c). Taking into account the slow winch dynamics, it allows us to neglect dynamics along rotational DOFs as well. To this end, state $\boldsymbol{\gamma}$ does not contain tilting roll φ and pitch θ.

When the double pendulum joint angles as well as the platform tilt q_5 are equal to zero, the COM is located under the suspension point, and the mapping matrix $\boldsymbol{O}$ has the form of a unit matrix. Then, the dynamics (5.7) can be rewritten in terms of the $\boldsymbol{\gamma}$ state as follows:

$$\boldsymbol{M}_r(\boldsymbol{\gamma})\ddot{\boldsymbol{\gamma}} + \boldsymbol{C}_r(\boldsymbol{\gamma}, \dot{\boldsymbol{\gamma}})\dot{\boldsymbol{\gamma}} + \boldsymbol{g}_r(\boldsymbol{\gamma}) = \underbrace{\begin{bmatrix} \tau_{x_c} \\ \tau_{y_c} \\ \tau_{z_c} \\ \boldsymbol{\tau}_m \end{bmatrix}}_{\boldsymbol{\tau}_\gamma} + \boldsymbol{\tau}_{ext,r}. \tag{5.8}$$

Here, $\boldsymbol{\tau}_\gamma = [\boldsymbol{\tau}_p,\ \boldsymbol{\tau}_m]^T$, and all elements with subscript "r" correspond to the reduced dynamics.

5.3.2 Control goals

Let us define the following control goals for our system:

1. The main task for aerial manipulator is to change the end effector Cartesian pose (three coordinates and three Euler angles), $\boldsymbol{x}_e \in \mathbb{R}^6$, expressed in the world frame toward desired value, $\boldsymbol{x}_e^{des}$. Let us define configuration of the end effector in terms of the $\boldsymbol{\gamma}$ as $\boldsymbol{x}_e = \boldsymbol{f}_e(\boldsymbol{\gamma})$, then our control goal is to provide: $\boldsymbol{x}_e - \boldsymbol{x}_e^{des} = 0$.

2. The second task is to cope with the static disturbances caused by robotic arm weight, i.e., neutralize gravity torque by keeping system COM, $\boldsymbol{x}_{com} \in \mathbb{R}^3$, under suspension point. Let us define the model COM location in inertial space as $\boldsymbol{x}_{com} = \boldsymbol{f}_{com}(\boldsymbol{\gamma})$, then our control goal is to keep horizontal components of this vector, i.e., x_{com} and y_{com}, as zeros.

3. The last task is injecting additional damping to the elbow (3-th) joint of the robotic arm. This task is introduced for further calculation convenience.

The second task indirectly ensures that unmeasured pendulum joints are close to zero when the oscillation damping controller is applied. Only in this case, we can state that the first task is fulfilled in the world frame since the utilized model is based only on the reduced state $\boldsymbol{\gamma}$.

In real mission, the robotic arm is under remote operator control [Lee et al., 2020], so the second task should have less priority [Dietrich et al., 2013], and it should not interrupt the first (main) one. Moreover, all control tasks should be structurally feasible at the same time. The last task has the least priority.

5.3.3 Controller derivation

To regulate the defined state $\boldsymbol{\gamma}$, in this chapter we adapt the Hierarchical impedance-based Whole-Body Controller [Coelho et al., 2021, Dietrich et al., 2021, Ott et al., 2011, Ott et al., 2015], see Figure 5-6. As it can be seen from the diagram, as input we set the desired position of the end effector, $\boldsymbol{x}_e^{des}$, while the desired position of the system COM, $\boldsymbol{x}_{com}^{des}$, is set to zero during the whole operation. The whole-body impedance-based controller produces the desired generalized torques for the robot joints, $\boldsymbol{\tau}_m$, and quasi joints of the platform, $\boldsymbol{\tau}_p$. Since the robotic arm is torque-controlled, it directly follows the desired command and provides the end

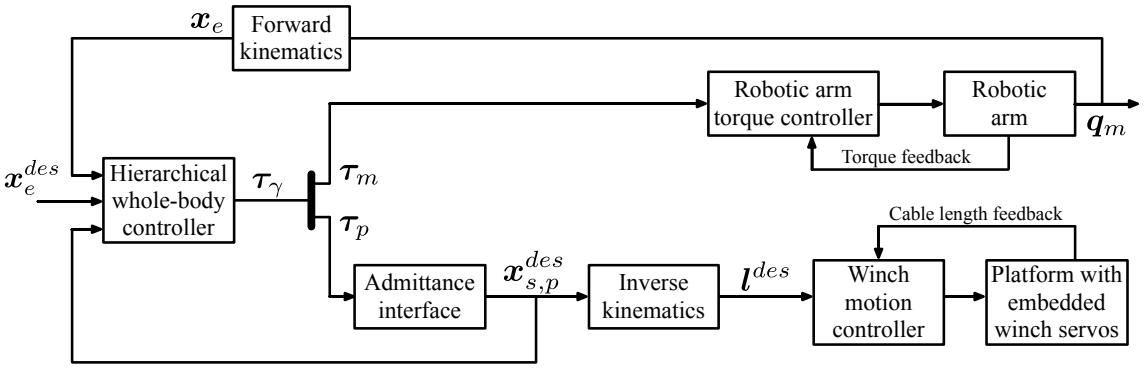

Figure 5-6: Hierarchical whole-body control diagram.

effector position, $\boldsymbol{x}_e$, as an output. The platform with integrated winches, on the other hand, is kinematically controlled. To this end, we first transform desired generalized torques $\boldsymbol{\tau}_p$ to the required motion along platform quasi joints, $\boldsymbol{x}_{s,p}^{des}$, by virtue of admittance interface (subsection 2.2.1) and further, we use the Inverse Kinematics (IK) to map it to the desired cable lengths. In parallel, $\boldsymbol{x}_{s,p}^{des}$ returns back to the controller model in order to update the location of the resulted system COM. In the following subsections, all aforementioned sub-blocks will be considered in detail.

5.3.3.1 Hierarchically decoupled dynamics

Following the task space definition presented in subsection 5.3.2, we can define task velocities:

$$\begin{aligned} \dot{\boldsymbol{x}}_e &= \boldsymbol{J}_1 \dot{\boldsymbol{\gamma}}, \\ \dot{\boldsymbol{x}}_{com} &= \boldsymbol{J}_2 \dot{\boldsymbol{\gamma}}, \\ \dot{q}_{m,3} &= \boldsymbol{J}_3 \dot{\boldsymbol{\gamma}}, \end{aligned} \tag{5.9}$$

here $\dot{\boldsymbol{x}}_e \in \mathbb{R}^6$ is the body velocity of the end effector, $\dot{\boldsymbol{x}}_{com} \in \mathbb{R}^3$ is the vector of translational velocities of model COM, $\dot{q}_{m,3} \in \mathbb{R}$ is the velocity of the robotic arm elbow joint. Besides, $\boldsymbol{J}_i = \frac{\partial \boldsymbol{f}_i(\boldsymbol{\gamma})}{\partial \boldsymbol{\gamma}}$ for $i \in \{1,\ 2,\ 3\}$, i.e., $\boldsymbol{J}_1 \in \mathbb{R}^{6\times 10}$, $\boldsymbol{J}_2 \in \mathbb{R}^{3\times 10}$, and $\boldsymbol{J}_3 \in \mathbb{R}^{1\times 10}$ are corresponding Jacobian matrices that have a full row rank during the operation.

Adapting approach presented in [Dietrich and Ott, 2019] for redundant robots, let us first introduce the *augmented Jacobian* for $i-$th task by stacking all priority

task Jacobians up to $i-$th as follows:

$$\boldsymbol{J}_i^{aug}(\boldsymbol{\gamma}) = \begin{bmatrix} \boldsymbol{J}_1(\boldsymbol{\gamma}) \\ ... \\ \boldsymbol{J}_i(\boldsymbol{\gamma}) \end{bmatrix}.$$

Then, augmented task velocity $\boldsymbol{V} \in \mathbb{R}^{10}$ is related to the joint velocities as follows:

$$\boldsymbol{V} = \begin{bmatrix} \dot{\boldsymbol{x}}_e \\ \dot{\boldsymbol{x}}_{com} \\ \dot{q}_{m,3} \end{bmatrix} = \underbrace{\begin{bmatrix} \boldsymbol{J}_1(\boldsymbol{\gamma}) \\ \boldsymbol{J}_2(\boldsymbol{\gamma}) \\ \boldsymbol{J}_3(\boldsymbol{\gamma}) \end{bmatrix}}_{\boldsymbol{J}_3^{aug}(\boldsymbol{\gamma})} \dot{\boldsymbol{\gamma}}, \tag{5.10}$$

Expressing the task velocities through the vector of joint velocities plays a vital role in the whole-body framework. To avoid interference between tasks, we need to decouple the task velocities at the acceleration level. To this end, dynamically consistent null-space projectors [Khatib, 1987] can be used:

$$\boldsymbol{N}_i(\boldsymbol{\gamma}) = \begin{cases} \boldsymbol{I}, & \text{for } i = 1 \\ \boldsymbol{I} - \boldsymbol{J}_{i-1}^{aug}(\boldsymbol{\gamma})^T \boldsymbol{J}_{i-1}^{aug}(\boldsymbol{\gamma})^{M+,T}, & \text{for } i = 2, 3 \end{cases}. \tag{5.11}$$

Here, the superscript $(.)^{M+}$ represents a dynamically consistent pseudoinverse [Dietrich et al., 2015] that is defined as:

$$\boldsymbol{J}_i(\boldsymbol{\gamma})^{M+} = \boldsymbol{M}_r(\boldsymbol{\gamma})^{-1} \boldsymbol{J}_i(\boldsymbol{\gamma})^T (\boldsymbol{J}_i(\boldsymbol{\gamma}) \boldsymbol{M}_r(\boldsymbol{\gamma})^{-1} \boldsymbol{J}_i(\boldsymbol{\gamma})^T)^{-1}.$$

By utilizing (5.11), we can dynamically decouple original Jacobian matrices in (5.9):

$$\bar{\boldsymbol{J}}_i(\boldsymbol{\gamma}) = \boldsymbol{J}_i(\boldsymbol{\gamma}) \boldsymbol{N}_i(\boldsymbol{\gamma})^T.$$

Then, we can formulate corresponding hierarchically decoupled task-space velocities as follows:

$$\underbrace{\begin{bmatrix} \boldsymbol{\nu}_1 \\ \boldsymbol{\nu}_2 \\ \boldsymbol{\nu}_3 \end{bmatrix}}_{\boldsymbol{\nu}} = \underbrace{\begin{bmatrix} \bar{\boldsymbol{J}}_1(\boldsymbol{\gamma}) \\ \bar{\boldsymbol{J}}_2(\boldsymbol{\gamma}) \\ \bar{\boldsymbol{J}}_3(\boldsymbol{\gamma}) \end{bmatrix}}_{\bar{\boldsymbol{J}}(\boldsymbol{\gamma})} \dot{\boldsymbol{\gamma}}. \tag{5.12}$$

Here, $\boldsymbol{\nu}$ indicates the vector of the task space velocities in dynamically decoupled coordinates, and $\bar{\boldsymbol{J}}(\boldsymbol{\gamma}) \in \mathbb{R}^{10\times10}$ is the *extended Jacobian* matrix that maps generalized velocities to the task velocities $\boldsymbol{\nu}$. Note that the $\bar{\boldsymbol{J}}(\boldsymbol{\gamma})$ is invertible due to complemented 3−rd task.

The new set of coordinates allows to receive hierarchically decoupled motion dynamics of the system (5.8):

$$\boldsymbol{\Lambda}(\boldsymbol{\gamma})\dot{\boldsymbol{\nu}} + \boldsymbol{\mu}(\boldsymbol{\gamma}, \dot{\boldsymbol{\gamma}})\boldsymbol{\nu} = \bar{\boldsymbol{J}}(\boldsymbol{\gamma})^{-T}(\boldsymbol{\tau}_{\gamma} + \boldsymbol{\tau}_{ext,r} - \boldsymbol{g_r}(\boldsymbol{\gamma})), \tag{5.13}$$

where $\boldsymbol{\Lambda}(\boldsymbol{\gamma}) = (\bar{\boldsymbol{J}}\boldsymbol{M}_r(\boldsymbol{q})^{-1}\bar{\boldsymbol{J}}^T)^{-1} = diag(\boldsymbol{\Lambda}_1,\ \boldsymbol{\Lambda}_2,\ \boldsymbol{\Lambda}_3)$ contains decoupled task inertias, and $\boldsymbol{\mu}(\boldsymbol{\gamma}, \dot{\boldsymbol{\gamma}}) = \bar{\boldsymbol{J}}^{-T}(\boldsymbol{C}_r(\boldsymbol{\gamma}, \dot{\boldsymbol{\gamma}}) - \boldsymbol{M}_r(\boldsymbol{q})\bar{\boldsymbol{J}}^{-1}\dot{\bar{\boldsymbol{J}}})\bar{\boldsymbol{J}}^{-1}$ is transformed Coriolis-centrifugal matrix.

The task hierarchy can be intuitively observed by expressing the relation between augmented task velocities $\boldsymbol{V}$ and hierarchically decoupled task-space velocities $\boldsymbol{\nu}$ [Dietrich and Ott, 2019, Garofalo and Ott, 2020]. Inserting (5.10) in (5.12), we can receive the following:

$$\boldsymbol{\nu} = \underbrace{\bar{\boldsymbol{J}}(\boldsymbol{\gamma})\boldsymbol{J}_3^{aug}(\boldsymbol{\gamma})^{-1}}_{\boldsymbol{T}(\boldsymbol{q})}\boldsymbol{V}.$$

Then, mapping $\boldsymbol{T}(\boldsymbol{q})$ is the lower-triangular matrix that projects the original task velocities one-to-one to the decoupled task velocities, i.e., $\boldsymbol{T}_{i,j} = \boldsymbol{I}$ for $i = j$, and ensures that the lower-priority level velocities do not disturb higher-priority ones, i.e., $\boldsymbol{T}_{i,j} = \boldsymbol{0}$ for $i < j$:

$$\boldsymbol{T}(\boldsymbol{q}) = \begin{bmatrix} \boldsymbol{I} & \boldsymbol{0} & \boldsymbol{0} \\ \boldsymbol{T}_{21} & \boldsymbol{I} & \boldsymbol{0} \\ \boldsymbol{T}_{31} & \boldsymbol{T}_{32} & \boldsymbol{I} \end{bmatrix}.$$

Dimensions of each element $\boldsymbol{T}_{i,j}$ correspond to the size of the original and decoupled task spaces.

5.3.3.2 Control law

Since all tasks exploit the same DOFs, a hierarchical whole-body controller is applied in order to ensure that the main task is fulfilled without being disturbed by the

second and third. The control law is formulated as follows:

$$\boldsymbol{\tau}_\gamma = \begin{bmatrix} \boldsymbol{\tau}_p \\ \boldsymbol{\tau}_m \end{bmatrix} = \boldsymbol{g_r}(\boldsymbol{\gamma}) + \boldsymbol{\tau}_\mu + \sum_{i=1}^{3} \bar{\boldsymbol{J}}_i^T \boldsymbol{F}_{i,ctrl} \tag{5.14}$$

with

$$\boldsymbol{\tau}_\mu = \sum_{i=1}^{3} \left(\bar{\boldsymbol{J}}_i^T \left(\sum_{j=1}^{i-1} \boldsymbol{\mu}_{i,j} \boldsymbol{\nu}_j + \sum_{j=i+1}^{3} \boldsymbol{\mu}_{i,j} \boldsymbol{\nu}_j \right) \right),$$

where $\boldsymbol{F}_{i,ctrl}$ corresponds to the control force for the $i-$th task and $\boldsymbol{\tau}_\mu$ is applied in order to decouple task dynamics at the velocity level. It compensates for the off-blockdiagonal submatrix of the Coriolis-centrifugal matrix $\boldsymbol{\mu}(\boldsymbol{\gamma}, \dot{\boldsymbol{\gamma}})$, i.e., $\boldsymbol{\mu_{12}} \in \mathbb{R}^{6\times 3}$, $\boldsymbol{\mu_{13}} \in \mathbb{R}^6$. Thus, all task control forces $\boldsymbol{F}_{i,ctrl}$ are expressed through all joint torques of the system in such a way that tasks are conducted without interference according to hierarchy. This aspect establishes the foundation of the *hierarchical whole-body control* framework.

Thus, by applying (5.14) to the (5.13), we receive fully decoupled dynamics equations as follows:

$$\boldsymbol{\Lambda}_i(\boldsymbol{\gamma})\dot{\boldsymbol{\nu}}_i + \boldsymbol{\mu}_{i,i}(\boldsymbol{\gamma}, \dot{\boldsymbol{\gamma}})\boldsymbol{\nu}_i = \boldsymbol{F}_{i,ctrl} + \bar{\boldsymbol{J}}_i(\boldsymbol{\gamma})^{-T} \boldsymbol{\tau}_{ext,r_i}$$

for $i \in \{1,\ 2,\ 3\}$.

With structural feasibility of all tasks and absence of external torques, the proposed control law (5.14) guarantees the asymptotic stability of the equilibrium point for the main task and conditional stability for the second and third tasks maintaining the overall passivity, as shown in [Dietrich et al., 2016, Ott et al., 2015].

5.3.3.3 Impedance control in the task space

To accomplish the desired tasks and achieve compliant behaviour on all hierarchical levels, the Cartesian impedance control is exploited [Caccavale et al., 1998, Zhang and Fasse, 2000]:

$$\begin{aligned} \boldsymbol{F}_{1,ctrl} &= \begin{bmatrix} -\boldsymbol{R}_e^T \boldsymbol{K}_{Pe} \boldsymbol{p}_e \\ -2\boldsymbol{R}_e^T \boldsymbol{E}(\eta_e, \boldsymbol{\epsilon}_e)^T \boldsymbol{K}_{Oe} \boldsymbol{\epsilon}_e \end{bmatrix} - \boldsymbol{K}_{De} \dot{\boldsymbol{x}}_e, \\ \boldsymbol{F}_{2,ctrl} &= -\boldsymbol{K}_{Pc} \boldsymbol{p}_c - \boldsymbol{K}_{Dc} \dot{\boldsymbol{x}}_{\boldsymbol{com}}, \\ \boldsymbol{F}_{3,ctrl} &= -K_{D_3} \dot{q}_{m,3}. \end{aligned} \tag{5.15}$$

Here, $\boldsymbol{F}_{1,ctrl}$ is the body wrench applied to the end effector, $\boldsymbol{F}_{2,ctrl}$ is the force of the secondary task before being projected in the null space of the first one, i.e., the components of the secondary task force that collide with the main task will be nullified after projection, and $\boldsymbol{F}_{3,ctrl}$ is the damping torque at the 3−th joint of the robotic arm. Moreover, the matrices $\boldsymbol{K}_{(.)}$ are positive definite gain matrices (subscripts p, o, d stand for positional stiffness, orientational stiffness, and damping, respectively), K_{D_3} is the damping gain, $\boldsymbol{R}_{(.)}, \boldsymbol{p}_{(.)}$ are the rotational and positional errors between the desired and current pose of the corresponding operational spaces (subscripts e and c stand for the end effector and COM), see the detailed definition of error elements in paragraph 2.1.1.1.6. Error corresponding to the first task is expressed in the tool frame, while the error of the second task is presented in the world frame. $\eta_{(.)}$ and $\boldsymbol{\epsilon}_{(.)}$ are the scalar and vector parts of a quaternion representation of $\boldsymbol{R}_{(.)}$, and the matrix $\boldsymbol{E}(\eta_{(.)},\ \boldsymbol{\epsilon}_{(.)}) = \eta_{(.)}\boldsymbol{I}_3 - \widehat{\boldsymbol{\epsilon}}_{(.)}$.

Taking into account the control force definition (5.15), formulated control law (5.14) can be applied directly to our system for the execution of all control tasks. However, while the robotic arm is torque controlled, the winch servos are position-controlled. Therefore, additional transformation is required.

5.3.3.4 Admittance interface

As it was mentioned in subsection 3.3.4, each winch contains an embedded motion controller and takes the cable length as the input. In order to operate the whole system at the torque level, the admittance interface is adapted [Dietrich et al., 2016, Iskandar et al., 2019]. It takes commanded forces in quasi joints as input to a virtual system with desired dynamics and produces the corresponding displacements as outputs which are further processed through IK for final cable length calculation. The exploitation of such an interface implies utilizing a high gain motion controller for the winch-based actuation, which can perfectly realize desired admittance dynamics despite external and internal (e.g., due to coupled dynamics) disturbances.

Passing $\boldsymbol{\tau}_p$ through the admittance interface with desired dynamics, the corresponding displacement of the platform, $\boldsymbol{x}_{s,p}^{des}$, is described by:

$$\boldsymbol{M}_{adm}\ddot{\boldsymbol{x}}_{s,p}^{des} + \boldsymbol{D}_{adm}\dot{\boldsymbol{x}}_{s,p}^{des} = \boldsymbol{\tau}_p, \tag{5.16}$$

where $\boldsymbol{M}_{adm} \in \mathbb{R}^{3\times3}$, $\boldsymbol{D}_{adm} \in \mathbb{R}^{3\times3}$ are positive inertia and damping diagonal matrices describing desired dynamics of the system, respectively.

Assuming that $\boldsymbol{x}_{s,p} \approx \boldsymbol{x}_{s,p}^{des}$, the overall system dynamics (5.8) can be rewritten:

$$\begin{bmatrix} \boldsymbol{M}_{adm} & \boldsymbol{0} \\ \boldsymbol{M}_{pm}(\boldsymbol{\gamma}) & \boldsymbol{M}_m(\boldsymbol{\gamma}) \end{bmatrix} \begin{bmatrix} \ddot{\boldsymbol{x}}_{s,p} \\ \ddot{\boldsymbol{q}}_m \end{bmatrix} + \begin{bmatrix} \boldsymbol{D}_{adm} & \boldsymbol{0} \\ \boldsymbol{C}_{pm}(\boldsymbol{\gamma},\ \dot{\boldsymbol{\gamma}}) & \boldsymbol{C}_m(\boldsymbol{\gamma},\ \dot{\boldsymbol{\gamma}}) \end{bmatrix} \begin{bmatrix} \dot{\boldsymbol{x}}_{s,p} \\ \dot{\boldsymbol{q}}_m \end{bmatrix} + \begin{bmatrix} 0 \\ \boldsymbol{g}_m(\boldsymbol{\gamma}) \end{bmatrix} = \begin{bmatrix} \boldsymbol{\tau}_p \\ \boldsymbol{\tau}_m \end{bmatrix}. \tag{5.17}$$

Here, the term $\boldsymbol{\tau_{ext}}$ is omitted since we do not measure external wrench applied to the system and assume that the designing controller is robust enough to cope with external perturbations. To estimate this term, the force-torque sensor at the end effector or tension force sensor in the rigging cables can be installed [Haddadin et al., 2017, Iskandar et al., 2021, Lu et al., 2005]. $\boldsymbol{M}_{pm}$ and $\boldsymbol{C}_{pm}$ are the inertia and Coriolis couplings between platform and manipulator which are corresponding submatrices of $\boldsymbol{M}_r(\boldsymbol{\gamma})$ and $\boldsymbol{C}_r(\boldsymbol{\gamma},\ \dot{\boldsymbol{\gamma}})$.

Following the [Dietrich et al., 2016], the control law (5.14) is extended with additional term to remove coupling effect between manipulator and platform in (5.17) due to admittance dynamics:

$$\boldsymbol{\tau}_\gamma = \boldsymbol{g_r}(\boldsymbol{\gamma}) + \boldsymbol{\tau}_\mu + \boldsymbol{\tau}_{comp} + \sum_{i=1}^{3} \bar{\boldsymbol{J}}_i^T \boldsymbol{F}_{i,ctrl}, \tag{5.18}$$

where $$\boldsymbol{\tau}_{comp} = \begin{bmatrix} \boldsymbol{0} \\ \boldsymbol{M}_{pm}(\boldsymbol{\gamma})\ddot{\boldsymbol{x}}_{s,p} + \boldsymbol{C}_{pm}(\boldsymbol{\gamma},\ \dot{\boldsymbol{\gamma}})\dot{\boldsymbol{x}}_{s,p} + \boldsymbol{g}_m(\boldsymbol{\gamma}) \end{bmatrix}.$$

It is worth noting that acceleration and velocities for $\boldsymbol{\tau}_{comp}$ term can be estimated from (5.16) without direct measurement.

It can be seen that in the admittance interface dynamics (5.16), there is no stiffness term. Indeed, the presence of the virtual spring would bring the system toward zero configuration as soon as the control force is removed, while we want the system to stay in the configuration it reaches even after releasing the control force.

As a final step, the IK for the rigging cable suspension should be defined. It takes as the input the displacement, $\boldsymbol{x}_{s,p}^{des}$, and provides cable lengths as the output.

5.3.3.5 Inverse kinematics

In order to control quasi joints, $\boldsymbol{x}_{s,p} = [x_c,\ y_c,\ z_c]^T$, via the lengths of the cables, the IK for the rigging cable suspension is formulated based on subsection 2.1.3. As shown in Figure 5-7, when pendulum joints are zeros, the following vector loop can be constructed:

$$\boldsymbol{l}_i^{des} = \boldsymbol{r} + \boldsymbol{R}_p^w(\boldsymbol{d} + \boldsymbol{a}_i). \tag{5.19}$$

Here, $\|\boldsymbol{l}_i^{des}\|$ is the length of the $i-$cable. The constant vector $\boldsymbol{a}_i$ represents the location of the $i-$th cable start point, W_i, relative to the platform GC, point C, see subsubsection 3.3.4.1. Vector $\boldsymbol{r} = [0,\ 0,\ z_c]^T$ connects the suspension point A with point K which indicates the system COM, point G, projected at the platform plane, see Figure 5-3b. A displacement between K and C is defined by vector $\boldsymbol{d}$. The vectors $\boldsymbol{a}_i$ and $\boldsymbol{d}$ are located in the plane of the platform. The rotation matrix $\boldsymbol{R}_p^w$ represents an orientation of the platform via roll and pitch $(\varphi,\ \theta)$ angles of the vector $\boldsymbol{q}_{s,p}$. Since it is in our interests to keep $\varphi,\ \theta$ angles as zeros, we impose $\boldsymbol{R}_p^w = \boldsymbol{I}$ such that $\boldsymbol{R}_p^w\boldsymbol{d} = [x_c,\ y_c,\ 0]^T$. Thus, for the desired platform displacement $[x_c,\ y_c,\ z_c]^T$, we calculate only such cable lengths that guarantee zero tilting angles and ensures the horizontal COM components under the suspension point. It is possible because inverse kinematics represents a fully determined nonlinear system of equations (5.19), which can be solved for any desired quasi-state.

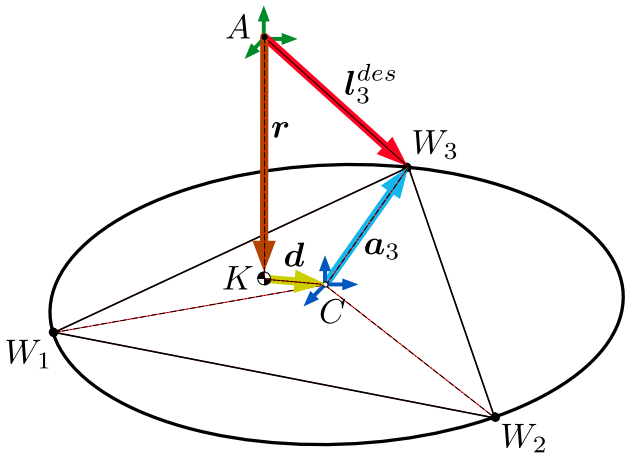

Figure 5-7: Inverse Kinematics for the rigging cable suspension.

5.3.4 Simulation study

The main goal of this subsection is to validate the ability to regulate the multi-DOF system COM using the whole-body framework[5].

The Luca Dynamics environment (subsection 2.1.4) calculates a system COM location and centroidal momentum matrix $\boldsymbol{A} = [\boldsymbol{A}_p,\ \boldsymbol{A}_l]^T$ [Garofalo et al., 2015, Orin and Goswami, 2008] which relates linear and angular momenta with joint velocities $\boldsymbol{\gamma}$. Then, for linear momentum $\boldsymbol{p}$ we can formulate the following:

$$\boldsymbol{p} = \boldsymbol{A}_p\dot{\boldsymbol{\gamma}} = (m_m + m_p)\dot{\boldsymbol{x}}_{com},$$

where $\dot{\boldsymbol{x}}_{com}$ is the velocities of the system COM.

Utilizing (5.9), the $\boldsymbol{J}_2$ can be found as follows:

$$\boldsymbol{J}_2 = \frac{\boldsymbol{A}_p}{m_m + m_p}.$$

Then, adapting the control law (5.18) for only one task we receive:

$$\begin{aligned}\boldsymbol{\tau}_\gamma &= \boldsymbol{g} + \boldsymbol{J}_2^T\boldsymbol{F}_{com},\\ \boldsymbol{F}_{com} &= \mathcal{PD}(\boldsymbol{x}_{com} - \boldsymbol{x}_{com}^{des}).\end{aligned}$$

Here, $\mathcal{PD}$ indicates the proportional-derivative operation on the error of the $\boldsymbol{x}_{com}$ location.

In order to validate the control law, we conducted a simulation in MATLAB Simulink. To this end, the model corresponding to the state $\boldsymbol{\gamma}$ was utilized. It contains 3 translational DOFs of the platform and 7 rotational DOFs of the robotic arm. As desired location of the COM the point $\boldsymbol{x}_{com}^{des} = [0.224,\ -0.3,\ 0.49]^T$ was chosen[6]. As a result, the controller generates forces applied to the platform and torques applied to the robotic arm joints, see Figure 5-8a. As shown in Figure 5-8b, the system COM location converges to the desired values by utilizing joint torques of the whole system within 4.3 seconds for the not properly tuned controller. As we will see in the following chapter, the possible COM displacement of the experimental setup presented in chapter 3 is roughly 1.5 times lower for critical configuration with horizontally stretched arm.

[5]The task hierarchy will be evaluated in the experimental studies in the following section.

[6]Our final control goal is to nullify the first two components of this vector, but here we use non-zero desired values just to validate approach.

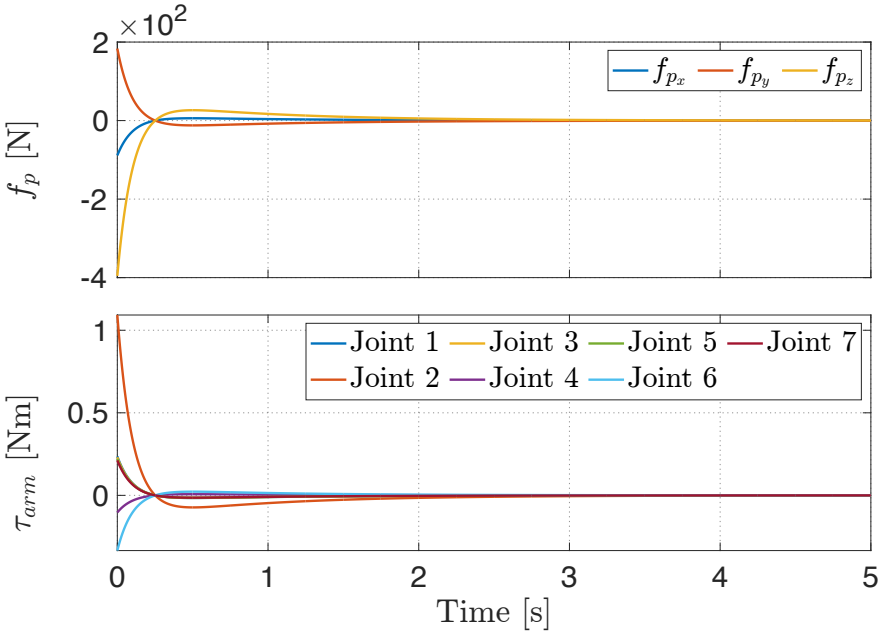

(a) Control forces applied to the platform (top) and torques applied to the arm joints (bottom)

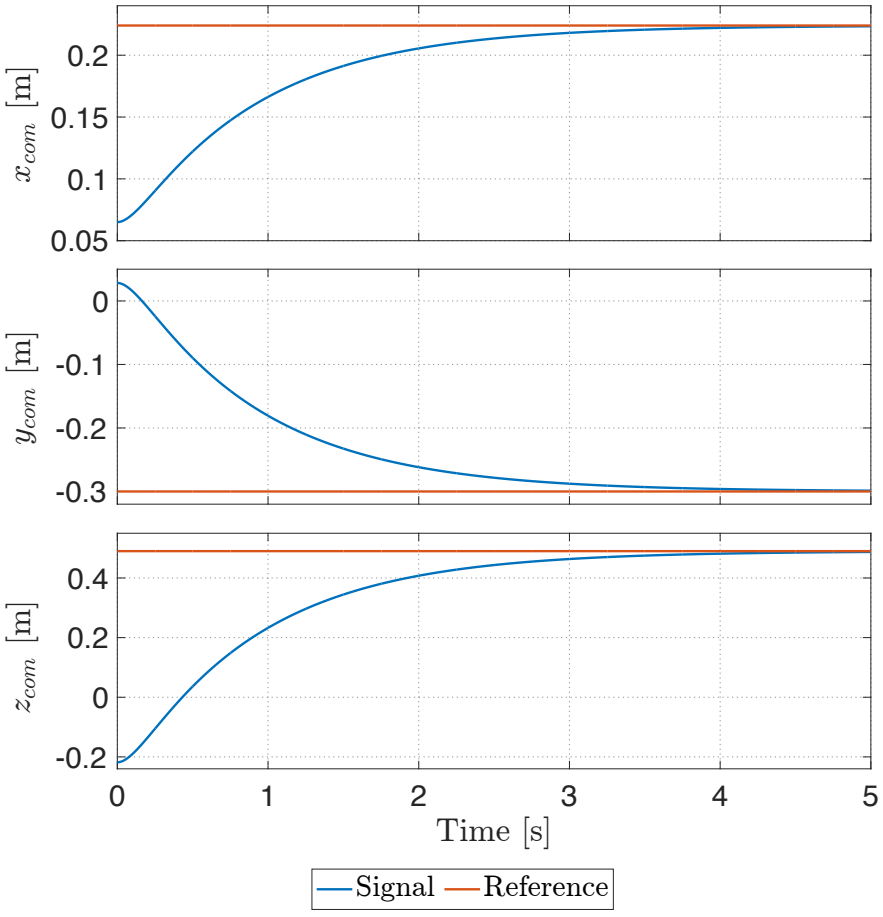

(b) Location of the system COM

Figure 5-8: Results of the simulation study on the whole-body control framework performance.

"As we say, I hope it works."

Edward F. Crawley

Chapter 6

Experimental investigation of the proposed control strategies

In this chapter, in order to validate the performance and functionality of the cable-suspended aerial manipulator concept regulated by the developed control algorithms, an extensive experimental investigation is carried out. In particular, we examine the behavior of the system:

- without any actuation through FFT analysis,
- controlled by the Optimal Oscillation Damping Controller (OODC),
- controlled by the Hierarchical impedance-based Whole-Body Controller (HWBC),
- controlled simultaneously by two controllers.

As a demonstrator, the crane-stationed SAM platform, see chapter 3 is utilized in two different setups: indoor and outdoor. Several experiments are conducted with the platform hanged to the ceiling in the laboratory. Depending on the controller and experimental conditions, various performance criteria are specified.

6.1 Experimental setup description

6.1.1 The demonstrator SAM

Developed cable-suspended aerial manipulator SAM, see Figure 6-1, is utilized in the experimental studies. The platform orientation and angular velocities are retrieved from the onboard IMU, the end effector pose is calculated using forward kinematics

Figure 6-1: The SAM and the author at the experimental session.

applied to the robotic arm joint sensor data, and the platform translational motion due to winch-based actuation is calculated using the forward kinematics applied to the collected cable length data. Exploited settings and weight of the system are specified in Table 6.1. The data logging frequency is different for each experiment, therefore it is specified directly in each experiment description as ν_{data}.

Parameter	**Value**	**Unit**
Propeller-based actuation control loop	200	Hz
Winch-based actuation control loop	200	Hz
Robotic arm control loop	1000	Hz
IMU raw data frequency	400	Hz
Platform weight	35.7	kg
Robotic arm weight	16.7	kg

Table 6.1: Settings and parameters of the SAM in the experimental sessions.

6.1.2 RMC laboratory

Several validation experiments were conducted in the RMC laboratory, see Figure 6-2a. In contrast to the crane-stationed environment, in the laboratory the SAM is hanged directly to the cable without the hook. Thus, the system behaves as a single spherical pendulum.

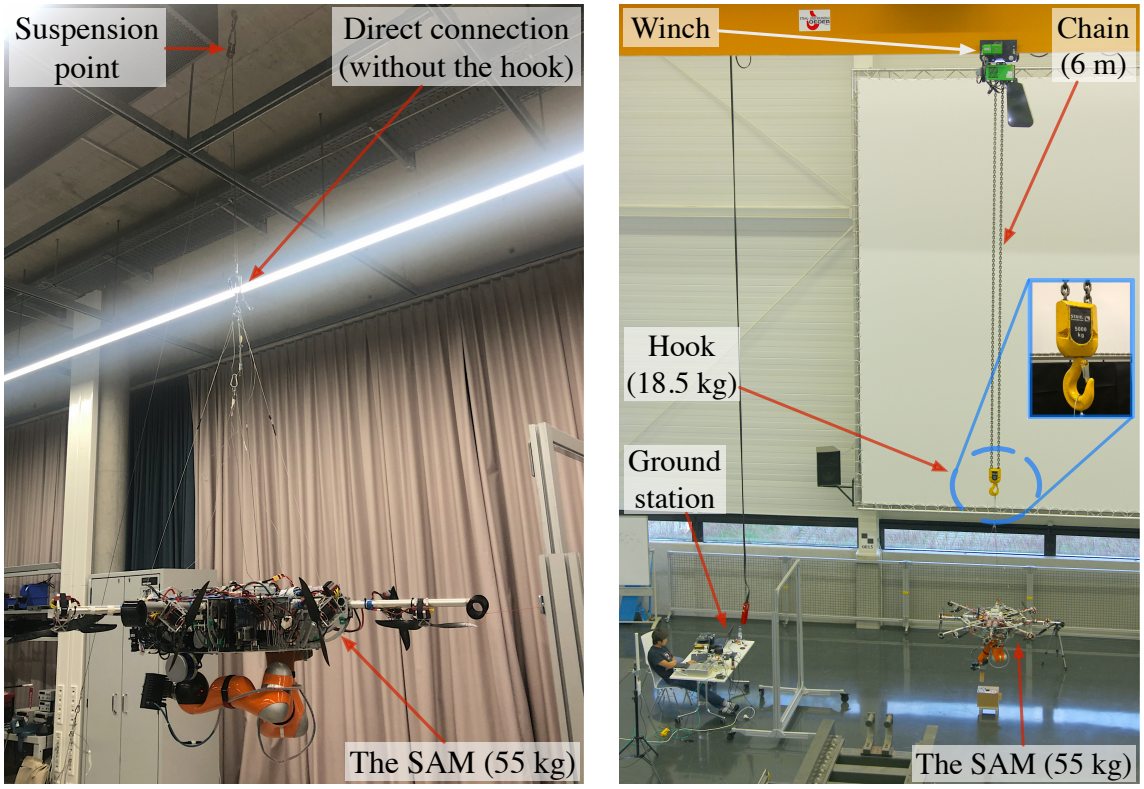

(a) Laboratory environment (b) Indoor environment

Figure 6-2: Experimental setups.

6.1.3 Indoor environment

The indoor experiment is located in the DLR Oberpfaffenhofen TechLab facility with integrated overhead crane Stahl ST50[1], see Figure 6-2b. The main characteristics of the indoor setup which were utilized in the optimization problem for the control law (4.14) are presented in Table 6.2.

Parameter	**Value**	**Unit**
Hook weight	18.5	kg
Chain density	2.85	$\frac{\text{kg}}{\text{m}}$
Length of the chain	6	m
Distance from the hook to the platform	2.2	m

Table 6.2: Weight-geometric parameters of the indoor setup.

[1]https://www.stahlcranes.com

6.1.4 Outdoor environment

The outdoor environment is based on a mini crane Hoeflon C6[2] and organized in DLR Oberpfaffenhofen site, see Figure 6-3a. The utilized crane can be transformed to the mobile platform on caterpillars, see Figure 6-3b, and is controlled remotely by the joystick. The main characteristics of the outdoor setup are presented in Table 6.3[3]. In contrast to the indoor environment, the outdoor experiment is challenging due to presence of wind, dust, different light conditions, and various obstacles. The wind reaches the value of 3-5 at the Beaufort scale being able to shake tree branches, straighten waving ribbon (see Figure 6-3c), shake the crane's jib, i.e., the suspension point, and tilt the platform for 2-3 degrees around roll and pitch angles.

For the indoor and outdoor environments: the suspension point and the hook correspond to the two passive spherical joints; the hook structure has a passive DOF around the yaw, i.e., the hook itself can rotate around the hook base; the crane chain can twist around a vertical axis.

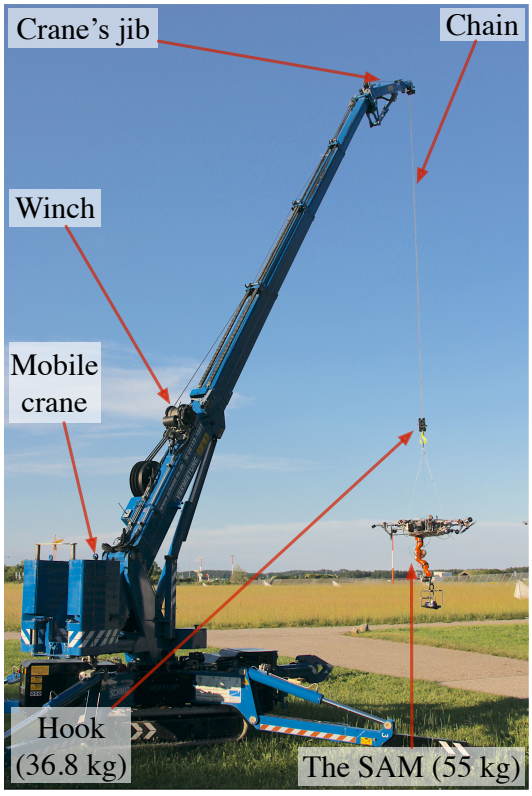

(a) Transformed crane

(b) Crane as the mobile platform

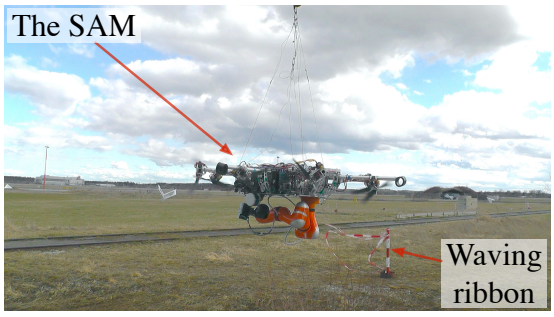

(c) Waving ribbon indicates the strong wind

Figure 6-3: Outdoor environment.

[2]https://www.hoeflon.com
[3]Wind data is obtained from https://www.meteoblue.com on 13.03.2021-19.03.2021.

Parameter	**Value**	**Unit**
Hook weight	36.86	kg
Length of the chain	5.6	m
Distance from the hook to the platform	1.9	m
Wind speed	10-35	$\frac{\text{km}}{\text{h}}$

Table 6.3: Weight-geometric parameters of the outdoor setup.

6.2 Frequency-based model validation

In subsection 4.2.1, we assumed to consider a crane-stationed cable-suspended aerial manipulator as a double pendulum. To see the validity of this assumption, we investigate oscillation modes (eigen- or natural frequencies) of the real hardware during the free motion after an external stimulation. To this end, we pulled the SAM to the side from the equilibrium point and then released to force it oscillating. Afterward, we applied the FFT to the collected onboard angular velocity in order to obtain a power spectrum and determine the eigenfrequencies of the system dynamics. As will be shown, in the resulted spectrum there exist two dominant frequency modes, and therefore, it is reasonable to model the system as a double pendulum. Based, on the oscillation frequencies, we calculated the optimal control gains for the control law (4.14) similar to the process described in subsection 4.3.5. Since in the experimental validation, we conduct tests utilizing the indoor and outdoor environments with different weight-geometric characteristics, we investigate them separately. Additionally, it is worth reminding that the obtained oscillation mode frequencies have much lower bandwidth in comparison with the rotational frequency of the spinning propeller (subsubsection 3.3.1.6), so there is no risk of a resonance.

Indoor environment

Oscillation mode frequencies ν_{slow} and ν_{fast} were obtained by oscillating the indoor setup with no actuation, see Figure 6-4. Consequently, the corresponding cutoff frequency for the low-pass filter (4.13) is calculated $\nu_{cutoff} = 0.76$ Hz.

In order to obtain a better understanding behind slow and fast oscillation frequencies, we introduce *normal modes* of the double pendulum, i.e., the motion where

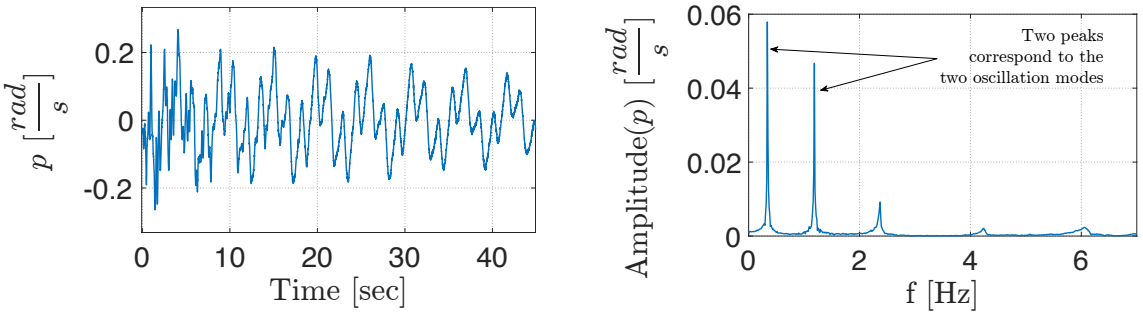

(a) $l_1 = 6$ m (b) $\nu_{slow} = 0.335$ Hz, $\nu_{fast} = 1.185$ Hz

Figure 6-4: Time-varying signal (left) of the angular velocity around x_b axis and corresponding single-sided amplitude spectrum (right) for the chain length l_1 in indoor setup. The low third eigenfrequency can be noticed. The nature of this frequency was not studied in detail, but we assumed that it corresponds to the wave frequency along the long chain. For lighter (in terms of the weight) chains, this frequency is not presented as it will be shown for the outdoor environment. The data was collected with $\nu_{data} = 107.97$ Hz.

both masses move with the same frequency. In case, if both masses moves with ν_{slow} in exactly same manner, the double pendulum behaves as the single pendulum. On another hand, when both masses oscillates with ν_{fast}, they produce an opposite motion, see Figure 6-5.

Based on conducted frequency analysis, the optimal gains for the OODC were

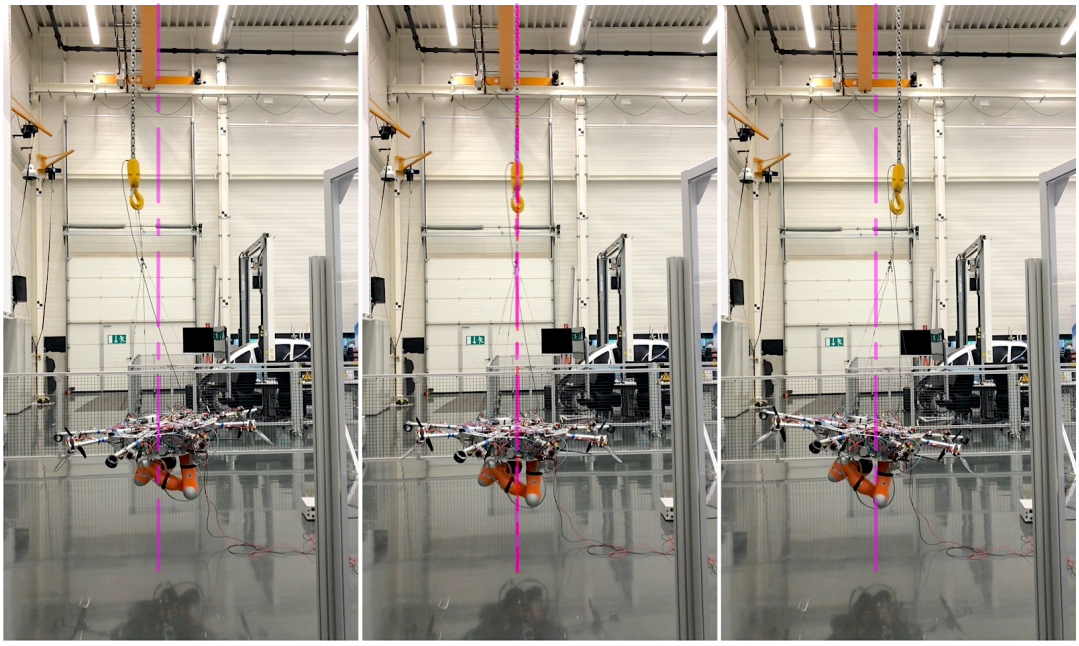

Figure 6-5: Normal mode excitation. Suspension point is fixed, platform changes orientation while keeping the position close to initial. At the same time, the hook appears on both (opposite) sides of the vertical axis.

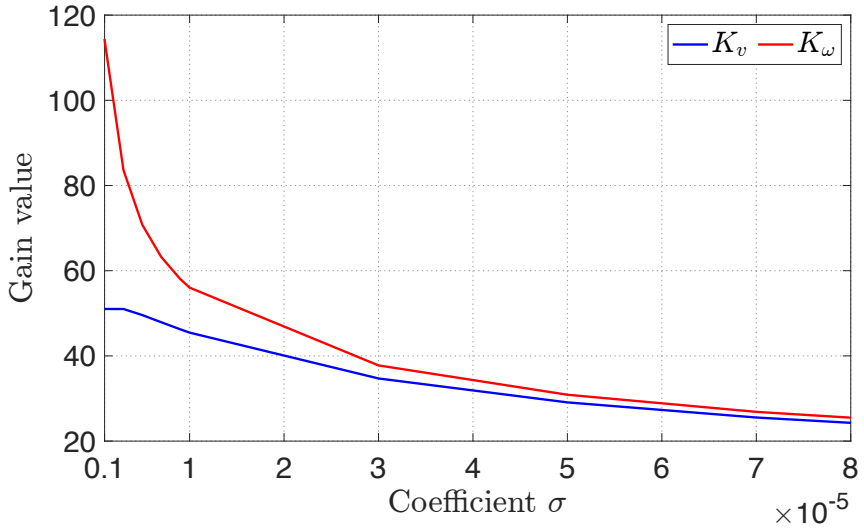

Figure 6-6: Relation between optimal control gains K_v, K_ω and parameter σ for the indoor environment.

calculated as a function of the σ parameter, see Figure 6-6.

Outdoor environment

Since in the outdoor environment we operate with tower-like crane (section 3.2), a free dynamics of the outdoor setup was investigated for various chain length, see Figure 6-7 (All data was collected with $\nu_{data} = 120.56$ Hz). As we can see for the short length of the crane chain $l_1 = 1.2$ m, the system behaves as a single pendulum. Time-domain angular velocity is presented as a sine signal, and corresponding frequency domain spectrum contains only 1 dominant peak for $\nu_{slow} = 0.4393$ Hz. As soon as the chain length exceeds the length of the second pendulum link (1.9 m), the system starts to demonstrate the double pendulum behavior. It fully conforms to the discussed theory, see subsection 4.2.3. It is worth mentioning that the linear density of the chain in mobile crane is less than for the overhead crane exploited in the indoor environment. To this end, the frequency domain contains only two peaks corresponding to the double pendulum motion without the wave-related frequency.

Due to internal damping in the double pendulum motion, the time transient signal is damped. However, since the damping value in the non-actuated system is very low, the signal demonstrates the periodic motion with decreasing amplitude. The peaks in the corresponding FFT represent the eigenfrequencies while the smear around the peak shows the sine wave decay. The slower the decay, the narrower the smear.

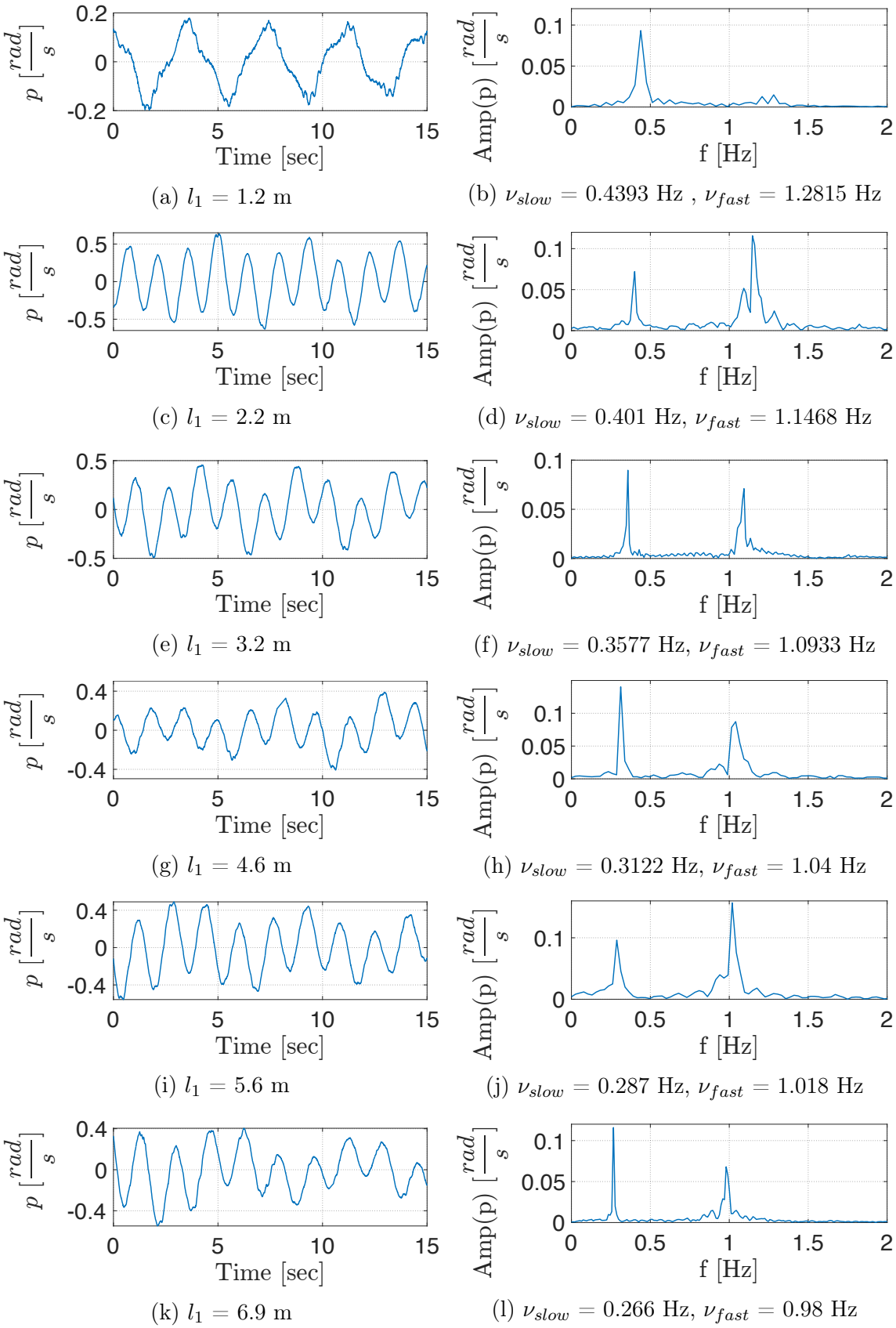

(a) $l_1 = 1.2$ m

(b) $\nu_{slow} = 0.4393$ Hz , $\nu_{fast} = 1.2815$ Hz

(c) $l_1 = 2.2$ m

(d) $\nu_{slow} = 0.401$ Hz, $\nu_{fast} = 1.1468$ Hz

(e) $l_1 = 3.2$ m

(f) $\nu_{slow} = 0.3577$ Hz, $\nu_{fast} = 1.0933$ Hz

(g) $l_1 = 4.6$ m

(h) $\nu_{slow} = 0.3122$ Hz, $\nu_{fast} = 1.04$ Hz

(i) $l_1 = 5.6$ m

(j) $\nu_{slow} = 0.287$ Hz, $\nu_{fast} = 1.018$ Hz

(k) $l_1 = 6.9$ m

(l) $\nu_{slow} = 0.266$ Hz, $\nu_{fast} = 0.98$ Hz

Figure 6-7: Angular velocity around x_b axis (left) and corresponding single-sided amplitude spectrum (right) for various chain lengths l_1 in the outdoor setup. Amp stands for Amplitude.

The optimal control gains for the OODC in the outdoor setup were obtained for the various cable chain length l_1 depending on the parameter σ, see Figure 6-8. It is worth noting that for the short crane chain lengths, the linear gain K_v has a concave shape.

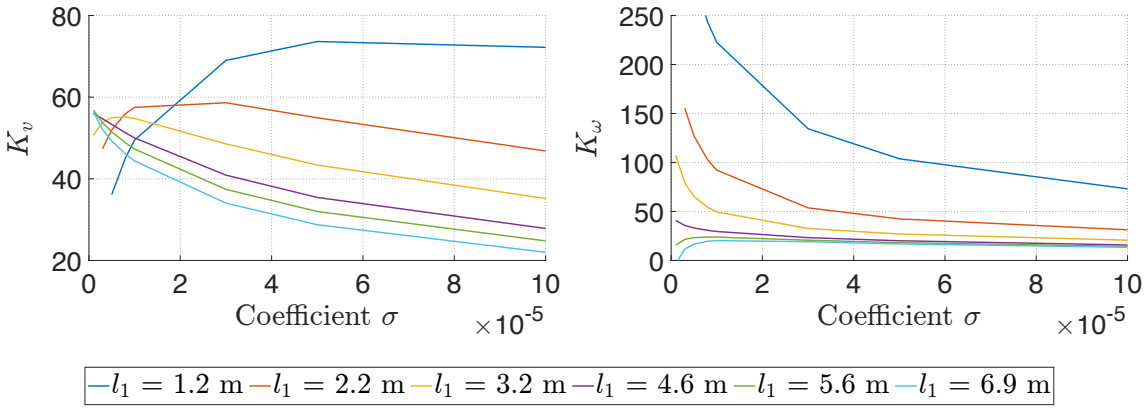

Figure 6-8: Relation between optimal control gains K_v (left), K_ω (right) and parameter σ for the various lengths of the first link l_1.

6.3 Geometric yaw controller

In order to validate an applicability of the geometric yaw controller described in Appendix A, an experiment for the setpoint yaw regulation of the SAM system using propeller-based actuation in the outdoor environment was conducted. The most significant performance criteria include the settling time and steady-state error.

The selected control gains are shown in the Table 6.4. Here, $K_{p,yaw}$ is $\boldsymbol{k_R}(3,\ 3)$, and $K_{d,r}$ is $\boldsymbol{k_\omega}(3,\ 3)$, i.e., control gains corresponding to the yaw channel of the control law (A.1). The $\mathcal{PD}$ gains are selected to demonstrate a slightly over-damped behavior.

As it can be seen in Figure 6-9, during the experiment the SAM followed the desired set of yaw angles [10, 40, 85, 10] degrees. The yaw angle of the platform

Gain	**Value**
$K_{p,yaw}$	21
$K_{d,r}$	29.28

Table 6.4: Geometric yaw controller gains.

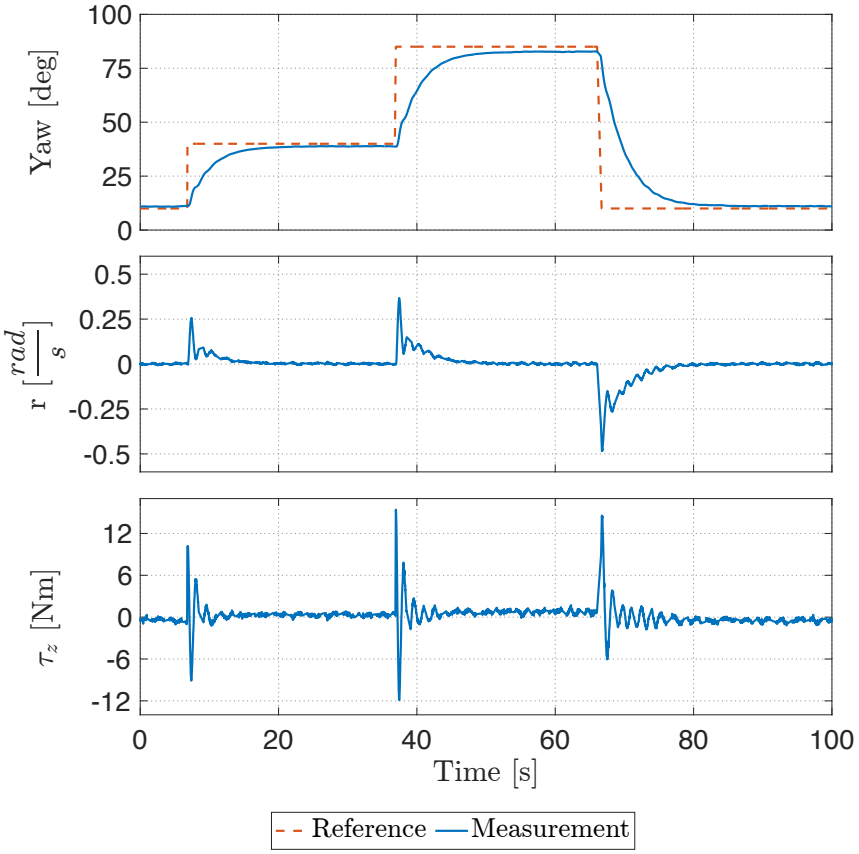

Figure 6-9: Results of the experiment: geometric yaw control. At $t = 0$ s, the SAM is located in the initial configuration of 10 deg, while at $t = 60$ s, the SAM is turned around vertical axis to 85 deg. The data was collected with $\nu_{data} = 26.42$ Hz.

converged to the desired setpoint, while the angular velocity r converged to the zero. The corresponding control torque τ_z of the (A.1) applied to the platform around the vertical axis is shown in the same figure (bottom plot).

Processing the results of the first step response of the platform, i.e., the turn from

(a) $t = 0$ s (b) $t = 60$ s

Figure 6-10: Illustration of the experiment: geometric yaw control. Configurations of the SAM platform at $t = 0$ s and at $t = 60$ s are shown. The purple dashed circle denotes the location of the landing pad.

10 to 40 degrees, the settling time (5%) of 12.6 seconds is estimated, while steady state error did not exceed 1.2 degrees. Such an error can be reduced by deriving more precise dynamic model and extending the control law with an integral term.

Figure 6-10 depicts the SAM platform configuration before and after yaw rotation. Shown results validate that the SAM yaw channel can be successfully controlled with a geometric yaw controller.

6.4 Optimal oscillation damping controller (OODC)

To corroborate simulation results, extensive experimental validation is carried out for the OODC. Namely, six experiments are conducted for the actuated platform:

- case of the robotic arm motion in the outdoor environment,
- case of the external disturbances in the indoor environment,
- case of the suspension point motion in the outdoor environment,
- case of the varying chain length in the outdoor environment,
- case of the single pendulum behavior (short chain length) in the outdoor environment,
- case of the switching between single and double pendulum controllers in the outdoor environment.

Motivated by the simulational studies in (4.3.6), the optimal control gains are chosen for the $\sigma = 5e^{-6}$ and presented in the Table 6.5. The main performance criterion is a dampening time. It is worth reminding that the gains are selected

Environment	**Gain**	**Value**
Outdoor setup	$K_{w,x} = K_{w,y}$	29.28
($l_1 = 5.6$ m)	$K_{v,x} = K_{v,y}$	54.35
Indoor setup	$K_{w,x} = K_{w,y}$	70
	$K_{v,x} = K_{v,y}$	48

Table 6.5: Optimal oscillation damping controller gains for $\sigma = 5e^{-6}$.

optimally to keep the balance between performance and power consumption. So, the controller might response in a more rigid (fast) way id needed by varying the weighing matrices $\boldsymbol{Q}$ and $\boldsymbol{R}$ in (4.17).

6.4.1 Case of the robotic arm motion

In this experiment, we investigate the behavior of the SAM platform while the robotic arm performs a jerky motion. To this end, the robotic arm end effector was controlled by the operator to follow the trajectory depicted in Figure 6-11. During

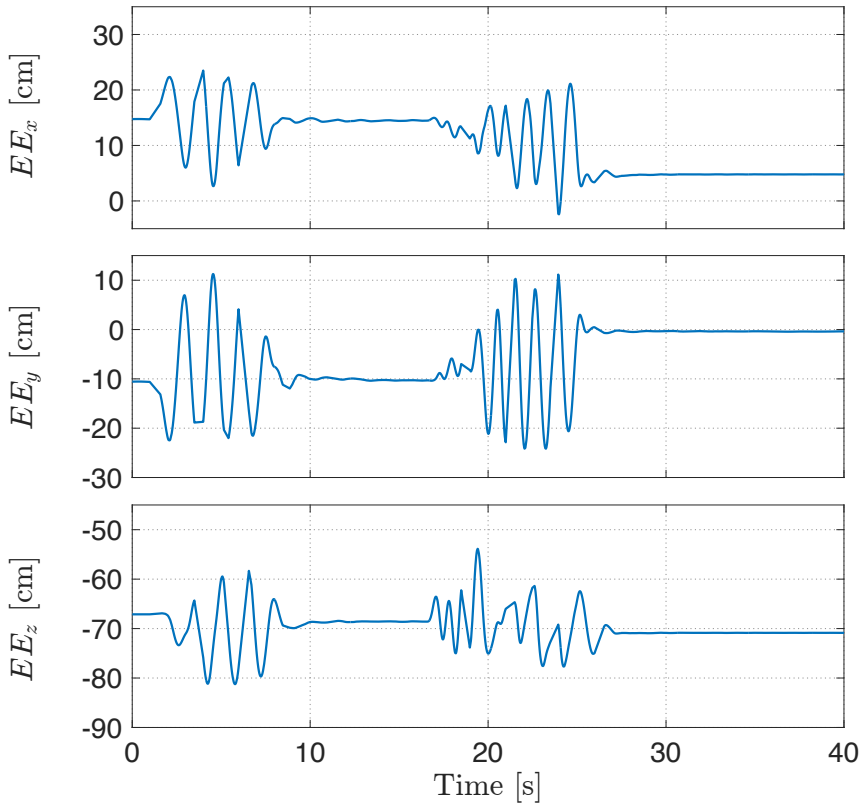

Figure 6-11: Results of the experiment: robotic arm motion. Robotic arm end effector position.

this motion, the joint velocities reached relatively high values of 2 $\frac{\text{rad}}{\text{s}}$ as shown in Figure 6-12. It is worth noting that in the real manipulation mission, the arm does not move so fast. Investigation of the arm jerky motion helps us to analyze a robustness to uncertainties of the proposed controller.

As a result, the propeller-based actuation dampened all disturbances caused by robotic arm motion during roughly 8 seconds while keeping the desired yaw angle of 130.89 degrees, see Figure 6-13. The corresponding angular velocities of the platform converged to the zero. As shown in Figure 6-14, an OODC-generated wrench (4.14)

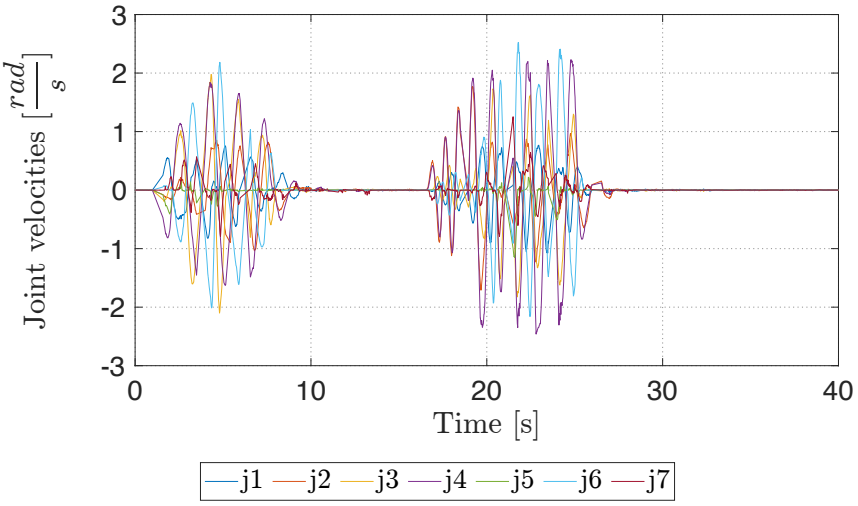

Figure 6-12: Results of the experiment: robotic arm motion. Robotic arm joint velocities.

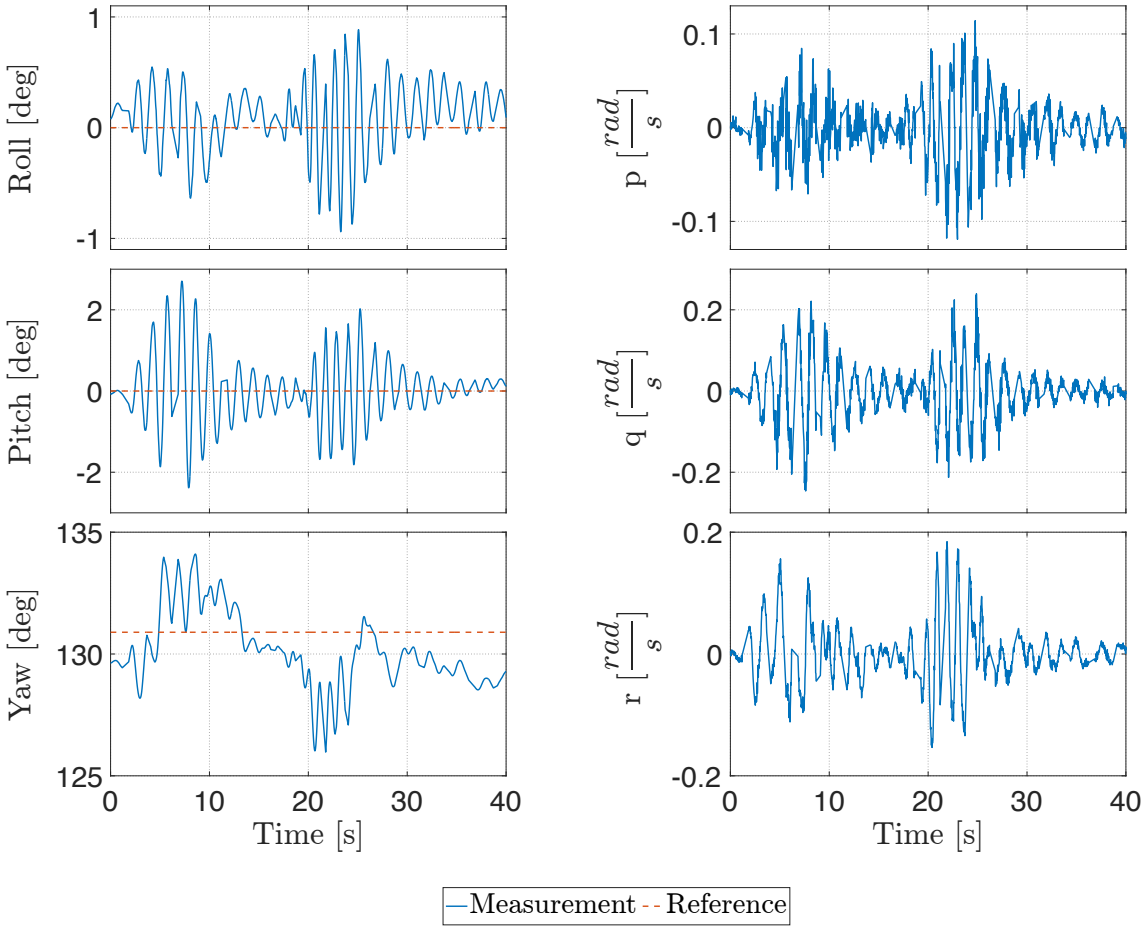

Figure 6-13: Results of the experiment: robotic arm motion. Roll, pitch, and yaw angles of the platform are depicted on the left, and corresponding angular velocities are shown on the right.

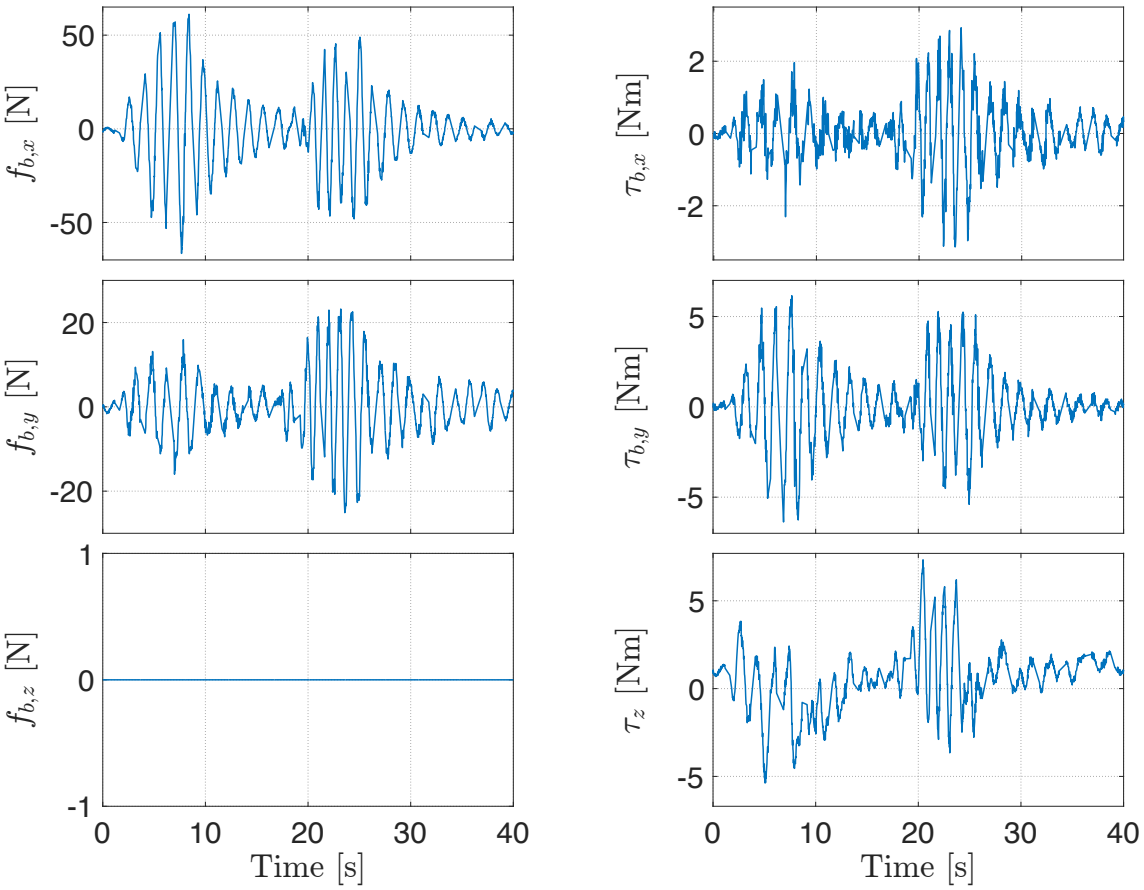

Figure 6-14: Results of the experiment: robotic arm motion. Generated wrench by propeller-based actuation.

includes the body forces $f_{b,x}$, $f_{b,y}$ and torques $\tau_{b,x}$, $\tau_{b,y}$ corresponding to the x_b and y_b axes, while the geometric yaw controller (A.1) generates the τ_z torque. All data was collected with $\nu_{data} = 33.13$ Hz.

6.4.2 Case of the external disturbances

In this experiment conducted in the indoor environment, the human operator applied external disturbance to excite the SAM by pulling and releasing the rope attached to the landing pad, while the controller was trying to dampen any oscillations. As shown in Figure 6-15, the controller quickly damped out the oscillation within 7 seconds, and the SAM gradually in underdamped manner converged to zero point keeping desired yaw as 25 degrees. Correspondingly, the angular velocities converged to zero.

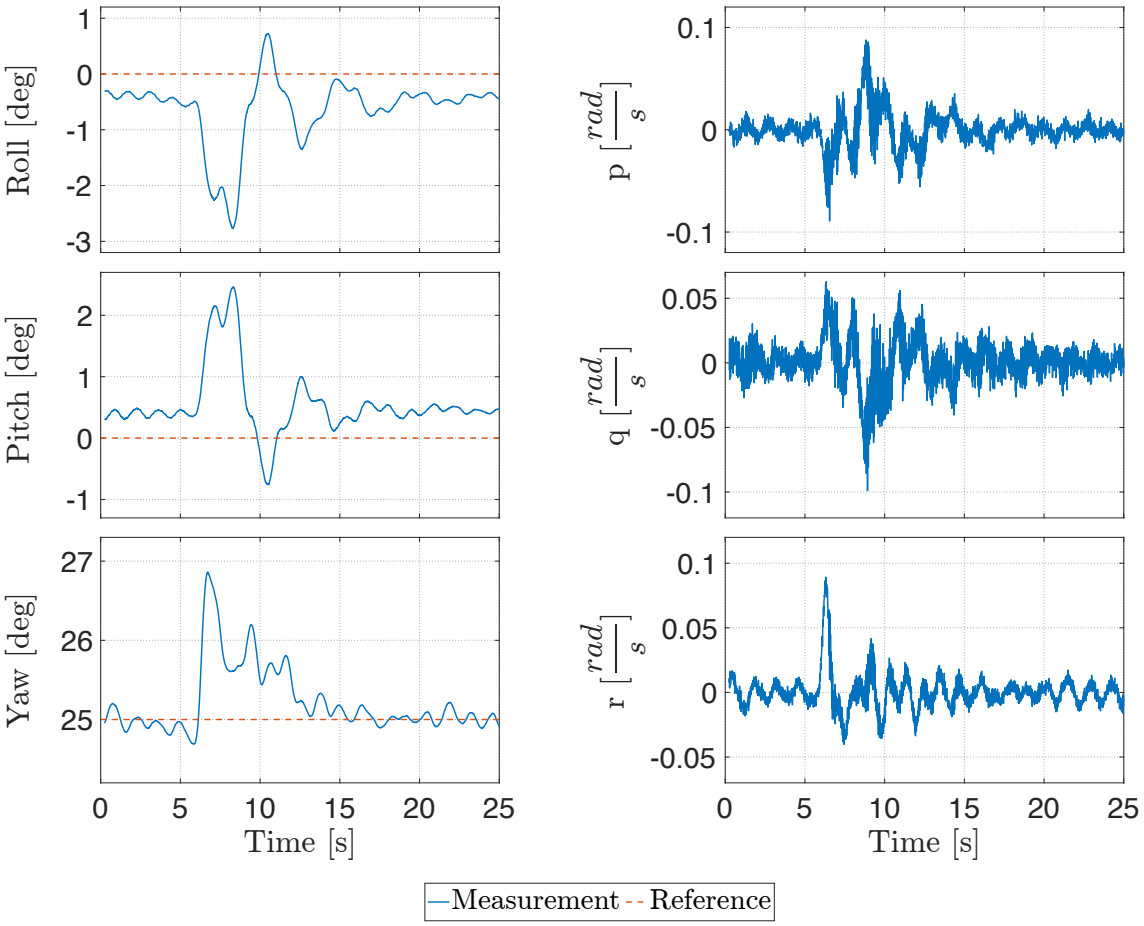

Figure 6-15: Results of the experiment: applying of the external disturbances. Roll, pitch, and yaw angles of the platform are depicted on the left, and corresponding angular velocities are shown on the right. The data was collected with $\nu_{data} = 107.91$ Hz.

6.4.3 Case of the suspension point motion

In order to validate robustness of the OODC to the suspension point motion, we moved the crane with switched off (passive platform) and switched on (active platform) propeller-based actuation. Namely, the crane was turned roughly for 90 de-

(a) Initial configuration (b) Middle configuration (c) Final configuration

Figure 6-16: Illustration of the experiment: suspension point motion. Crane direct (clockwise) motion around the vertical axis.

grees around the vertical axis and back in such a way that direct motion was performed with slow speed while return motion was conducted fastly (roughly twice of the slow motion speed). The direct motion is depicted in Figure 6-16. The data was collected with $\nu_{data} = 122.06$ Hz.

6.4.3.1 Passive platform

Firstly, we turned the crane while the platform was switched off, see Figure 6-17. It can be seen, that after slow crane motion (green zone), the platform oscillation did not exceed 2 degrees around roll and pitch, while the fast motion (red zone) caused oscillation of 4-5 degrees around the same axes.

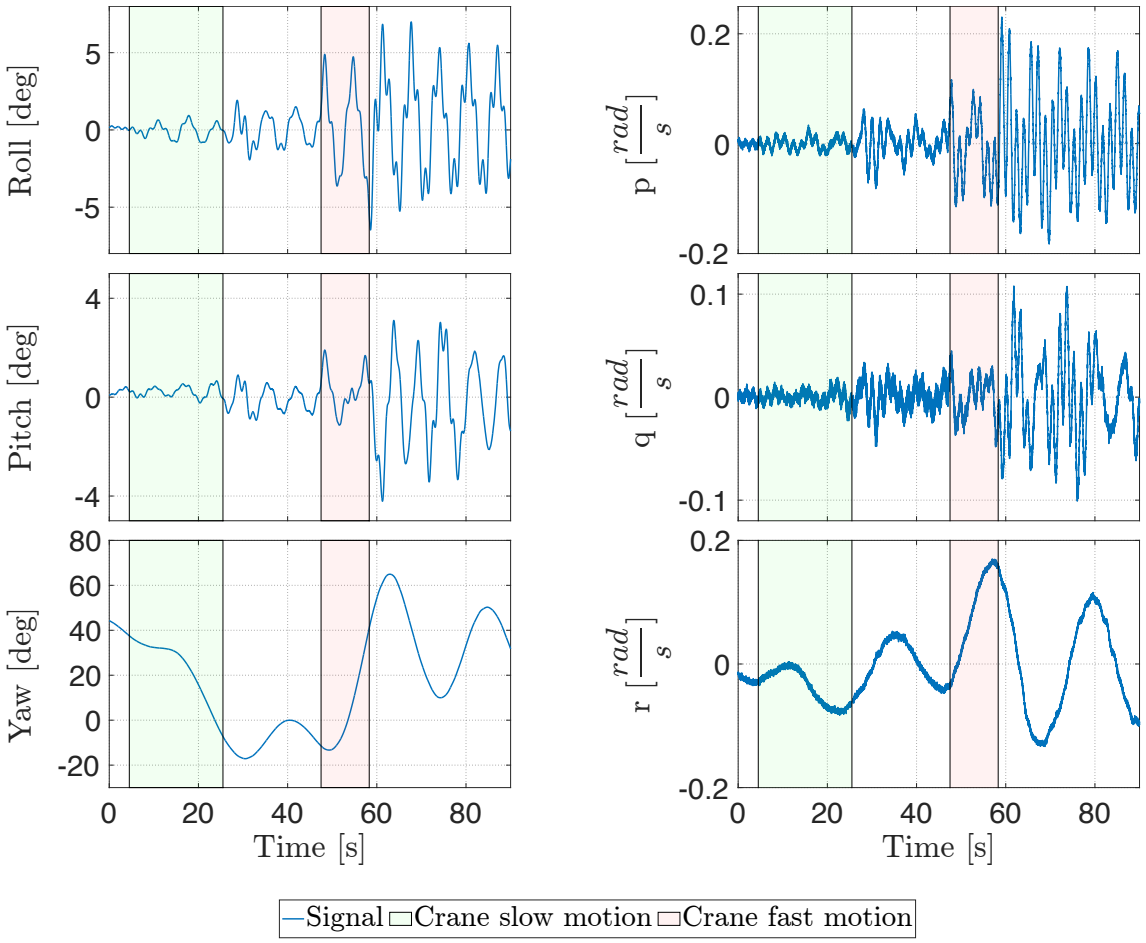

Figure 6-17: Results of the experiment: suspension point motion for the passive platform. Roll, pitch, and yaw angles of the platform are depicted on the left, and corresponding angular velocities are shown on the right.

6.4.3.2 Active platform

Secondly, we switched OODC on, and repeated the same experiment. It can be seen in Figure 6-18, that after the end of the slow and fast motion period, the controller dampened all oscillations within 9 seconds while keeping yaw angle close to the desired at 35 degrees. At the same time, oscillations around roll and pitch reached maximum 2.2 degrees.

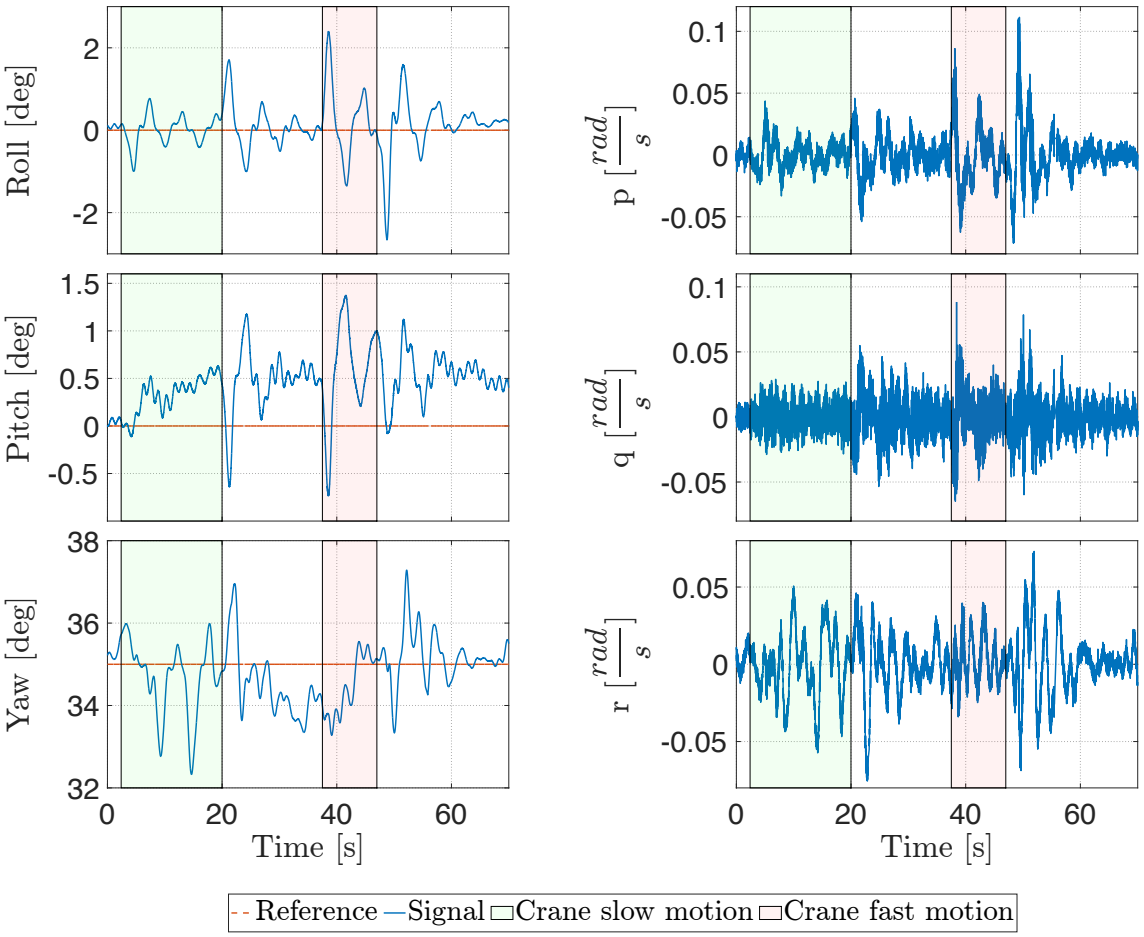

Figure 6-18: Results of the experiment: suspension point motion for the active platform. Roll, pitch, and yaw angles of the platform are depicted on the left, and corresponding angular velocities are shown on the right.

6.4.4 Case of the varying chain length

In order to further investigate robustness of the OODC to the system uncertainties, i.e., evaluate the sensitivity to the varying parameters, we tuned the controller for the crane chain length $l_1 = 5.6$ meters and then lifted the hook up (yellow zone) by reducing the cable length till $l_1 = 2$ meters. Afterward, we repeated previous

(a) Lowered configuration (b) Lifted configuration (c) Lifted and turned configuration

Figure 6-19: Illustration of the experiment: varying chain length. The SAM lifting and direct (clockwise) rotation around vertical axis was performed by the crane.

experiment with turning suspension point clockwise with slow speed and counter-clockwise with the fast speed around the vertical axis, see Figure 6-19. Moreover, in the middle of the fast (return) motion at t = 90 second, the crane was suddenly shut down and turned on again (dark blue zone), see Figure 6-20. In the end, the hook was lowered down (yellow zone) till original $l_1 = 5.6$ meters. So, it can be seen that even for not properly tuned controller, the performance remained reasonable, and OODC dampened oscillations caused by slow and fast motion within 9-13 seconds while keeping the desired yaw angle of 65 degrees.

6.4.5 Case of the short chain length

After reducing the length of the crane chain, i.e., setting it equal to the second link length, $l_1 = 1.9$ meters, we conducted the crane motion similar to described in subsection 6.4.3. First, the slow clockwise motion (green zone) was performed by crane around the vertical axis, after that the fast return motion (red zone) was conducted. The control gains for the control law (C.1) of the single pendulum are shown in Table 6.6. Here, $K_{p,x}$ is the $\boldsymbol{K}_{\mathrm{p}}(1,\ 1)$, $K_{p,y}$ is the $\boldsymbol{K}_{\mathrm{p}}(2,\ 2)$, $K_{v,x}$ is the

Gain	**Value**
$K_{p,yaw}$	21
$K_{d,r}$	45
$K_{p,x} = K_{p,y}$	3.82
$K_{v,x} = K_{v,y}$	54.18

Table 6.6: Oscillation damping controller gains for the single pendulum case.

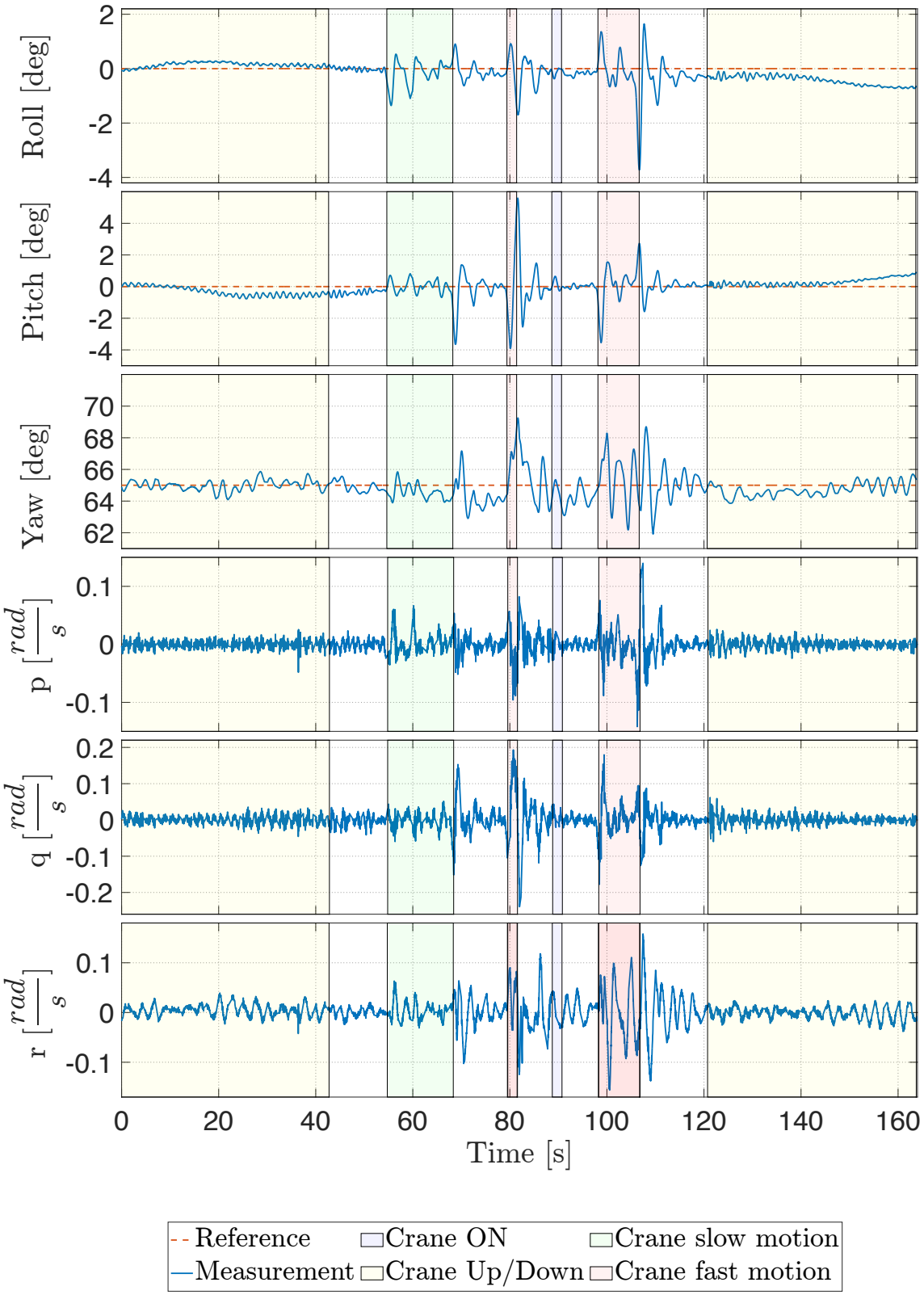

Figure 6-20: Results of the experiment: varying chain length. Roll, pitch, and yaw angles of the platform are depicted on the top, and corresponding angular velocities are shown in the bottom. The data was collected with $\nu_{data} = 31.67$ Hz.

$\boldsymbol{K}_{\mathrm{v}}(1,\ 1)$, and $K_{v,y}$ is the $\boldsymbol{K}_{\mathrm{v}}(2,\ 2)$ for the control law (C.1). The data was collected with $\nu_{data} = 35.5$ Hz.

The results of the experiment with passive platform are shown in Figure 6-21, while results of the same experiment with the active platform are depicted in

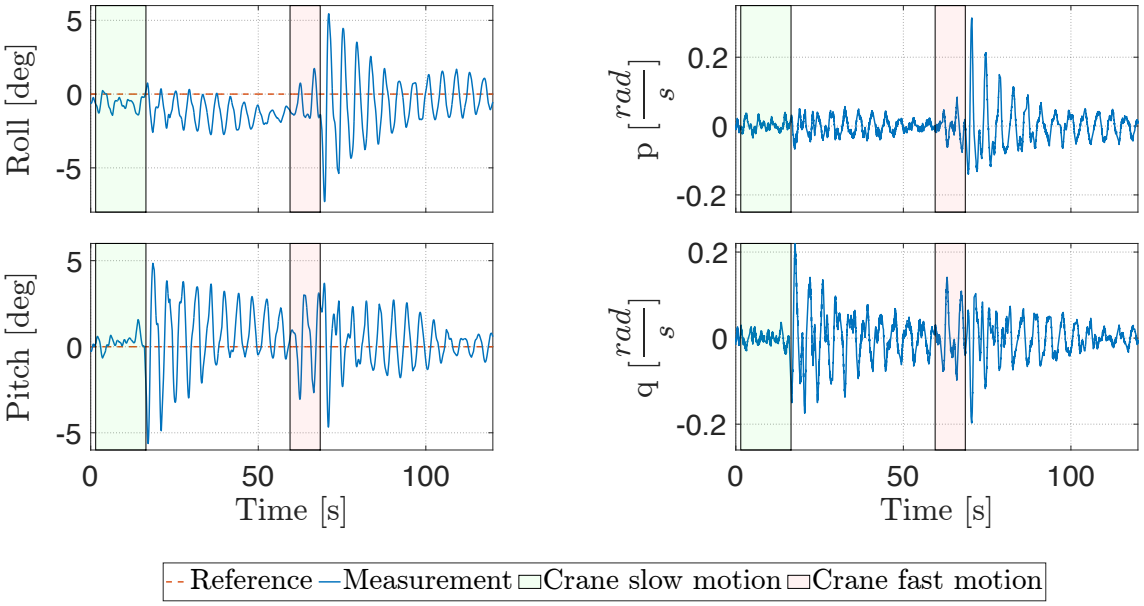

Figure 6-21: Results of the experiment: single pendulum case of the passive platform. Roll and pitch angles of the platform are depicted on the left, and corresponding angular velocities are shown on the right.

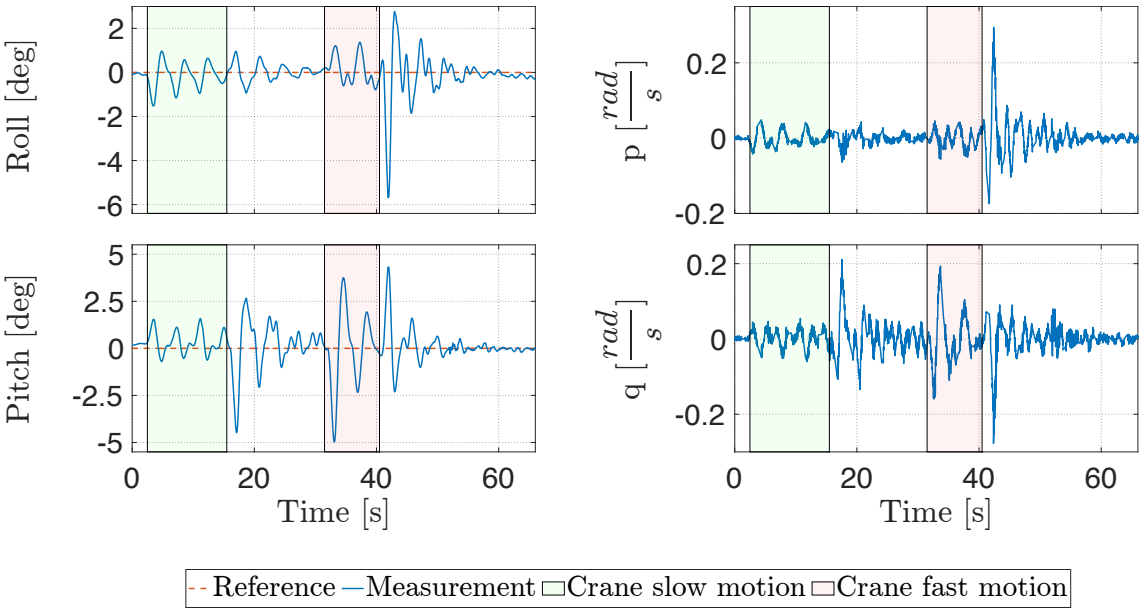

Figure 6-22: Results of the experiment: single pendulum case of the active platform. Roll and pitch angles of the platform are depicted on the left, and corresponding angular velocities are shown on the right.

Figure 6-22. It is seen that for the passive platform after motion stop, the platform started to oscillate with slowly decaying rate, while the active platform dampened oscillations within 8 seconds.

6.4.6 Case of the switching controllers

The last experiment in the validation of the OODC is aimed at the investigation of the switching transient between OODC and oscillation damping controller for the single pendulum. During the experiment, the system started at the lowered configuration with $l_1 = 5.6$ meters with active OODC as shown in Figure 6-19 (a). Then, at t = 12 seconds, the system was lifted up till $l_1 = 1.9$ meters as shown in Figure 6-19 (b). At this moment, the controllers were switched between each other, so the control law (4.14) was switched to the (C.1). As it can be seen in Figure 6-23, the switching did not affect performance, and the total angle error along roll and pitch remained within 1 degree.

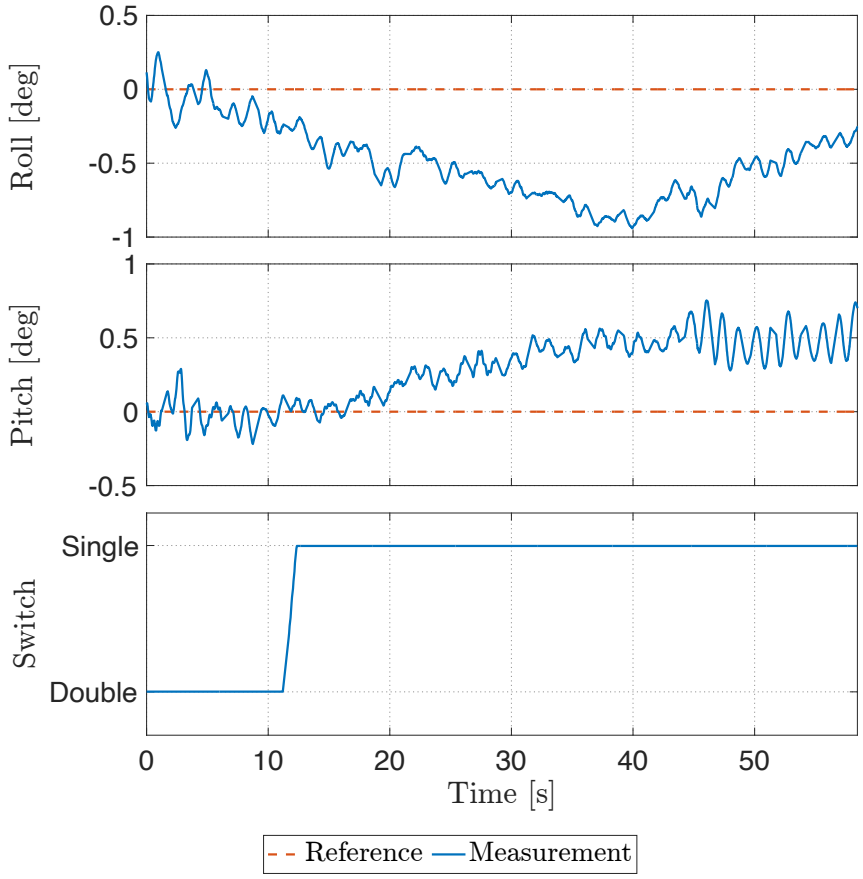

Figure 6-23: Results of the experiment: switching between single and double pendulum controllers. The data was collected with $\nu_{data} = 39.65$ Hz.

6.5 Hierarchical impedance-based whole-body controller (HWBC)

In order to investigate the winch-based actuation performance and validate proposed control law (5.18) for the HWBC, we conduct three experiments in the RMC laboratory:

- arbitrary motion of the end effector,
- pure vertical motion of the end effector,
- pick and place of the cage for the mobile robot.

In the first two experiments, the robotic arm motion is preprogrammed to follow a specific trajectory, while in the third one, it is controlled manually by the operator.

The SAM dynamics for the reduced state $\boldsymbol{\gamma}$ is simulated onboard in the Luca Dynamics environment (subsection 2.1.4) which provides required task Jacobians (5.9), $\boldsymbol{J}_1$, $\boldsymbol{J}_2$, and $\boldsymbol{J}_3$, in real-time based on the model (5.8) with mass-inertia parameters presented in Table 6.7. In all experiments, the platform was manually stabilized before the start, and propellers were used only to keep the constant yaw angle without applying the oscillation damping. Since experiments are conducted in the laboratory, the system behaves as the single pendulum, so the initial manual

Node	Mass [kg]	I_{xx} [kg m^2]	I_{yy} [kg m^2]	I_{zz} [kg m^2]
Platform	30	4.2	4.2	8.4
Link 1	2.71	0.078	0.077	0.006
Link 2	2.71	0.031	0.005	0.031
Link 3	2.54	0.160	0.160	0.005
Link 4	2.50	0.033	0.005	0.028
Link 5	1.30	0.085	0.085	0.026
Link 6	1.57	0.004	0.003	0.004
Link 7	2	0.164	0.181	0.073

Table 6.7: Mass and inertia properties of the system utilized in the model.

Controller	Gain	Value
The first task	$\boldsymbol{K}_{Pe}$	$230 \cdot \text{diag}(1.2\ 1.2\ 1.7)$
	$\boldsymbol{K}_{d,trans}$	$20 \cdot \text{diag}(1\ 1\ 1)$
	$\boldsymbol{K}_{Oe}$	$165 \cdot \text{diag}(1\ 1\ 1)$
	$\boldsymbol{K}_{d,rot}$	$10 \cdot \text{diag}(1\ 1\ 1)$
The second task	$\boldsymbol{K}_{Pc}$	$570 \cdot \text{diag}(1\ 1\ 1)$
	$\boldsymbol{K}_{Dc}$	$560 \cdot \text{diag}(1\ 1\ 1)$
Admittance interface	$\boldsymbol{M}_{adm}$	$0.8 \cdot \text{diag}(1\ 1\ 1)$
	$\boldsymbol{D}_{adm}$	$1.6 \cdot \text{diag}(1\ 1\ 1)$

Table 6.8: Hierarchical impedance-based whole-body controller gains.

stabilization is enough to avoid significant oscillations during the experiments. The stiffness and damping matrices of the impedance controller (5.15) for two tasks as well as inertia and damping matrices of the admittance interface (5.16) are presented in Table 6.8. Here, $\boldsymbol{K}_{d,trans}$ and $\boldsymbol{K}_{d,rot}$ are submatrices of the damping matrix $\boldsymbol{K}_{De}$.

It is worth noting that despite complete decoupling between control tasks guaranteed by the controller (5.18), the demonstrated performance is not expected to be perfect. There are several reasons for that:

- the controller relies on the accurate system dynamics model which is hard to obtain:
  - the real system might contain joint friction, backlash, and other uncertainties which are not considered in the model,
  - the real platform tilts which significantly affects the gravity term. Used model-based gravity compensation does not take this tilting into account,
  - the payload of the end effector brings additional uncertainty and should be added in the model as well, e.g., by utilizing FTS,
- the selected control gains are not optimal and can be further tuned for better performance,
- the impedance-based controller is a $\mathcal{PD}$-based controller, so a steady-state

error might remain (increasing a translational stiffness and adding the intergral term should reduce such an error),

- the response of the system is slightly delayed due to use of the admittance interface,
- the intrinsic hardware contains computational error.

Nevertheless, reached performance should be enough to validate approach efficiency. Thus, the main performance criterion is fulfillment of both control tasks: regulating the end effector and nullifying the horizontal terms of the COM. Since the command to the end effector has the time-varied delay, only the value of the second task error (with constant desired value of zero) will be evaluated.

6.5.1 Arbitrary motion of the end effector

During the first experiment, the manipulator end effector moved along the preprogrammed trajectory which lay significantly beyond the common workspace of the SAM platform. The *common workspace* is located strictly below the platform, so any motion on the side of the SAM frame is considered as beyond the workspace. Such a motion should force the system to tilt due to displaced COM under the gravitational field. We conducted this experiment twice with switched winch-based actuation on and off in order to compare behavior. As a result, with operating winches, the end effector reached desired position while COM of the system remained under the suspension point keeping the platform horizontal. At the same time, disabling the winches led to the platform tilting, see Figure 6-24a.

As we can see, for the first control task, the proposed centralised whole-body controller with active winches demonstrated better performance for the translational motion and comparable performance for the rotational motion of the end effector, see Figure 6-25. It is worth mentioning that presented data, related to the robotic arm and platform translational motion, is extracted directly from the real-time model, which does not take into account the tilting of the platform due to gravity. So, the real performance of the system with switched winch-based actuation off is even worse for the first control task.

The second task, as we can see in Figure 6-26, is also fulfilled. With active winches, the platform kept horizontal orientation, while corresponding terms of the COM had close to zero values. Indeed, root mean square error (RMSE) for the

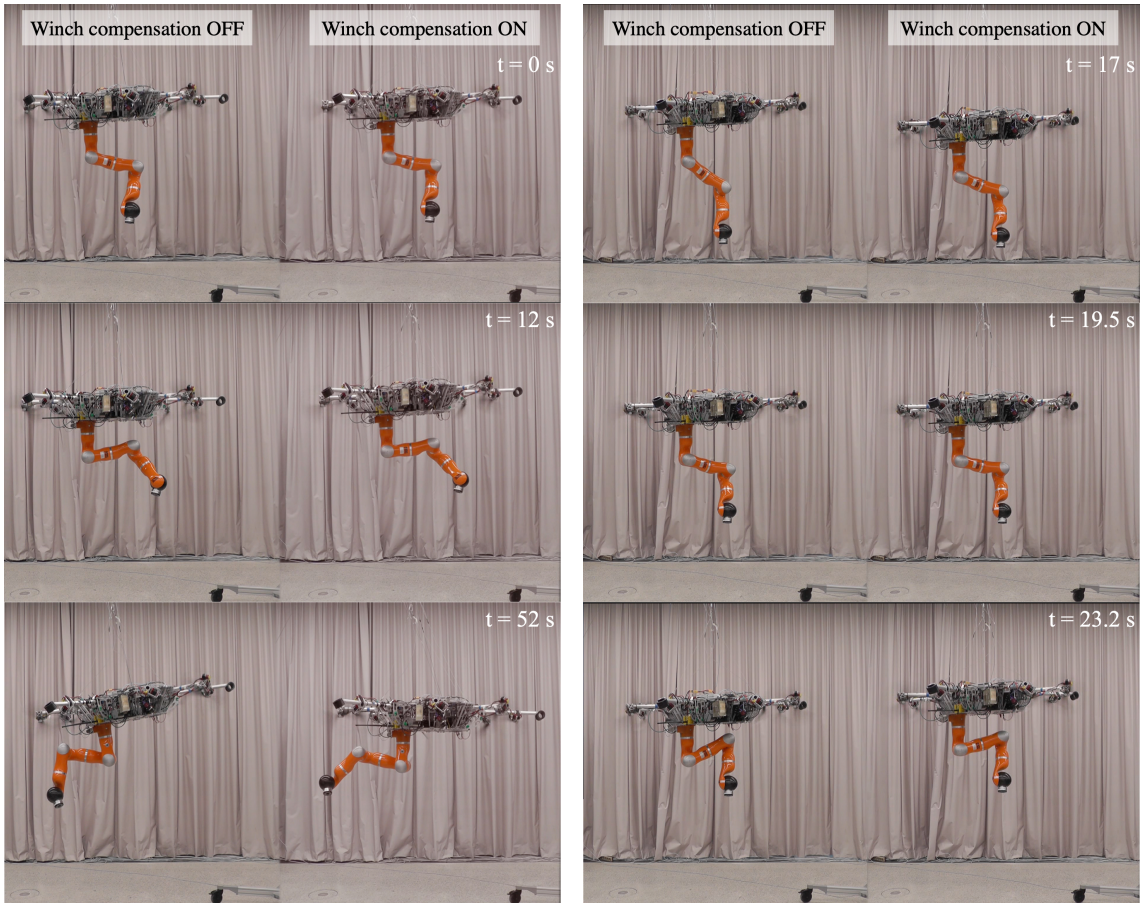

(a) Programmed motion of the end effector along the arbitrary trajectory

(b) Programmed motion of the end effector along the vertical axis

Figure 6-24: Illustration of the experiments: programmed motion of the end effector. Comparative behavior of the system following the same reference trajectory for the end effector with switched HWBC on (right) and off (left) is shown.

second task based on the model data is 0.32 mm along x axis and 0.35 mm along y axis while maximum deviation from zero is 0.9 mm and 1.3 mm along x and y axes, respectively. So, the compensation of the gravitational torque was performed by the platform motion. When we switched HWBC off and repeated the experiment, the result was the opposite: the platform kept zero location while COM was moved. The data was collected with $\nu_{data} = 11.64$ Hz.

6.5.2 Pure vertical motion of the end effector

Integration of the winch-based actuation brought additional redundancy to the manipulation. In order to reach desired position by the end effector, whole-body control distributes efforts among both, robotic arm and winch-actuated platform. To this

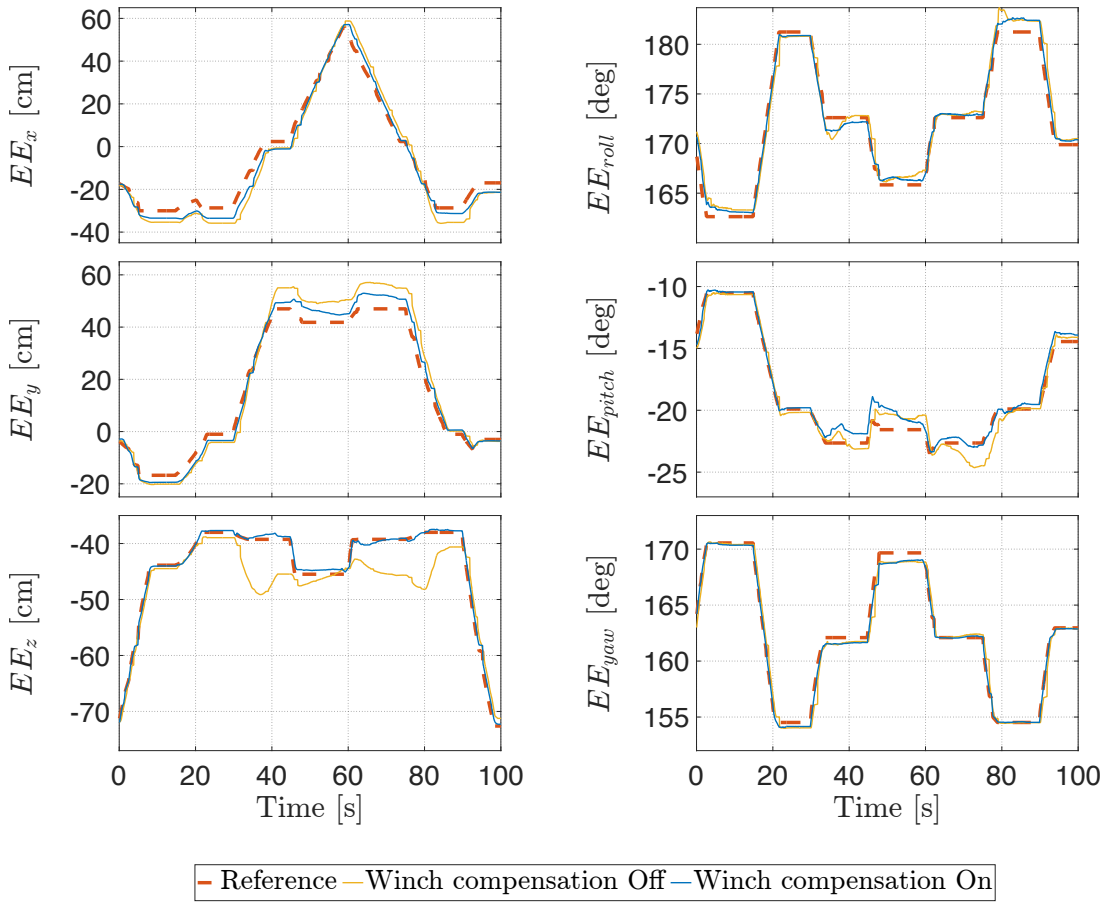

Figure 6-25: Results of the experiment: programmed motion of the end effector along the arbitrary trajectory. First task: comparative behavior of the end effector motion programmed for the same trajectory with and without HWBC.

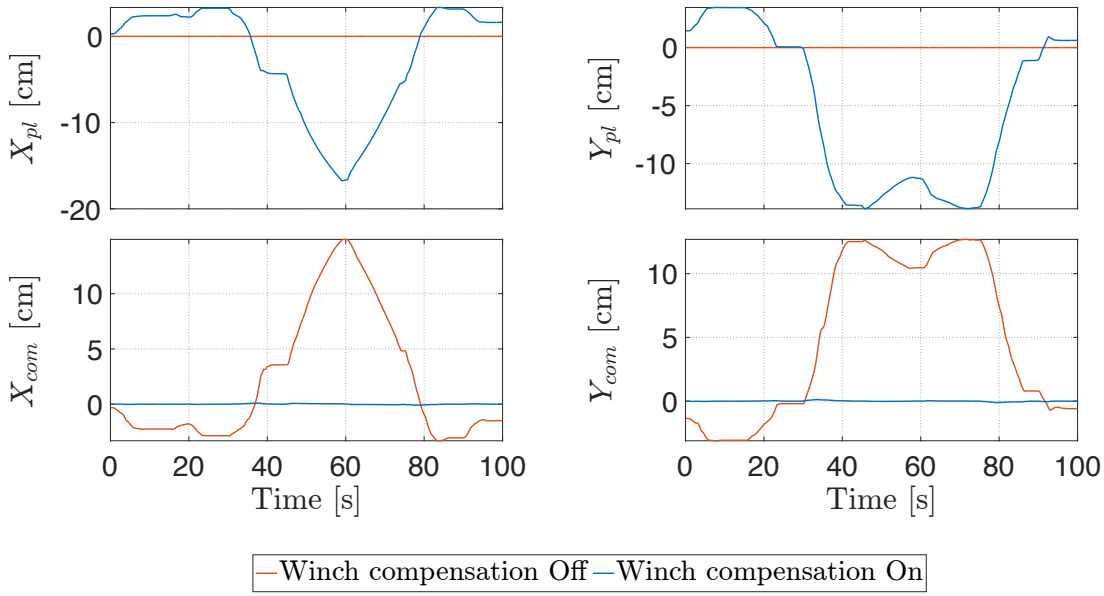

Figure 6-26: Results of the experiment: programmed motion of the end effector along the arbitrary trajectory. Second task: comparative behavior of the platform motion during programmed manipulator motion with and without HWBC.

end, robotic arm performs less motion than it would without winch contribution to reach the same point in the space. It allows to avoid singular configurations for the robotic arm in some directions, in particular, fully stretched configuration in the vertical direction.

To this end, the goal of the second experiment is to analyse changes in the manipulability of the robotic arm. Due to the fact, that usually the SAM performs operations below itself, the biggest manipubalibility degradagtion might be observed along the vertical motion. To this end, we performed preprogrammed jerky motion by cycling the position of the end effector up and down with switched winch-based actuation on and off, see Figure 6-24b. For both experiments, we calculated the manipulability elipsoid for the arm based on (2.5).

As it can be seen in Figure 6-27, the system with active winches followed the commanded trajectory with less error, and a significant contribution was done by

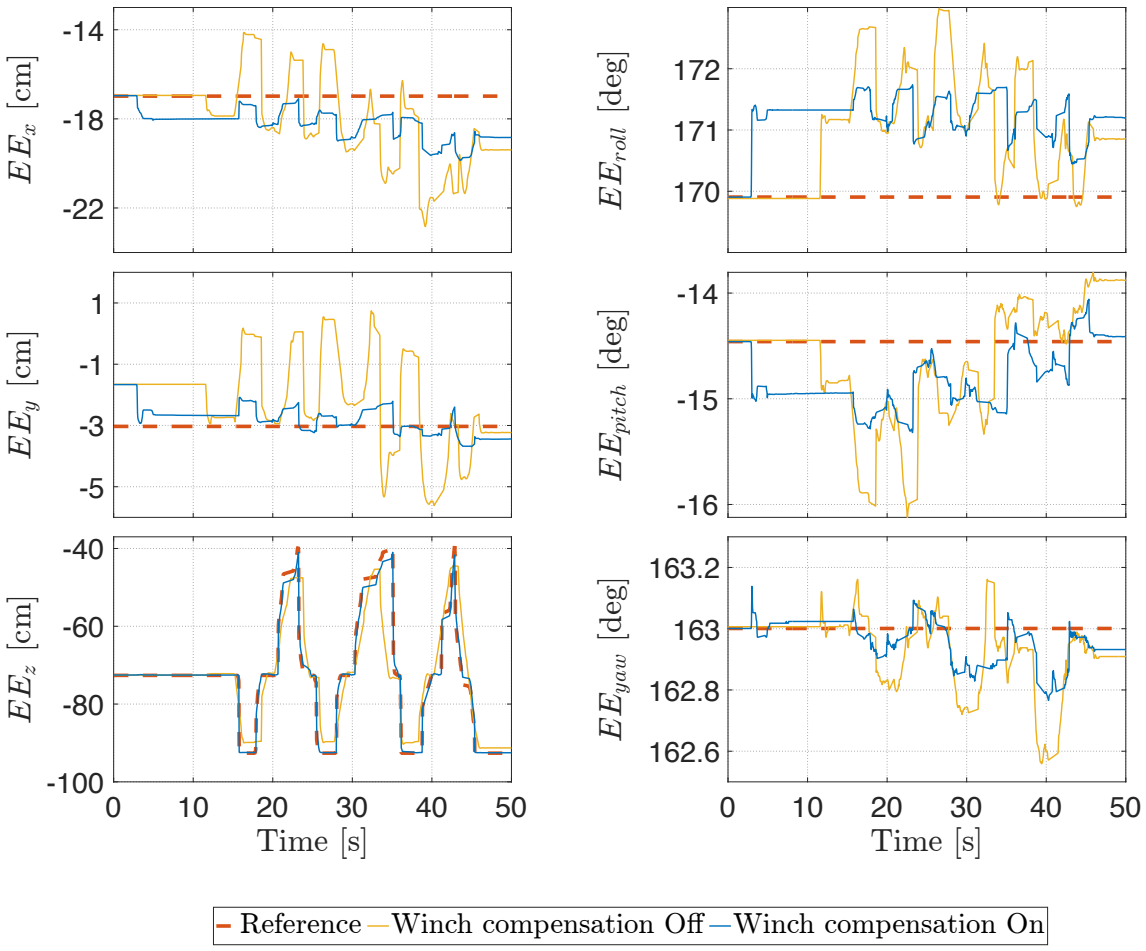

Figure 6-27: Results of the experiment: programmed motion of the end effector along the vertical axis. First task: comparative behavior of the end effector motion programmed for the same trajectory with and without HWBC.

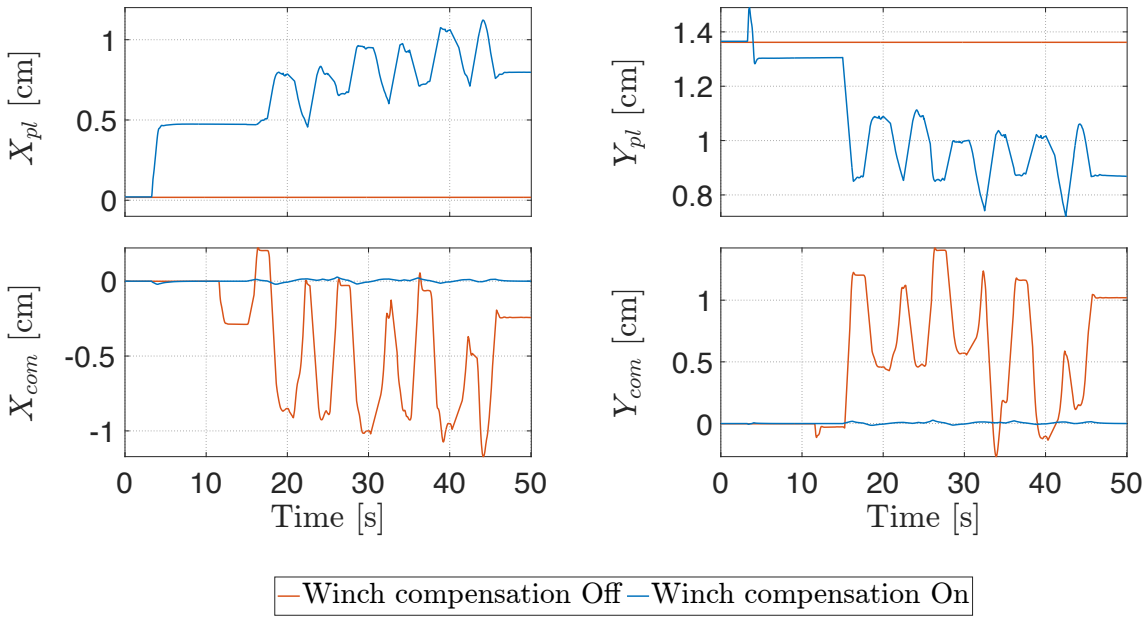

Figure 6-28: Results of the experiment: programmed motion of the end effector along the vertical axis. Second task: comparative behavior of the platform motion during programmed manipulator motion with and without HWBC.

winch-based actuation. Indeed, we can observe in Figure 6-24b that in the system with switched winches off the robotic arm had to move along vertical axis much more in order to fulfill the task: from the almost stretched configuration to the close proximity to the platform. At the same time, in the system with switched winch-based actuation on, the whole-body controller distributed required efforts among the arm and platform moving the robotic arm only slightly around the neutral position. Although the motion of the end effector was strictly vertical, the robotic arm reconfiguration affected the COM displacement as well. With HWBC, the second control task was successfully performed, see Figure 6-28. The RMSE for this task is 0.027 mm along x axis and 0.006 mm along y axis while maximum deviation from zero is 0.20 mm and 0.06 mm along x and y axes, respectively.

It is interesting to notice, that due to internal robotic arm reconfiguration, the manipulability was growing for both cases, with switched winches on and off, see Figure 6-29. When system did not exploit the winches, the robotic arm moved significantly and had lower ellipsoid volume at the bottom configuration (when the arm is almost stretched, see the top picture in Figure 6-24b). At the same time at the top configuration, it had higher volume of the manipulability elispoid due to possibility to reconfigure itself in more ways. However, in this case the arm elbow was located in close proximity to the platform which might cause undesired collision

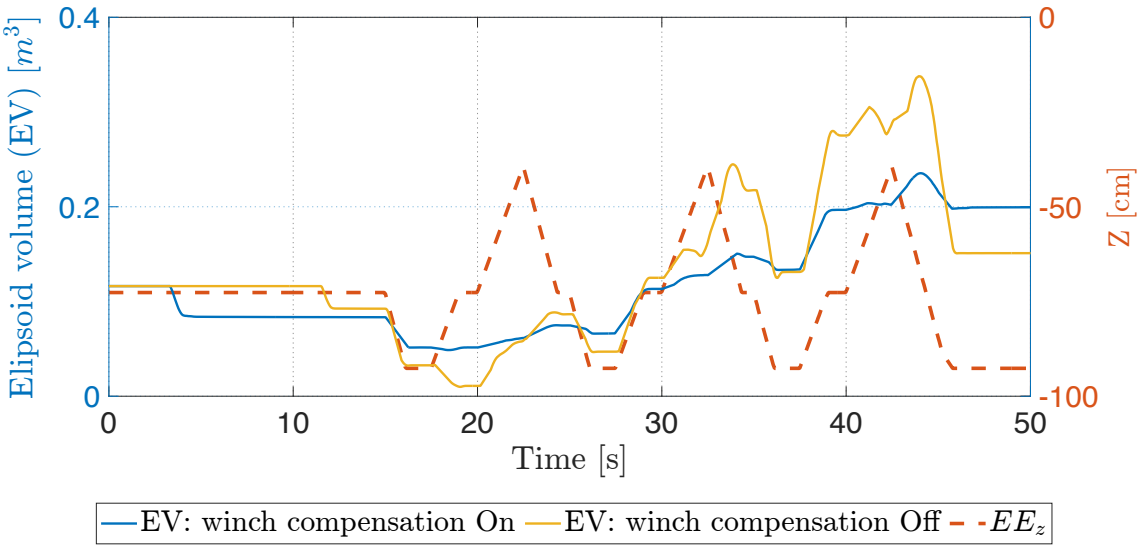

Figure 6-29: Results of the experiment: programmed motion of the end effector along the vertical axis. Manipulability analysis: comparative robotic arm manipulability during programmed manipulator motion with and without HWBC versus Z end effector command. EV stands for the ellipsoid volume.

for certain end effector commands. The data was collected with $\nu_{data} = 12.55$ Hz.

6.5.3 Pick and place

In order to validate applicability of the total framework, the pick and place mission was conducted. The task was to pick and move the empty cage from the metallic case to the pipe. At the tip of the end effector, the 3D-printed hook was installed, that can pick up the special fixture attached to the cage. The snapshots of the mission are depicted in Figure 6-30. In this experiment, the end effector was controlled remotely by unprepared operator using joystick with force feedback. Such an approach is considered as real one for the system control, i.e., the shared control [Abbink et al., 2018, Coelho et al., 2021, Quere et al., 2020] when the operator is responsible for certain tasks, and the rest tasks are performed automatically. The data was collected with $\nu_{data} = 44.16$ Hz.

From the snapshots it can be seen that platform kept its own orientation close to the horizontal while height of the platform was adapting to assist the robotic arm: winches pulled the platform up and down in order to reduce stretching of the manipulator. In Figure 6-31, the commanded trajectory and real motion of the end effector is presented. The trajectory can be described by several steps:

- t = 0-60 s: initial positioning,

- t = 60-80 s: leveling the hook with the fixture at the cage,
- t = 80-120 s: preparing to pick up the cage keeping the hook parallel to the fixture,
- t = 120-150 s: picking the cage up and lifting it,

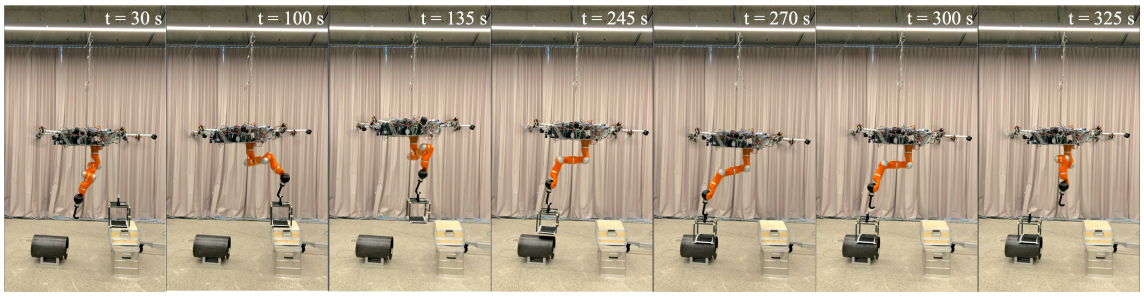

Figure 6-30: Illustration of the experiment: pick and place of the cage for the mobile robot. Snapshots demonstrate the process of picking the cage at metalic box and placing it at the pipe.

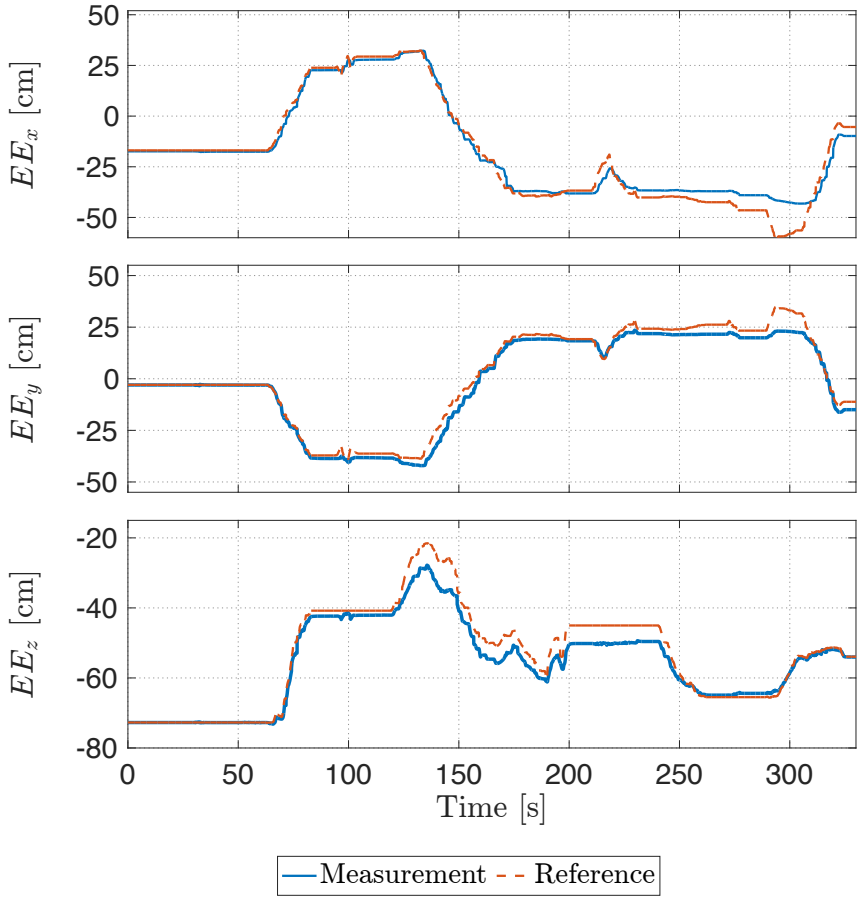

Figure 6-31: Results of the experiment: pick and place of the cage. First task: the translational motion of the end effector in accordance with operator joystick command.

- t = 150-180 s: the first attempt to put the cage on the pipe,
- t = 190-200 s: lifting the cage after unsuccessful attempt (the cage was placed with a wrong orientation with respect to the pipe),
- t = 200-240 s: preparing for the second attempt,
- t = 240-260 s: lowering the cage during the second attempt,
- t = 260-290 s: removing the hook from the fixture in horizontal plane while keeping EE_z,
- t = 290-325 s: bringing the hook below the platform center.

The second task performance is shown in Figure 6-32. As we can see, in real

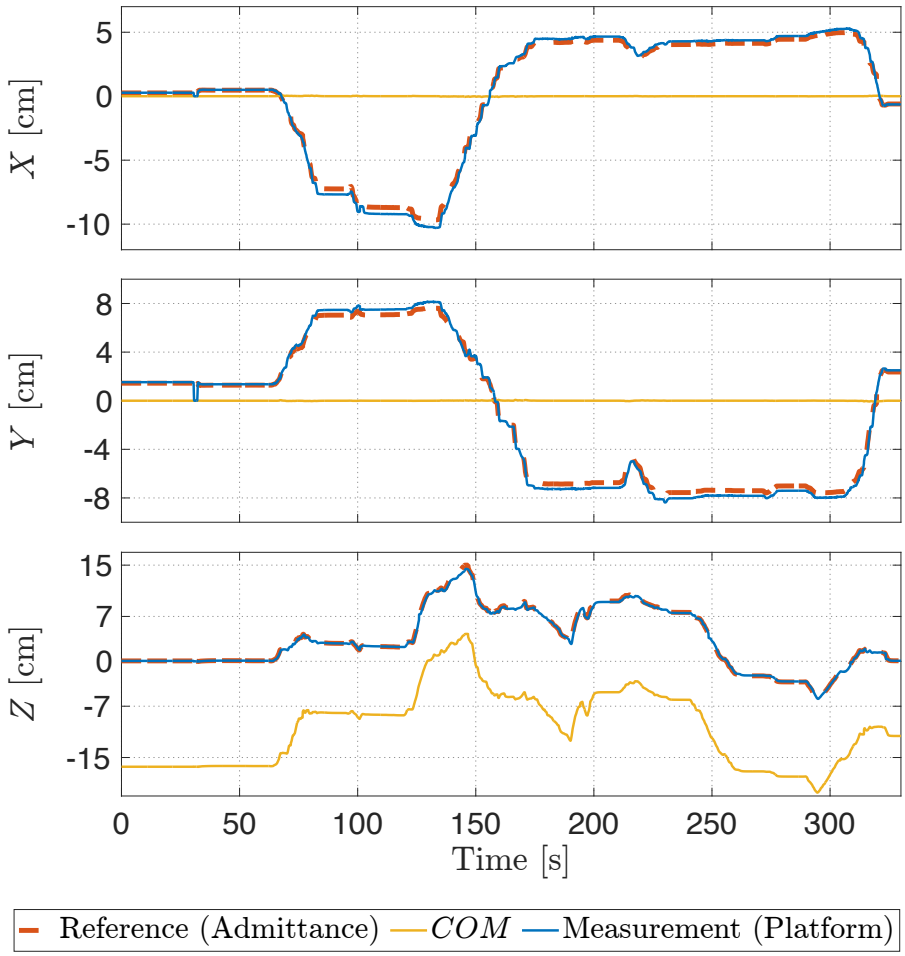

Figure 6-32: Results of the experiment: pick and place of the cage. Second task: the platform motion during joystick-controlled end effector motion. Admittance interface performance: motion of the platform in accordance with admittance interface command.

mission with end effector control performed by operator, the HWBC fully provided a designed capabilities, i.e., the COM in horizontal plane was close to zero while the platform GC was shifted in the horizontal plane in order to compensate for the disturbing gravitational torque and in the vertical plane in order to assist the robotic arm motion. The RMSE for the second task is 0.13 mm along x axis and 0.12 mm along y axis while maximum deviation from zero is 0.85 mm and 0.77 mm along x and y axes, respectively. Also, Figure 6-32 demonstrates the behavior of the winch-based actuation in response to the input from the admittance interface. The motion of the platform was calculated by using the forward kinematics based on the logged cable lengths. We can see that during the real mission winch-based actuation provided a sufficient accuracy, i.e., good tracking performance with average delay of 0.39 s along x_b, 0.24 s along y_b, and 0.29 s along z_b axis, by following the admittance interface command. The maximum delay for given admittance interface parameters reached 1.2 s. The obtained delay might be decreased by further tuning the admittance interface.

6.6 Integration of the OODC and the HWBC

In this section, we investigate the simultaneous operation of the designed two controllers, i.e., the OODC for the propeller-based actuation and the HWBC for the winch-based actuation and kinematically redundant robotic arm, for the stabilization of the SAM platform, as is depicted in Figure 3-29. To this end, two experiments are conducted in the outdoor environment:

- case of the robotic arm motion,
- platform null-space motion control.

In both experiments, the robotic arm and platform were controlled manually by the operator with a 2 DOFs joystick with force-feedback. It is worth discussing the mutual influence of the controllers. Since both actuations operate at the various bandwidths, there is no tangible mutual influence. Indeed, the winch-based actuation utilizes only slow robotic arm motion feedback while the propeller-based actuation uses IMU-based feedback. Additionally, it is worth mentioning that configuration of the robotic arm directly affects the overall system COM location, which ideally should be subject of the OODC. In our case, we consider COM displacement not significant, so OODC is constantly applied to the GC of the platform.

6.6.1 Case of the robotic arm motion

In the first experiment, the operator manually controlled the trajectory of the robotic arm end effector while both controllers were switched on. Namely, following control tasks were performed: oscillation damping of the pendulum joints[4], compensation for the gravitational torque by utilizing the winches, and control of the end effector, see Figure 6-34. It can be seen from the plot, that the error in the Z-channel of the end effector motion was about 10 cm. This error is caused by additional payload at the end effector with weight (cage with dummy mobile inspection robot) of 6.5 kg, see Figure 6-33. This error might be reduced by increasing the stiffness gains in the Z-direction for the first control task of the HWBC or by adding the weight of the end effector payload to the model. The data was collected with a low average frequency $\nu_{data} = 1.5188$ Hz, so the logged signal are discontinuous (non-smooth). Moreover, the logging frequency was not constant, so some spikes might be observed.

6.6.2 Platform null-space control

High-redundancy of the system allows to integrate an additional control task while maintaining the high performance of the rest tasks, see subsection 5.3.2. For ex-

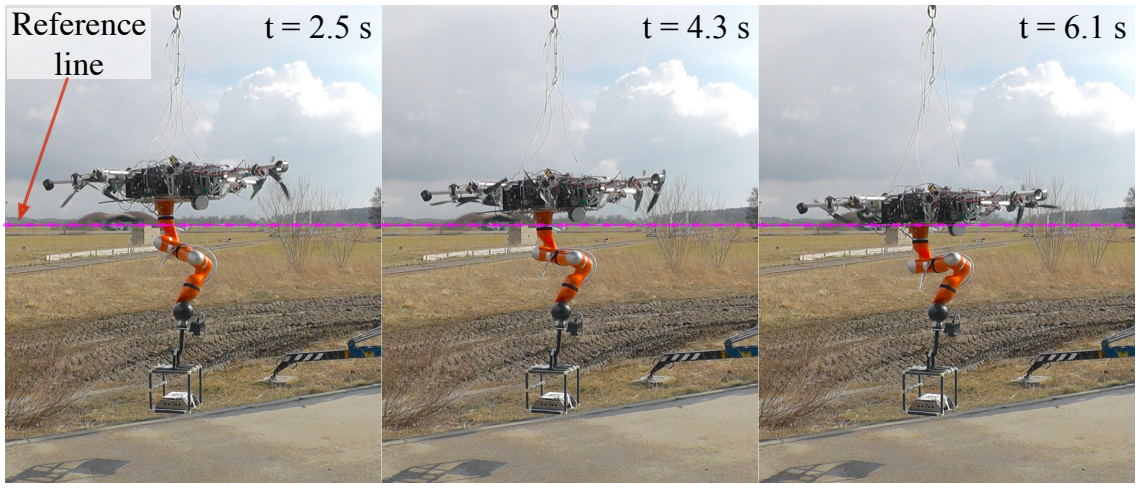

Figure 6-33: Illustration of the experiment: null-space control of the platform along the vertical axis. Snapshots demonstrate the vertical displacement of the platform, i.e., top, middle, and bottom configurations, with the same pose of the end effector. Purple reference line through the top of the service building is depicted in order to conveniently track the shift of the platform.

[4]It is worth mentioning that OODC affects the platform orientation indirectly through. The angular velocity data is ommited for the sake of brevity.

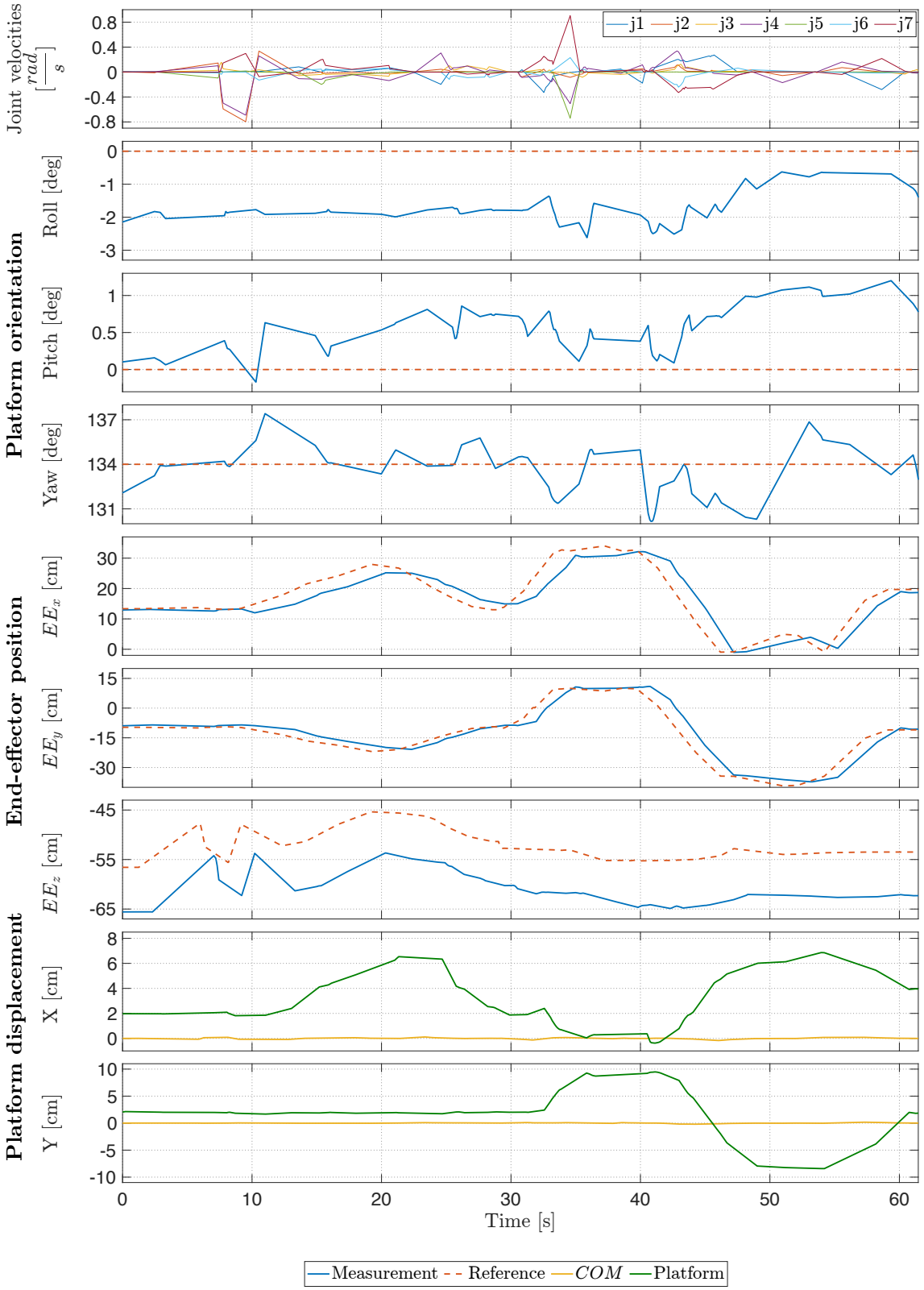

Figure 6-34: Results of the experiment: robotic arm motion for the case of simultaneous operating controllers. Top plot represents the joint velocities of the robotic arm. The next three plots present the orientation of the platform. The further 5 plots show the first and the second control task performance of the HWBC, i.e., the end effector position and horizontal displacement of the platform.

(a) t = 28.3 s (b) t = 35.5 s

Figure 6-35: Illustration of the experiment: null-space control of the platform around the vertical axis. Snapshots demonstrate the change of the platform orientation around yaw while keeping the same pose of the robotic arm end effector. Purple dashed circle shows the particular footpad location.

ample, the platform itself might be controlled along the vertical axis, z_p of the $\mathcal{F}_p$, while keeping end effector at the desired pose and zero gravitational torque. Such a capability might be useful in a number of cases, e.g., when we need to change a perspective of the onboard cameras or when we want to reduce the power consumption in the winch servos (longer rigging cable requires less torque at the motor for operation). To this end, we placed in the null-space two tasks: vertical motion of the platform and yaw motion of the platform. Both tasks are controlled in the same impedance-based manner (5.15) with control gains presented in Table 6.9.

In Figure 6-33 and Figure 6-35, the experimental scenario is shown. The SAM platform carried the cage with dummy mobile robot (the total weight of the end effector payload is 6.5 kg) by robotic arm. First, the operator manually commanded the platform to move up- and downwards while maintaining the rest configuration of the paltform (the pose of the end effector is conservative as seen with respect to to the shown part of the road). After that, the operator commanded to turn the platform around the yaw while keeping the rest configuration. Results of the experiment are depicted in Figure 6-36. As we can see in figure, while maintaining the end effector pose close to the original and keeping the system horizontal COM location close to zero, the platform was shifted first on 10 cm upwards and then on 16 cm downwards (red zone). After that, the platform was turned around the yaw for 31 degrees CCW, then for 48 degrees CW, and finally for 22 degrees CCW again (green zone).

It is worth mentioning that stiffness gains of the end effector were not high enough for such a heavy payload which was not declared in the model. As the result, in the EE_z channel we can observe 8 cm difference between desired and real signal. The

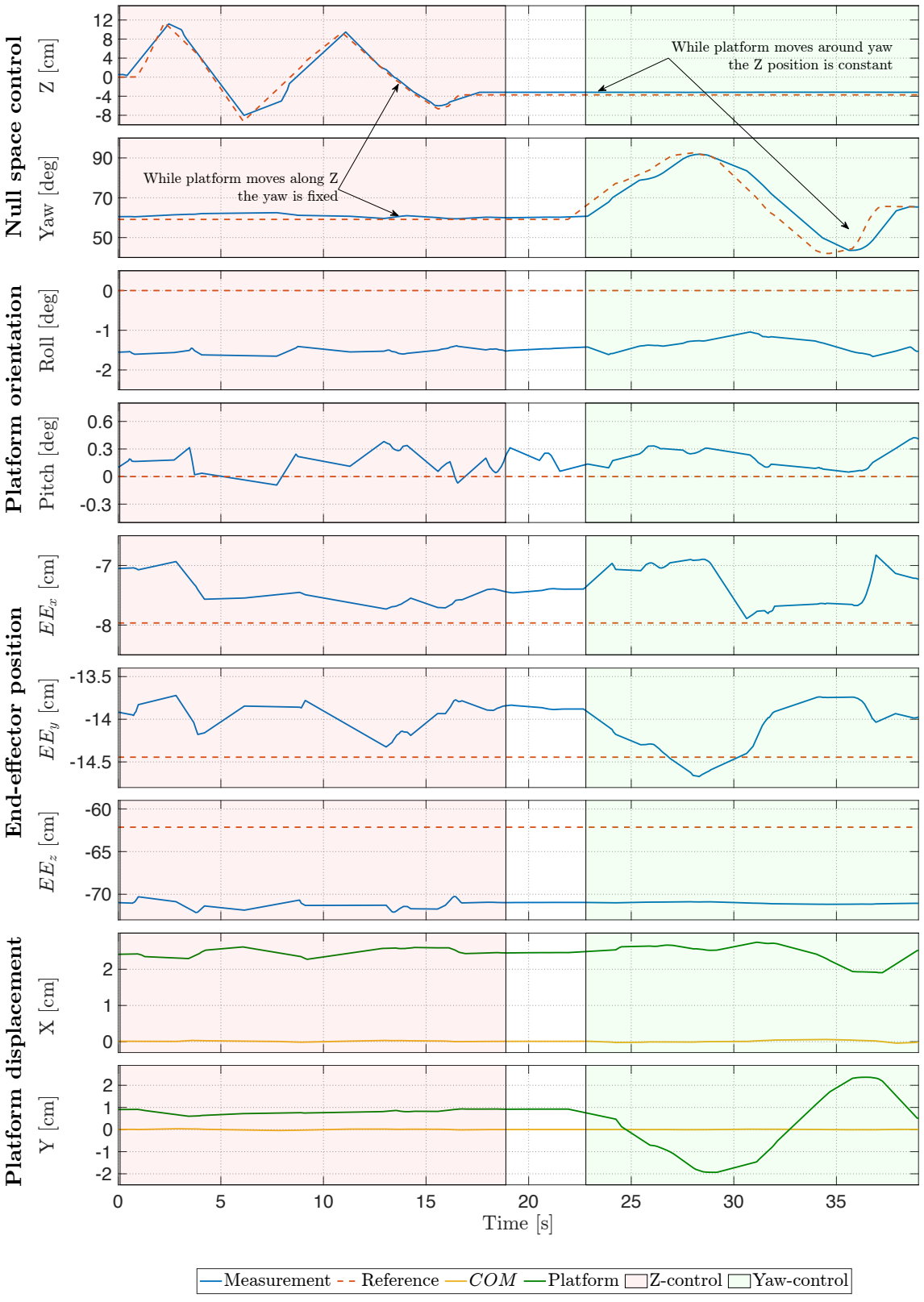

Figure 6-36: Results of the experiment: null-space control of the platform. The first two plots represent the null-space motion of the platform along and around the vertical axis. The next two plots demonstrate the orientation of the platform around roll and pitch. The further 5 plots show the first and the second control task performance of the HWBC, i.e., the end effector position and horizontal displacement of the platform.

Controller	Gain	Value
EE_z	$K_{p,d}$	50
	$K_{d,d}$	27
Pl_{yaw}	$K_{p,yaw}$	200
	$K_{d,yaw}$	100

Table 6.9: Null-space controller gains.

rest tasks demonstrated reasonable performance. Average frequency of the logging data was $\nu_{data} = 2.92$ Hz, so the logged signal is discontinuous (non-smooth).

6.7 Deployment of the foldable landing gear

As was mentioned in subsection 3.3.3, the three out of eight frame arms have the dual use. They serve as the frame arm during the operation, and as the landing legs

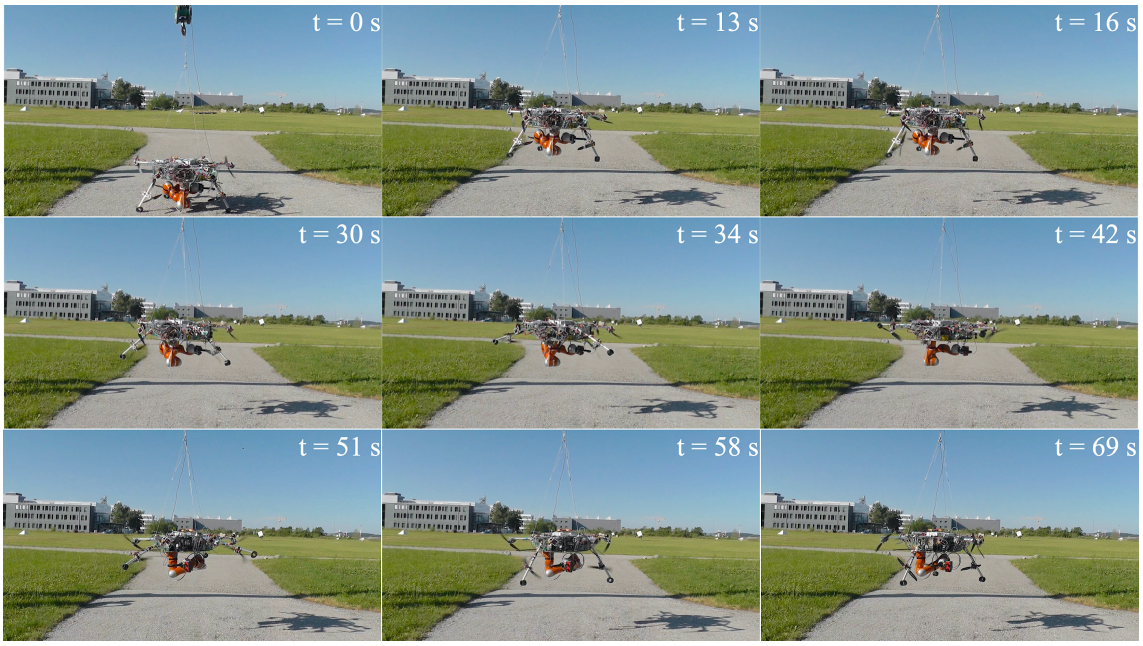

Figure 6-37: Illustration of the experiment: deployment of the foldable landing gear. Snapshots demonstrate the landed SAM (t = 0 s), the lifting of the passive SAM (t = 13 s), the start of the propeller spinning (t = 16 s), the lifting of the legs (to the arms) by the upward thrust while keeping the desired yaw utilizing the propellers located at the fixed 5 arms (t = 30-42 s), as soon as the legs are transformed to the arms and blocked by the locker mechanism the controller switches the oscillation damping (now shown) on, the lowering of the arms (to the legs) by gravity with damping by the thrust while keeping the constant yaw (t = 42-58 s), the passive SAM ready to be lowered by the crane (t = 69 s).

Process	**Initial locker state**	**Thrust command**	**Interim locker state**	**Thrust command**	**Final locker state**
Taking-off	Open	↑	Closed	↓	Closed
Landing	Closed	↑	Open	↓	Closed

Table 6.10: State machine logic for the landing gear control.

during parking. During landing and taking-off, the legs are regulated by a finite-state machine which has two states for the locker mechanism: *open* and *closed*. At the open state, the leg can slide freely in the vertical plane, while at the closed state the locker mechanism fix the leg either in upper (arm) or bottom (leg) position. The snapshots demonstrating taking off and landing are shown in Figure 6-37. The logic behind the state machine is briefly depicted in Table 6.10.

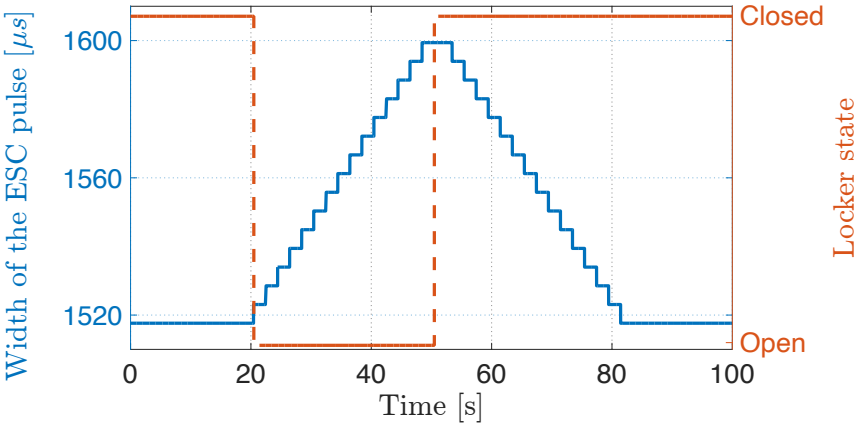

(a) Taking-off

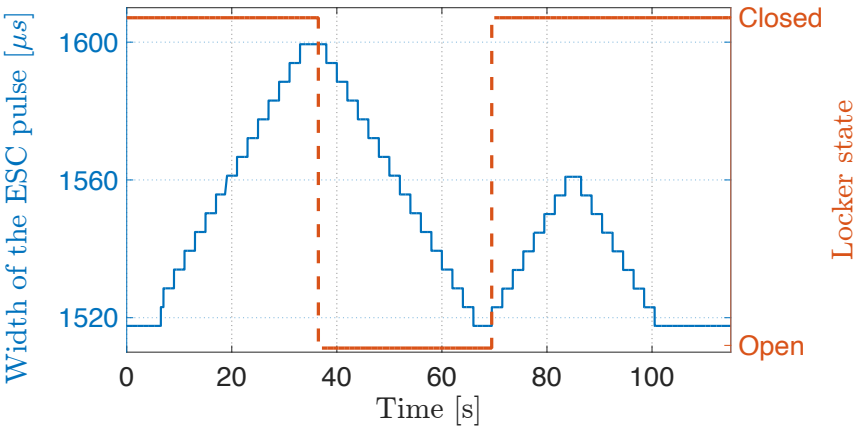

(b) Landing

Figure 6-38: State machine commands for the leg control.

During the taking-off, a transition of the leg to the arm is performed. In the beginning of motion (t = 20 s), legs are at the open state, and slowly increasing thrust lifts them till the upper position. When the legs are fully lifted (t = 52 s), the locker mechanism is switched to the closed state to fix the configuration, after which the thrust is reduced, see Figure 6-38a. During landing, the opposite procedure occurs with one additional step. Due to mechanical displacement of the locker groove and the servo shaft bar at the bottom position, after the main cycle a complementary command which aims to fit the shaft into the groove is exploited, see Figure 6-38b. At the bottom position, we turn the shaft of the locker mechanism to the closed state and fit it to the groove by shaking each leg with an amplitude around 5 degrees.

It is worth noting that time of the landing and taking off is strictly depending on the command and BLDC slew rate. For our settings, the taking off process takes approximately 60 seconds, while landing takes about 95 seconds.

"The reward of the young scientist is the emotional thrill of being the first person in the history of the world to see something or to understand something. Nothing can compare with that experience."

Cecilia Payne-Gaposchkin, 1977

Chapter 7

Field investigation in the industrial-like environment

As was highlighted in chapter 1, the cable-suspended aerial manipulation technology has a high practical potential to many industrial applications. The conducted research and engineering work on the development of the cable-suspension aerial manipulator was performed within H2020 AEROARMS project which the main goal is the integration of the academic research to the industrial applications.

To assess the developed technology performance, robustness, and operational safety, the experimental validation within the DLR Oberpfaffenhofen outdoor testing ground similar (mock-up) to the real industrial environment, described in subsection 6.1.4, is performed. Namely, three industrial-like experiments are conducted utilizing the SAM platform regulated by designed control strategies, i.e., OODC and HWBC:

- deployment of a mobile inspection robot at the remotely located pipeline,
- placing peg into a hole with a ∼1-2 mm gap at the remotely located box,
- turning the valve at the remotely located spot.

Each experiment was preceded by a pre-flight check which included tests of the main operational blocks, i.e., sensors (IMU, cameras), actuation systems (propeller-based actuation, winch-based actuation, robotic arm), battery level, power and communication between on-board functional nodes and ground station.

It is essential to highlight that each experiment contains a free flight as well as the interaction with the environment. The presented results should demonstrate the

potential impact of the scientific advancements on the industry and the possibility of applying the cable-suspended aerial manipulator in commercial projects.

7.1 Deployment of the mobile inspection robot

7.1.1 Inspection crawler

Let us first introduce the mobile inspection robot that is exploited in the experimental session. Namely, the Tri-Wheel-Inspection-Crawler (TRIC), see Figure 7-1, from GE Inspection Robotics[1] is utilized. Among its key features, it is worth highlighting the following:

- omnidirectional magnetic drives (three magnetic wheels) that allow the crawler to safely move along and around the convex and concave surfaces, i.e., outside and inside the pipe, see Figure 7-2,
- integrated electrical conductivity and ultrasonic testing sensors, visual inspection sensors, and wireless communication,
- ability to operate with the pipe diameter bigger than 300 mm,
- the robot can cross only the steps with a height of 0.5 mm,
- in operational mode, the robot moves approximately with the speed of $25\frac{\text{mm}}{\text{sec}}$,

Figure 7-1: Mobile inspection robot TRIC.

[1] https://inspection-robotics.com/tric/

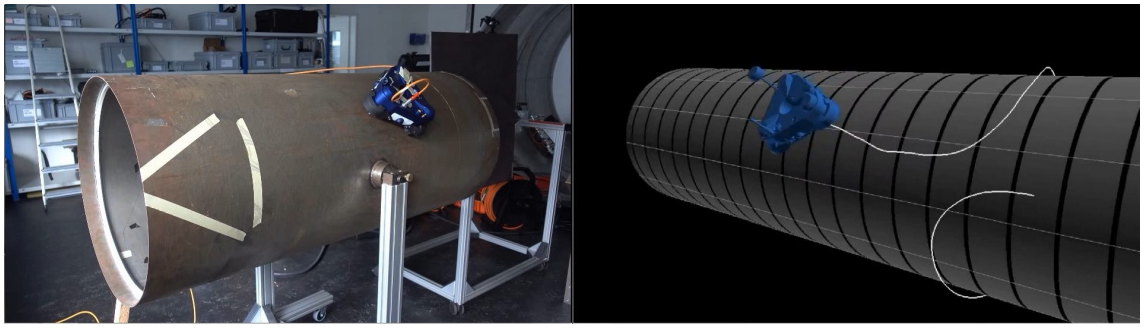

Figure 7-2: The crawler TRIC operates on the pipe (left) and simultaneously localizes itself (right).[2]

- the weight of the crawler with an integrated battery is roughly 6.5 kg.

7.1.2 Deployment strategy

In order to provide safe delivery and retrieval of the mobile inspection robot TRIC to the remotely located pipe by the flying system, the special deployment cage is proposed. The deployment cage has the size roughly 2 mm bigger than the TRIC dimension in all horizontal directions. It contains a flexible rubber plate with integrated magnetic pads (for each wheel) to prevent the TRIC from falling out of the cage, i.e., to fix the robot during transportation. At the top of the cage, a fixture for the pickling up by a tool, i.e., a hook, is attached, see Figure 7-3a.

The cage should be placed and stabilized on the top of the pipe during the deployment while the robot drives out of it. Considering the crawler speed mentioned

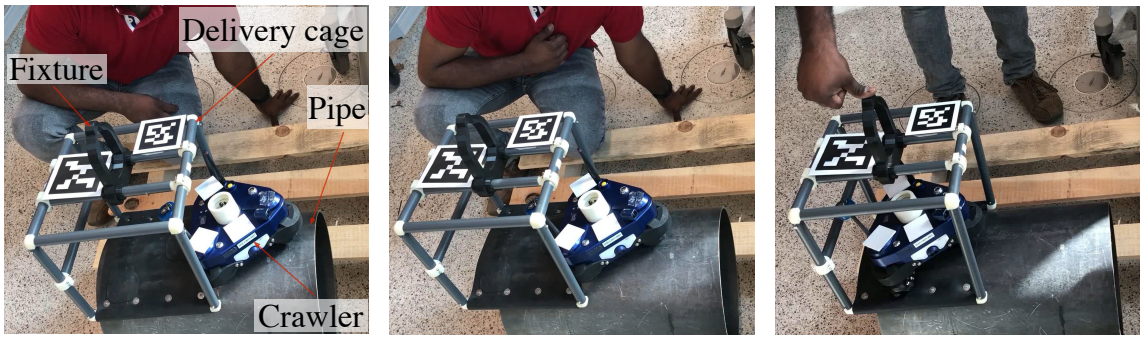

(a) The crawler is at the beginning of the movement toward the cage

(b) The crawler pushes the free-placed cage instead of getting in

(c) The crawler moves in the cage pressed by external vertical force (by human thumb)

Figure 7-3: Crawler deployment and retrieval strategy.

[2]The snapshot is taken from the demo video on https://inspection-robotics.com/tric/.

above, it takes approximately 10 seconds for the robot to move in or out of the cage completely. So, during the 10 seconds, reliable interaction with the environment should be performed.

During the retrieval of the TRIC, the cage should be fixed in front of the robot. Indeed, when the TRIC drives on the rubber plate, it reduces the magnetic force between magnetic wheels and the pipe. In the case of the free-placed cage, the robot would just push it, see Figure 7-3b. In order to allow retrieval of the TRIC, a significant vertical force should be applied on the top of the cage, see Figure 7-3c. During the operation, this pressing should be performed by the robotic arm.

7.1.3 Mission description

We had to deploy the inspection crawler on the remotely-located pipe employing the SAM in the experimental mission. This experiment aimed to validate the cable-suspended aerial manipulator concept and was conducted at the early development stage (June 2019), so the oscillation damping controller for the single pendulum was utilized only (Appendix C) for the system stabilization.

Task details

The overall task is depicted in Figure 7-4a. Initially, the SAM is located in the

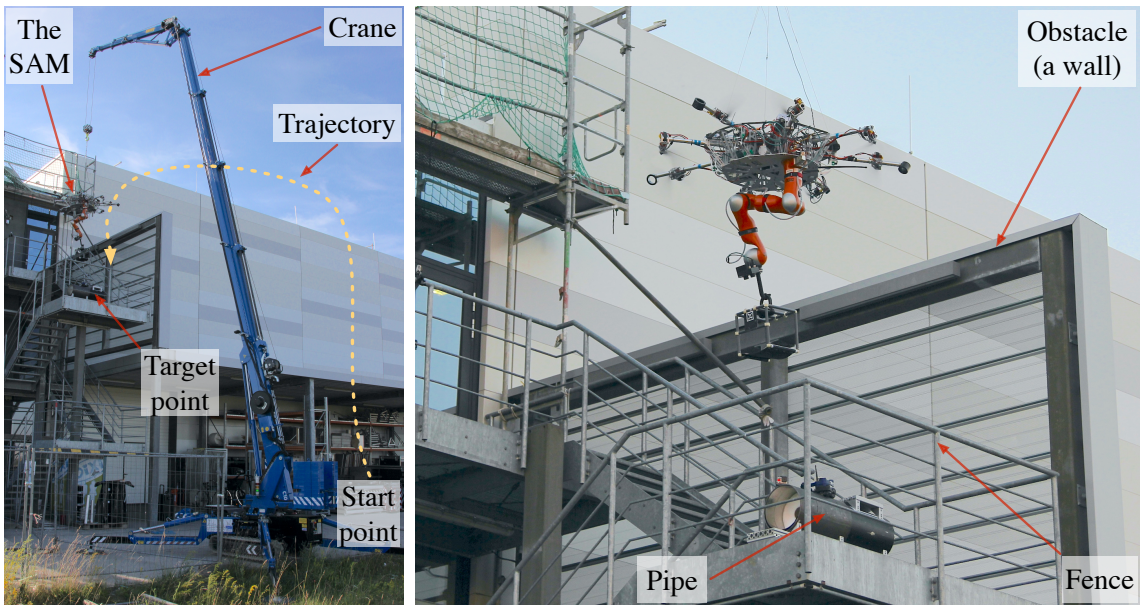

(a) The task description (b)The obstacle details

Figure 7-4: Industrial mock-up at the DLR Oberpfaffenhofen.

landing configuration at a *start point*. Then, the crane should lift it up to perform taking off. After that, the SAM should pick up the cage located close to the start point. Next, the crane should bring the platform with the cage to the *target point*, where the pipe is placed, close to the desired *trajectory* in order to overcome the obstacle on the way. Finally, the crawler should be deployed at the *pipe*. The retrieval of the crawler should be done in the opposite sequence.

The pipe is located on a platform roughly 8 meters above the ground and surrounded by different obstacles, i.e., a bar-based fence, a wall, see Figure 7-4b. Thus, the manipulation should be performed in a constrained narrow environment in close proximity to the obstacles. It is worth noting that to increase the difficulty of the mission, the most minor pipe diameter at which the crawler can operate was used.

Ground station

The ground station is deployed in the specially-equipped van, see Figure 7-5a. Mission operators, i.e., crawler operator, robotic arm operator, and perception oper-

(a) Outside view

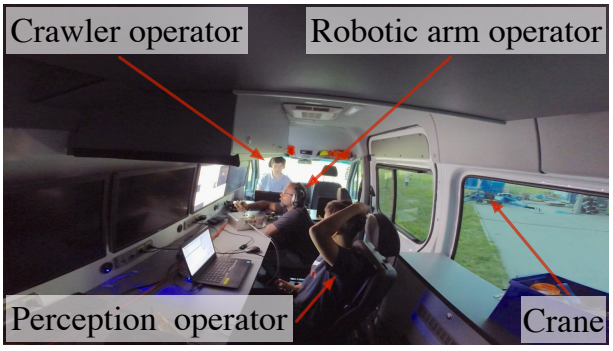

(b) Inside view

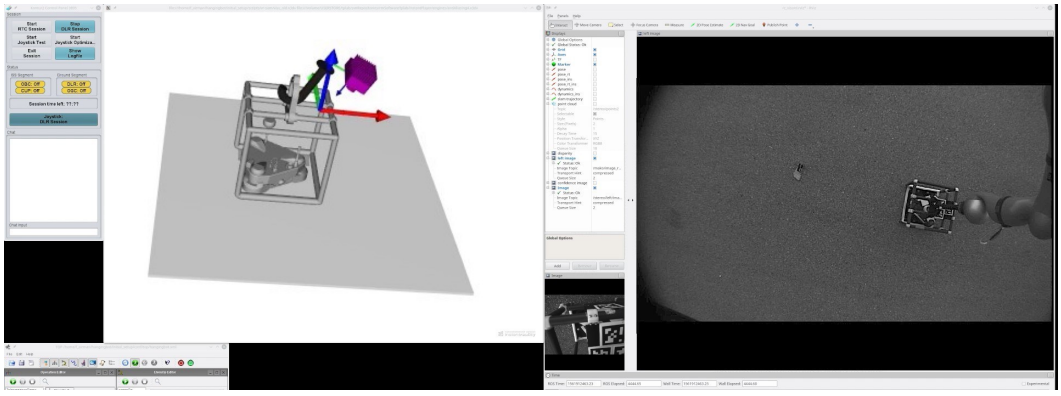

(c) Operation panel with camera feedback (right figure, eye-to-hand view) and 3D visualization of manipulation area (left figure, 3D view with depth)

Figure 7-5: The ground station for the mission control.

(a) Landed flying system (b) Cage picking (c) Cage lifting

Figure 7-6: The cage grasping.

ator, were conveniently engaging from it, see Figure 7-5b. Since the flight controllers function autonomously during the experiment, the flight control operator was outside with a red button ready to interrupt the mission in case of an emergency. Thus, control of the whole manipulation operation is performed with no direct sight to the manipulation area, i.e., pipe, or to the SAM platform, so all processes, including cage grasping, placement on the pipe, crawler deployment and retrieval, are conducted either autonomously or based on the sensor information. At the same time, the crane operator was outside as well and had direct visual feedback on the SAM transportation trajectory.

The robotic arm and crawler operators are provided with different tools for telemetry, haptic, audio, and visual feedback. The control station of the robotic arm teleoperator is equipped with multiple control panels for conveying the feedback information, see Figure 7-5c, including visual feedback from the monocular camera on the platform and 3D reconstructed visualization (virtual reality visualization) with depth information of the manipulation area [Lee et al., 2020] from the stereo camera attached to the end effector. Moreover, the force feedback is provided by the haptic input device (joystick). Therefore, the robotic operator could interact with the remote environment through the robot while receiving haptic information about it.

Grasping the cage

Initially, the SAM is located in the landed configuration, see Figure 7-6a. After lifting by the crane and transforming the landing legs to the frame arms (section 6.7), the SAM grasps the cage, which contains the crawler located close by. To this end, the SAM is moved by the crane so that the cage is conveniently placed inside the

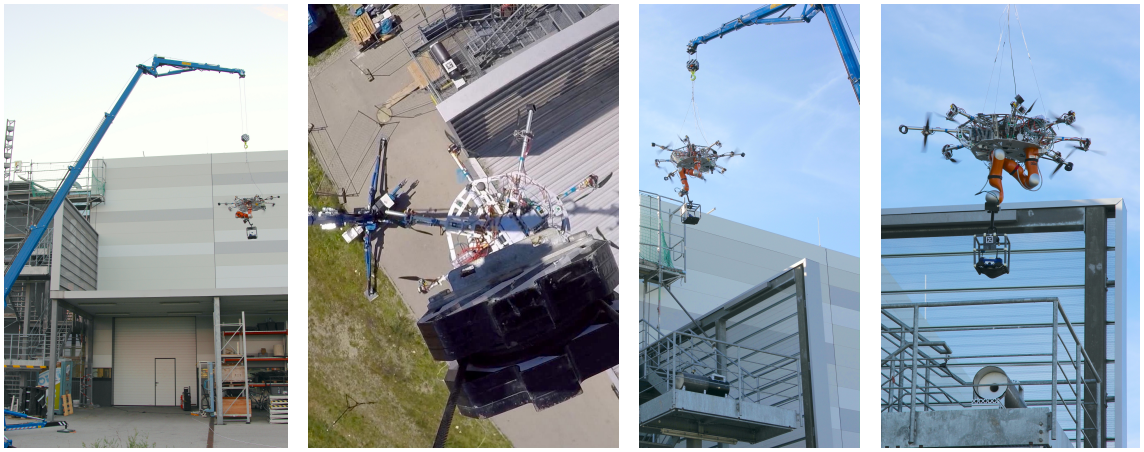

(a) Lifting the SAM at the required height

(b) Overcoming the wall (top view)

(c) Overcoming the wall (side view)

(d) Lowering the SAM toward the pipe

Figure 7-7: The SAM transportation.

manipulator workspace, see see Figure 7-6b. The onboard cameras detect the cage and estimate a relative pose of the cage with respect to the tool (the 3D printed hook). With this aid, the operator telemanipulates the tool and grasps the cage, during which the force feedback (weight of the cage with the crawler) also supports him to realize that the cage has been lifted off from the ground, see see Figure 7-6c.

Transportation to the target point

Once the manipulator has grasped the cage with the crawler, the next step is to transport the system to the target pipe location. To this end, the robotic arm has a fixed configuration during the transportation, so the platform actuation and crane perform the main work.

In the selected outdoor scenario, there are multiple obstacles that the SAM has to avoid until it reaches the target location. The crane is remotely controlled to avoid these obstacles, and in the end, the SAM platform is located above the target pipe, see Figure 7-7. It has to be mentioned that severe oscillations of the cage can result in the crawler falling off. Thus, the oscillation damping functionality of the SAM platform plays a major role during this period and cancels out even significant oscillations created during the crane motion.

It is worth noting that since oscillation damping controller for the single pendulum was utilized, the main motion during the transportation was performed by the crane, and the crane's chain length during the whole period was kept short enough

for excluding the double pendulum behavior. The chain length was only reduced in order to overcome the wall, see Figure 7-7c.

Crawler deployment

Deployment of the crawler requires precise placement of the cage on the pipe. To this end, the monocular camera detects the target pipe, and the orientation of the SAM is autonomously aligned to match it utilizing yaw control, see Figure 7-8b. The pipe's tracking also helps visualize the relative position of the cage with respect to the pipe in the virtual reality environment presented to the operator. These two features support the operator to place the cage properly on the pipe to deploy the crawler safely. The crawler operator then remotely controls the mobile inspection robot to move out of the cage. During this period, the teleoperator pushes down the cage toward the pipe applying a vertical downward force (Figure 7-8c), so the crawler and the cage do not lose contact from the pipe, which might lead to the falling off of the crawler to the ground. Accurate force regulation for this contact maintenance is achieved because of the force feedback provided to the operator through the haptic joystick. Once the crawler is entirely out of the cage, the empty cage is lifted up, and the SAM goes back to the base station, see Figure 7-8d, while the crawler performs the pipe inspection, see Figure 7-9.

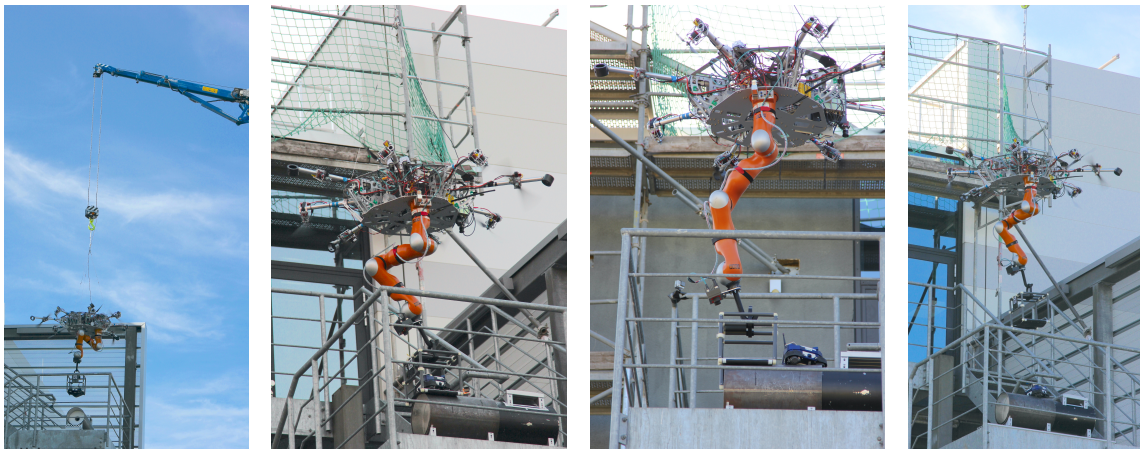

(a) Lowering the cage with the SAM, so the pipe appears in the robotic arm workspace

(b) Aligning the cage with the pipe so the crawler can safely drive out

(c) Pressing the cage by the hook toward the pipe for safe crawler extraction

(d) Lifting the empty cage by the SAM

Figure 7-8: The crawler deployment on the pipe.

(a) The crawler after the cage lifting

(b) The crawler drove to another edge of the pipe

Figure 7-9: The inspecting crawler.

Crawler retrieval

As the crawler has completed the task, the empty cage is transported to the pipe by the SAM, see Figure 7-10a. The transportation of the SAM with an empty cage is similar to the described above. Once the cage is properly placed and pressed to the pipe, see Figure 7-10b, the crawler operator remotely controls it into the cage. During this action, he uses both: the front camera of the crawler as well as the monocular camera on the SAM platform to position and move the crawler

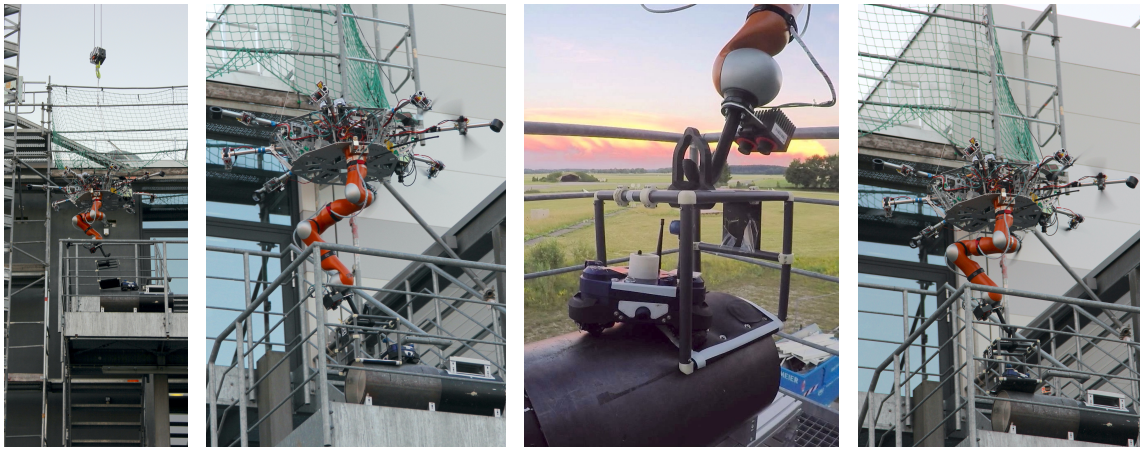

(a) Approaching the pipe with the empty cage

(b) Pushing the cage toward the pipe, so crawler can move in

(c) The crawler is halfway into the cage pressed by the tool (the hook)

(d) Lifting up the cage with the crawler

Figure 7-10: The crawler retrieval from the pipe.

properly into the cage. As the crawler is completely inside the cage, the robotic arm teleoperator pulls the cage up into the air, see Figure 7-10d.

The SAM landing

The SAM, along with the crawler, is taken back to the base station by the crane, where the teleoperator places the cage on the ground, see Figure 7-11a. Then, the landing process starts with reconfiguring the robotic arm from the operational to the parking position and lowering the legs, see Figure 7-11b. Finally, the crane puts the platform down till it touches the ground. After that, all propulsion units are switched off, see Figure 7-11c. It is worth noting that the crawler is supposed to inspect the pipe during the day, so it was extracted close to the night. It can be seen that at the end of the mission, the daylight is almost gone.

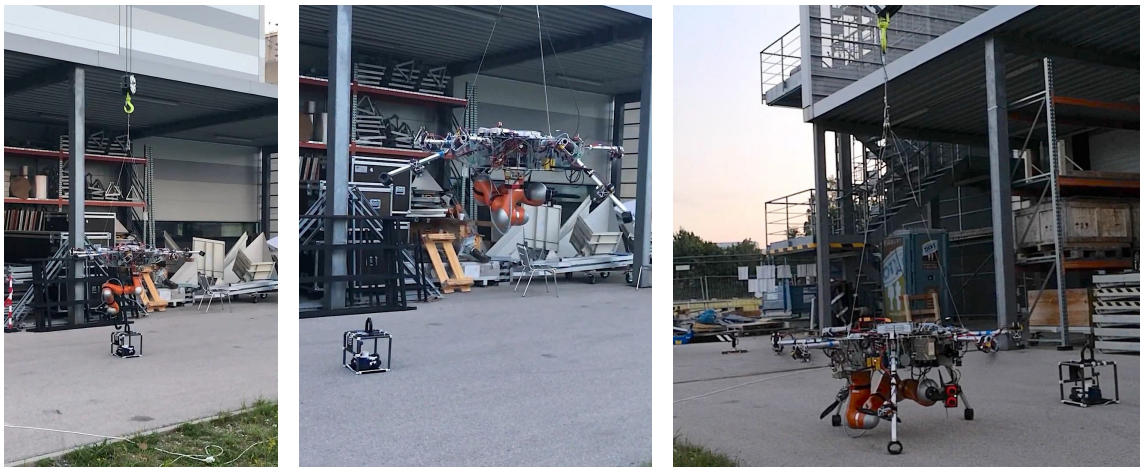

(a) Placing the cage with the crawler on the ground

(b) Lowering the legs

(c) Landed system

Figure 7-11: Landing of the SAM.

7.2 Peg-in-hole assembly

The peg-in-hole is a demonstrative robotic task that requires a physical interaction with an environment. Namely, this task implies placing the peg into the fixed hole by the robotic manipulator [Park et al., 2013]. The hole is slightly (1-2 mm) bigger than the peg dimensions, so the FTS sensor is utilized to "feel" the hole location by measuring the reaction wrench when the peg is touching the hole's edges.

(a) Lowering the SAM toward the box

(b) Adjusting the distance between the platform and the box by null-space control of the platform along vertical axis

Figure 7-12: The setup for the peg-in-hole assembly.

In our setup, the peg tool and the box with the hole are manufactured from the wood, see Figure 7-12a. The SAM was hanged on the crane with a long chain, so both controllers for the platform, i.e., OODC and HWBC, were utilized to provide better performance and high safety. The custom-made 6 DOFs FTS was mounted at the end effector before the tool.

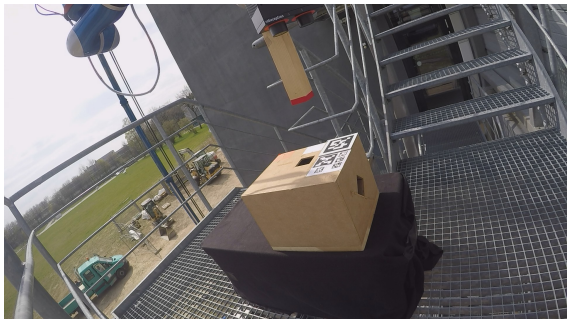

(a) Approaching the box with a peg

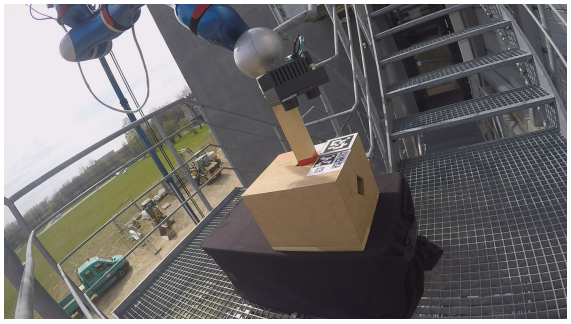

(b) Aligning the peg with a hole

(c) Inserting the peg into the hole

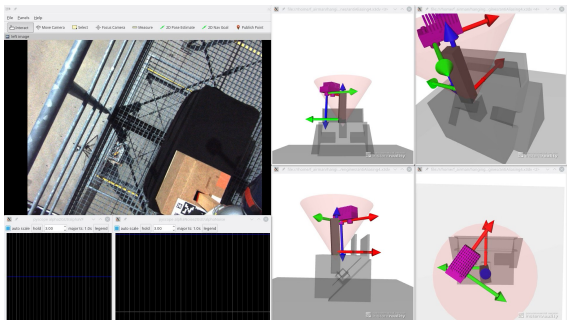

(d) Operation panel with camera feedback (left) and 3D visualization of the manipulation area (right) during the peg and hole aligning

Figure 7-13: The peg-in-hole assembly performed by the SAM.

In order to reduce the distance between the cage and the platform, winch-based actuation was utilized. Distance adjusting helped to avoid singularity in the robotic arm during the peg insertion. Although the crane could assist with this task, the regulation by winches allows the more precise motion, see Figure 7-12b. It is easy to observe the height adjusting by comparing the proximity of the SAM frame to the fence.

Peg insertion process is demonstrated by snapshots taken by GoPro camera, see Figure 7-13. It is worth mentioning that 3D visualization (Figure 7-13d) serves as an excellent assistant for the aligning peg and hole in all dimensions, see Figure 7-13b. As a result, due to the operation of the platform controllers, the base was almost motionless, and the peg was placed in the hole, see Figure 7-13c, smoothly.

7.3 Valve turn

The developed approach for the aerial manipulation has shown high efficiency in safety, performance, and reliability in the experiments above. Therefore, it was decided to apply the developed system to solve the real industrial problem in the inspection and maintenance. Namely, the turning of the remotely located ball-type valve with a lever handle should be performed by the SAM under the control of designed algorithms.

To this end, at the tip of the wooden peg, the wooden tip with a groove was additionally attached. The mentioned groove should be aligned with a valve lever

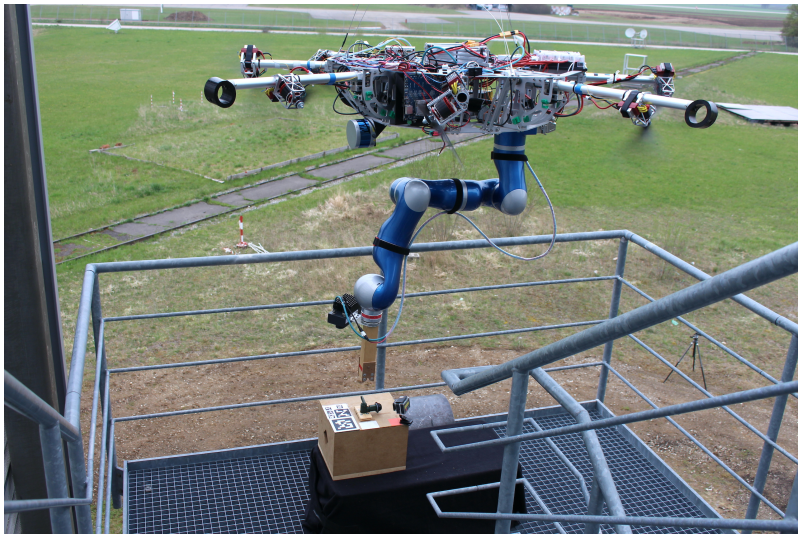

Figure 7-14: The setup for turning the valve.

handle and then turned by the rotational motion of the robotic arm end effector while keeping its pose static. The standard valve was attached to a similar peg and placed in the wooden box hole. The general view of the setup is shown in Figure 7-14. Both controllers for the SAM platform, i.e., OODC and HWBC, were activated for this mission conduction.

The valve turning process is demonstrated by six snapshots taken by the GoPro camera, see Figure 7-15. As it can be seen, the valve was turned roughly for 90 degrees by the robotic arm end effector.

The robotic arm end effector pose during this mission is shown in Figure 7-16. Two vertical dashed green lines partition the whole process to the three zones:

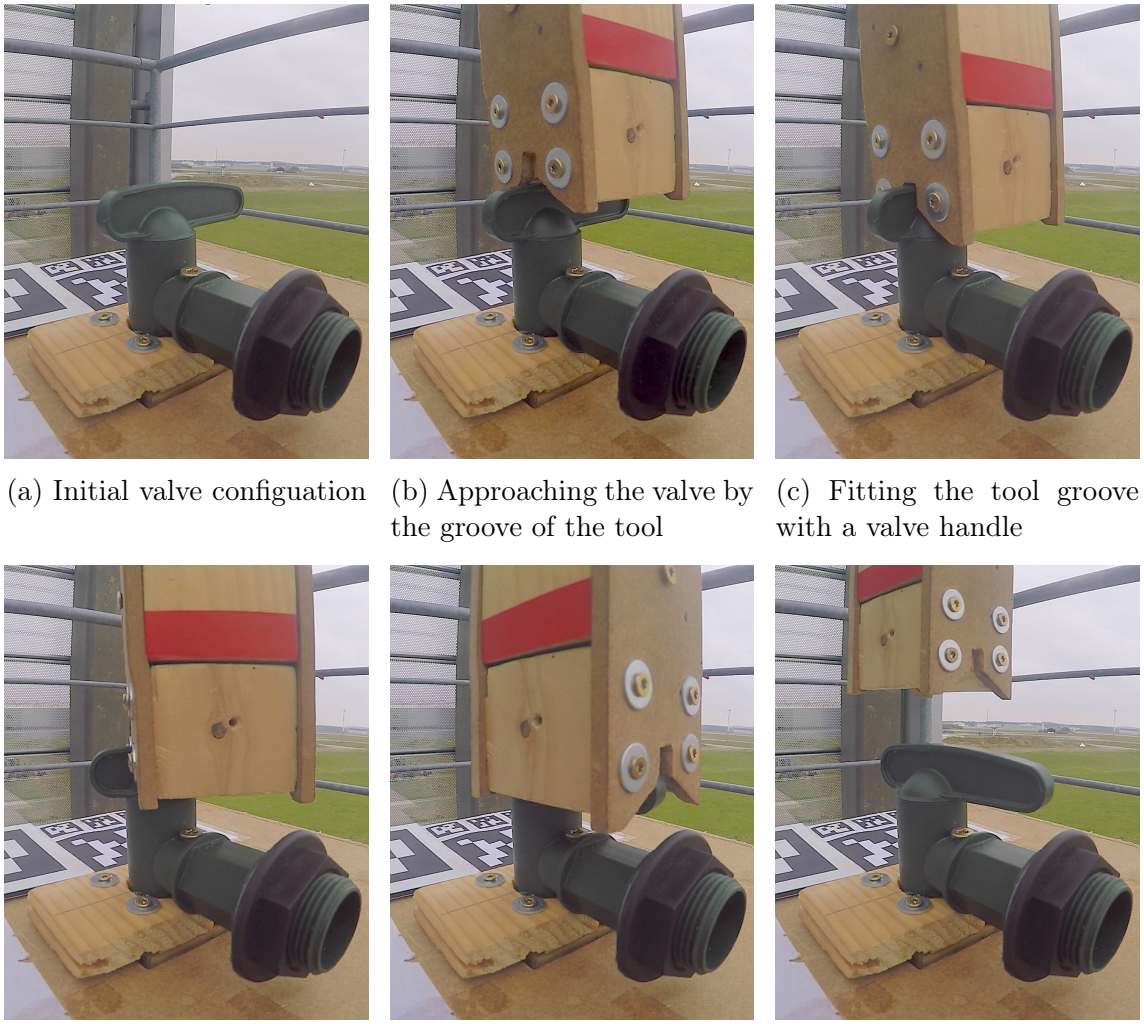

(a) Initial valve configuation

(b) Approaching the valve by the groove of the tool

(c) Fitting the tool groove with a valve handle

(d) Turning the valve handle by rotation of the end effector for roughly 45 degrees

(e) Turning the valve handle by rotation of the end effector for 87.5 degrees

(e) Lifting the tool from the valve

Figure 7-15: The valve turn performed by the SAM.

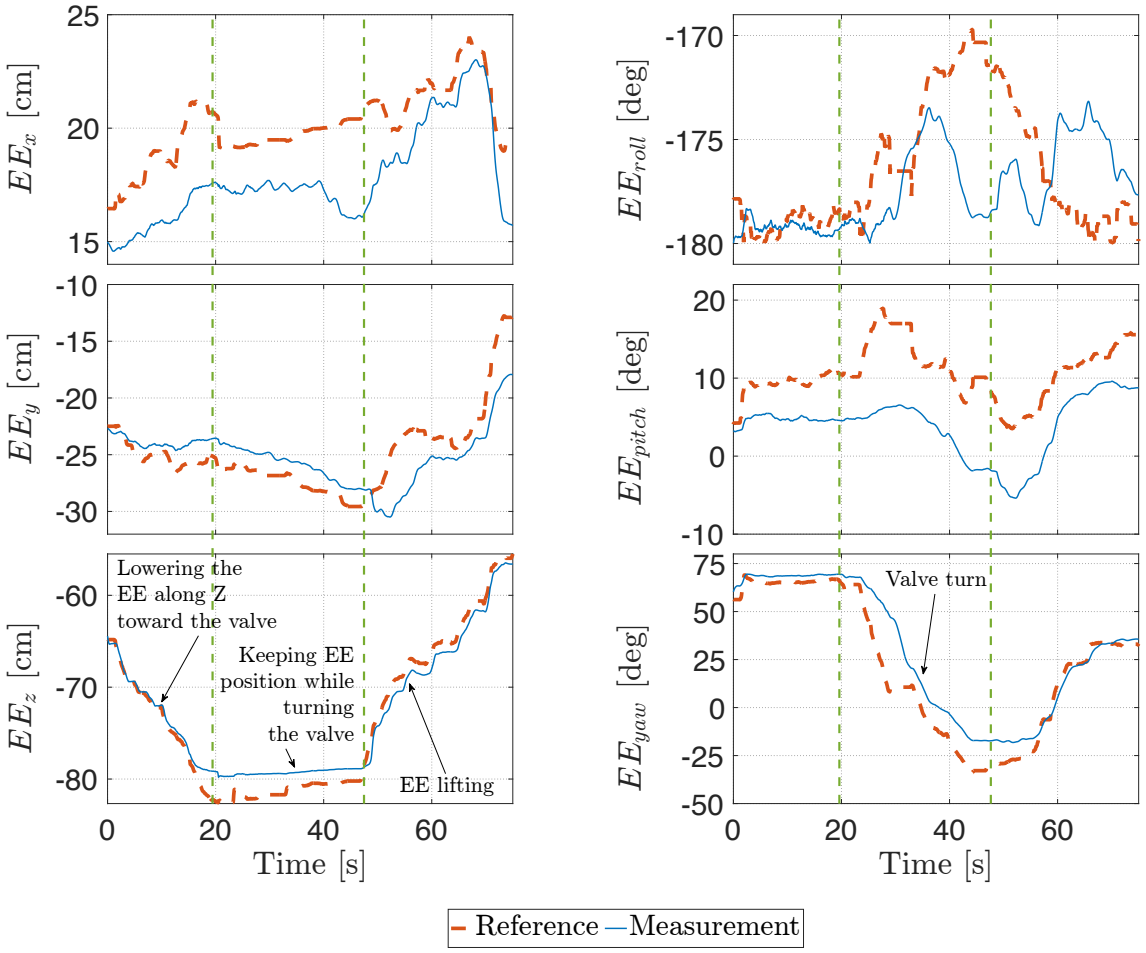

Figure 7-16: Results of the valve turn mission. First task: the end effector pose manually commanded by the operator utilizing the joystick. Vertical green lines separate the period [19.9, 47] seconds during which the valve was turned.

1. [0, 19.9] seconds: lowering and aligning the tool groove with the valve handle,
2. [19.9, 47] seconds: turning the valve by changing the orientation of the end effector while keeping the end effector position,
3. [47, 74] seconds: lifting the tool from the valve handle.

It can be seen from the figure that besides the end effector yaw rotation for 87.5 degrees, from 69.5 to -18 degrees, there are roughly 5 degrees commands around the end effector roll and pitch. It might be explained by the tool frame orientation. The translational motion of the end effector during valve turn is almost constant.

The orientation of the platform and corresponding angular velocities are depicted in Figure 7-17. It can be seen that OODC well-performed its own duties by dampening oscillations while regulating the yaw toward the desired value. It is worth mentioning that a specific torque was applied to the valve handle by the robotic

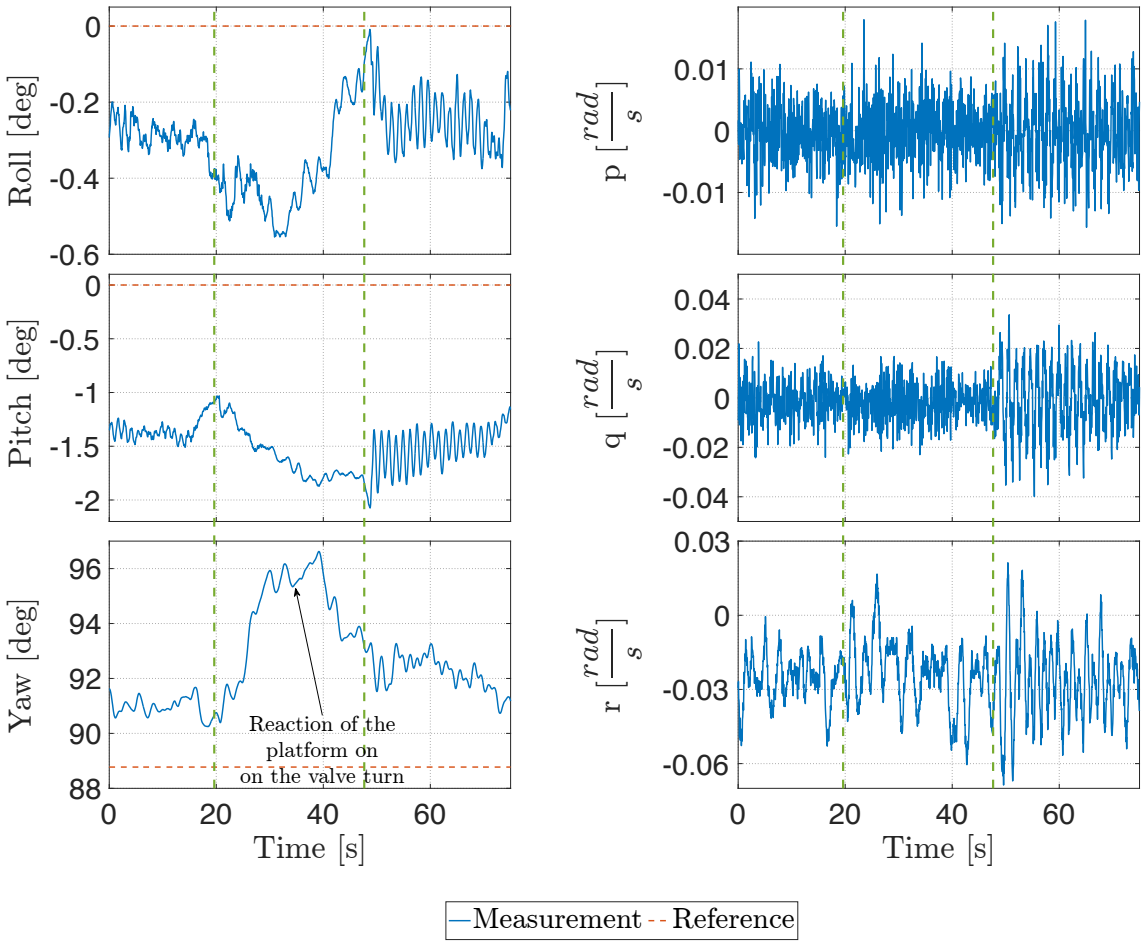

Figure 7-17: Results of the valve turn mission. The platform roll, pitch, and yaw angles are depicted on the left, and corresponding angular velocities are shown on the right. Vertical green lines separate the period [19.9, 47] seconds during which the valve was turned.

arm end effector during the valve turn. Due to coupling between the manipulator and the platform, the latter reacted by turning around the yaw in the opposite direction for roughly 5 degrees. However, the yaw controller returned the platform back by utilizing the propeller-based actuation as soon as the valve turning was complete. Increasing $\mathcal{PD}$ gains and adding the integral term to the yaw control law would compensate for the aforementioned error. Moreover, it can be observed the static error of 1.5 degrees around the platform pitch, which normally should be compensated by HWBC. The error is caused by the unbalanced platform with non-symmetric weight distribution, which is not considered in the model.

Effect of the HWBC is demonstrated in Figure 7-18. It can be seen that despite the non-zero platform pitch angle, the integrated controller was regulating the system toward zero horizontal terms of the COM based on the symmetric platform

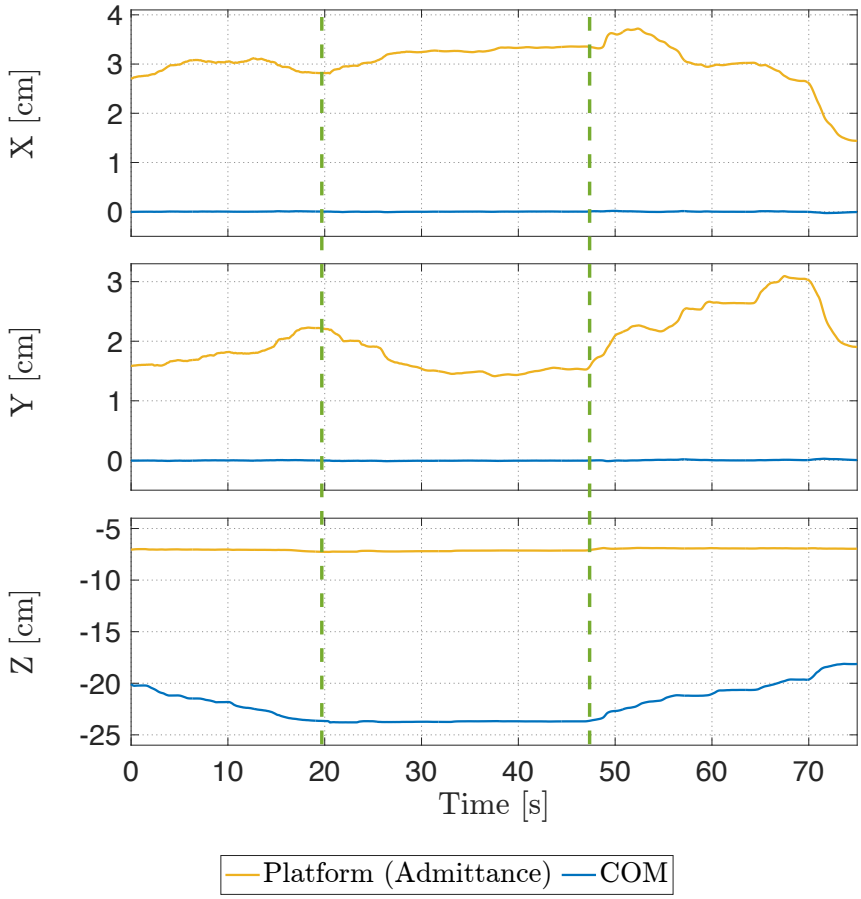

Figure 7-18: Results of the valve turn mission. Second task: the platform and COM motion during mission conduction. Vertical green lines separate the period [19.9, 47] seconds during which the valve was turned.

model (uniform cylinder). It was performed by shifting the platform along the admittance interface commands generated by HWBC utilizing the winch servos. It can be seen that in the vertical (Z) channel, the base kept its own height constantly, which means that the vertical COM projection was varying only due to the manipulator motion. Indeed, while the manipulator was lowered to the valve handle by 15 cm, the total COM was lowered for 3.7 cm. As soon as the manipulator was pulled up, the COM was raised as well.

The logging data was collected with the frequency of $\nu_{data} = 20$ Hz.

"Everything is possible. The impossible just takes longer."

Dan Brown

Chapter 8

Conclusion

In the last chapter, we provide a concise summary of the major results and contributions, main lessons learned during technology field investigation, existing limitations of the cable-suspended aerial manipulation concept as well as designed control strategies, and outlook on future work.

8.1 Summary

In today's world, inspection and maintenance have become the subject of digitalization and robotization to make people's work easier, safer, and more efficient. Robots serve as a tool to assist in tasks that include a high risk for human lives or a high probability of human error.

One such tool is the aerial manipulator. It is used to perform various operations that might require contact with the environment: high-altitude work (inspection, maintenance, repair), work in a hazardous (toxic) environment for people (collection soil samples), or transporting goods. The demand arises from the oil and gas, construction, chemicals, nuclear, and other industries, which imply strict requirements for the flying system's safety and performance. To this end, the primary Research Question of this thesis was formulated as follows (**chapter 1**): how to enhance manipulation performance and operational safety for the aerial manipulation in industrial applications, e.g., valve turn, peg-in-hole assembly? The generated hypothesis that addressed the research question stated that an adequately controlled cable-suspended stabilizing platform equipped with a robotic arm can provide high performance and safety in aerial robotic manipulation..

In general, the control of an aerial manipulator with high precision is challenging

due to dynamic and static disturbances that affect the aerial base, such as wind, sensor signal noise, couplings with payload, as well as the COM displacement due to arm articulation or applied external forces from the environment. As a result, in contrast to the fixed-base manipulators, such systems can fluctuate in the air and are more sensitive to external factors. Therefore, the general control goal for the cable-suspended stabilizing platform in the scope of this thesis can be formulated as follows: the cable-suspended aerial system should keep the state of the platform close to the motionless to facilitate the manipulation process. In other words, we have to ensure a quasi-fixed base for the robotic arm to perform manipulation tasks precisely.

To dissect and test the aforementioned hypothesis as well as to satisfy the general control goal, three *research objectives* were defined:

RO1 To develop a robust control approach that can compensate for dynamic disturbances during transportation and manipulation of the cable-suspended platform without access to the system entire state and characterize its performance.

RO2 To develop a control approach to facilitate a manipulation performance of cable-suspended platform endowed with kinematically redundant robotic manipulator by compensation for static disturbances and evaluate its performance.

RO3 To assess manipulation performance and operational safety of the cable-suspended stabilizing platform through extensive experimental studies in a similar to the industrial environment.

In the following, a brief overview of each chapter contribution with respect to the defined research objectives is described.

The cable-suspended aerial manipulation is a sophisticated concept that is weakly covered by the research and engineering community. To this end, first of all, the design ideas and developments of the particular experimental demonstrator, a novel cable-suspended aerial manipulator SAM, were highlighted in **chapter 3**. The SAM is equipped with two actuations: fully-actuated propeller-based actuation and winch-based actuation, for stabilization and enhancing the manipulation performance. The first actuation contains eight propellers and can generate an omnidirectional wrench for the compensation of dynamic disturbances. The second one includes three winches, each of which can control the length of the rigging cable

connecting the suspension point, i.e., the hook's frame and the flying platform. It allows controlling the platform displacement relative to the winch suspension point. Therefore, slow winches with integrated breaks compensate for the static deviations, e.g., the COM displacement. As the main carrier of the cable-suspended aerial system, the mobile crane is proposed. The carrier supports the weight of the SAM, and as a result, actuation systems should not compensate for the gravity. Consequently, the platform can have reasonable dimensions that allow working in a complex narrow environment. Additionally, it is worth highlighting the transformable landing gear that allows the SAM to have a larger workspace for manipulation without any restrictions created by the standard landing gear, e.g., skids. The main engineering contributions performed by the author in the scope of this chapter include formulation of the technical requirements for the actuation systems via conducting simulational studies, thrust identification of the propeller-based actuation, analysis of the force and torque envelopes produced by the propeller-based actuation, development of the CANopen stack for QNX Neutrino RtOS for communication of the central computer (FCC) with winch-based actuation, and integration of the real-time control framework with target hardware.

Investigation of the obtained concept of the cable-suspended aerial manipulator has brought into focus the need to develop the appropriate control strategies. Due to the cable suspension, the system exerted the manipulation-disturbing pendulum-like behavior. Therefore, the primary control goal deeply investigated and tackled in **chapter 4** was set as the oscillation damping. Namely, the Optimal Oscillation Damping Controller (OODC) was designed, applied, and validated in simulation studies. This contribution is entirely devoted to the **RO1**. First of all, the system behavior was analyzed in detail. It turned out that the flying platform suspended to the crane's hook and constrained utilizing the suspension crane's chain evolves according to the spherical double pendulum model with a strong dependence on the pendulum weight-geometric parameters, including the hook weight and length of the chain of the crane. The most crucial challenge was the absence of information about the full state of the system since among sensors for the task, only the single onboard IMU was implied as available. Moreover, the pendulum can be controlled only indirectly by generating a damping wrench at the tip of the second link by the propeller-based actuation. As a solution for such a task formulation, the OODC was proposed and designed. The controller is based on constructing an estimator of the system angular velocities and minimizing linear-quadratic cost function that balances high system performance and low power consumption. The resulting controller

dissipates the oscillation with the desired balance between performance and power consumption. It is robust to the task because it does not require model parameters and utilizes only a reliable IMU sensor. Moreover, by virtue of the optimal gains, we can easily tune the gains for different operating conditions. Additionally, the global stability of the closed-loop system under the designed controller was shown.

Chapter 5 addressed the modeling and control of the winch-based actuation system in pair with the redundant robotic arm. The winch cabling suspension was modeled as a closed-chain dynamics and further transformed to the equal serial-chain dynamics, which is instantaneously feasible w. r. t. the defined holonomic constraints. This transformation allowed to access direct translational motion of the platform instead of the rigging cable length and to formulate two intuitive control tasks. The first one is to keep the end effector in the desired pose. The second one is to shift the system COM to compensate for the gravity-generated disturbing torque caused by the robotic arm weight. Thus, the vector connecting the suspension point and the overall COM of the platform (including the manipulator) is aligned with the gravity vector regardless of the robotic arm configuration, and the total weight does not generate the disturbing gravitational torque. In order to regulate both tasks, the Hierarchical impedance-based Whole-Body Controller (HWBC) was utilized. Based on the real-time model, it generates control torques for the robotic arm and platform. The controlled torque is directly used for the robotic arm and transformed through the admittance interface for the position-controlled winches. The selected impedance-based strategy provides the ability to interact with the environment compliantly and contributes to additional safety and effectiveness during the task execution. Thus, the central contribution of this chapter, modeling the complex constrained system dynamics with the following model transforming for the hierarchical whole-body controller, captures the **RO2**.

Extensive experimental validation and investigation of the aforementioned theoretical contributions was performed in the **chapter 6**. As the demonstrator system, the SAM presented in **chapter 3** was utilized. Experiments were conducted in various conditions, including specially equipped indoor and outdoor environments exploiting the crane as the carrier. We started with a frequency-based model validation of the cable-suspended aerial manipulator to confirm the double pendulum behavior assumed in the control design. Further, OODC was tested in the various experiments, including compensation for external disturbances, robotic arm motion, and suspension point motion, i.e., the crane. The controller demonstrated the ability

to compensate for the strong oscillations within 7-8 seconds for selected gains. Additionally, the robustness of the tuned controller during a varying the chain length was studied.

To the best of author knowledge, in this thesis it was the first time when the winch-based cable-driven suspension was utilized for the aerial manipulation. So, analysis of benefits and performance validation for winch-based actuation as well as adapted HWBC were studied through a set of experiments. Driven by the controller, the system effectively maintained a horizontal orientation keeping horizontal terms of the COM at zero while the robotic arm performed various operations. Namely, the arm was commanded to move in the worst possible configuration within the accessible workspace that affects the COM location. According to the controller model data, the COM was kept close to zero with RMSE of 0.32 mm along x axis and 0.35 mm along y axis while maximum deviation from zero were 0.9 mm and 1.3 mm along x and y axes, respectively. Received results showed the applicability of the proposed actuation system as well as applied control framework to the real scenarios for implementing complex aerial manipulation tasks. At the end of the 6-th chapter, the workability of the SAM driven by two controllers, OODC and HWBC, simultaneously was validated.

The proposed concept of cable-suspended aerial manipulation contributes to state of the art in aerial manipulation field. The three experimental missions in the industrial-like environment were conducted in **chapter 7** in order to emphasize the practical importance and viable commercial application of the proposed concept as well as designed control algorithms in a complex high-altitude environment. The first mission was devoted to the deployment of the heavy (6.5 kg) mobile inspection robot at the remotely-located pipe. The second mission demonstrated the assembly capabilities of the concept by performing the peg-in-hole assembly. Finally, the real industrial task, turning a valve with the lever handle, was performed. All missions were successfully completed by the operator without direct visual contact at the manipulation area, demonstrating the high safety and performance of the concept and the designed controllers. Received successful results within this and previous chapter allowed to reach the **RO3**.

8.2 Lessons learned

Based on the field investigation of the cable-suspended aerial manipulator performance, we came up with certain lessons about the applicability of this kind of technology in commercial tasks.

The suspension of the aerial platform helps to perform the manipulation tasks in terms of safety and performance. Indeed, the compact size allowed to operate in a narrow complex environment with obstacles without any collisions. Moreover, the platform could be fastly stabilized by the OODC so that the manipulation could be performed with precise positioning of the end effector tool. The oscillation damping is essential to perform a manipulation task using a suspended aerial system. It decreased the operational time for the operator to conduct missions. It is worth highlighting that the robust yaw controller is critical during the mission since manipulation with a spinning platform is hardly possible.

The HWBC allowed to keep the platform horizontal during the mission regardless of the robotic arm configuration. First of all, it made the manual manipulation process more convenient for the operator. Secondly, it helped to avoid the data jumps in the onboard sensors and perception system, including visual feedback for the operator. Thus, dual actuation confronted almost all types of disturbances that, in the end, made the operation more convenient, safe, and fast.

The required manipulation efforts in the industrial-like environment make the completely automated solution hardly possible for the considered tasks due to the presence of sudden disturbances in the outdoor environment (e.g., the wind) as well as due to the lack of high robustness of the sensors and perception system. The sharing control functionality that implies the use of both operator control and automation components makes the whole system safe, robust, and versatile. Moreover, the gained experience with aerial manipulation has shown that redundancy in the manipulator (in our case, it has 7 DOF) helps to avoid the singular configuration of the robotic arm and makes the operation conduction easier.

Exploiting the FTS attached to the end effector allowed to perform the interaction tasks with the environment more reliably, safely, and faster. Thus, during the deployment of the crawler, it was possible to press the cage toward the pipe with the required vertical force. At the same time, due to the FTS, it was possible to align the peg with a hole and feel the turning of the valve through the haptic feedback. It makes the operator experience similar to the case in which he performs the mission

personally by hand.

The performance of the cable-suspended aerial manipulation concept was validated with a mobile crane. The crane is a widely accessible platform for the industrial application areas, e.g., oil refinery or nuclear plant. The crane as the carrier has the following advantages:

- safe operation of the cable-suspended aerial manipulator: collisions with obstacles could be easily avoided, missions could be performed in narrow environments,
- high payload,
- wide availability of the system,
- no flight permissions is required,
- easier compliance with the safety regulations of the production plants.

8.3 Limitations

Despite the high efficiency and robustness of the investigated concept, the cable-suspension aerial manipulation has its own technological limitations. The main drawback of the concept includes an inability to operate above the platform. It restricts the use of the system in some applications, e.g., an inspection of the bridge bottom. Moreover, the operation of the presented platform SAM is not possible in the presence of copious dust or water drops since there is no water- and dust-proof integrated capabilities that might be required in the industrial environment.

Designed OODC does not consider the vertical crane jib oscillation, which might be induced by the sudden drop of the heavy payload or harsh environment contact. Also, the OODC is robust but sensitive to the cable chain length, which is unknown in general. So, some additional feedback from the crane to the aerial manipulator is desirable.

The performance of the HWBC is highly dependable on the system model precision. It means that each specific flying system should be manually adapted to the controller before start. In particular, the weight distribution within the platform and robotic arm dynamics should be well-known for calculating the gravitational torque precisely. Moreover, the feedback from the Force Torque Sensor (FTS) is required to

adapt the model during the interaction with the environment. Additionally, the efficient gain tuning rule for all control nodes in the scope of the sophisticated controller is required for better performance.

Finally, an optimization of the energy consumption by both actuation systems is required in order to keep the balance between high performance and battery level.

8.4 Future work

In the scope of one thesis, it is impossible to cover all aspects of the topic, so some of them will be addressed in future work.

Concerning the applications, deeper interactivity and immersion of the robotic arm operator into the operational environment would facilitate the mission execution. To this end, the virtual 3D environment that the operator uses at the display could be integrated into the virtual reality headset (glasses) to feel himself right in the operational spot while being in the office.

Moreover, for many industrial tasks, e.g., turning a gate valve with a circular handle, installing the nut while keeping the bolt, or other assembly operations where two components need to be controlled separately, two hands are desired. Therefore, the exploitation of two robotic arms on one platform provides human dexterity for complex tasks, especially for high-precision applications. So, the dexterous manipulation capabilities should be integrated and investigated. It is worth noting that due to the high payload capacity of the crane, the number of arms would not significantly affect the platform composition and dimensions.

In terms of the performance, a reliable and robust perception system is required. It would allow access to the system full state in real-time and perform not just more efficient oscillation damping but also the horizontal motion, whole-body control for all available DOFs, and other elaborated control strategies. It could be achieved by fusing the various sensor information, including onboard GPS, cameras, IMU, LiDAR. Moreover, it might help to avoid the necessity of getting any feedback from the crane carrier, i.e., chain length.

Additionally, it is worth investigating the redundancy of the propeller-based actuation. It contains eight propellers, while only seven are required for omnidirectionality. Thus, extra DOF could be used for fault tolerance or efficient energy consumption strategies. The energy cost estimation should be also performed for the winch-based actuation.

Furthermore, the performance might be increased on the actuator level by integrating the motor speed feedback from the ESC telemetry to the BLDC. It would allow keeping the motor thrust tolerant to the battery voltage level and motor characteristics, and, consequently, the performance of the proposed control schemes.

Finally, integration of the sensors for the winch cable tension measurement would allow the control of the whole system on the force-torque level for more quick and robust adaptation to any changes in the environment.

Appendices

Appendix A

Geometric yaw controller

The cabling of the suspended aerial manipulator does not put any constraints on the yaw motion. To this end, the control of the yaw channel might be performed in the same way as for the free rigid body. The rotational dynamics and kinematics of the rigid body, see subsubsection 2.1.1.3, can be described as follows:

$$\begin{aligned} \boldsymbol{Y}\dot{\boldsymbol{\omega}} + \boldsymbol{\omega} \times \boldsymbol{Y}\boldsymbol{\omega} &= \boldsymbol{u}, \\ \dot{\boldsymbol{R}} &= \boldsymbol{R}\hat{\boldsymbol{\omega}}. \end{aligned}$$

Let us define the rotational angle and velocity error as follows:

$$\begin{aligned} \boldsymbol{e}_{\boldsymbol{R}} &= \frac{1}{2}(\boldsymbol{R}_d^T\boldsymbol{R} - \boldsymbol{R}^T\boldsymbol{R}_d)^\vee, \\ \boldsymbol{e}_{\boldsymbol{\omega}} &= \boldsymbol{\omega} - \boldsymbol{R}^T\boldsymbol{R}_d\boldsymbol{\omega}_d. \end{aligned}$$

Then, the control law for the orientation of the free rigid body can be formulated as follows:

$$\boldsymbol{u} = \begin{bmatrix} \tau_x \\ \tau_y \\ \tau_z \end{bmatrix} = -\boldsymbol{k}_{\boldsymbol{R}}\boldsymbol{e}_{\boldsymbol{R}} - \boldsymbol{k}_{\boldsymbol{\omega}}\boldsymbol{e}_{\boldsymbol{\omega}} + \boldsymbol{\omega} \times \boldsymbol{Y}\boldsymbol{\omega}. \tag{A.1}$$

Here, $\boldsymbol{k}_{\boldsymbol{R}} \in \mathbb{R}^{3\times3}$ and $\boldsymbol{k}_{\boldsymbol{\omega}} \in \mathbb{R}^{3\times3}$ are diagonal positive matrices of the proportional and derivative control gains, respectively.

The last term of the vector $\boldsymbol{u}$ can be used for the yaw control of the suspended aerial manipulator.

Appendix B

Spherical double pendulum modeling

By excluding yaw motion from the dynamic equations of motion for the spherical double pendulum, the state of generalized coordinates has the following form: $\tilde{\boldsymbol{q}} = [q_1,\ q_2,\ q_3,\ q_4]^T$, where q_1 and q_2 are the roll and pitch angles of the hook motion in the world frame, q_3 and q_4 are the roll and pitch angles of the suspended aerial platform with respect to to the frame attached to the hook and with axes parallel to the world frame.

Then, the location of the hook and platform in the inertial frame is defined as follows:

$$\boldsymbol{r}_1 = \begin{bmatrix} x_h \\ y_h \\ z_h \end{bmatrix} = R_y(q_2)R_x(q_1) \begin{bmatrix} 0 \\ 0 \\ -l_1 \end{bmatrix}, \tag{B.1}$$

$$\boldsymbol{r}_2 = \begin{bmatrix} x_p \\ y_p \\ z_p \end{bmatrix} = \begin{bmatrix} x_h \\ y_h \\ z_h \end{bmatrix} + R_y(q_4)R_x(q_3) \begin{bmatrix} 0 \\ 0 \\ -l_2 \end{bmatrix}. \tag{B.2}$$

By taking derivative of (B.1) and (B.2) with respect to time, we can write down:

$$\dot{\boldsymbol{r}}_1 = \boldsymbol{J}_1\dot{\tilde{\boldsymbol{q}}},$$
$$\dot{\boldsymbol{r}}_2 = \boldsymbol{J}_2\dot{\tilde{\boldsymbol{q}}}.$$

Then, the inertia tensor can be formulated as follows:

$$\tilde{\boldsymbol{M}} = m_1\boldsymbol{J}_1^T\boldsymbol{J}_1 + m_2\boldsymbol{J}_2^T\boldsymbol{J}_2.$$

Appendix C

Oscillation damping controller for the single pendulum

The coordinates of the platform in the case of the single pendulum model are:

$$\boldsymbol{r}_p = \begin{bmatrix} x_p \\ y_p \\ z_p \end{bmatrix} = \boldsymbol{R}_b^w \begin{bmatrix} 0 \\ 0 \\ -l \end{bmatrix},$$

where $l = l_1 + l_2$. Furthermore, the platform linear body velocities v_x^b and v_y^b are related with body angular velocities $\boldsymbol{\omega}_b = [p,\ q,\ r]^T$ as follows:

$$\boldsymbol{v}_p = \begin{bmatrix} v_x^b \\ v_y^b \\ 0 \end{bmatrix} = \begin{bmatrix} -lq \\ lp \\ 0 \end{bmatrix}.$$

Then, the damping force of the body wrench might have the proportional-derivative ($\mathcal{PD}$) form:

$$\boldsymbol{f}_b = \begin{bmatrix} f_{bx} \\ f_{by} \\ f_{bz} \end{bmatrix} = -\boldsymbol{R}_w^b \boldsymbol{K}_{\mathrm{p}} \boldsymbol{r}_p - \boldsymbol{K}_{\mathrm{v}} \boldsymbol{v}_p. \tag{C.1}$$

Here, $\boldsymbol{R}_w^b = (\boldsymbol{R}_b^w)^{-1}$, $\boldsymbol{K}_{\mathrm{p}} \in \mathbb{R}^{3\times3}$ and $\boldsymbol{K}_{\mathrm{v}} \in \mathbb{R}^{3\times3}$ are positive diagonal gain matrices. As a result, a generated wrench should be composed of f_{bx}, f_{by}, and τ_z, with nullified rest components. Here, τ_z is the control torque around the yaw axis received in Appendix A.

Appendix D

Derivation of matrices $\boldsymbol{A}$, $\boldsymbol{S}$, $\boldsymbol{B}$, and $\boldsymbol{O}$ for the HWBC

Matrix A

Projecting the equation (5.2) on the world frame axes, we receive the following:

$$\begin{aligned} Ox &: q_4\cos(q_3) + q_7\cos(q_6) = L\cos(q_5), \\ Oy &: q_4\sin(q_3) + q_7\sin(q_6) = L\sin(q_5). \end{aligned} \tag{D.1}$$

Here, $L = BE$ is the diameter of the platform base.

In order to obtain the matrix $\boldsymbol{A} \in \mathbb{R}^{2\times 6+m}$, let us take a time derivatives of (D.1) and present it in the matrix form:

$$\underbrace{\begin{bmatrix} 0 & 0 \\ -q_4\sin q_3 & q_4\cos q_3 \\ \cos q_3 & \sin q_3 \\ L\sin(q_5) & -L\cos(q_5) \\ -q_7\sin(q_6) & q_7\cos(q_6) \\ \cos(q_6) & \sin(q_6) \\ \mathbf{0}_m & \mathbf{0}_m \end{bmatrix}^T}_{=\boldsymbol{A}^T(\boldsymbol{q})} \dot{\boldsymbol{q}} = 0.$$

Matrix S

Let us split the received matrix $\boldsymbol{A}$ as: $\boldsymbol{A} = [\boldsymbol{A}_{\boldsymbol{\delta}},\ \boldsymbol{A}_{\boldsymbol{z}}]^T$. The first term $\boldsymbol{A}_{\boldsymbol{\delta}}$ includes the components related to the vector of independent generalized coordinates $\boldsymbol{\delta} =$

$[q_1,\ q_4,\ q_5,\ q_7,\ \boldsymbol{q}_m]^T \in \mathbb{R}^{4+m}$, and the second one - dependent generalized coordinates $\boldsymbol{z} = [q_3,\ q_6]^T \in \mathbb{R}^2$. As it was mentioned in (5.4), the matrix $\boldsymbol{S}$ should comply with $\boldsymbol{S}^T(\boldsymbol{q})\boldsymbol{A}^T(\boldsymbol{q}) = 0$. To this end, let us define it as $\boldsymbol{S} = [\boldsymbol{I}_{(4+m)\times(4+m)}, -\boldsymbol{A}_{\boldsymbol{z}}^{-1}\boldsymbol{A}_{\boldsymbol{\delta}}]^T \in \mathbb{R}^{(6+m)\times(4+m)}$ [My and Hoan, 2019], then[1]:

$$\boldsymbol{S}^T(\boldsymbol{q})\boldsymbol{A}^T(\boldsymbol{q}) = \begin{bmatrix} \boldsymbol{I}_{(4+m)\times(4+m)} & -\boldsymbol{A}_{\boldsymbol{\delta}}^T\boldsymbol{A}_{\boldsymbol{z}}^{-T} \end{bmatrix} \begin{bmatrix} \boldsymbol{A}_{\boldsymbol{\delta}}^T \\ \boldsymbol{A}_{\boldsymbol{z}}^T \end{bmatrix} = \boldsymbol{A}_{\boldsymbol{\delta}}^T - \boldsymbol{A}_{\boldsymbol{\delta}}^T\boldsymbol{A}_{\boldsymbol{z}}^{-T}\boldsymbol{A}_{\boldsymbol{z}}^T = 0.$$

Matrix B

Projecting the equation (5.2) on the world frame axes, we can receive the forward kinematics for the point C using two branches of the closed chain.
For the first branch:

$$\begin{aligned} x_c &= l_1\sin(q_1) - q_4\cos(q_3) + \frac{L}{2}\cos(q_5), \\ y_c &= -l_1\cos(q_1) - q_4\sin(q_3) + \frac{L}{2}\sin(q_5). \end{aligned} \tag{D.2}$$

For the second branch:

$$\begin{aligned} x_c &= l_1\sin(q_1) + q_7\cos(q_6) - \frac{L}{2}\cos(q_5), \\ y_c &= -l_1\cos(q_1) + q_7\sin(q_6) - \frac{L}{2}\sin(q_5). \end{aligned} \tag{D.3}$$

By squaring and adding the equations (D.2) and (D.3), we can express IK parameters with excluded q_3 and q_6 as follows:

$$\begin{aligned} q_4 &= \sqrt{(\frac{L}{2}\cos(q_5) + l_1\sin(q_1) - x_c)^2 + (\frac{L}{2}\sin(q_5) - l_1\cos(q_1) - y_c)^2}, \\ q_7 &= \sqrt{(\frac{L}{2}\cos(q_5) - l_1\sin(q_1) + x_c)^2 + (\frac{L}{2}\sin(q_5) + l_1\cos(q_1) + y_c)^2}. \end{aligned} \tag{D.4}$$

Taking derivatives of the (D.4) along the $\boldsymbol{q}_p = [x_c,\ q_5,\ y_c]^T$, we can receive differential kinematics connecting the vector of *independent generalized coordinates*, $\boldsymbol{\delta}$, and *quasi-state vector of feasible motions*, $\boldsymbol{\eta}$, i.e.[Jafari Harandi et al., 2019]:

$$\dot{\boldsymbol{\delta}} = \boldsymbol{B}\dot{\boldsymbol{\eta}}.$$

[1]Splitting the matrix $\boldsymbol{A}$ in shown way requires reorder of variables in the state as $[\boldsymbol{\delta},\ \boldsymbol{z}]^T$.

Here, analytical Jacobian matrix $\boldsymbol{B}$ can be expressed as:

$$\boldsymbol{B} = \begin{bmatrix} I_{1\times1} & \mathbf{0}_{1\times3} & \mathbf{0}_{1\times m} \\ \mathbf{0}_{3\times1} & \boldsymbol{J}_p & \mathbf{0}_{3\times m} \\ \mathbf{0}_{m\times1} & \mathbf{0}_{m\times3} & \boldsymbol{I}_{m\times m} \end{bmatrix},$$

where $\boldsymbol{J}_p$ includes mapping received from differentiating (D.4):

$$\boldsymbol{J}_p^T = \begin{bmatrix} \dfrac{x_c - \dfrac{L}{2}\cos(q_5) - l_1\sin(q_1)}{q_4} & 0 & \dfrac{x_c + \dfrac{L}{2}\cos(q_5) - l_1\sin(q_1)}{q_7} \\ \dfrac{L(l_1\cos(q_1-q_5) - \sin(q_5)x_c + \cos(q_5)y_c)}{2q_4} & 1 & \dfrac{L(l_1\cos(q_1-q_5) - \sin(q_5)x_c + \cos(q_5)y_c)}{2q_7} \\ \dfrac{y_c - \dfrac{L}{2}\sin(q_5) + l_1\cos(q_1)}{q_4} & 0 & \dfrac{y_c + \dfrac{L}{2}\sin(q_5) + l_1\cos(q_1)}{q_7} \end{bmatrix}. \tag{D.5}$$

In the case, when $q_1 = 0$, (D.5) can be rewritten as follows:

$$\boldsymbol{J}_p^T(q_1=0) = \begin{bmatrix} \dfrac{x_c - \dfrac{L}{2}\cos(q_5)}{q_4} & 0 & \dfrac{x_c + \dfrac{L}{2}\cos(q_5)}{q_7} \\ \dfrac{L(l_1\cos(q_5) - \sin(q_5)x_c + \cos(q_5)y_c)}{2q_4} & 1 & \dfrac{L(l_1\cos(q_5) - \sin(q_5)x_c + \cos(q_5)y_c)}{2q_7} \\ \dfrac{y_c - \dfrac{L}{2}\sin(q_5) + l_1}{q_4} & 0 & \dfrac{y_c + \dfrac{L}{2}\sin(q_5) + l_1}{q_7} \end{bmatrix}.$$

Matrix O

To relate actuated torques $\tilde{\boldsymbol{\tau}}_a$ with generalized torques $\tilde{\boldsymbol{\tau}}$ of the system (5.6), let us define the Jacobian matrix $\boldsymbol{Y} \in \mathbb{R}^{(3+m)\times(4+m)}$ which equals to the $\boldsymbol{B}$ without the row corresponding to the non-controllable coordinate, i.e., q_5. Then, relation can be formulated as follows:

$$\underbrace{\begin{bmatrix} \boldsymbol{\tau}_{q_1} \\ \tau_{x_c} \\ \tau_{q_5} \\ \tau_{y_c} \\ \boldsymbol{\tau}_m \end{bmatrix}}_{\tilde{\boldsymbol{\tau}}} = \underbrace{\boldsymbol{Y}^T\underline{\boldsymbol{Y}}^{-T}}_{\boldsymbol{O}^T} \underbrace{\begin{bmatrix} \boldsymbol{\tau}_{q_1} \\ \tau_{x_c} \\ \tau_{y_c} \\ \boldsymbol{\tau}_m \end{bmatrix}}_{\tilde{\boldsymbol{\tau}}_a},$$

here $\underline{\boldsymbol{Y}} \in \mathbb{R}^{(3+m)\times(3+m)}$ is Jacobian $\boldsymbol{Y}$ without column corresponding to the DOF that we do not aim to control, i.e., q_5. It is worth noting that $\boldsymbol{O}$ maps τ_{x_c} and τ_{y_c} without scaling and does not affect the $\boldsymbol{\tau}_{q_1}$ and $\boldsymbol{\tau}_m$ at all. Resulted τ_{q_5} in this case contains weighted sum of τ_{x_c} and τ_{y_c}.

Bibliography

[1] Mti 100-series description. URL `https://www.xsens.com/products/mti-100-series/`. [accessed 5-September-2019].

[2] David A Abbink, Tom Carlson, Mark Mulder, Joost CF De Winter, Farzad Aminravan, Tricia L Gibo, and Erwin R Boer. A topology of shared control systems—finding common ground in diversity. *IEEE Transactions on Human-Machine Systems*, 48(5):509–525, 2018.

[3] Abdulghafoor Salehzadeh Aghdam, Mohammad B Menhaj, Farshad Barazandeh, and Farzane Abdollahi. Cooperative load transport with movable load center of mass using multiple quadrotor uavs. In *2016 4th International Conference on Control, Instrumentation, and Automation (ICCIA)*, pages 23–27. IEEE, 2016.

[4] Albert Albers, Simon Trautmann, Thomas Howard, Trong Anh Nguyen, Markus Frietsch, and Christian Sauter. Semi-autonomous flying robot for physical interaction with environment. In *IEEE Conference on Robotics Automation and Mechatronics (RAM)*, pages 441–446, 2010.

[5] Alin Albu-Schäffer, Sami Haddadin, Ch Ott, Andreas Stemmer, Thomas Wimböck, and Gerhard Hirzinger. The dlr lightweight robot: design and control concepts for robots in human environments. *Industrial Robot: an international journal*, 2007.

[6] Alin Albu-Schäffer, Christian Ott, and Gerd Hirzinger. A unified passivity-based control framework for position, torque and impedance control of flexible joint robots. *The international journal of robotics research*, 26(1):23–39, 2007.

[7] Ghulam Muhammad Ali, Joe Kosa, Ahmed Bouferguene, and Mohamed Al-Hussein. Competitive assessment of ice and frozen silt mat for crane ground support using finite-element analysis. *Journal of Construction Engineering and Management*, 147(6):04021038, 2021.

[8] Mike Allenspach, Karen Bodie, Maximilian Brunner, Luca Rinsoz, Zachary Taylor, Mina Kamel, Roland Siegwart, and Juan Nieto. Design and optimal control of a tiltrotor micro-aerial vehicle for efficient omnidirectional flight. *The International Journal of Robotics Research*, 39(10-11):1305–1325, 2020.

[9] Altitec, 2019. URL `https://theogm.com/wp-content/uploads/2019/07/turbine-blade-tech.jpg`.

[10] Francesco Amato. *Robust control of linear systems subject to uncertain time-varying parameters*, volume 325. Springer, 2006.

[11] Haruhiko Asada and J-JE Slotine. *Robot analysis and control*. John Wiley & Sons, 1986.

[12] Peter M Asaro. The labor of surveillance and bureaucratized killing: new subjectivities of military drone operators. *Social semiotics*, 23(2):196–224, 2013.

[13] Federico Augugliaro, Ammar Mirjan, Fabio Gramazio, Matthias Kohler, and Raffaello D'Andrea. Building tensile structures with flying machines. In *2013 IEEE/RSJ International Conference on Intelligent Robots and Systems*, pages 3487–3492. IEEE, 2013.

[14] Manohari Balasingam. Drones in medicine—the rise of the machines. *International journal of clinical practice*, 71(9):e12989, 2017.

[15] Teun J Bartelds, Alex Capra, Salua Hamaza, Stefano Stramigioli, and Matteo Fumagalli. Compliant aerial manipulators: Toward a new generation of aerial robotic workers. *Robotics and Automation Letters*, 1(1):477–483, 2016.

[16] Shishir Bashyal and Ganesh Kumar Venayagamoorthy. Human swarm interaction for radiation source search and localization. In *2008 IEEE Swarm Intelligence Symposium*, pages 1–8. IEEE, 2008.

[17] PM Basset, A Tremolet, and T Lefebvre. Rotary wing uav pre-sizing: past and present methodological approaches at onera. *AerospaceLab*, (8):1–12, 2014.

[18] Jeremy Begey, Loic Cuvillon, Maximilien Lesellier, Marc Gouttefarde, and Jacques Gangloff. Dynamic control of parallel robots driven by flexible cables and actuated by position-controlled winches. *IEEE Transactions on Robotics*, 35(1):286–293, 2018.

[19] Lidia María Belmonte, Rafael Morales, and Antonio Fernández-Caballero. Computer vision in autonomous unmanned aerial vehicles—a systematic mapping study. *Applied Sciences*, 9(15):3196, 2019.

[20] Mordechai Ben-Ari and Francesco Mondada. *Elements of Robotics*. Springer, 2018. ISBN 978-3-319-62532-4. doi:10.1007/978-3-319-62533-1. URL `https://doi.org/10.1007/978-3-319-62533-1`.

[21] Markus Bernard and Konstantin Kondak. Generic slung load transportation system using small size helicopters. In *IEEE International Conference on Robotics and Automation (ICRA)*, pages 3258–3264, 2009.

[22] Wojciech Blajer. A geometric unification of constrained system dynamics. *Multibody System Dynamics*, 1(1):3–21, 1997.

[23] Karen Bodie, Maximilian Brunner, Michael Pantic, Stefan Walser, Patrick Pfändler, Ueli Angst, Roland Siegwart, and Juan Nieto. An omnidirectional aerial manipulation platform for contact-based inspection. In *2019 Robotics: Science and Systems*, volume XV, 2019.

[24] Rogerio Bonatti, Yanfu Zhang, Sanjiban Choudhury, Wenshan Wang, and Sebastian Scherer. Autonomous drone cinematographer: Using artistic principles to create smooth, safe, occlusion-free trajectories for aerial filming. In *International Symposium on Experimental Robotics*, pages 119–129. Springer, 2018.

[25] Per Henrik Borgstrom, Brett L Jordan, Gaurav S Sukhatme, Maxim A Batalin, and William J Kaiser. Rapid computation of optimally safe tension distributions for parallel cable-driven robots. *IEEE Transactions on Robotics*, 25(6): 1271–1281, 2009.

[26] P. Bosscher, A. T. Riechel, and I. Ebert-Uphoff. Wrench-feasible workspace generation for cable-driven robots. *IEEE Transactions on Robotics*, 22(5): 890–902, 2006. doi:10.1109/TRO.2006.878967.

[27] Coleman Brosilow and Babu Joseph. *Techniques of model-based control*. Prentice Hall Professional, 2002.

[28] BL Burks, GA Armstrong, PL Butler, and P Boissiere. Combined long reach and dexterous manipulation for waste storage tank applications. Technical report, Oak Ridge National Lab., TN (United States), 1991.

[29] Alvaro Caballero, Manuel Béjar, A Rodriguez-Castaño, and Aníbal Ollero. Motion planning for long reach manipulation in aerial robotic systems with two arms. In *2017 European Conference on Mobile Robots (ECMR)*, pages 1–7. IEEE, 2017.

[30] Alvaro Caballero, Alejandro Suárez, Fran Real, Victor M Vega, Manuel Bejar, Angel Rodriguez-Castaño, and Anibal Ollero. First experimental results on motion planning for transportation in aerial long-reach manipulators with two arms. In *2018 IEEE/RSJ International Conference on Intelligent Robots and Systems (IROS)*, pages 8471–8477. IEEE, 2018.

[31] Fabrizio Caccavale, Ciro Natale, Bruno Siciliano, and Luigi Villani. Resolved-acceleration control of robot manipulators: A critical review with experiments. *Robotica*, 16(5):565–573, 1998.

[32] *CANopen application layer and communication profile*. CAN in Automation (CiA) e. V., Nuremberg BY, Germany, 2011. Accessed: Oct 30, 2020.

[33] Luis Evaristo Caraballo, José Miguel Díaz-Báñez, Iván Maza, and Aníbal Ollero. The block-information-sharing strategy for task allocation: A case study for structure assembly with aerial robots. *European Journal of Operational Research*, 260(2):725–738, 2017.

[34] Jessica R Cauchard, Jane L E, Kevin Y Zhai, and James A Landay. Drone & me: an exploration into natural human-drone interaction. In *Proceedings of the 2015 ACM international joint conference on pervasive and ubiquitous computing*, pages 361–365, 2015.

[35] Soon-Jo Chung, Aditya Avinash Paranjape, Philip Dames, Shaojie Shen, and Vijay Kumar. A survey on aerial swarm robotics. *IEEE Transactions on Robotics*, 34(4):837–855, 2018.

[36] Andre Coelho, Harsimran Singh, Konstantin Kondak, and Christian Ott. Whole-body bilateral teleoperation of a redundant aerial manipulator. In *2020 IEEE International Conference on Robotics and Automation (ICRA)*, pages 9150–9156. IEEE, 2020.

[37] Andre Coelho, Yuri Sarkisov, Xuwei Wu, Hrishik Mishra, Harsimran Singh, Alexander Dietrich, Antonio Franchi, Konstantin Kondak, and Christian Ott. Whole-body teleoperation and shared control of redundant robots with applications to aerial manipulation. *Journal of Intelligent & Robotic Systems*, 102 (1):1–22, 2021.

[38] Andre Coelho, Yuri S Sarkisov, Jongseok Lee, Ribin Balachandran, Antonio Franchi, Konstantin Kondak, and Christian Ott. Hierarchical control of redundant aerial manipulators with enhanced field of view. In *2021 International Conference on Unmanned Aircraft Systems (ICUAS)*, pages 994–1002. IEEE, 2021.

[39] Peter Corke. *Robotics, vision and control: fundamental algorithms in MATLAB® second, completely revised*, volume 118. Springer, 2017.

[40] John J Craig. *Introduction to robotics: mechanics and control, 3/E*. Pearson Education India, 2009.

[41] Phillip M Cunio, Alessandra Babuscia, Zachary J Bailey, Hemant Chaurasia, Rahul Goel, Alessandro A Golkar, Daniel Selva, Eric Timmons, Babak E Cohanim, Jeffrey A Hoffman10, et al. Initial development of an earth-based prototype for a lunar hopper autonomous exploration system. In *AIAA SPACE 2009 Conference & Exposition*, 2009.

[42] Tarak Damak, Dorsaf Elleuch, et al. Robust model-free control for robot manipulator under actuator dynamics. *Mathematical Problems in Engineering*, 2020:1–11, 2020.

[43] P Damodharan and Krishna Vasudevan. Sensorless brushless dc motor drive based on the zero-crossing detection of back electromotive force (emf) from the line voltage difference. *IEEE Transactions on Energy Conversion*, 25(3): 661–668, 2010.

[44] Alexander Dietrich and Christian Ott. Hierarchical impedance-based tracking control of kinematically redundant robots. *IEEE Transactions on Robotics*, 36(1):204–221, 2019.

[45] Alexander Dietrich, Christian Ott, and Alin Albu-Schäffer. Multi-objective compliance control of redundant manipulators: Hierarchy, control, and stability. In *2013 IEEE/RSJ International Conference on Intelligent Robots and Systems*, pages 3043–3050. IEEE, 2013.

[46] Alexander Dietrich, Christian Ott, and Alin Albu-Schäffer. An overview of null space projections for redundant, torque-controlled robots. *The International Journal of Robotics Research*, 34(11):1385–1400, 2015.

[47] Alexander Dietrich, Kristin Bussmann, Florian Petit, Paul Kotyczka, Christian Ott, Boris Lohmann, and Alin Albu-Schäffer. Whole-body impedance control of wheeled mobile manipulators. *Autonomous Robots*, 40(3):505–517, 2016.

[48] Alexander Dietrich, Xuwei Wu, Kristin Bussmann, Marie Harder, Maged Iskandar, Johannes Englsberger, Christian Ott, and Alin Albu-Schäffer. Practical consequences of inertia shaping for interaction and tracking in robot control. *Control Engineering Practice*, 114:104875, 2021.

[49] Gen Endo, Tetsuo Hagiwara, Yoshihide Nakamura, Hiroyuki Nabae, and Koichi Suzumori. A proposal of super long reach articulated manipulator with gravity compensation using thrusters. In *2018 IEEE/ASME International Conference on Advanced Intelligent Mechatronics (AIM)*, pages 1414–1419. IEEE, 2018.

[50] Boris V Ermolenko, Georgy V Ermolenko, Yulia A Fetisova, and Liliana N Proskuryakova. Wind and solar pv technical potentials: Measurement methodology and assessments for russia. *Energy*, 137:1001–1012, 2017.

[51] Antonio Franchi and Anthony Mallet. Adaptive closed-loop speed control of bldc motors with applications to multi-rotor aerial vehicles. In *2017 IEEE International Conference on Robotics and Automation (ICRA)*, pages 5203–5208. IEEE, 2017.

[52] Antonio Franchi, Ruggero Carli, Davide Bicego, and Markus Ryll. Full-pose tracking control for aerial robotic systems with laterally bounded input force. *Transactions on Robotics*, 34(2):534–541, 2018.

[53] Gustavo M. Freitas, Antonio C. Leite, and Fernando Lizarralde. Kinematic control of constrained robotic systems. *Sba: Controle & Automacao Sociedade Brasileira de Automatica*, 22:559 – 572, 12 2011. ISSN 0103-1759. doi:10.1590/S0103-17592011000600002. URL `http://www.scielo.br/scielo.php?script=sci_arttext&pid=S0103-17592011000600002&nrm=iso`.

[54] Chiara Gabellieri, Yuri S Sarkisov, Andre Coelho, Lucia Pallottino, Konstantin Kondak, and Min Jun Kim. Compliance control of cable-suspended aerial manipulator using hierarchical control framework. In *2020 IEEE/RSJ International Conference on Intelligent Robots and Systems (IROS)*, pages 7196–7202. IEEE/RSJ, 2020. doi:10.1109/IROS45743.2020.9340703.

[55] Devlin A. Gandy, 2020. URL https://www.nbcnews.com/science/science-news/ancient-stone-tools-suggest-first-people-arrived-america-earlier-thought-n1234578.

[56] Stanisław Gardecki, Andrzej Kasiński, Adam Bondyra, and Przemysław Gasior. Multirotor aerial platform with manipulation system-static disturbances. In *International Conference Automation*, pages 357–366. Springer, 2017.

[57] Gianluca Garofalo and Christian Ott. Hierarchical tracking control with arbitrary task dimensions: Application to trajectory tracking on submanifolds. *IEEE Robotics and Automation Letters*, 5(4):6153–6160, 2020.

[58] Gianluca Garofalo, Christian Ott, and Alin Albu-Schaffer. On the closed form computation of the dynamic matrices and their differentiations. In *IEEE/RSJ International Conference on Intelligent Robots and Systems (IROS)*, pages 2364–2359, 2013.

[59] Gianluca Garofalo, Bernd Henze, Johannes Englsberger, and Christian Ott. On the inertially decoupled structure of the floating base robot dynamics. *IFAC-PapersOnLine*, 48(1):322–327, 2015.

[60] Guido Gioioso, Antonio Franchi, Gionata Salvietti, Stefano Scheggi, and Domenico Prattichizzo. The flying hand: A formation of uavs for cooperative aerial tele-manipulation. In *2014 IEEE International conference on robotics and automation (ICRA)*, pages 4335–4341. IEEE, 2014.

[61] Sami Haddadin, Alessandro De Luca, and Alin Albu-Schäffer. Robot collisions: A survey on detection, isolation, and identification. *IEEE Transactions on Robotics*, 33(6):1292–1312, 2017.

[62] Mahmoud Hamandi, Kapil Sawant, Marco Tognon, and Antonio Franchi. Omni-plus-seven (o7+): An omnidirectional aerial prototype with a minimal number of unidirectional thrusters. In *2020 International Conference on Unmanned Aircraft Systems (ICUAS)*, pages 754–761. IEEE, 2020.

[63] Mahmoud Hamandi, Federico Usai, Quentin Sablé, Nicolas Staub, Marco Tognon, and Antonio Franchi. Survey on aerial multirotor design: a taxonomy based on input allocation. 2020.

[64] Kim Hartmann and Keir Giles. Uav exploitation: A new domain for cyber power. In *2016 8th International Conference on Cyber Conflict (CyCon)*, pages 205–221. IEEE, 2016.

[65] Tomislav Haus, Matko Orsag, and Stjepan Bogdan. Design considerations for a large quadrotor with moving mass control. In *2016 International Conference on Unmanned Aircraft Systems (ICUAS)*, pages 1327–1334. IEEE, 2016.

[66] Tomislav Haus, Matko Orsag, and Stjepan Bogdan. Mathematical modelling and control of an unmanned aerial vehicle with moving mass control concept. *Journal of Intelligent & Robotic Systems*, 88(2-4):219–246, 2017.

[67] Bernd Henze, Alexander Dietrich, and Christian Ott. An approach to combine balancing with hierarchical whole-body control for legged humanoid robots. *IEEE Robotics and Automation Letters*, 1(2):700–707, 2015.

[68] Guillermo Heredia, AE Jimenez-Cano, I Sanchez, Domingo Llorente, V Vega, J Braga, JA Acosta, and Aníbal Ollero. Control of a multirotor outdoor aerial manipulator. In *2014 IEEE/RSJ international conference on intelligent robots and systems*, pages 3417–3422. IEEE, 2014.

[69] Wolfgang Hoenig, Christina Milanes, Lisa Scaria, Thai Phan, Mark Bolas, and Nora Ayanian. Mixed reality for robotics. In *2015 IEEE/RSJ International Conference on Intelligent Robots and Systems (IROS)*, pages 5382–5387. IEEE, 2015.

[70] Neville Hogan. Impedance control: An approach to manipulation: Part i—theory. 1985.

[71] Felix Huber, Konstantin Kondak, Kai Krieger, Dominik Sommer, Marc Schwarzbach, Maximilian Laiacker, Ingo Kossyk, Sven Parusel, Sami Haddadin, and Alin Albu-Schäffer. First analysis and experiments in aerial manipulation using fully actuated redundant robot arm. In *2013 IEEE/RSJ International Conference on Intelligent Robots and Systems*, pages 3452–3457. IEEE, 2013.

[72] Adrian Ilka. Matlab/octave toolbox for structurable and robust output-feedback lqr design. *IFAC-PapersOnLine*, 51(4):598–603, 2018.

[73] Javier Irizarry, Masoud Gheisari, and Bruce N Walker. Usability assessment of drone technology as safety inspection tools. *Journal of Information Technology in Construction (ITcon)*, 17(12):194–212, 2012.

[74] Maged Iskandar and Sebastian Wolf. Dynamic friction model with thermal and load dependency: modeling, compensation, and external force estimation. In *International Conference on Robotics and Automation (ICRA)*, pages 7367–7373. IEEE, 2019.

[75] Maged Iskandar, Gabriel Quere, Annette Hagengruber, Alexander Dietrich, and Jörn Vogel. Employing whole-body control in assistive robotics. In *IEEE International Conference on Intelligent Robots and Systems*, pages 5643–5650, 2019.

[76] Maged Iskandar, Christian Ott, Oliver Eiberger, Manuel Keppler, Alin Albu-Schäffer, and Alexander Dietrich. Joint-level control of the dlr lightweight robot sara. In *Proc. of the 2020 IEEE/RSJ International Conference on Intelligent Robots and Systems*, pages 8903–8910. IEEE, 2020.

[77] Maged Iskandar, Oliver Eiberger, Alin Albu-Schäffer, Alessandro De Luca, and Alexander Dietrich. Collision detection, identification, and localization on the dlr sara robot with sensing redundancy. In *2021 IEEE International*

Conference on Robotics and Automation (ICRA), pages 3111–3117. IEEE, 2021.

[78] M. R. Jafari Harandi, H. Damirchi, S. a. Khalilpour seyedi, and H. D. Taghirad. Point-to-point motion control of an underactuated planar cable driven robot. In *2019 27th Iranian Conference on Electrical Engineering (ICEE)*, pages 979–984, 2019. doi:10.1109/IranianCEE.2019.8786746.

[79] AE Jimenez-Cano, Jesús Martin, Guillermo Heredia, Aníbal Ollero, and R Cano. Control of an aerial robot with multi-link arm for assembly tasks. In *IEEE International Conference on Robotics and Automation (ICRA)*, pages 4916–4921, 2013.

[80] AE Jimenez-Cano, J Braga, Guillermo Heredia, and Aníbal Ollero. Aerial manipulator for structure inspection by contact from the underside. In *2015 IEEE/RSJ international conference on intelligent robots and systems (IROS)*, pages 1879–1884. IEEE, 2015.

[81] Zeeshan Kaleem and Mubashir Husain Rehmani. Amateur drone monitoring: State-of-the-art architectures, key enabling technologies, and future research directions. *IEEE Wireless Communications*, 25(2):150–159, 2018.

[82] Mina Kamel, Sebastian Verling, Omar Elkhatib, Christian Sprecher, Paula Wulkop, Zachary Taylor, Roland Siegwart, and Igor Gilitschenski. The voliro omniorientational hexacopter: An agile and maneuverable tiltable-rotor aerial vehicle. *IEEE Robotics & Automation Magazine*, 25(4):34–44, 2018.

[83] Arvid QL Keemink, Matteo Fumagalli, Stefano Stramigioli, and Raffaella Carloni. Mechanical design of a manipulation system for unmanned aerial vehicles. In *IEEE International Conference on Robotics and Automation (ICRA)*, pages 3147–3152, 2012.

[84] Hassan K Khalil. *Nonlinear control*. Pearson Higher Ed, 2014.

[85] Hossein Bonyan Khamseh, Farrokh Janabi-Sharifi, and Abdelkader Abdessameud. Aerial manipulation—a literature survey. *Robotics and Autonomous Systems*, 107:221–235, 2018.

[86] Oussama Khatib. A unified approach for motion and force control of robot manipulators: The operational space formulation. *IEEE Journal on Robotics and Automation*, 3(1):43–53, 1987.

[87] Oussama Khatib. Lecture notes: Advanced robotic manipulation, 2005.

[88] Dong-Hyun Kim, Yong-Guk Go, and Soo-Mi Choi. An aerial mixed-reality environment for first-person-view drone flying. *Applied Sciences*, 10(16):5436, 2020.

[89] Min Jun Kim, Ribin Balachandran, Marco De Stefano, Konstantin Kondak, and Christian Ott. Passive compliance control of aerial manipulators. In

2018 IEEE/RSJ International Conference on Intelligent Robots and Systems (IROS), pages 4177–4184. IEEE, 2018.

[90] Min Jun Kim, Konstantin Kondak, and Christian Ott. A stabilizing controller for regulation of uav with manipulator. *Robotics and Automation Letters*, 3 (3):1719–1726, 2018.

[91] Min Jun Kim, Jianjie Lin, Konstantin Kondak, Dongheui Lee, and Christian Ott. Oscillation damping control of pendulum-like manipulation platform using moving masses. *IFAC-PapersOnLine*, 51(22):465–470, 2018.

[92] Min Jun Kim, Fabian Beck, Christian Ott, and Alin Albu-Schäffer. Model-free friction observers for flexible joint robots with torque measurements. *IEEE Transactions on Robotics*, 35(6):1508–1515, 2019.

[93] Suseong Kim, Seungwon Choi, and H Jin Kim. Aerial manipulation using a quadrotor with a two dof robotic arm. In *IEEE/RSJ International Conference on Intelligent Robots and Systems (IROS)*, pages 4990–4995, 2013.

[94] Suseong Kim, Hoseong Seo, Jongho Shin, and H Jin Kim. Cooperative aerial manipulation using multirotors with multi-dof robotic arms. *IEEE/ASME Transactions on Mechatronics*, 23(2):702–713, 2018.

[95] Konstantin Kondak, Felix Huber, Marc Schwarzbach, Maximilian Laiacker, Dominik Sommer, Manuel Bejar, and Aníbal Ollero. Aerial manipulation robot composed of an autonomous helicopter and a 7 degrees of freedom industrial manipulator. In *2014 IEEE International Conference on Robotics and Automation (ICRA)*, pages 2107–2112. IEEE, 2014.

[96] Konstantin Kondak, Felix Huber, Marc Schwarzbach, Maximilian Laiacker, Dominik Sommer, Manuel Bejar, and Aníbal Ollero. Aerial manipulation robot composed of an autonomous helicopter and a 7 degrees of freedom industrial manipulator. In *2014 IEEE international conference on robotics and automation (ICRA)*, pages 2107–2112. IEEE, 2014.

[97] Wouter Kool, Fiery A Cushman, and Samuel J Gershman. When does model-based control pay off? *PLoS computational biology*, 12(8):e1005090, 2016.

[98] Christopher Korpela, Matko Orsag, and Paul Oh. Towards valve turning using a dual-arm aerial manipulator. In *2014 IEEE/RSJ International Conference on Intelligent Robots and Systems*, pages 3411–3416. IEEE, 2014.

[99] Christopher M Korpela, Todd W Danko, and Paul Y Oh. Mm-uav: Mobile manipulating unmanned aerial vehicle. *Journal of Intelligent & Robotic Systems*, 65(1-4):93–101, 2012.

[100] W. Kraus, V. Schmidt, P. Rajendra, and A. Pott. System identification and cable force control for a cable-driven parallel robot with industrial servo drives. In *2014 IEEE International Conference on Robotics and Automation (ICRA)*, pages 5921–5926, 2014. doi:10.1109/ICRA.2014.6907731.

[101] V Kučera and Carlos E De Souza. A necessary and sufficient condition for output feedback stabilizability. *Automatica*, 31(9):1357–1359, 1995.

[102] Sen M Kuo and Ajay B Puvvala. Effects of frequency separation in periodic active noise control systems. *IEEE transactions on audio, speech, and language processing*, 14(5):1857–1866, 2006.

[103] Robert Ladig, Hannibal Paul, Ryo Miyazaki, , and Kazuhiro Shimonomura. Aerial manipulation using multirotor uav: A review from the aspect of operating space and force. *Journal of Robotics and Mechatronics*, 33(2):196–204, 2021. doi:10.20965/jrm.2021.p0196.

[104] E. Lanteigne, W. Gueaieb, D. Robillard, and S. Recoskie. Unmanned airship design with sliding ballast: Modeling and experimental validation. In *2016 International Conference on Unmanned Aircraft Systems (ICUAS)*, pages 1246–1253, 2016. doi:10.1109/ICUAS.2016.7502527.

[105] Byung-Yoon Lee, Hae-In Lee, Dong-Wan Yoo, Gun-Hee Moon, Dong-Yeon Lee, Yun young Kim, and Min-Jea Tahk. Study on payload stabilization method with the slung-load transportation system using a quad-rotor. In *European Control Conference (ECC)*, pages 2097–2102. IEEE, 2015.

[106] Jongseok Lee, Ribin Balachandran, Yuri S Sarkisov, Marco De Stefano, Andre Coelho, Kashmira Shinde, Min Jun Kim, Rudolph Triebel, and Konstantin Kondak. Visual-inertial telepresence for aerial manipulation. In *2020 IEEE International Conference on Robotics and Automation (ICRA)*, pages 1222–1229. IEEE, 2020. doi:10.1109/ICRA40945.2020.9197394.

[107] Taeyoung Lee, Melvin Leok, and N Harris McClamroch. Geometric tracking control of a quadrotor uav on se (3). In *49th IEEE conference on decision and control (CDC)*, pages 5420–5425, 2010.

[108] Frank L Lewis, Draguna Vrabie, and Vassilis L Syrmos. *Optimal control*. John Wiley & Sons, 2012.

[109] George A Lindsay. Pressure energy and bernoulli's principle. *American Journal of Physics*, 20(2):86–88, 1952.

[110] Vincenzo Lippiello and Fabio Ruggiero. Exploiting redundancy in cartesian impedance control of uavs equipped with a robotic arm. In *IEEE/RSJ International Conference on Intelligent Robots and Systems (IROS)*, pages 3768–3773, 2012.

[111] Johan Löfberg. Yalmip: A toolbox for modeling and optimization in matlab. In *Proceedings of the CACSD Conference*, volume 3. Taipei, Taiwan, 2004.

[112] R. Lozano. *Unmanned Aerial Vehicles Embedded Control*. John Wiley-ISTE Ltd, 2010. URL `https://hal.archives-ouvertes.fr/hal-00449932`.

[113] Shujun Lu, Jae Heon Chung, and Steven A Velinsky. Human-robot collision detection and identification based on wrist and base force/torque sensors. In *Proceedings of the 2005 IEEE international Conference on Robotics and Automation*, pages 3796–3801. IEEE, 2005.

[114] Teppo Luukkonen. Modelling and control of quadcopter. *Independent research project in applied mathematics, Espoo*, 22:22, 2011.

[115] Guang Ma and Wenlong Cai. Design and application of model free controller. In *2011 International Conference on Electric Information and Control Engineering*, pages 2058–2061. IEEE, 2011.

[116] Kurt Magnus. *Vibrations*. Blackie & Son, 1965.

[117] Eduard Marmet. Windows cleaners of the burj khalifa at work, 2019. URL `https://live.staticflickr.com/65535/47092933624_055498abe0_b.jpg`.

[118] C Mavroidis, S Dubowsky, and V Raju. End-point control of long reach manipulator systems. *Proc. 9th World Congr. IFToMM*, pages 1740–1744, 1995.

[119] *EPOS4 Firmware Specification*. Maxon Motor AG, Sachseln OW, Switzerland, 2019. Accessed: Oct 30, 2020.

[120] *Maxon catalog*. Maxon motor AG, 2020. URL `https://www.maxongroup.de/medias/sys_master/root/8841936830494/EN-524.pdf`.

[121] *Maxon catalog*. Maxon motor AG, 2021. URL `https://www.maxongroup.com/medias/sys_master/root/8884194803742/EN-21-506-507-508-513.pdf`.

[122] *Maxon catalog*. Maxon motor AG, 2021. URL `https://www.maxongroup.com/medias/sys_master/root/8882781421598/EN-21-410-411.pdf`.

[123] *Maxon catalog*. Maxon motor AG, 2021. URL `https://www.maxongroup.com/medias/sys_master/root/8884126482462/EN-21-493-494.pdf`.

[124] *Maxon catalog*. Maxon motor AG, 2021. URL `https://www.maxongroup.com/medias/sys_master/root/8881624973342/EN-21-152.pdf`.

[125] Vicente Mayor, Rafael Estepa, Antonio Estepa, and German Madinabeitia. Deploying a reliable uav-aided communication service in disaster areas. *Wireless Communications and Mobile Computing*, 2019, 2019.

[126] Michael McGrath, David Howard, and Richard Baker. A lagrange-based generalised formulation for the equations of motion of simple walking models. *Journal of biomechanics*, 55:139–143, 2017.

[127] Rafik Mebarki, Vincenzo Lippiello, and Bruno Siciliano. Image-based control for dynamically cross-coupled aerial manipulation. In *2014 IEEE/RSJ International Conference on Intelligent Robots and Systems*, pages 4827–4833. IEEE, 2014.

[128] Jean-Pierre Merlet and Julien Alexandre-dit Sandretto. The forward kinematics of cable-driven parallel robots with sagging cables. In *Cable-Driven Parallel Robots*, pages 3–15. Springer, 2015.

[129] Nathan Michael, Jonathan Fink, and Vijay Kumar. Cooperative manipulation and transportation with aerial robots. *Autonomous Robots*, 30(1):73–86, 2011.

[130] Balmukund Mishra, Deepak Garg, Pratik Narang, and Vipul Mishra. Drone-surveillance for search and rescue in natural disaster. *Computer Communications*, 156:1–10, 2020.

[131] Ryo Miyazaki, Rui Jiang, Hannibal Paul, Koji Ono, and Kazuhiro Shimonomura. Airborne docking for multi-rotor aerial manipulations. In *2018 IEEE/RSJ International Conference on Intelligent Robots and Systems (IROS)*, pages 4708–4714. IEEE, 2018.

[132] Ryo Miyazaki, Rui Jiang, Hannibal Paul, Yanzhao Huang, and Kazuhiro Shimonomura. Long-reach aerial manipulation employing wire-suspended hand with swing-suppression device. *IEEE Robotics and Automation Letters*, 4(3): 3045–3052, 2019.

[133] Ryo Miyazaki, Hannibal Paul, Takamasa Kominami, and Kazuhiro Shimonomura. Wire-suspended device control based on wireless communication with multirotor for long reach-aerial manipulation. *IEEE Access*, 8:172096–172104, 2020.

[134] Hongwei Mo and Ghulam Farid. Nonlinear and adaptive intelligent control techniques for quadrotor uav–a survey. *Asian Journal of Control*, 21(2):989–1008, 2019.

[135] UM Rao Mogili and BBVL Deepak. Review on application of drone systems in precision agriculture. *Procedia computer science*, 133:502–509, 2018.

[136] Abdullah Mohiuddin, Taha Tarek, Yahya Zweiri, and Dongming Gan. A survey of single and multi-uav aerial manipulation. *Unmanned Systems*, 8(02): 119–147, 2020.

[137] David Morin. Normal modes. *Harvard University. http://www. people. f as. harvard. edu/djmorin/waves/normalmodes. pdf*, 2002.

[138] John J Murray and Gilbert H Lovell. Dynamic modeling of closed-chain robotic manipulators and implications for trajectory control. *IEEE Transactions on Robotics and Automation*, 5(4):522–528, 1989.

[139] Richard M Murray. *A mathematical introduction to robotic manipulation*. CRC press, 1994.

[140] Chu Anh My and Vu Minh Hoan. Kinematic and dynamic analysis of a serial manipulator with local closed loop mechanisms. *Vietnam Journal of Mechanics*, 41(2):141–155, 2019.

[141] Jawad Nagi, Alessandro Giusti, Luca M Gambardella, and Gianni A Di Caro. Human-swarm interaction using spatial gestures. In *2014 IEEE/RSJ International Conference on Intelligent Robots and Systems*, pages 3834–3841. IEEE, 2014.

[142] Syed Ahsan Raza Naqvi, Syed Ali Hassan, Haris Pervaiz, and Qiang Ni. Drone-aided communication as a key enabler for 5g and resilient public safety networks. *IEEE Communications Magazine*, 56(1):36–42, 2018.

[143] Varun Nayak, Christos Papachristos, and Kostas Alexis. Design and control of an aerial manipulator for contact-based inspection. *arXiv preprint arXiv:1804.03756*, 2018.

[144] Jorg Neupert, Tobias Heinze, Oliver Sawodny, and Klaus Schneider. Observer design for boom cranes with double-pendulum effect. In *2009 IEEE Control Applications,(CCA) & Intelligent Control,(ISIC)*, pages 1545–1550. IEEE, 2009.

[145] A. Ollero, G. Heredia, A. Franchi, G. Antonelli, K. Kondak, A. Sanfeliu, A. Viguria, J. R. Martinez-de Dios, F. Pierri, J. Cortes, A. Santamaria-Navarro, M. A. Trujillo Soto, R. Balachandran, J. Andrade-Cetto, and A. Rodriguez. The aeroarms project: Aerial robots with advanced manipulation capabilities for inspection and maintenance. *IEEE Robotics & Automation Magazine*, 25(4):12–23, Dec 2018.

[146] Anibal Ollero and Bruno Siciliano. *Aerial robotic manipulation*. Springer, 2019.

[147] Anibal Ollero, Marco Tognon, Alejandro Suarez, Dongjun Lee, and Antonio Franchi. Past, present, and future of aerial robotic manipulators. *IEEE Transactions on Robotics*, 2021.

[148] David E Orin and Ambarish Goswami. Centroidal momentum matrix of a humanoid robot: Structure and properties. In *2008 IEEE/RSJ International Conference on Intelligent Robots and Systems*, pages 653–659. IEEE, 2008.

[149] Matko Orsag, Christopher Korpela, Paul Oh, Stjepan Bogdan, and Anibal Ollero. *Aerial Manipulation*. Springer, 2018.

[150] C. Ott, M. A. Roa, and G. Hirzinger. Posture and balance control for biped robots based on contact force optimization. In *2011 11th IEEE-RAS International Conference on Humanoid Robots*, pages 26–33, Oct 2011.

[151] Christian Ott, Ranjan Mukherjee, and Yoshihiko Nakamura. Unified impedance and admittance control. In *2010 IEEE international conference on robotics and automation*, pages 554–561. IEEE, 2010.

[152] Christian Ott, Alexander Dietrich, and Alin Albu-Schäffer. Prioritized multi-task compliance control of redundant manipulators. *Automatica*, 53:416–423, 2015.

[153] Hyeonjun Park, Ji-Hun Bae, Jae-Han Park, Moon-Hong Baeg, and Jaeheung Park. Intuitive peg-in-hole assembly strategy with a compliant manipulator. In *IEEE ISR 2013*, pages 1–5. IEEE, 2013.

[154] Sangyul Park, Jeongseob Lee, Joonmo Ahn, Myungsin Kim, Jongbeom Her, Gi-Hun Yang, and Dongjun Lee. Odar: Aerial manipulation platform enabling omnidirectional wrench generation. *IEEE/ASME Transactions on mechatronics*, 23(4):1907–1918, 2018.

[155] Joshua Michael Peschel and Robin Roberson Murphy. On the human–machine interaction of unmanned aerial system mission specialists. *IEEE Transactions on Human-Machine Systems*, 43(1):53–62, 2012.

[156] Andreas Pott and Werner Kraus. Determination of the wrench-closure translational workspace in closed-form for cable-driven parallel robots. In *2016 IEEE International Conference on Robotics and Automation (ICRA)*, pages 882–887. IEEE, 2016.

[157] Prairie Aerial. "1500' tv tower." nov. 11, 2014. [YouTube video], 2014. URL `https://www.youtube.com/watch?v=f1BgzIZRfT8`.

[158] Gabriel Quere, Annette Hagengruber, Maged Iskandar, Samuel Bustamante, Daniel Leidner, Freek Stulp, and Jörn Vogel. Shared control templates for assistive robotics. In *2020 IEEE International Conference on Robotics and Automation (ICRA)*, pages 1956–1962. IEEE, 2020.

[159] Liyana Ramli, Zaharuddin Mohamed, Auwalu M Abdullahi, Hazriq Izzuan Jaafar, and Izzuddin M Lazim. Control strategies for crane systems: A comprehensive review. *Mechanical Systems and Signal Processing*, 95:1–23, 2017.

[160] Reuben Raz, Aviv Rosen, and Tuvia Ronen. Active aerodynamic stabilization of a helicopter/sling-load system. *Journal of Aircraft*, 26(9):822–828, 1989.

[161] Raymond L Robb. Hybrid helicopters: compounding the quest for speed. *Vertiflite*, 52(2), 2006.

[162] Fabio Ruggiero, Vincenzo Lippiello, and Anibal Ollero. Aerial manipulation: A literature review. *Robotics and Automation Letters*, 3(3):1957–1964, 2018.

[163] Markus Ryll, Davide Bicego, and Antonio Franchi. Modeling and control of fast-hex: a fully-actuated by synchronized-tilting hexarotor. In *IEEE/RSJ International Conference on Intelligent Robots and Systems (IROS)*, 2016.

[164] Koichi Sakata, Hiroyoshi Asaumi, Kazuyuki Hirachi, Kazuaki Saiki, and Hiroshi Fujimoto. Frequency separation self resonance cancellation for vibration suppression control of a large-scale stage using multiple position sensors. In

IECON 2013-39th Annual Conference of the IEEE Industrial Electronics Society, pages 6478–6483. IEEE, 2013.

[165] M Sanfourche, J Delaune, G Le Besnerais, H De Plinval, J Israel, Ph Cornic, A Treil, Y Watanabe, and A Plyer. Perception for uav: Vision-based navigation and environment modeling. *AerospaceLab*, (4):p–1, 2012.

[166] Yuri S Sarkisov, Grigoriy A Yashin, Evgeny V Tsykunov, and Dzmitry Tsetserukou. Dronegear: A novel robotic landing gear with embedded optical torque sensors for safe multicopter landing on an uneven surface. *IEEE Robotics and Automation Letters*, 3(3):1912–1917, 2018. doi:10.1109/LRA.2018.2806080.

[167] Yuri S Sarkisov, Grigoriy A Yashin, Evgeny V Tsykunov, and Dzmitry Tsetserukou. Dronegear: a compliant robotic landing gear for multicopters. In *3-rd Skoltech-MIT conference: Collaborative Solutions for Next Generation Education, Science and Technology*. Skoltech, 2018.

[168] Yuri S Sarkisov, Min Jun Kim, Davide Bicego, Dzmitry Tsetserukou, Christian Ott, Antonio Franchi, and Konstantin Kondak. Development of SAM: cable-suspended aerial manipulator. In *2019 International Conference on Robotics and Automation (ICRA)*, pages 5323–5329. IEEE, 2019. doi:10.1109/ICRA.2019.8793592.

[169] Yuri S Sarkisov, Min Jun Kim, Andre Coelho, Dzmitry Tsetserukou, Christian Ott, and Konstantin Kondak. Optimal oscillation damping control of cable-suspended aerial manipulator with a single imu sensor. In *2020 IEEE International Conference on Robotics and Automation (ICRA)*, pages 5349–5355. IEEE, 2020. doi:10.1109/ICRA40945.2020.9197055.

[170] Luis Sentis and Oussama Khatib. Synthesis of whole-body behaviors through hierarchical control of behavioral primitives. *International Journal of Humanoid Robotics*, 2(04):505–518, 2005.

[171] Guanya Shi, Xichen Shi, Michael O'Connell, Rose Yu, Kamyar Azizzadenesheli, Animashree Anandkumar, Yisong Yue, and Soon-Jo Chung. Neural lander: Stable drone landing control using learned dynamics. In *2019 International Conference on Robotics and Automation (ICRA)*, pages 9784–9790. IEEE, 2019.

[172] Kazuhiro Shimonomura. Aerial manipulation with wire-suspended devices. In *Aerial Robotics workshop*, 2019.

[173] Bruno Siciliano and Oussama Khatib. *Springer Handbook of Robotics*. Springer-Verlag, Berlin, Heidelberg, 2007. ISBN 354023957X.

[174] Bruno Siciliano, Lorenzo Sciavicco, Luigi Villani, and Giuseppe Oriolo. *Robotics: modelling, planning and control*. Springer Science & Business Media, 2010.

[175] Bora Simmons. *Nonformal Environmental Education Programs: Guidelines for Excellence*. NAAEE National Project for Excellence in Environmental Education, 2015. ISBN 1-884008-89-5.

[176] William Singhose and Dooroo Kim. Manipulation with tower cranes exhibiting double-pendulum oscillations. In *Proceedings 2007 IEEE International Conference on Robotics and Automation*, pages 4550–4555. IEEE, 2007.

[177] William Singhose, Dooroo Kim, and Michael Kenison. Input shaping control of double-pendulum bridge crane oscillations. *Journal of Dynamic Systems, Measurement, and Control*, 130(3), 2008.

[178] *JIVE Pro 120+ HV Operation Manual*. SOBEK Drives GmbH, 2017. URL `https://www.kontronik.com/en/products/speedcontroller/speedcontroller1/jive-pro/jive-pro-120-hv.html`.

[179] *KONTRONIK PYRO Motors Operation Manual*. SOBEK Drives GmbH, 2017. URL `https://www.kontronik.com/en/products/motors/pyro/pyro-650/pyro-650-65.html`.

[180] Zoltán S Spakovszky, M Greitzer, and I Waitz. Thermodynamics and propulsion. *web.mit.edu/16.unified/www/SPRING/propulsion/notes/notes.html*, 2008.

[181] Stantec. Biennial inspection of the george washington bridge, 2017. URL `http://www.stantec.com/content/dam/stantec/images/projects/0013/george-washington-bridge-inspection.jpg`.

[182] Nicolas Staub, Davide Bicego, Quentin Sablé, Victor Arellano, Subodh Mishra, and Antonio Franchi. Towards a flying assistant paradigm: the othex. In *IEEE International Conference on Robotics and Automation (ICRA)*, 2018.

[183] A Suárez, AM Giordano, K Kondak, G Heredia, and A Ollero. Flexible link long reach manipulator with lightweight dual arm: Soft-collision detection, reaction, and obstacle localization. In *IEEE International Conference on Soft Robotics (RoboSoft)*, pages 406–411, 2018.

[184] Alejandro Suárez, Guillermo Heredia, and Anibal Ollero. Lightweight compliant arm with compliant finger for aerial manipulation and inspection. In *IEEE/RSJ International Conference on Intelligent Robots and Systems (IROS)*, pages 4449–4454, 2016.

[185] Alejandro Suárez, Antonio Enrique Jimenez-Cano, Victor Manuel Vega, Guillermo Heredia, Angel Rodriguez-Castaño, and Anibal Ollero. Design of a lightweight dual arm system for aerial manipulation. *Mechatronics*, 50:30–44, 2018.

[186] Alejandro Suárez, P Sanchez-Cuevas, M Fernandez, M Perez, Guillermo Heredia, and Anibal Ollero. Lightweight and compliant long reach aerial manipulator for inspection operations. In *IEEE/RSJ International Conference on Intelligent Robots and Systems (IROS)*, pages 6746–6752, 2018.

[187] Alejandro Suárez, Fran Real, Victor M Vega, Guillermo Heredia, Angel Rodriguez-Castaño, and Anibal Ollero. Compliant bimanual aerial manipulation: Standard and long reach configurations. *IEEE Access*, 8:88844–88865, 2020.

[188] Chin Pei Tang. Lagrangian dynamic formulation of a four-bar mechanism with minimal coordinates, 2010.

[189] Dante Tezza and Marvin Andujar. The state-of-the-art of human–drone interaction: A survey. *IEEE Access*, 7:167438–167454, 2019.

[190] Justin Thomas, Joe Polin, Koushil Sreenath, and Vijay Kumar. Avian-inspired grasping for quadrotor micro uavs. In *ASME International Design Engineering Technical Conferences & Computers and Information in Engineering Conference*, 2013.

[191] Emanuel Todorov, Tom Erez, and Yuval Tassa. Mujoco: A physics engine for model-based control. In *2012 IEEE/RSJ International Conference on Intelligent Robots and Systems*, pages 5026–5033. IEEE, 2012.

[192] Marco Tognon. *Theory and Applications for Control and Motion Planning of Aerial Robots in Physical Interaction with particular focus on Tethered Aerial Vehicles*. PhD thesis, Institut national des sciences appliquées de Toulouse, 2018.

[193] Marco Tognon and Antonio Franchi. Omnidirectional aerial vehicles with unidirectional thrusters: Theory, optimal design, and control. *Robotics and Automation Letters*, 3(3):2277–2282, 2018.

[194] Teodor Tomic, Korbinian Schmid, Philipp Lutz, Andreas Domel, Michael Kassecker, Elmar Mair, Iris Lynne Grixa, Felix Ruess, Michael Suppa, and Darius Burschka. Toward a fully autonomous uav: Research platform for indoor and outdoor urban search and rescue. *IEEE robotics & automation magazine*, 19(3):46–56, 2012.

[195] Nguyen Khoi Tran. *Modeling and Control of a Quadrotor in a Wind Field*. McGill University (Canada), 2016.

[196] Dzmitry Tsetserukou, Naoki Kawakami, and Susumu Tachi. Vibration damping control of robot arm intended for service application in human environment. In *8th IEEE-RAS International Conference on Humanoid Robots*, pages 441–446. IEEE, 2008.

[197] Evgeny Tsykunov, Ruslan Agishev, Roman Ibrahimov, Luiza Labazanova, Akerke Tleugazy, and Dzmitry Tsetserukou. Swarmtouch: Guiding a swarm of micro-quadrotors with impedance control using a wearable tactile interface. *IEEE transactions on haptics*, 12(3):363–374, 2019.

[198] N. Vahrenkamp, T. Asfour, G. Metta, G. Sandini, and R. Dillmann. Manipulability analysis. In *2012 12th IEEE-RAS International Conference on Humanoid Robots (Humanoids 2012)*, pages 568–573, 2012. doi:10.1109/HUMANOIDS.2012.6651576.

[199] Kimon P. Valavanis and George J. Vachtsevanos. *Handbook of Unmanned Aerial Vehicles*. Springer Publishing Company, Incorporated, 2014. ISBN 9048197066.

[200] Joshua Vaughan, Dooroo Kim, and William Singhose. Control of tower cranes with double-pendulum payload dynamics. *IEEE Transactions on Control Systems Technology*, 18(6):1345–1358, 2010.

[201] Daniele Ventura, Michele Bruno, Giovanna Jona Lasinio, Andrea Belluscio, and Giandomenico Ardizzone. A low-cost drone based application for identifying and mapping of coastal fish nursery grounds. *Estuarine, Coastal and Shelf Science*, 171:85–98, 2016.

[202] Vojtech Veselỳ. Static output feedback controller design. *Kybernetika*, 37(2): 205–221, 2001.

[203] Vojtech Veselỳ. Robust output feedback controller design for linear parametric uncertain systems. *Journal of electrical engineering*, 53(5-6):117–125, 2002.

[204] Vojtech Veselỳ. Robust controller design for linear polytopic systems. *Kybernetika*, 42(1):95–110, 2006.

[205] Daniel KD Villa, Alexandre S Brandão, and Mário Sarcinelli-Filho. A survey on load transportation using multirotor uavs. *Journal of Intelligent & Robotic Systems*, pages 1–30, 2019.

[206] Robert L Williams II. Inverse kinematics and singularities of manipulators with offset wrist. *International Journal of Robotics and Automation*, 14(1): 1–8, 1999.

[207] Sebastian Wolf and Maged Iskandar. Extending a dynamic friction model with nonlinear viscous and thermal dependency for a motor and harmonic drive gear. In *2018 IEEE International Conference on Robotics and Automation (ICRA)*, pages 783–790. IEEE, May 2018.

[208] World Channel. "extreme jobs - high voltage power line inspection." may 8, 2016. [YouTube video], 2016. URL `https://www.youtube.com/watch?v=9YmFHAFYwmY&t`.

[209] Grigoriy A Yashin, Daria Trinitatova, Ruslan T Agishev, Roman Ibrahimov, and Dzmitry Tsetserukou. Aerovr: Virtual reality-based teleoperation with tactile feedback for aerial manipulation. In *2019 19th International Conference on Advanced Robotics (ICAR)*, pages 767–772. IEEE, 2019.

[210] Arda Yiğit, Gustave Grappe, Loïc Cuvillon, Sylvain Durand, and Jacques Gangloff. Preliminary study of an aerial manipulator with elastic suspension. In *2020 IEEE International Conference on Robotics and Automation (ICRA)*, pages 4287–4293. IEEE, 2020.

[211] Arda Yiğit, Miguel Arpa Perozo, Loïc Cuvillon, S. Durand, and J. Gangloff. Novel omnidirectional aerial manipulator with elastic suspension: Dynamic control and experimental performance assessment. *IEEE Robotics and Automation Letters*, 6:612–619, 2021.

[212] Kazuya Yoshida, Constantinos Mavroidis, and Steven Dubowsky. Impact dynamics of space long reach manipulators. In *Proceedings of IEEE International Conference on Robotics and Automation*, volume 2, pages 1909–1916. IEEE, 1996.

[213] Mami Yoshikawa, Atsushi Iwatani, and Jun Ishikawa. Damping control of suspended load for truck cranes in consideration of control input dimension. In *International Conference on Advanced Engineering Theory and Applications*, pages 436–446. Springer, 2017.

[214] Jonathan Zerihan and Xin Zhang. Aerodynamics of a single element wing in ground effect. *Journal of aircraft*, 37(6):1058–1064, 2000.

[215] Chi Zhang, Xiaoguang Zhou, Hang Zhao, Aini Dai, and Huiling Zhou. Three-dimensional fuzzy control of mini quadrotor uav trajectory tracking under impact of wind disturbance. In *2016 International Conference on Advanced Mechatronic Systems (ICAMechS)*, pages 372–377. IEEE, 2016.

[216] Guangyu Zhang, Yuqing He, Bo Dai, Feng Gu, Liying Yang, Jianda Han, and Guangjun Liu. Aerial grasping of an object in the strong wind: robust control of an aerial manipulator. *Applied Sciences*, 9(11):2230, 2019.

[217] Shilong Zhang and Ernest D Fasse. Spatial compliance modeling using a quaternion-based potential function method. *Multibody System Dynamics*, 4 (1):75–101, 2000.

[218] Moju Zhao, Tomoki Anzai, Fan Shi, Xiangyu Chen, Kei Okada, and Masayuki Inaba. Design, modeling, and control of an aerial robot dragon: A dual-rotor-embedded multilink robot with the ability of multi-degree-of-freedom aerial transformation. *IEEE Robotics and Automation Letters*, 3(2):1176–1183, 2018.